ABSTRACT

Title of dissertation: Accretion Physics Through the Lens of the Observer: Connecting Fundamental Theory with Variability from Black Holes

James Andrew Hogg, Doctor of Philosophy, 2018

Dissertation directed by: Professor Christopher Reynolds
Department of Astronomy

Variability is a generic feature of accretion onto black holes. In both X-ray binaries and active galactic nuclei, variability is observed on nearly all accessible timescales and across the entire electromagnetic spectrum. On different timescales and at different wavelengths it has unique signatures that can be used to characterize the accretion processes generating the emission and probe the accretion disks, which would otherwise be impossible. Despite having been observed for over fifty years, interpreting this variability is difficult. Simple phenomenological models have been used to explain the behaviors and geometries of the observed accretion disk, but they have yet to be rigorously tested in a full magnetohydrodynamic framework. In this dissertation we use high-resolution numerical models to investigate: (1) "propagating fluctuations" in mass accretion rate that give rise to the nonlinear signatures of accretion on viscous timescales, (2) the dynamics of truncated accretion disks which are invoked to explain the spectral variation of outbursting

X-ray binaries and the bifurcation of AGN accretion states, and (3) the large-scale magnetic dynamo behavior in thick and thin accretion disks.

We find that the structured variability readily seen in the light curves from accreting black holes (i.e. log-normal flux distributions, linear relations between the RMS and the flux, and radial coherence) quickly and naturally grows from the MRI-driven turbulence and that these properties translate into photometric variability. For the first time, we identify the large-scale magnetic dynamo as the source of the low-frequency modulations of the disk stress that cause this structure. We introduce a bistable cooling law into hydrodynamic and magnetohydrodynamic simulations to study the manifestation of a truncated accretion disk in each regime. We find that rather than a truncation edge, the transition is better described by a "truncation zone" when the angular momentum transport and heating is governed by MRI-driven turbulence instead of a true viscosity. Additionally, we find that the hot gas in the simulation buoyantly rises in a gentle outflow and eventually fills the entire volume, instead of simply being confined to the innermost region. The outflow interacts with the disk body and enhances the magnetic stresses, which could produce stronger quasiperiodic variability. Finally, we conduct an investigation of the large-scale magnetic dynamo using a suite of four global magnetohydrodynamic disk simulations with scaleheight ratios of $h/r = \{0.05, 0.1, 0.2, 0.4\}$. Most notably, the organization that is prevalent in accretion disk simulations and described as a "butterfly pattern" does not occur when $h/r \geq 0.2$, despite the dynamo action still operating efficiently.

Accretion Physics Through the Lens of the Observer: Connecting Fundamental Theory with Variability from Black Holes

by

James Andrew Hogg

Dissertation submitted to the Faculty of the Graduate School of the
University of Maryland, College Park in partial fulfillment
of the requirements for the degree of
Doctor of Philosophy
2018

Advisory Committee:
Professor Christopher Reynolds, Chair/Advisor
Professor Coleman Miller
Professor Richard Mushotzky
Dr. Lisa Winter, External Examiner
Professor William Dorland, Dean's Representative

Preface

The research presented in Chapters 2-5 of this dissertation has been published in *The Astrophysical Journal* and is presented here with minimal modification. Each chapter corresponds to the following papers:

- Chapter 2 - *"Testing the Propagating Fluctuations Model with a Long, Global Accretion Disk Simulation," The Astrophysical Journal*, Volume 826, Issue 1, Article ID. 40, 20 pp. (2016)

- Chapter 3 - *"The Dynamics of Truncated Black Hole Accretion Disks. I. Viscous Hydrodynamic Case," The Astrophysical Journal*, Volume 843, Issue 2, Article ID. 80, 15 pp. (2017)

- Chapter 4 - *"The Dynamics of Truncated Black Hole Accretion Disks. II. Magnetohydrodynamic Case ," The Astrophysical Journal*, Volume 854, Issue 1, Article ID. 6, 17 pp. (2018)

- Chapter 5 - *"The Influence of Accretion Disk Thickness on the Large-scale Magnetic Dynamo," The Astrophysical Journal*, , Volume 861, Issue 1, Article ID. 24, 15 pp. (2017)

To me, the contents of this dissertation form a coherent story. In the first act, we investigate propagating fluctuations in mass accretion rate and in the second act we explore the dynamics of truncated accretion disks. In the third act, we focus on a reoccurring character who always seems to be tangled up in the action as we search for the driver of variability in our simulations - the large-scale magnetic dynamo.

Many of the same topics are revisited in each chapter and the story develops as new pieces of evidence come to light. We see how each of the many characters driving the disk behavior builds off, depends on, and, ultimately, affects the others. At times, it may seem like the story was written with the dynamo as the main character from the outset. This could not be further from the truth as the dynamo was only meant to be a minor player. We originally wrote it into the story at each juncture for its novelty, but ended up discovering it serves the role of the mysterious figure who lurks in the background and connects all the otherwise unexplainable occurrences in our story. At the end we try to uncover its identity, and do a little, but it manages to just remain in the shadows.

I'm not sure where the story goes from here or how it ends, but it leaves me with a few questions. What makes the dynamo tick? Are there other important characters who have yet to make their debut? Maybe there is an accomplice or two? It seems like the series is just beginning and the answers to these questions must come in a sequel or two....

Dedication

To those who open it and learn something new.

Acknowledgments

More often than not, my life as a graduate student mirrored the accretion disks I studied. There was an underlying bulk flow taking me in the right direction, but I often felt like I was chaotically getting knocked about by hiccups like codes that mysteriously crash or paper introductions that I just couldn't write. Often these frustrations were quickly followed by successes that forced me in the opposite emotional direction, like telescope proposals being accepted despite unlikely odds or great conversations at conferences.

To properly thank everyone who has helped me along my way to a Ph.D. and aided in dampening the intrinsic instabilities of graduate school would require a document as long as this dissertation. Nevertheless, I would like to thank everyone in the Astronomy department at UMD, including the faculty, staff, post docs, students I taught as a T.A., and of course my fellow graduate students. These people made it a great place to work for six years and I feel incredibly lucky to have been surrounded by such great folks.

I will forever be grateful for the mentorship of Chris Reynolds and it is hard to encapsulate all that it has meant. His foresight and expertise enabled these projects, but even more than that, his supervision shaped who I became as a scientist. I always felt like an equal in our partnership and he always encouraged me to pursue my own ideas. Consequently, many of the rabbit holes I went down were dead ends, but they helped build intuition for the problem, and it taught me that failure is an unavoidable part of creating new knowledge. A few were not dead ends and turned

into results or accomplishments that I am incredibly proud of, so I am thankful for the opportunities.

While this dissertation focuses on work done as a graduate student at the University of Maryland, my Ph.D. journey and scientific training actually began 1507 miles away at the University of Colorado. In Boulder I gained my first real research experience under the supervision of Lisa Winter. That work sparked my interest in accretion physics which led to the work presented here. I am certain I would not have been as successful in graduate school (or even gotten in) if I had not had her guidance. Her selflessness, knowledge, and enthusiasm mean the world to me, and I am thrilled she has agreed to serve as a member of my advisory committee.

Earning a Ph.D. is taxing on those around you. I am thankful for the support and love from my family and girlfriend over the last six years. Any time I needed reassurance or a confidence boost I came to them and, while they willingly encouraged me and offered support, I know it passed on a lot of undue stress. This degree is as much yours as it is mine.

I would be remiss without acknowledging the companionship of my cat, Stella, throughout my grad school adventure. Oddly enough she was born on August 29, 2012, which my first day as a University of Maryland student, so she has been with me since the beginning. Despite her best efforts to contribute to my papers by walking across my keyboard, her text was never (knowingly) included in the submitted work, so she has never received authorship credit. If there are any egregious typos in this work, please attribute them to her.

Table of Contents

List of Tables

List of Figures

List of Abbreviations

ADAF	Advection Dominated Accretion Flow
AGN	Active Galactic Nucleus
Be	Bernoulli Parameter
BHB	Black Hole Binary
CAR	Continuous Time, Auto-Regressive
CDAF	Convection Dominated Accretion Flow
CV	Cataclysmic Variable
D.o.F	Degrees of Freedom
EMF	Electromotive Force
GBHB	Galactic Black Hole Binary
GRRMHD	General Relativity, Radiation Magnetohydrodynamics
HD	Hydrodynamics
IMBH	Intermediate Mass Black Hole
ISCO	Innermost Stable Circular Orbit
LLAGN	Low-Luminosity Active Galactic Nucleus
LSST	Large Synoptic Survey Telescope
MCMC	Markov Chain Monte Carlo
MHD	Magnetohydrodynamics
MRI	Magnetorotational Instability
NICER	Neutron star Interior Composition Explorer
OU	Ornstein-Uhlenbeck
PDF	Probability Density Function
PSD	Power Spectral Density
QPO	Quasi-Periodic Oscillation
RHD	Radiation Hydrodynamics
RMS	Root-Mean Square
SED	Spectral Energy Distribution

SMBH Supermassive Black Hole

TESS Transiting Exoplanet Survey Satellite

UMD University of Maryland
UV Ultraviolet

YSO Young Stellar Object

Chapter 1: Introduction

Gas accretion onto compact objects remains one of the great unsolved problems in astrophysics. The accretion process, broadly, is the process of a massive body acquiring mass by drawing in material from its surrounding environment courtesy of its gravitational attraction. From the smallest scales of pebble-sized chondrule accumulation from the solar nebula that forms comets and asteroids up to the largest possible scales of large galaxy clusters pulling in gas and smaller galactic halos from the cosmic web, we see many different forms of accretion. While they are all fascinating, this dissertation will focus on the accretion processes occurring in gas disks around black holes. In particular, we model black hole accretion flows with the overarching goal of connecting accretion physics with spectral and photometric variability that can be observed with telescopes and used to probe black hole systems. We explore the physics driving "propagating fluctuations in mass accretion rate" in Chapter 2 and the dynamics of truncated accretion disks in Chapter 3 and Chapter 4. Throughout this dissertation work the large-scale magnetic dynamo consistently appears as a key player in the disk behavior so we dedicate Chapter 5 to characterizing its properties as the disk scale-height ratio is changed.

We begin here by reviewing the basics of black holes, accretion theory, and

accretion disk modeling before diving into the main thesis where the individual studies are discussed. This is meant to serve as a general overview of accretion and introductions to each of the specific topics studied are kept to the relevant chapters. This chapter closes with a brief discussion of how this dissertation fits into the advancement of accretion physics at large, and the dissertation closes with a summary of the main results and what lies on the horizon. The essence of this thesis and what we hope to convey is that more physically grounded variability models are desperately needed to fully leverage the next generation of time-domain surveys, we are in the midst of an exciting period of rapid advancement, and there are many fundamental aspects of accretion still to be uncovered.

1.1 Black Holes

Black hole systems fall into two classes. The first is occupied by stellar mass black holes which form as the final remnants of massive stars. A star of mass greater than $M_* \geq 30$ $M_\odot$ will spend several million years on the main sequence fusing hydrogen into helium. As the fuel is exhausted, heavier elements are consumed and the star evolves off the main sequence. Following several periods of burning successively heavier and heavier elements, the star is left with an iron core. At this point the heating mechanism is removed since no more energy can be extracted. Lacking thermal support against its own self-gravity, the massive star is doomed to collapse upon itself in a sudden, catastrophic event. This event typically leads to one of the shortest lived and most violent events in the cosmos - a supernova explosion.

In less than a second, a black hole of a few to tens of solar masses is formed and the remaining material is ejected. Alternatively, there is mounting evidence some of the higher mass stellar mass black holes may be formed from direct collapse, i.e. with no explosion in a "failed" supernova (Adams et al., 2017a,b; Gerke et al., 2015; Heger et al., 2003).

The majority of these massive stars are found in binary systems. If the binary survives the supernova, the black hole from the progenitor massive star and the companion star will be in close proximity when the secondary evolves off the main sequence itself. When the envelope of the secondary star's atmosphere expands past the Roche lobe it feels a greater pull to the black hole. It will then be accreted and can be seen as an X-ray binary.

The second class of black holes, supermassive black holes (SMBHs), are roughly a million times more massive than stellar mass black holes and believed to reside in the center of all galaxies. Observationally, $\approx 10\%$ of all SMBHs are active galactic nuclei (AGNs) because they are actively accreting at high rates. Dynamical processes in the host galaxy or gravitational interactions with other galaxies can drive dust and gas from the interstellar medium to the center and feed the SMBH. At lower levels, accretion can occur when outflows from massive stars in the center of the galaxy provide a background of ambient gas. In more exotic cases, stars that wander too close to a quiescent black hole can get ripped apart and trigger an accretion episode in a tidal disruption event.

Even though they are common to most massive galaxies, the origin of SMBHs remains a mystery and is vigorously debated in the literature. At high redshift,

i.e. early cosmic time, massive quasars have been discovered. Current theories hypothesize they must have formed initially at high masses by the direct collapse of massive gas clouds, through runaway collisions of stars or black holes in clusters, or from the first stars like stellar mass black holes. These scenarios all have challenges they must overcome before being fully accepted.

The important influence of SMBHs on galaxy formation and evolution is not debated, however. Through feedback processes, i.e. radiative and mechanical energy injection, the energy released through accretion can regulate the growth and development of galaxies and star formation. The quintessential example is the $M - \sigma$ relationship where the mass of the central supermassive black hole is seen to scale with the velocity dispersion of the host galaxy bulge. This relation is typically interpreted as an example of mechanical feedback from outflows launched by the accretion disk around the SMBH acting on its host galaxy, or at least evidence of a mutual evolution between the comparatively small scales of the accretion environment of the black hole and the larger galaxy in which it lives.

Despite the discrepancy between masses, the diversity in environments, and the differences in initial feeding, the two classes of black hole systems seem to be quite similar. This similarity has led stellar mass black hole systems to be referred to as "microquasars" as they essentially look like scaled down AGNs in their behaviors and properties. For our theoretical exploration of the accretion physics powering these objects, it suggests the same processes are operating in both types of systems and motivates a general approach for understanding their properties. In fact, much of what will be studied has application in most, if not all, ionized accretion disks,

including those around accreting white dwarfs (CV systems) and neutron stars.

Before proceeding, this introduction would be remiss by failing to mention a third class that has been hypothesized to exist with masses of ≈ 1000 $M_\odot$ between the two standard black hole populations, aptly named "intermediate mass" black holes (IMBHs). Several candidates of black holes belonging to this elusive species have been found, but they come with ambiguity. If they exist, these black holes may have primordial origins so positively identifying an IMBH would bolster the direct collapse models of massive black hole formation. However, much of the difficulty in finding IMBHs is that their mass determinations are typically based on their luminosity, which is assumed to obey the Eddington limit, discussed below. A number of IMBH candidates have recently been show to be super-Eddington pulsars, but it is not known if black holes can produce super-Eddington luminosities.

1.2 The Accretion Problem

Before diving into the advanced numerical modeling of this dissertation, it is prudent to frame the context for this work by revisiting the analytics that underpin accretion theory in order to build an intuitive understanding of the governing processes.

The simplest accretion imaginable is a central massive object embedded within a uniform medium of zero angular momentum. This scenario is referred to as Bondi accretion after the seminal work of Bondi (1952) and results in a gas inflow that will be steady and spherically symmetric. This problem has two characteristic length

scales. The first is called the Bondi radius,

$$r_B = \frac{GM}{c_{s,\infty}^2}$$

where G is the gravitational constant, M is the mass of the central object, and $c_{s,\infty}^2$ is the sound speed of the ambient medium with the sound speed being set by the gas pressure P and gas density, ρ,

$$c_s = \sqrt{\frac{\gamma P}{\rho}}. \tag{1.1}$$

This is the farthest radius where the gravitational pull of the object is strong enough to dominate the gas motions and ρ first begins to increase above the ambient value. This is often called the "accretion radius", r_{acc}. The second length scale is the sonic radius, r_s

$$r_s = \frac{GM}{2c_s^2}.$$

Two fundamental equations govern the gas dynamics of the inflow and the location where the gas must become transonic. These are the (stationary and spherically symmetric) continuity equation

$$\frac{d\rho}{dr} = \frac{\rho}{vr^2}\frac{d(vr^2)}{dr} \tag{1.2}$$

and the Euler equation describing the gas momentum

$$v\frac{dv}{dr} + \frac{1}{\rho}\frac{dP}{dr} + \frac{GM}{r} = 0. \tag{1.3}$$

Combining and rearranging gives an equation of the form,

$$\frac{1}{2}\left(1 - \frac{c_s^2}{v^2}\right)\frac{d(v^2)}{dr} = -\frac{GM}{r^2}\left[1 - \left(\frac{2c_s^2 r}{GM}\right)\right]. \tag{1.4}$$

This equation has six distinct families, but accretion from a static distant reservoir is only allowed when the inward flow becomes transonic at r_s as the radial velocity of the flow accelerates from subsonic to supersonic. In a Bondi flow the mass accretion rate is determined by the properties of the ambient medium as well as the mass of the accretor,

$$\dot{M} = 4\pi q_s \frac{G^2 M^2 \rho_\infty}{c_{s,\infty}^3}, \tag{1.5}$$

where,

$$q_s(\gamma) = \frac{1}{4}\left(\frac{2\gamma}{5-3\gamma}\right)^{(5-3\gamma)/(2\gamma-2)}, \tag{1.6}$$

and is a function of the adiabatic index, γ. For an ideal gas, $\gamma = 5/3$, $q_s = 1/4$.

In this idealized case, $\dot{M}$ can be arbitrarily high. However, associated with the infall is the release of gravitational potential energy,

$$\Delta E_{acc} = \frac{GMm}{R_*} \tag{1.7}$$

where m is the mass of an individual particle and R_* is the surface of the accretor, or in the extreme case of a (non-spinning) black hole, the Schwarschild radius,

$$R_s = \frac{2GM}{c^2}. \tag{1.8}$$

It is reasonable to assume that much of this energy is released in the form of electromagnetic radiation. Radiation fields from a central point exert a pressure

$$P_{rad} = \frac{L}{4\pi R^2 c} \tag{1.9}$$

that is proportional to the source luminosity (L) and inversely to the square of the local radius (R). This pushes back against the gas with a force

$$F_{rad} = P_{rad}\kappa m \tag{1.10}$$

and impedes the inflow. For our application we are primarily concerned with ionized flows where

$$\kappa = \sigma_T / m_p \tag{1.11}$$

and σ_T is the cross-section provided by Thomson scattering of the photons on the electrons which drag the protons, i.e. the dominant mass, m_p. Setting this equal to the gravitational force on a proton, a critical upper limit on the luminosity is found,

$$L_{Edd} = \frac{4\pi G M c m_p}{\sigma_T}. \tag{1.12}$$

If the luminosity exceeds this value (the Eddington luminosity), presumably due to an exceptionally high accretion rate, particles will on average feel a net outward push that slows or halts accretion. Below this limit, the luminosity will be

$$L_{acc} = \frac{GM\dot{M}}{R_*} \tag{1.13}$$

if all of the kinetic energy of the gas is given up to radiation.

The simplicity of the spherical Bondi accretion flow also breaks down if the gas has any angular momentum when it is fed from large distances as a nonzero specific angular momentum prevents it from accreting directly. Instead, shocks and other dissipative processes circularize the gas and cause it to settle into the lowest energy orbit around the central object corresponding to its specific angular momentum. This orbit will be circular and have a radius of

$$R_c = \frac{l^2}{GM} \tag{1.14}$$

where $l = Rv_\phi$ is the specific angular momentum. In the absence of angular momentum transport, the gas will orbit indefinitely. However, if there is a source of

viscosity, ν, and there is a radial shear, then neighboring annuli can exchange angular momentum. For Keplerian orbits in a Newtonian gravitational potential the angular velocity is,

$$\Omega_K(R) = \left(\frac{GM}{R^3}\right)^{1/2}, \tag{1.15}$$

and the shear arising from this differential rotation is,

$$R\frac{d\Omega}{dR} = \frac{3}{2}\Omega. \tag{1.16}$$

By assuming the gas radiates its thermal energy away efficiently, we can make the "thin disk" approximation, where we treat the disk in two dimensions by integrating vertically through a height, h, to get a surface density,

$$\Sigma = \rho h. \tag{1.17}$$

The torque that a specific annulus feels from the one directly exterior that it is in contact with is,

$$Y(R) = 2\pi\nu R^3\Sigma\frac{d\Omega}{dR}. \tag{1.18}$$

Additionally, the annulus we are considering is also the source of torque for its interior neighbor, therefore, the *net* torque this one annulus feels is equal to $\partial Y/\partial R\, dR$.

Looking at Equation 1.18, we see that the torque will always be negative for a Keplerian disk so angular momentum is being transported outward. As a parcel of gas loses angular momentum it sinks deeper into the gravitational potential. The mass accretion rate at an annulus in the disk is thus given by the mass within an annuli and the velocity at which it flows inwards

$$\dot{M} = -2\pi R\Sigma v_R. \tag{1.19}$$

We expect the inwards velocity to be quite low and since it will be negative, we multiply by -1 so the mass accretion rate is positive for the sake of convention.

We can now write two conservation laws that describe the mass accretion and the angular momentum transport. The mass conservation is given by

$$R\frac{\partial \Sigma}{\partial t} + \frac{\partial}{\partial R}(R\Sigma v_r) = 0, \tag{1.20}$$

and the conservation of angular momentum equation becomes,

$$R\frac{\partial}{\partial t}(\Sigma R^2\Omega) + \frac{\partial}{\partial R}(R\Sigma v_r R^2\Omega) = \frac{1}{2\pi}\frac{\partial Y}{\partial R}. \tag{1.21}$$

These two conservation laws can be combined to yield the disk evolution equation for a Keplerian disk,

$$\frac{\partial \Sigma}{\partial t} = \frac{3}{R}\frac{\partial}{\partial R}\left[R^{\frac{1}{2}}\frac{\partial}{\partial R}(\nu\Sigma R^{\frac{1}{2}})\right]. \tag{1.22}$$

For illustration, we for now discuss a steady thin disk and take ν to be constant, but will discuss the evolution of an accretion disk with a time variable effective viscosity and the dramatic affect it has on the disk behavior in Chapter 2. By removing the time dependence, we arrive at,

$$\nu\Sigma = \frac{\dot{M}}{3\pi}\left[1 - \left(\frac{R_*}{R}\right)^{1/2}\right]. \tag{1.23}$$

With this expression we can examine some scalings. Taking the limit that $R_* << R$, we find that $\Sigma \approx \dot{M}/(3\pi\nu)$ and $v_r \approx -3\nu/(2R)$. For a fixed accretion rate, this a basically a statement about the flow continuity in that the surface density decreases as you increase the viscosity and the radial velocity increases. Furthermore, the radial velocity decreases with increasing radius, as would be expected since the

overall disk evolution is slower further out as the dynamical timescale,

$$t_{dyn} = \sqrt{\frac{R^3}{GM}}, \tag{1.24}$$

increases. Finally, for a given viscosity, the surface density increases with increased accretion rate. Basically, this is the statement that denser disks accrete at a higher rate than less dense disks for a given angular momentum transport efficiency.

Through the mutual torquing of annuli work is done and the gas heats. To maintain the thin disk, this energy is radiated away in the electromagnetic radiation that we observe. The viscous dissipation rate per unit plane surface area is given by,

$$D(R) = \frac{Y(R)}{4\pi R}\frac{d\Omega}{dR} = \frac{1}{2}\nu\Sigma\left(R\frac{d\Omega}{dR}\right)^2, \tag{1.25}$$

which becomes

$$D(R) = \frac{3GM\dot{M}}{8\pi R^3}\left[1 - \left(\frac{R_*}{R}\right)^{1/2}\right]. \tag{1.26}$$

This basic observable is completely independent of the nature of the viscosity provided it regulates both the mass accretion and dissipation.

So far, we have made much headway in understanding accretion without specifying exactly *what* gives rise to the disk's viscosity. In fact, understanding the source of the effective viscosity in the disk and its behavior remains a central focus for all of accretion theory. The densities around compact objects are generally too low to have a significant molecular viscosity from the interaction of individual particles. Estimates of the Reynolds number, or the ratio of the fluid inertia to viscous dissipation, for a luminous accreting black hole place $Re > 10^{14}$ (Frank et al., 2002) which is much too high to allow for any appreciable angular momentum transfer.

However, hydrodynamic flows with high Reynolds numbers have a unique characteristic: turbulence develops easily. This was recognized by Shakura & Sunyaev (1973) as a viable way to drive accretion and serves as the foundation of the "α-prescription" which is still commonly used to describe disk accretion. Their key insight was that turbulence can introduce a stress,

$$T_{r\phi} = \nu \rho R \frac{d\Omega}{dR}. \tag{1.27}$$

The effective turbulent kinematic viscosity, ν, with units of $length^2/time$, can be linked to the length scale of the turbulence eddies and their velocities,

$$\nu = v_{turb} l_{turb}. \tag{1.28}$$

Turbulent eddies are expected be some fraction of the disk height and they will be less than the sound speed since any supersonic gas will quickly shock and force the gas to be subsonic. These assumptions can be subsumed into the α-parameter such that,

$$\nu = \alpha c_s h = \alpha \left(\frac{h}{r}\right)^2 \Omega, \tag{1.29}$$

where $0 < \alpha < 1$ and is a dimensionless scaling parameter. They also proposed that with an α-parameter the local vertically averaged stress can be related directly to the local vertically averaged total pressure as

$$T_{r\phi} = \alpha P. \tag{1.30}$$

It is worth nothing that strictly this α-parameter is 2/3 the previous α parameter associated with the turbulent properties. This term is often neglected since it is of order unity, but it can be the source of ambiguity.

Introducing the α-parameter allows for an estimate of the viscous time,

$$t_{visc} \sim \frac{t_{dyn}}{\alpha(h/r)^2}. \tag{1.31}$$

Unsurprisingly, a larger accretion efficiency (higher α) leads to shorter viscous times and faster gas inspiral. Similarly, thinner disks have longer accretion times for a given α, since the turbulent eddies span a smaller range of radii and the sound speed is lower because the disk is cooler.

Parameterizing the viscosity this way allows the disk structure to be determined. Shakura & Sunyaev (1973) found three distinct regions that can form, depending on the disk temperature. The first is a radiation dominated regime where the pressure from radiation is greater than the thermal pressure and the dominant opacity comes from electron scattering. Importantly, the disk scale height is independent of radius and depends only on the mass accretion rate

$$h_{rad} = \frac{3\kappa\dot{M}}{8\pi c}, \tag{1.32}$$

with a fixed opacity, κ. Radiation pressure dominated disks are expected for $M = 10$ $M_\odot$ black holes when the luminosity exceeds $L \geq 3 \times 10^{37}$ ergs s^{-1} and for $M = 10^7$ $M_\odot$ SMBHs when $L > 5 \times 10^{43}$ ergs s^{-1}. The second disk region occurs if thermal gas pressure dominates, but electron scattering is still the dominant source of opacity. The final possible region is a gas pressure dominated region where free-free emission dominates.

The work in this dissertation will focus formally on the gas pressure dominated systems, but it is worth a slight digression to mention the curious behavior

of radiation pressure dominated accretion disks. The linear dependence of the viscous stress in the α-formalism on the total pressure introduces two instabilities that were recognized shortly after the α-prescription was proposed (e.g. Lightman, 1974; Lightman & Eardley, 1974; Pringle et al., 1973; Shakura & Sunyaev, 1976), but have yet to be fully understood.

Firstly, there is a local thermal instability. The heating rate of an α-disk has the form,

$$Q^+ \sim 2hrT_{r\phi}\left|\frac{d\Omega}{dR}\right|. \tag{1.33}$$

In radiation pressure dominated regions the viscous stress heating the disk is given by,

$$T_{r\phi} = \frac{\alpha a T^4}{3}, \tag{1.34}$$

where a is the radiation density constant. Taking the radiation pressure as the main support, the disk thickness in hydrostatic equilibrium is expressed in terms of temperature (rather than $\dot{M}$ as before)

$$h = \frac{2aT^4}{3\Sigma\Omega}. \tag{1.35}$$

Using Equation 1.34 and Equation 1.35 in Equation 1.33, means that locally, for a constant α and Σ, the heating rate will scale as $Q^+ \propto T^8$. The cooling in this disk, on the other hand, is given by

$$Q^- \sim \frac{4caT^4}{3\kappa\Sigma}. \tag{1.36}$$

and therefore scales as $Q^- \propto T^4$. With this steep temperature scaling of the disk heating coupled to the less responsive cooling, a small perturbation away from equilibrium will cause the disk to catastrophically heat with a positive perturbation

or catastrophically cool with a negative perturbation. Piran (1978) identified the following inequality to describe this scenario

$$\left.\frac{\partial \ln Q^{+}}{\partial \ln T}\right|_{\Sigma} > \left.\frac{\partial \ln Q^{-}}{\partial \ln T}\right|_{\Sigma}. \tag{1.37}$$

Initially, simulations investigating the stability of accretion disks found that the disks were stable because of time delays between the stress that injects energy and the response of the pressure once the energy is dissipated (Hirose et al., 2009; Turner et al., 2002). However, those simulations were diffusive and the simulation domain was small. The same initial disk conditions are unstable to thermal runaway when evolved under different algorithms (Jiang et al., 2013) and other independent simulations also find thermal instability (Fragile et al., 2018). Recent work finds that there is not a clear delineation between a disk being stable or unstable, but rather there is a probabilistic component as fluctuations can delay the instability or stave it off completely in some realizations of the same conditions (Janiuk & Misra, 2012; Ross et al., 2017). The work of Jiang et al. (2016) showed that changes in the iron opacity for hot AGN disks can provide a stabilizing effect that prevents thermal instability on one side of the iron "bump."

The second instability arises from a counterintuitive property of the angular momentum transportation when radiation provides the dominant pressure. The vertically integrated viscous stress is given by,

$$W = 2\alpha h P, \tag{1.38}$$

for which we can use equation 1.35 and see that all else being constant, $W \propto \Sigma^{-1}$. This is because the temperature and pressure are independent of the gas density,

unlike the gas pressure dominated disk regions. Consequently, rings form in the disk as lower Σ annuli have higher integrated stress so material is driven into the denser regions of lower stress. These rings are expected to have widths of order h. The numerical evidence of this instability developing is shaky because of resolution concerns, but simulations find evidence that rings of material can form on timescales consistent with this viscous instability (Mishra et al., 2016).

1.3 The Magnetorotational Instability

The α-disk model of Shakura & Sunyaev (1973) provided a reasonable angular momentum transport mechanism in accretion disks, but no instability was identified that could drive the turbulence. For an unmagnetized accretion disk whose gas follows Keplerian orbits, the Rayleigh criterion for hydrodynamic stability is satisfied because the angular momentum profile increases with radius so no turbulence is expected. To reconcile this discrepancy and the significant challenge it posed, Shakura & Sunyaev invoked magnetic fields to explain the anomalous behavior. Accretion disks around black holes and other compact objects are hot and ionized, therefore it is reasonable to expect one of the many magnetohydrodynamic (MHD) instabilities is at play. In a groundbreaking paper seventeen years later, Balbus & Hawley (1991) proved this intuition correct with the rediscovery of the magnetorotational instability (MRI). This instability had previously been discovered by Velikhov (1959) and Chandrasekhar (1960) to explain the stability of Couette flow in the presence of a magnetic field, but its applicability to accretion disks was not appreciated for over

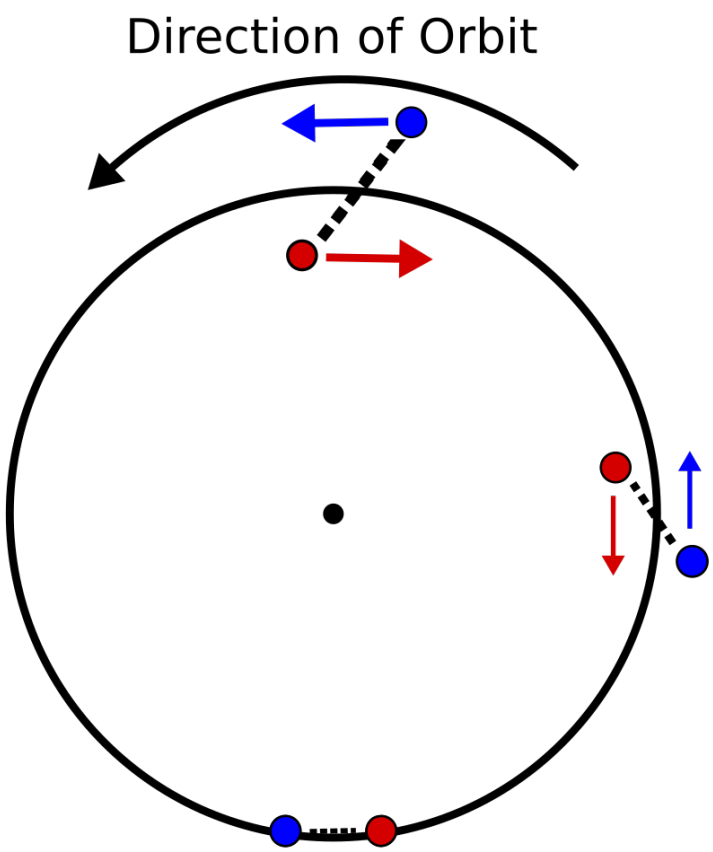

Figure 1.1: Illustration of the basic principle behind the angular momentum transport between two initially neighboring particles that separate and the growth of the MRI. The dashed line represents the spring-like magnetic field tethering the two particles. The arrows' direction shows how the force is felt and the size corresponds to the amplitude.

three decades.

Conceptually, the MRI is relatively simple and arises by slightly perturbing gas on circular orbits and stretching two elements of gas connected with a magnetic field. Independently, each one of these actions would introduce restorative forces that lead to stable, oscillatory behavior. If gas on a circular orbit is nudged radially inwards, it has an excess of angular momentum for its new radius and it will want to move to larger radii. Similarly, if it is pushed outwards, the dearth of angular

momentum will make it fall inwards. The epicyclic frequency,

$$\kappa = \left(\frac{2\Omega}{R} \frac{d(R^2\Omega)}{dR} \right)^{1/2}, \tag{1.39}$$

is the natural frequency of the oscillation. Separately, if two gas elements threaded with a magnetic field are pulled apart, they feel a tension force proportional to $(\mathbf{B} \cdot \nabla)\delta\mathbf{B}$ for a small induced field,

$$\delta\mathbf{B} = (\mathbf{B} \cdot \nabla)\boldsymbol{\xi} = ikB\boldsymbol{\xi} \tag{1.40}$$

where k is the wavenumber, $\boldsymbol{\xi}$ is a small spatial displacement and B is the total magnetic field strength (a scalar). Using the Alfvén velocity,

$$v_{Az}^2 = \frac{B_z^2}{4\pi\rho}, \tag{1.41}$$

the system takes the form of a simple harmonic oscillator and effectively acts like a system with a spring constant equal to $(\boldsymbol{k} \cdot \boldsymbol{v}_A)^2$ in its linear growth phase.

Coupling the effects of these two normally stabilizing effects leads to the dramatic instability that powers accretion. In an idealized sense, the local, differentially rotating disk can be thought of as two neighboring annuli where the inner element orbits more quickly. If the two annuli are tethered by magnetic fields, the field will be stretched as the inner annulus pulls ahead of the outer annulus. The field resists this stretching and tries to enforce rigid rotation. This tugging applies a negative torque on the inner annulus and a positive torque on the outer annulus, thus causing the inner annulus to lose angular momentum and sink to smaller radii while the opposite happens to the outer radii. This further stretches the field, enhances the

tension force, and exacerbates the infall, leading to instability. An illustration of this scenario is shown in Figure 1.1.

The simplest manifestation of the MRI involves an initial field that is purely poloidal. Geometrically, the problem is treated in cylindrical coordinates (R, θ, ϕ) with axisymmetric perturbations with the spacetime dependence $e^{i(\mathbf{k}_R R+\mathbf{k}_z z-\omega t)}$. The background flow is taken to be constant on cylinders, the magnetic field is weak so that its initial state has a negligible influence, and $B_R = 0$. Finally, the Boussinesq approximation of incompressibility ($\nabla \cdot \mathbf{v} = 0$) is used so magnetoacoustic modes can be ignored. In terms of the vertical wavenumber, k_z, the dispersion relation takes the form:

$$\frac{k^2}{k_z^2}\widetilde{\omega}^4 - \left[\kappa^2 + \left(\frac{k_R}{k_z}N_z - N_R\right)^2\right]\widetilde{\omega}^2 - 4\Omega^2 k_z^2 v_{Az}^2 = 0. \tag{1.42}$$

In this equation $k^2 = k_z^2 + k_R^2$,

$$\widetilde{\omega}^2 = \omega^2 - k_z^2 v_{Az}^2, \tag{1.43}$$

and N_z^2 and N_R^2 are the vertical and radial elements of the Brunt-Väisälä frequency,

$$N^2 = N_R^2 + N_z^2 = -\frac{3}{5\rho}(\nabla P) \cdot (\nabla \ln P\rho^{-5/3}) \tag{1.44}$$

of buoyant oscillations in the atmosphere.

Stability demands $\omega^2 > 0$, giving the following stability criterion,

$$k_z^4 v_{Az}^4 + k_z^2 v_{Az}^2 \left(N^2 + \frac{d\Omega^2}{d\ln R}\right) + N_z^2 \frac{d\Omega^2}{d\ln R} > 0. \tag{1.45}$$

For a buoyantly stable disk with $N_R, N_z > 0$, the stability criterion is satisfied if,

$$\frac{d\Omega^2}{dR} > 0. \tag{1.46}$$

This will always lead to instability for astrophysical Keplerian-like accretion disks with $\Omega \propto R^{-3/2}$ no matter how weak the magnetic field since some unstable wavenumber in the perturbation will be accessible. The growth rate of the instability is fast,

$$|\omega_{MRI}| = \frac{1}{2}\left|\frac{d\Omega}{d\ln R}\right|, \tag{1.47}$$

or $\omega = 0.75\Omega$ for a Keplerian accretion disk, and corresponds to a wavelength of,

$$\lambda_{MRI} = 2\pi\sqrt{\frac{16}{15}}\frac{v_{Az}}{\Omega}. \tag{1.48}$$

It should be noted that there is an upper limit to the strength of the magnetic field that can seed the MRI. If the field is so strong that the ratio of the gas pressure to pressure from the magnetic field is less than a value of 3, the critical wavelength of the MRI exceeds the disk height and thus cannot drive the instability.

Assuming the necessary conditions are met, the instability will grow, become non-linear, and ultimately saturate in a turbulent state. The early growth of the MRI resembles a vertical, interchange instability. At the end of the linear growth phase the channel solution becomes unstable to parasitic secondary Kelvin-Helmholtz type instabilities (Goodman & Xu, 1994), evolves nonlinearly, and eventually saturates in a state of subequipartition between the magnetic pressure and thermal pressure (a ratio of $\sim 1 : 10$) with the field dominated by its toroidal component. The saturation of the MRI driven turbulence is a crucial component in understanding how angular momentum is transported in accretion disks, but is still poorly understood. Dynamical equations have been derived to describe the local kinematic and magnetic stresses in the disk which ultimately associate saturation with the dissipation of turbulent the kinetic and magnetic energies (Kato

& Yoshizawa, 1995; Ogilvie, 2003). The helicity (winding) of the turbulent eddies and magnetic field has also been invoked as a way to mediate the saturation as the magnetic helicity can back react on the kinetic helicity and restrict further growth (Blackman & Field, 2002). It has also been proposed that the MRI may saturate when the growth rate of the secondary parasitic modes is comparable to its own (Pessah & Goodman, 2009).

As a final comment on the MRI, it is important to mention that MRI driven turbulence is much more nuanced than that envisioned in the simple α-disk and in some respects is fundamentally different. The details of the differences are thoroughly presented in Pessah et al. (2008), but essentially the two key assumptions that frame the α-disk model are: 1) that the disk stress can be treated as a vertically averaged shear viscosity and 2) that the stress depends linearly on the shear rate. Real astrophysical disks, however, are much more complex than a simple vertically averaged thin disk model can properly capture since vertical gradients and correlations within the flow have to be fully considered, which can violate the first assumption. This is a less serious indiscretion than the second assumption, however. Analytical models predict, and numerical models confirm, that there is indeed a non-linear scaling of the disk stress with shear parameter. Luckily, this has little effect on our work and we will frequently refer to the α-model despite this discrepancy. The MHD simulations used in the studies of this dissertation use either Newtonian or pseudo-Newtonian gravitational potentials so the shear rate is nearly constant for the bulk of the disks used in the analyses. Nevertheless, it is crucial to be mindful of this sensitivity because in other contexts, like a star accreting from a disk where

the gas has to decelerate to match the stellar rotation, there can be strong changes in the shear which can break the assumptions of the α-disk.

1.4 Techniques for Simulating Accretion Disks

Analytic theory is essential for understanding the accretion phenomenon, but only numerical models can capture the global and nonlinear behaviors of the turbulence. To date, a large and rich body of simulation work has been dedicated to studying how MRI driven turbulence behaves and transports angular momentum including studies using unstratified shearing boxes (e.g. Hawley & Balbus, 1991; Hawley et al., 1995), stratified shearing boxes (e.g. Brandenburg et al., 1995; Stone et al., 1996), unstratified global models (e.g. Armitage, 1998; Armitage & Reynolds, 2003; Armitage et al., 2001; Hawley, 2001; Sorathia et al., 2012), stratified global disk models (e.g. Hawley, 2000; Hawley & Krolik, 2001; Reynolds & Miller, 2009; Sorathia et al., 2010), relativistic global models (e.g. De Villiers et al., 2003; Gammie et al., 2003; McKinney, 2006), and global models with radiative transfer (e.g. Jiang et al., 2014; McKinney et al., 2014; Sądowski et al., 2015). Here, we present a general overview of the fundamentals of accretion disk simulation, some points of caution, and the two algorithms applied in this dissertation.

Like all modeling efforts, simulating accretion disks is a game of approximation. Fully capturing the physics of an accreting system would require simulating the motions of each and every particle, and the forces acting upon them. While this is a noble goal, it is impossible. Luckily, a few simplifying assumptions make the

problem tractable and allow us to create models that seem to resemble physical systems. The starting point for most accretion disk simulations, and where we will begin, is to consider the gas as either a magnetized or viscous fluid, depending on the aims of the study. The codes used in this dissertation are grid-based which means the physical domain is divided into cells defined by a numerical mesh and the calculations are made based on the values of the discrete cells and their neighbors. This approach offers many benefits because the fluid equations are known well and the calculations can be made in coordinates that naturally lend themselves to the problem. In our case we will use spherical coordinates which is a more natural way to follow the geometry and scaling in the calculation, rather than a rectilinear geometry, for instance. Additionally, the full volume can easily be divided into sub-domains that can largely evolve independently so a single CPU core does not need to know the state of the entire simulated disk, and instead only the values of cells around the perimeter of the sub-domain volume. At each time step, each core performs the calculation for the sub-volume of the disk it is assigned and only needs to communicate with the cores performing calculations on the other nearby regions in the simulation. This allows the simulations to be parallelized efficiently so the calculation can be distributed across thousands of cores on a supercomputer.

Grid-based simulations bring their own technical challenges, though. The timestep needed to stably integrate the evolution for a cell in a given direction x is set by the shortest crossing time scaled by the Courant-Friedrichs-Lewy (C_0) number. In hydrodynamics the shortest crossing time is set by the summation of the fluid velocity and sound speed while in MHD the crossing time is set by the

velocity plus the speed of the fast magnetosonic wave,

$$\Delta t_x = \frac{C_0 \Delta x}{|v| + c_{f,x}}. \tag{1.49}$$

In cylindrical and spherical coordinate systems a constant opening angle in the ϕ- and/or θ- directions means the innermost cells set the minimum timestep because they are the smallest physically and these locations are also where the highest velocities in an accretion disk are found. For the outer portions of the disk where the evolution is slower, this spends unnecessary computational time integrating smaller timesteps than are required which can greatly enhance the computational costs and adds unnecessary numerical error. The most modern codes, although not the codes used in this dissertation, work around this algorithmically by implementing adaptive meshes to adjust the refinement in different regions of the grid mesh and by using adaptive time stepping that will integrate different regions in comparable times, e.g. evolving the inner region of an accretion disk simulation for several timesteps before evolving the outer region.

A larger concern comes from simulating turbulence on a grid. When energy is injected, it cascades to larger wavenumbers, and is ultimately deposited into thermal energy on a dissipative scale. It is currently impossible to capture the full separation of scales needed to properly model the inertial range of the cascade, especially in global simulations like those presented in this dissertation. As such, much effort has gone into understanding what resolutions are needed to produce consistent macroscale behaviors. Local shearing box simulations, where a small portion of a larger disk is modeled, have been invaluable in providing a more detailed

understanding of the small-scale turbulence that can't otherwise be captured. A set of convergence criteria have been established by many dedicated resolution studies that serve as guidelines of "best practice" for resolvability in numerical models. The resolution requirements needed to model MRI-driven turbulence and the robustness of simulations that abide by these has nearly reached consensus, but it is an issue that must constantly be revisited. Throughout the chapters studying MHD disks we will discuss the previous resolution studies in more depth and rigorously demonstrate that our models are well-resolved.

There are numerical worries in MHD simulations as well. The solenoidal constraint, $\nabla \cdot \mathbf{B} = 0$, must be fulfilled at all times and grid-based codes do not do this naturally. Several elegant solutions have been developed to rectify this shortcoming and here we use the method of constrained transport (Evans & Hawley, 1988). When considering a single cell in the grid mesh, there are several locations by which we can define it, for instance the geometric center of the cell, the centers of the faces that define it, or even the midpoints along the cell edges. Depending on the type of variable (i.e. scalar or vector, density or magnetic field), certain positions are more amenable. Constrained transport works by staggering the mesh and integrating the magnetic fluxes from the induction equation directly using Stokes' theorem,

$$\frac{db_x}{dt} dA + \oint \mathcal{E} \cdot d\mathbf{l} = 0. \tag{1.50}$$

For a cell face with an area dA and a direction normal to the surface x, the electromotive force $\mathcal{E}$ is calculated along the edges of the face and used to update the face centered magnetic field, denoted as b rather than the cell-centered magnetic field

(B). Since each face acts as the interface between two cells in a certain direction, there is a precise cancelation between the two cell's outwardly directed field. This cancelation ensures that any magnetic field initialized as divergence free will remain divergence free to machine accuracy as it is evolved.

Turning to the actual calculation performed, the computational problem of simulating an accretion disk can be boiled down to integrating a set of hyperbolic partial differential equations of the form,

$$\frac{\partial \mathbf{U}}{\partial t} + \nabla \cdot \mathbf{f}(\mathbf{U}) = \mathbf{S}(\mathbf{U}), \tag{1.51}$$

in the most abstract sense. This equation describes the changes in the conserved quantities state vector, $\mathbf{U}$, which describes the fluid's mass, momentum, and energy. The three terms denote the temporal change of $\mathbf{U}$, the fluxes for each element in $\mathbf{U}$, $\mathbf{f}(\mathbf{U})$, and any source terms, $\mathbf{S}(\mathbf{U})$, which includes effects like artificial cooling. To close the equations, an equation of state for the gas is included and in MHD the induction equation is also needed.

The first type of algorithm used to solve this problem is the finite differencing method used by the *Zeus* MHD code and used for the disk simulations presented in Chapter 2. The second is the finite volume method used by the *PLUTO* code and used in simulations presented in Chapters 3, 4, and 5. In discussing these algorithms here, we mean to provide a brief overview of the important concepts and general philosophies behind the simulation methods since specifics about each code can be found in the supporting documentation, referred to in the relevant chapters. Additionally, the details of each simulation presented in this dissertation (including

the equations evolved, grid configurations, initial conditions, quality checking, etc.) is kept to the appropriate chapter.

The *Zeus* code is the older and simpler of the two. The basic approach taken in a finite difference scheme is to evolve the values of $\mathbf{U}$ for a point in space and can be illustrated by considering a one-dimensional cell, I_i spanning $I_i = [x_{i-1/2}, x_{i+1/2}]$ at a time t^n with size $\Delta x = x_{i+1/2} - x_{i-1/2}$. In the simplest form the conservation equations are discretized as,

$$\frac{d}{dt}\mathbf{U}(x,t) = \mathbf{f}(\mathbf{U}(x_{i-1/2},t)) - \mathbf{f}(\mathbf{U}(x_{i+1/2},t)). \tag{1.52}$$

Integrating in time by the timestep between t^n and t_{n+1} according to the CFL condition and rearranging, this equation becomes,

$$\begin{aligned}\mathbf{U}(x,t^{n+1}) = \mathbf{U}(x,t^n) &+ \int_{t^n}^{t^{n+1}} \mathbf{f}(\mathbf{U}(x_{i-1/2},t))dt \\ &- \int_{t^n}^{t^{n+1}} \mathbf{f}(\mathbf{U}(x_{i+1/2},t))dt.\end{aligned} \tag{1.53}$$

Defining

$$\mathbf{U}_i^n = \frac{1}{\Delta x}\int_{x_{i-1/2}}^{x_{i+1/2}} \mathbf{U}(x,t^n)dt \tag{1.54}$$

and

$$\mathbf{f}_{i\pm1/2} = \frac{1}{\Delta t}\int_{t^n}^{t^{n+1}} \mathbf{f}(\mathbf{U}(x_{i\pm1/2},t))dt \tag{1.55}$$

the simple Eulerian form of the next timestep is given by

$$\mathbf{U}_i^{n_1} = \mathbf{U}_i^n + \frac{\Delta t}{\Delta x}(\mathbf{f}_{i-1/2} - \mathbf{f}_{i+1/2}). \tag{1.56}$$

The actual algorithm used by *Zeus* uses more advanced and accurate than outlined here, but we only mean to demonstrate the underlying principles of the method.

In practice, for each iteration/timestep in the integration *Zeus* solves the system of equations in three general substeps. The first step is the "source" step which takes the state **U** and solves the finite difference approximations to the momentum and energy equations. The second step evolves the magnetic fields using the method of characteristics within the framework of the method of constrained transport. The method of characteristics accounts for the propagation of Alfvén waves by including the magnetic tension. Not only is this an important physical component of the MHD disk, but it improves stability by removing artificial large amplitude, high frequency waves introduced by boundaries and discontinuities. The final step is the "transport" step which handles the advection of the fluid through each zone. This step solves the finite-difference approximations, but in integral form so that the flux of material is evolved.

One of the benefits of *Zeus* is that its relative simplicity translates into algorithmic speed. This performance means that computational resources are used very efficiently so simulations can be run for long durations and at higher resolutions than might be possible with other codes. For our application in studying the development of propagating fluctuations in mass accretion rate, this was paramount and made *Zeus* the ideal code for the investigation. However, this performance gain comes at the cost of formal overall energy conservation. While mass is conserved since step three evolves the integral form of the equations and there are no sources terms for the density in step one, the total energy is not conserved because internal energy is evolved which introduces grid errors from the source terms.

PLUTO is distinct from *Zeus* in many ways. Primarily, the conservation

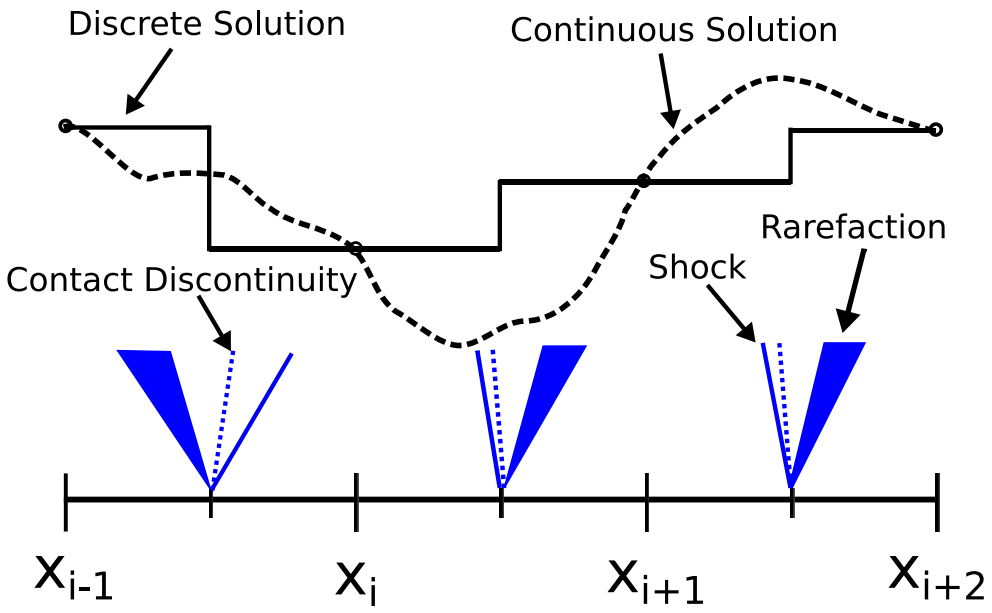

Figure 1.2: Schematic of cell discretization in the Riemann problem with first-order spatial reconstruction for a generic variable. The bar height represents the cell's value. The dashed line indicates the continuous solution the cells are approximating. Overlaid in blue is a representation of the propagation of the contact discontinuities, left and right going shocks, and rarefactions induced by the sharp discontinuities. Here, the vertical direction is meant to represent the forward propagation in time between a time t_n and t_{n+1}.

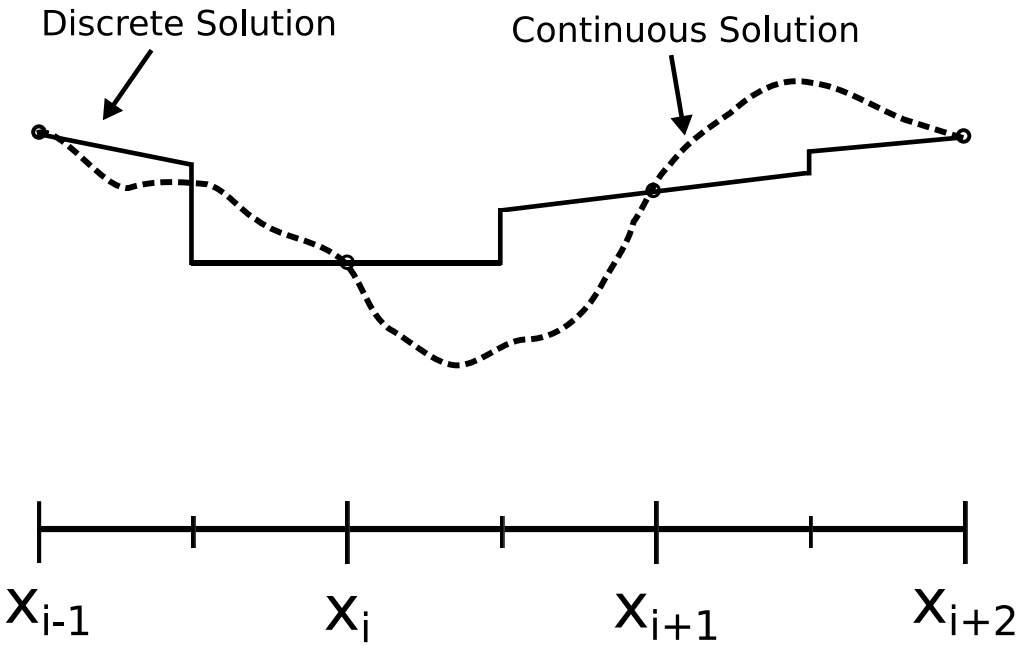

Figure 1.3: Schematic of cell discretization in the Riemann problem with second-order spatial reconstruction for a generic variable where height represent its value. The dashed line indicates the continuous solution the cells are approximating. Notice how the discontinuities are more mild than the first-order accurate case and therefore better describe the true solution.

equations are solved with a volume integrated approach, also known as a Godunov method after Sergei Godunov who first developed this method in 1959, where the focus is on the entire quantity within a cell, rather than an individual point. To understand the finite volume method conceptually, we can again consider a one-dimensional cell, I_i spanning $I_i = [x_{i-1/2}, x_{i+1/2}]$ at a time t^n with size $\Delta x = x_{i+1/2} - x_{i-1/2}$. Now, we will consider the conservation equations in integral form,

$$\frac{d}{dt}\int_{x_{i-1/2}}^{i+1/2} \mathbf{U}(x,t)dx = \mathbf{F}(\mathbf{U}(x_{i-1/2},t)) - \mathbf{F}(\mathbf{U}(x_{i+1/2},t)), \tag{1.57}$$

with $\mathbf{F}(\mathbf{U}(x_{i-1/2},t))$ denoting the total flux through the cell surface on that side summed over the area. Integrating in time and rearranging, this equation becomes,

$$\int_{x_{i-1/2}}^{x_{i+1/2}} \mathbf{U}(x,t^{n+1})dx = \int_{x_{i-1/2}}^{x_{i+1/2}} \mathbf{U}(x,t^n)dx + \int_{t^n}^{t^{n+1}} \mathbf{F}(\mathbf{U}(x_{i-1/2},t))dt - \int_{t^n}^{t^{n+1}} \mathbf{F}(\mathbf{U}(x_{i+1/2},t))dt. \tag{1.58}$$

Defining

$$\mathbf{U}_i^n = \frac{1}{\Delta x}\int_{x_{i-1/2}}^{x_{i+1/2}} \mathbf{U}(x,t^n)dt \tag{1.59}$$

and

$$\mathbf{F}_{i\pm1/2} = \frac{1}{\Delta t}\int_{t^n}^{t^{n+1}} \mathbf{F}(\mathbf{U}(x_{i\pm1/2},t))dt \tag{1.60}$$

the simple Eulerian form of the next timestep is given by

$$\mathbf{U}_i^{n_1} = \mathbf{U}_i^n + \frac{\Delta t}{\Delta x}(\mathbf{F}_{i-1/2} - \mathbf{F}_{i+1/2}). \tag{1.61}$$

The benefit of this volume integrated formulation is that it is conservative to machine precision so that flow properties like the total energy are properly accounted for.

Like *Zeus*, the *PLUTO* code solves the conservation equations of HD or MHD in three substeps during each iteration; however, the actual algorithmic methods used by *PLUTO* are quite distinct and overall more rigorous. First, interpolation routines reconstruct a piecewise polynomial approximation of the state from cell averages. For our work we use a linear reconstruction which is second order accurate.

Next, the numerical fluxes are calculated. This is more challenging than in the finite difference schemes because the discontinuity at each cell interface must be accounted for. If the value at the interface is calculated by a simple average of the neighboring cell values, for instance, unphysical oscillations appear in the solution as the nonlinear development across the interfaces affects the linear approximation. Instead, it must be treated as a Riemann problem and use approximate solvers to capture effects from left and right moving shock waves, rarefaction fans, and contact discontinuities that would develop. A schematic of these components are shown in Figure 1.2 for a first order accurate spatial reconstruction to help visualize the role of the different waves and the impact of implementing a linear reconstruction in improving the accuracy of the solution. Figure 1.3 shows the second order accurate spatial reconstruction. By evolving the change in the integrated amount of a given quantity like energy and momentum contained within the cell volume based on the total fluxes through the cell surfaces, the code is fully conservative.

In the final step, the state is marched forward in time. For this work we rely on Runge-Kutta methods which improve accuracy by evaluating the timestep integral

in multiple stages, s, per step of size h. These methods can be generalized as,

$$y_{n+1} = y_n + \sum_{i=1}^{s} b_i k_i, \tag{1.62}$$

where,

$$k_i = hy'\left(t_m + c_i h, t_m + \sum_{j=1}^{i-1} a_{ij} k_j\right) \tag{1.63}$$

where i goes from 1 to s and a, b, and c are coefficients.

Overall, the extra machinery of the finite volume method in *PLUTO* makes it slower than the finite difference method used in *Zeus*. Still, it is fast enough to enable the long-duration, high-resolution simulations that are performed in this dissertation. With this slight performance sacrifice comes many crucial benefits. For instance, we use *PLUTO* to model HD and MHD disks with a bistable cooling function to trigger thermal instability. It is essential to faithfully capture the thermally driven dynamics in these simulations which mandates a fully conservative code is used instead of a non-conservative finite difference type code.

1.5 The Dissertation in Context

Variability was one of the first distinguishing properties of quasars. Matthews & Sandage (1963) found that 3C 48 showed 0.4 mag variation over 13 months. They identified the emission as coming from an area of less than two-tenths of a parsec based on the light travel time of the emission. At that time, it was not known that this was a SMBH system so the large variability along with its unexplained Doppler broadened Balmer lines made it an enigma. Other early studies of similarly odd radio sources with large redshifts in their spectra also found more rapid variability

on timescales of days to weeks(e.g. Sandage, 1964; Sharov & Efremov, 1963; Smith & Hoffleit, 1963). Modern X-ray studies of AGN find appreciable variability on timescales of hours and even minutes. As an extreme example of variability, several "changing-look" AGNs have been found where the accretion luminosity appears to abruptly decrease.

Variability is also a strong characteristic of X-ray binaries. Due to their high temperatures, they can only really be observed at high energies in the X-rays. As such, observations must be done in space and it took slight longer to discover these objects than it did for quasars. Once they were discovered, however, they provided the first widely accepted proof for the existence of black holes with the discovery of X-rays from Cygnus X-1 (Bolton, 1971, 1972) and have offered a wealth of knowledge about accretion physics. The benefit of studying accretion in X-ray binaries is that they grant access to variability on all important accretion timescales. With satellites like the *Rossi X-ray Timing Explorer* (RXTE), accretion could be studied from dynamical timescales, thanks to its millisecond timing resolution, up to feeding events that caused it to go into outburst because of its 17-year long mission.

The minuscule apparent size of X-ray binaries and AGNs on the sky prevents imaging these systems. In lieu of this direct method of studying the accretion physics occurring within them, indirect methods must be used. The most powerful probe we have of these perplexing objects is their variability in electromagnetic radiation because signatures of the accretion physics are imprinted on the emission. In the fifty years that variability has been studied, a rich phenomenology has developed, yet a disconnect remains between the fundamental theoretical principles describing

accretion and the interpretation of astrophysical black hole observations.

This is not to say accretion theory is lacking - quite the contrary, in fact. The analytic theory, which we have provided a brief introduction to here, is vast and well-developed. The rise of robust simulations has been central to pushing forward on this front and achieving many victories, including verifying the chief angular momentum transport mechanism is MRI-driven turbulence. Local shearing-box simulations have explored the development of this turbulence and global simulations investigated the fundamental properties of both thick and thin accretion disk geometries. There are now major pushes to develop spectral models from simulations, understand the launching of jets and outflows from disks, properly include the effects from radiative physics on the flow, and even model accretion disks around binary black holes.

We currently find ourselves in a unique time where time domain astronomy has become a major focus and there several current and future telescopes like NICER, *TESS*, and LSST whose primary goals are to survey the variable sky. Coupled with the growing capability of simulations, there is a fortunate confluence of observational and theoretical developments that will allow for an unprecedented advancement in our understand of black hole accretion. To enable this, though, more reliable simulations are needed that can be connected to empirical signatures. Many conclusions drawn from spectral and timing studies are based on simple analytical arguments. The primary goal of this dissertation is to help provide a theoretical grounding for several common models of photometric variability observed from these systems. We specifically target two accretion scenarios that are commonly invoked to explain observations: propagating fluctuations in mass accretion Chapter 2 and truncated

accretion disks Chapters 3 and 4. Broadly speaking, we aim to establish the validity of the scenario and study the variability and manifestation in MHD. Throughout this work, we shed light on modifications that exist from standard α-disk models and reveal the reoccurring role of the magnetic dynamo. The dynamo is so significant in the disk evolution that we conduct a studied dedicated to studying its sensitivity to disk height Chapter 5.

Chapter 2: Propagating Fluctuations In Mass Accretion Rate

2.1 Introduction

There is increasing evidence that the interplay between the local angular momentum transport from magnetohydrodynamic (MHD) turbulence and the more global accretion flow shapes the behavior of the mass accretion (e.g. Sorathia et al., 2010). The primary goal of this chapter is to connect MHD accretion disk theory with one of the most widely discussed phenomenological models for global disk variability, the propagating fluctuations model. We explore how a stochastically varying effective viscosity leads to the growth of so-called "propagating fluctuations" in our long, global accretion disk simulation and relate the behavior of our simulation to observable properties from accreting black holes.

The viscous behavior of the disk ultimately arises because of net internal stress due to correlated fluctuations in the magnetic field and correlated fluctuations in gas velocity (Balbus & Papaloizou, 1999). These correlated fluctuations lead to the Maxwell stress ($M_{R\phi} = -B_R B_\phi / 4\pi$) and the Reynolds stress ($R_{R\phi} = \rho v_R \delta v_\phi$), respectively. Following the α-prescription, the effective α from the net stress is thus

the ratio of the volume averaged stress to the volume averaged pressure,

$$\alpha = \frac{\langle M_{R\phi} + R_{R\phi} \rangle}{\langle P \rangle}. \tag{2.1}$$

This serves to parameterize the effectiveness of angular momentum loss by the stresses acting on the gas in the disk. In this chapter we use angled brackets to denote a volume average for a given quantity, U, where

$$\langle U(t) \rangle = \frac{\int U(t, r, \theta, \phi) r^2 \sin\theta \mathrm{d}r\mathrm{d}\theta\mathrm{d}\phi}{\int r^2 \sin\theta \mathrm{d}r\mathrm{d}\theta\mathrm{d}\phi}. \tag{2.2}$$

Turbulent fluctuations in the disk will naturally lead to stochastic variability in the effective α and provide an intuitive explanation for the existence of broadband photometric variability observed in both galactic black hole binaries (GBHBs) and active galactic nuclei (AGNs). The photometric variability is observed across several decades in frequency, typically in the form of aperiodic "flicker" type noise. Employing a stochastic α, Lyubarskii (1997) developed a model for this flicker noise by linearizing the standard geometrically thin, optically thick accretion disk evolution equations. The model was limited to small perturbations in α, but it reproduced the power spectrum of the fluctuations and laid the foundation for the subsequent development of the propagating fluctuations model.

The propagating fluctuations model has since taken a more generalized form and served as a phenomenological description for the structure and organization of the broadband variability for GBHBs and AGNs. The evolution of a geometrically thin, optically thick accretion disk (in units where $G = M = c = 1$) is governed by a nonlinear diffusion equation (Pringle, 1981),

$$\frac{\partial \Sigma}{\partial t} = \frac{3}{R} \frac{\partial}{\partial R} \Big[R^{\frac{1}{2}} \frac{\partial}{\partial R} (\nu \Sigma R^{\frac{1}{2}}) \Big], \tag{2.3}$$

where R is the distance from the central engine, $\nu(\Sigma; R, t)$ is the local effective viscosity in the disk, and $\Sigma(R, t)$ is the local surface density. In this equation, the diffusive redistribution of angular momentum depends on the product of the effective viscosity and the local surface density. If the effective viscosity fluctuates, the instantaneous mass accretion rate ($\dot{M}$) at each point in the disk is thus the product of the many prior stochastic events. A consequence of the multiplicative combination is that fluctuations in $\dot{M}$ will tend to be preserved as they accrete as higher density regions will typically have higher $\dot{M}$ and lower density regions will typically have lower $\dot{M}$. Additionally, since the viscous time increases with radii, higher frequency fluctuations will be imposed on the accretion flow as material moves inwards. This will lead to the development of a hierarchical structure in the fluctuations with the smaller, high frequency fluctuations imposed upon the larger, low frequency fluctuations.

The appeal of the propagating fluctuations model is that it explains three properties of black hole variability that have been difficult to reproduce with other variability models. First, GBHB and AGN light curves are log-normally distributed (Gaskell, 2004; Uttley et al., 2005) which is accounted for through the multiplicative combination of many independent fluctutations. Second, and related to the log-normal distribution, the root-mean square (RMS) of the flux variability in the light curves of both GBHBs and AGNs depends linearly on the flux level (Gaskell, 2004; Negoro & Mineshige, 2002), the so-called RMS-flux relationship. This indicates the mass accretion rate variation has a constant fractional amplitude and that the mechanism driving variability is, therefore, independent of the accretion

rate (Uttley & McHardy, 2001). Finally, coherent fluctuations in the emission at different wavebands from GBHBs have frequency dependent time lags with variability in higher energy bands lagging variability in lower energy bands (Nowak et al., 1999a,b). This "hard lag" is believed to be a signature of fluctuations in the accretion flow moving to smaller radii in the disk where the emission temperature is higher.

Despite the success the propagating fluctuations model has had in explaining the phenomenology of GBHB and AGN variability, the model has yet to be examined in the context of modern MHD theory. To date, the model has been examined in the context of geometrically-thin (vertically-integrated) α-disks in which some stochasticity is imposed upon α. How well this viscous behavior translates into an MHD disk is unknown. Particularly challenging is the timescales on which α fluctuates and drives variability within the accretion flow. Lyubarskii (1997) prescribes α fluctuations to be slow, of order the viscous time. However, if fluctuations in α are solely due to turbulent fluctuations, we might expect them to be on the dynamical timescale. Cowperthwaite & Reynolds (2014) show, using a semi-analytic model, that propagating fluctuations only exist if fluctuations in α occur at sufficiently low frequencies. If the frequency of α fluctuations is too high, they found that $\dot{M}$ fluctuations are damped out and the nonlinear features of the variability do not develop. Therefore, fluctuations in the effective-α on timescales longer than the dynamical timescale are needed to reproduce the phenomenology seen in the variability.

In this chapter, we perform the first detailed analysis of propagating fluctuations in the context of a long-duration, MHD accretion disk simulation. We show

that the well-known quasi-periodic dynamo induces slow fluctuations in the effective α that then drive propagating fluctuations. In Section 2.2 we introduce the simulation and perform a convergence study. Section 2.3 presents a brief discussion of the nature of the turbulence. In Section 2.4, we investigate the relationship of the quasi-periodic disk dynamo and angular momentum transport, finding that it imposes an intermediate-timescale modulation of the effective α. We then examine the variability of both the mass accretion rate (Section 2.5) and a proxy for bolometric radiative luminosity (Section 2.6) finding that both quantities display the non-linear variability characteristics of real sources and that the coherence of these quantities across the disk is exactly as expected in the propagating fluctuations picture. In Section 2.7, we place our results into a broader context, and then conclude in Section 2.8.

2.2 Numerical Model and Convergence

In this section, we describe the construction and convergence properties of our numerical model. In brief, we evolve a three-dimensional ideal MHD simulation in order to study the local and global dynamics of a geometrically-thin (constant opening angle $h/r = 0.1$) accretion disk. Given our focus on the time-variability of the accretion flow, the crux of our problem is the evolution of the MHD turbulent dynamics and how it influences the long-timescale behavior of the disk. Thus, we concentrate our computational resources into the high-spatial resolution and the long duration of the simulation. We demonstrate below that the numerical grid

is of high enough resolution that the macroscopic behavior of the disk turbulence is converged and insensitive to increases in resolution. As a penalty, we simplify the physics to the bare minimum. We employ non-relativistic ideal MHD, and a pseudo-Newtonian gravitational potential to emulate the dynamical effects of a general relativistic potential, including the presence of an inner-most circular orbit (ISCO). We use a simple cooling function to keep the disk thin, but otherwise neglect all radiation physics. Renderings of density and magnetic turbulent structure of our fiducial disk simulation are shown in Figure 2.1.

2.2.1 Simulation Setup

Our simulation employs the finite-difference MHD code *Zeus-MP v2* (Hayes et al., 2006; Stone & Norman, 1992a,b). *Zeus-MP* solves the differential equations of ideal compressible MHD,

$$\frac{D\rho}{Dt} = -\rho\nabla\cdot\mathbf{v}, \tag{2.4}$$

$$\rho\frac{D\mathbf{v}}{Dt} = -\nabla P + \frac{1}{4\pi}(\nabla\times\mathbf{B})\times\mathbf{B} - \rho\nabla\Phi, \tag{2.5}$$

$$\rho\frac{D}{Dt}\left(\frac{e}{\rho}\right) = -P\nabla\cdot\mathbf{v} - \Lambda, \tag{2.6}$$

$$\frac{\partial\mathbf{B}}{\partial t} = \nabla\times(\mathbf{v}\times\mathbf{B}), \tag{2.7}$$

where

$$\frac{D}{Dt} \equiv \frac{\partial}{\partial t} + \mathbf{v}\cdot\nabla. \tag{2.8}$$

to second order accuracy in space. The method of constrained transport is used to maintain zero divergence in the magnetic field to machine precision. The ex-

plicit integration time step is set by the usual Courant conditions, and is first-order accurate in time.

We begin by defining our fiducial simulation. The simulation domain is covered by spherical coordinates (R, θ, ϕ) and spans $R \in [4\mathrm{r_g}, 145\mathrm{r_g}], \theta \in [\pi/2 - 0.5, \pi/2 + 0.5], \phi \in [0, \pi/3)$, shown in Figure 2.1. The zone aspect ratio is approximately $\Delta R : R\Delta\theta : R\Delta\phi = 2 : 1 : 2$ and each scale height is resolved with 28 θ-zones. Outflowing boundary conditions were used for the $\pm R$ and $\pm\theta$ boundaries and periodic boundary conditions were used in the ϕ direction. The most trivial implementation of the outflowing boundary conditions in ZEUS-MP does not enforce the divergence free condition required of the magnetic field at the boundary interface. Therefore, we modified the standard ZEUS-MP boundaries to conserve $\nabla \cdot \mathbf{B} = \mathbf{0}$ across the R- and θ-boundaries.

The simulation domain was broken into a well-resolved inner region ($r < 45r_g$), used for our analysis, and an outer region with poorer resolution to act as a gas reservoir. The gas reservoir mitigates the effect of secular decay from the draining of material from the disk over the course of the simulation. The radial spacing in the inner region logarithmically increases in R from 4-45 r_g. In all, the simulation has $N_R \times N_\theta \times N_\phi = 512 \times 288 \times 128 = 1.89 \times 10^7$ zones in this region. The ΔR spacing in the outer region logarithmically increases from $45 - 145r_g$ and a total of $N_R \times N_\theta \times N_\phi = 128 \times 288 \times 128 = 4.72 \times 10^6$ zones in this region.

We approximate the gravitational field around a nonrotating black hole with

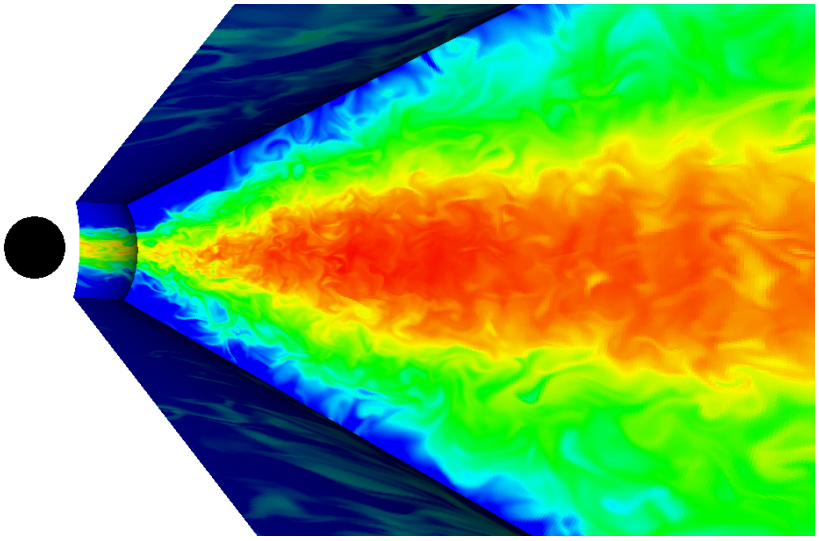

(a) Gas Density

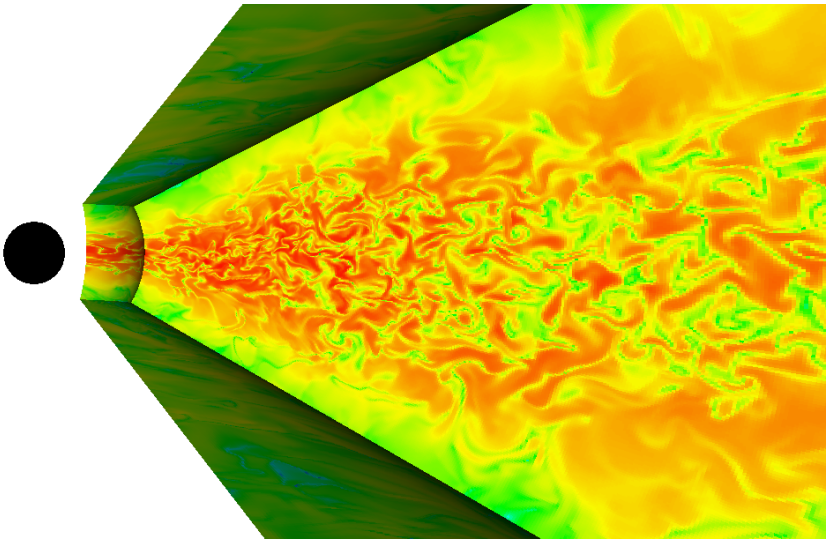

(b) $|\mathbf{B^2}|$

Figure 2.1: Snapshots of ρ (a) and $|\mathbf{B^2}|$ (b) in the fiducial simulation used in our analysis at t=0, the point we take to be the beginning of science analysis after the initial transient behavior has died off and the turbulence had saturated.

a pseudo-Newtonian gravitational potential (Paczyńsky & Wiita, 1980) of the form:

$$\Phi = -\frac{GM}{R - 2r_{\rm g}}, \qquad r_{\rm g} \equiv \frac{GM}{c^2}. \tag{2.9}$$

With this potential, several important aspects of a general relativistic gravity field are captured including an ISCO (at $6r_g$) and the qualitative change of radial shear in the disk.

A $\gamma = 5/3$ adiabatic equation of state is used for the gas. An initially axisymmetric thin disk was initialized with constant midplane density and radially decreasing pressure corresponding to an isothermal vertical profile:

$$\rho(R, \theta) = \rho_0 \exp\left(-\frac{\cos^2\theta}{2(h/r)^2 \sin^2\theta}\right), \tag{2.10}$$

and

$$p(R, \theta) = c_s^2 \ \rho(R, \theta) \tag{2.11}$$

where,

$$c_s^2 = \frac{GMR(h/R)^2 \sin^2\theta}{(R - 2r_{\rm g})^2}, \tag{2.12}$$

locally.

The disk is initialized to a scale height of $h/r = 0.1$ and was maintained by an *ad hoc*, optically thin cooling function similar to Noble et al. (2009). The cooling function plays the role of the real physical processes and removes energy at a rate equivalent to the thermal time of the disk ($\tau_{\rm cool} = 10\tau_{\rm orb} \sim \tau_{\rm orb}/\alpha$), as was done in O'Neill et al. (2011). If the gas energy in a cell is above the target energy, $e_{\rm targ} \propto \rho v_\phi^2 (h/r)^2$, it is cooled over the cooling time. The cooling function used is $\Lambda = f(e - e_{\rm targ})/\tau_{\rm cool}$, where $f = 0.5[(e - e_{\rm targ})/|e - e_{\rm targ}| + 1]$. The switch

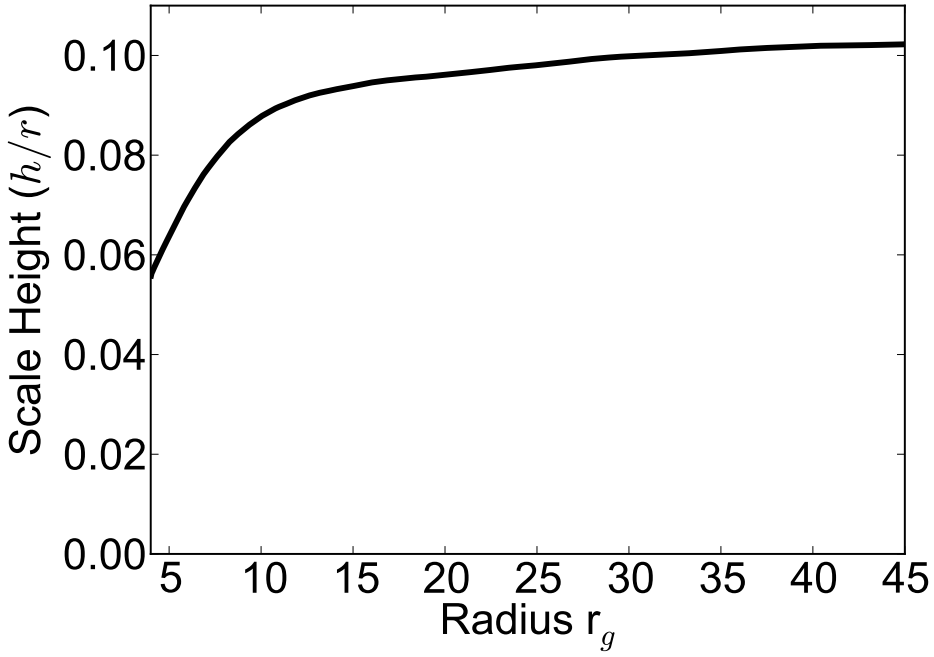

Figure 2.2: Radial profile of the time averaged disk scale height, h/r, during the length of the simulation. The cooling function maintains an aspect ratio of $h/r \approx 0.1$ throughout the simulation. In the inner regions ($r \leq 10r_g$) the ISCO is strongly felt by the gas and the disk is thinner, the so-called "turbulent edge" (Krolik & Hawley, 2002). Throughout this chapter we will calculate quantities within one scale height of the disk. Since the cooling function maintains the aspect ratio fairly well, these calculations are done within our target scale height of $h/r \approx 0.1$.

function, f, acts as a threshold function and is zero when $e_{\rm targ} > e$. Figure 2.2 shows the radial profile of the time averaged aspect ratio of the disk during the length of the simulation and it can be seen that the cooling function effectively keeps the disk near the target h/r value. Throughout this chapter we calculate quantities within one disk scale height and, therefore, use our target value as $h/r = 0.1$ in these calculations. A protection routine is implemented to ensure the density and pressure values do not become artificially small and/or negative.

The gas was initialized with a purely azimuthal velocity field and a weak magnetic field. The local velocity is set so that the effective centripetal force balances the gravitational force. A series of weak, large-scale poloidal magnetic field loops are set for the initial magnetic field configuration (e.g. Reynolds & Miller 2009) to seed the MRI. The loops were set from the vector potential $\mathbf{A} = (A_r, A_\theta, A_\phi)$ to ensure the initial field was divergence free and had the form:

$$A_\phi = A_0 p^{\frac{1}{2}} f(r,\theta) \sin\left(\frac{2\pi r}{5h}\right), A_r = A_z = 0, \tag{2.13}$$

where A_0 is a normalization constant, $f(r,\theta)$ is an envelope function that is 1 in the body of the disk and smoothly goes to 0 at $r = r_{ISCO}, r_{out}$ and 3 scale heights above the disk. The alternating field polarity is set by the final multiplicative term such that loops have a radial wavelength of $5h$. The A_0 constant was set to initialize the disk to an average ratio of gas- to magnetic-pressure of $\beta = 500$.

The following analysis treats the simulation after the MRI has saturated and transient behavior from initialization has died away. $\mathbf{B}$ and e reach a quasi-steady state in the well-resolved region of the disk and the MRI saturates, as measured by the convergence metrics discussed in Section 2.2.2, after approximately 200 ISCO orbits ($12,320\, GM/c^3$). We take this point to be $t = 0$. The simulation was then run for 1410 ISCO orbits ($86,856\, GM/c^3$). In the interest of data management, the values of $\mathbf{B}$, $\mathbf{v}$, e, and ρ were output every two ISCO orbits ($123.2\, GM/c^3$).

2.2.2 Convergence

The issue of convergence is forefront when considering the reliability of results from any *ab initio* accretion disk simulation because the MHD turbulence that mediates angular momentum transport has structure on the smallest accessible scales. With this type of simulation, the macroscopic behavior can have a resolution dependence if the turbulent scales dominating the shear stresses are not adequately resolved (Guan et al., 2009; Hawley et al., 2013; Sorathia et al., 2012). As a preface to our study of variability, here we assess the degree to which we are adequately resolving the turbulent dynamics using two measures. Firstly, we examine the resolvability of the fastest growing linear MRI mode through the commonly employed quality factors introduced by Noble et al. (2010). Secondly, to characterize the non-linear saturation of the turbulence, we use the magnetic tilt angle. Using these diagnostics, we compare our fiducial (long) simulation with higher resolution comparison simulations.

The first set of diagnostics used to measure resolvability were the vertical and azimuthal quality factors (Noble et al., 2010), $Q_\theta = \lambda_{MRI}/R\Delta\theta$ and $Q_\phi = \lambda_C/R\Delta\phi$, respectively. Q_θ and Q_ϕ measure resolvability through the number of grid cells per fastest-growing MRI wavelength, λ_{MRI}, and critical toroidal field length, λ_C where

$$\lambda_{MRI} = \frac{2\pi|B_\theta|}{\sqrt{\rho}\,\Omega(r)} \quad , \quad \lambda_C = \frac{2\pi|B_\phi|}{\sqrt{\rho}\,\Omega(r)}. \tag{2.14}$$

Using the quality factors, we characterized the global resolvability of the disk. The local values of Q_θ and Q_ϕ were calculated in every voxel of the well-resolved

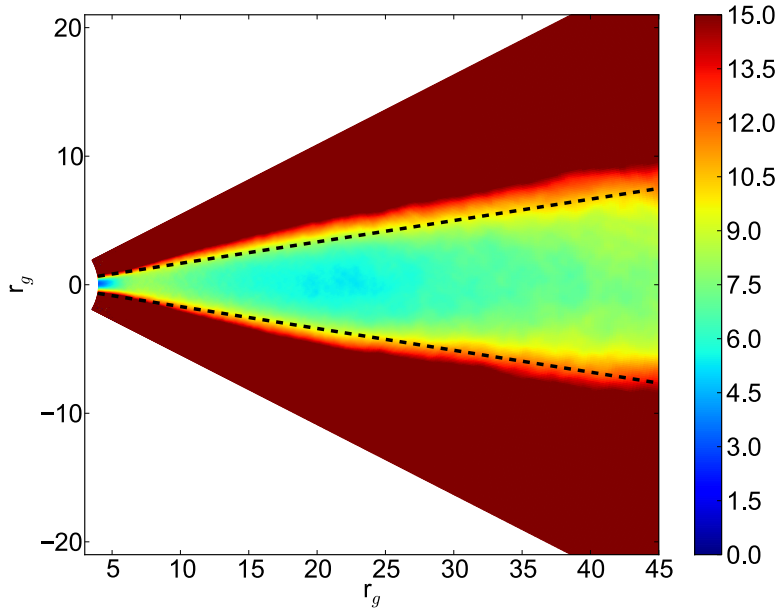

(a) Q_θ

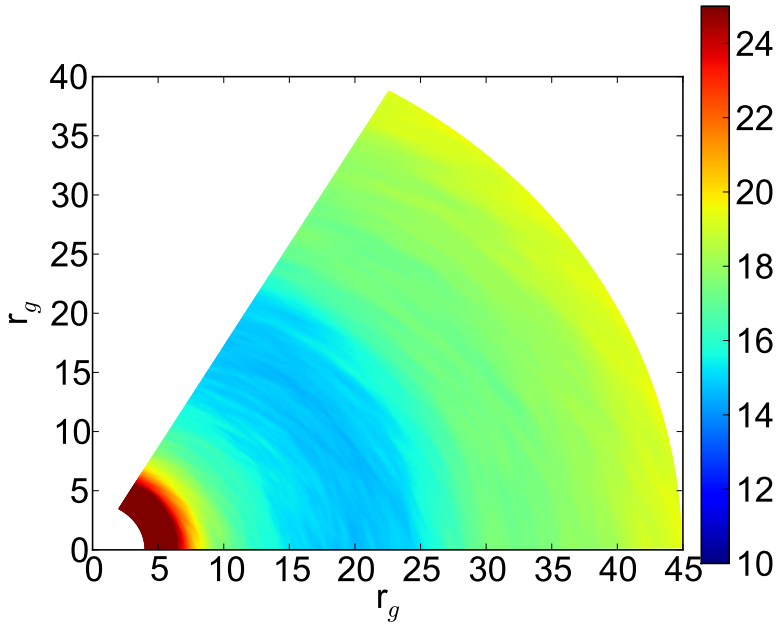

(b) Q_ϕ

Figure 2.3: Plots of temporally and azimuthally averaged Q_θ (a) and temporally and vertically averaged Q_ϕ (b). One scale height (1h) above and below the disk is shown as dashed black lines in (a).

region $(4 - 45\, r_g)$ for every data dump after the transient behavior in the disk had died away ($t = 0$ onwards). The volume-weighted average was calculated for each quality factor by averaging over in the region within one scale height above and below the disk mid-plane to get the instantaneous value and then over the entire duration of the simulation to get a temporal average. The averaging was restricted to the body of the disk because we want the most conservative estimate of the resolvability of the simulation. In the highly magnetized, low-density coronal regions the quality factors are very high and, if included, the quality factors would appear artificially high, overestimating how well we resolve the MRI. We find $\langle Q_\theta \rangle = 7.0$ and $\langle Q_\phi \rangle = 15.2$, a bit below the nominal resolvability criteria of $\langle Q_\theta \rangle = 10$ (Hawley et al., 2011).

In addition to the global averages, we are interested in how the resolvability depends on the position within the grid. Shown in Figure 2.3 is the time and azimuthally averaged profile of Q_θ, as well as the time and polar average profile of Q_ϕ. The average of Q_θ was calculated as a function of r and θ by averaging over entire ϕ domain. As we did in our global average, the vertical averaging over the polar angle in our calculation of Q_ϕ is only done in the region within one scale height above and below the disk to exclude the coronal region. The spatial variation can be seen in both quantities, but no apparent "dead zones" of gross under-resolution are present.

These quality factors probe the ability of the simulation to resolve linear MRI modes but do not address the structure of the (non-linear) saturated turbulence.

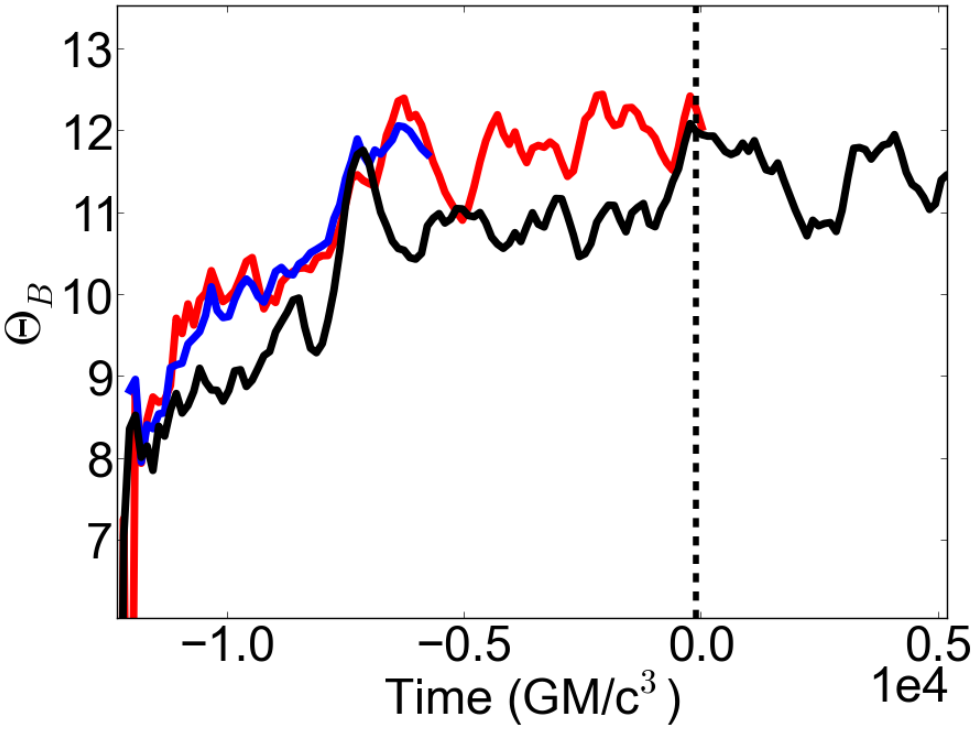

Figure 2.4: Evolution of magnetic tilt angle, Θ_B, for long, fiducial disk simulation (black line), high resolution wedge simulation (red line), and high resolution 2π simulation (blue line). The t=0 time we set use in our analysis is marked by the black dashed line. The evolution of the long disk simulation used for the science run in our chapter has been truncated to only show the initial saturation of the turbulence and a short time period short after, but continues for $86,856\,GM/c^3$. Θ_B grows similarly in all three simulations and saturates at the same value, $\Theta_B \approx 11 - 12°$. The black dashed line indicates t=0 used in our analysis.

Table 2.1: Simulation Parameters

Simulation	$\Delta\phi$	ISCO Orbits	N_R	N_θ	N_ϕ	$H/\Delta z$
Fiducial	$\pi/3$	1610	640	288	128	28.8
HiResWedge	$\pi/3$	204	1280	576	256	57.6
HiRes2π	2π	110	1280	576	256	57.6

Table 2.2: Resolution Diagnostics

Simulation	$\langle Q_z \rangle$	$\langle Q_\theta \rangle$	$\langle \alpha \rangle$	$\langle \beta \rangle$	Θ_B
Fiducial	8.1	20.5	0.12	23.4	10.5°
HiResWedge	27.2	43.0	0.15	6.5	12.1°
HiRes2π	18.4	11.8	0.09	7.9	11.6°

Thus, we additionally measure the average in-plane magnetic tilt angle,

$$\Theta_B = -\arctan\left(\left\langle \frac{B_r}{B_\phi} \right\rangle\right), \tag{2.15}$$

the value of which is closely connected to the processes by which the MHD turbulence saturates (Hawley et al., 2011, 2013; Pessah, 2010; Sorathia et al., 2012). We note that, given the dominance of B_ϕ over the other field components, the tilt angle is approximately given by

$$\Theta_B = \arcsin(\alpha_M \beta)/2, \tag{2.16}$$

where α_M is the Maxwell stress normalized by the magnetic pressure,

$$\alpha_M = \frac{\langle -2 B_R B_\phi \rangle}{\langle P \rangle}, \tag{2.17}$$

and β is the ratio of gas pressure to magnetic pressure,

$$\beta = \frac{P}{\langle |B^2| \rangle}. \tag{2.18}$$

The magnetic tilt angle is directly tied to the effectiveness of angular momentum transport at a given field strength and can be used to probe whether a given simulation has correctly captured the non-linear saturation of the MHD turbulence.

We calculate Θ_B within the mid-plane regions of the disk, restricting to half a scale height above and below the disk midplane in the well-resolved region. The

temporally averaged magnetic tilt (neglecting the first 200 ISCO orbits) is $\overline{\Theta_B} \approx 11.3^\circ$ (Fig. 2.4), comparable to estimates from both analytic theory (Pessah, 2010) and previous high-resolution local (Hawley et al., 2011) and global (Hawley et al., 2013; Sorathia et al., 2012) simulations.

We further assess the fidelity of our fiducial simulation by performing two additional high-resolution comparison runs. The first comparison simulation had the exact same geometry as the fiducial simulation, but twice the resolution in each of the three dimensions (hence voxels of $1/8^{th}$ the volume). The second comparison simulation also doubles the number of zones in each of the three dimensions, but then extends the domain to include the full 2π in azimuth. Both of these comparison simulations possess $N_R \times N_\theta \times N_\phi = 1280 \times 576 \times 256 = 1.89 \times 10^8$ total zones with a vertical resolution of 56 θ-zones per disk scale-height. Of course, the $\Delta R : R\Delta\phi$ ratio was larger in the 2π higher resolution simulation due to the extension of the ϕ domain. The evolution of Θ_B for the simulation used in our analysis and the two test simulations is shown in Figure 2.4.

In the higher resolution simulations the evolution of Θ_B is slightly faster than our fiducial run, but settles at similar levels as the MRI-driven turbulence saturates. One difference between the development of the turbulence in the comparison simulations and our fiducial run is that our fiducial run has a transient spike in magnetic tilt angle $5,790\, GM/c^3$ (94 ISCO orbits) into the initialization. From visual inspection, we see the growth and break-up of a large channel flow in the disk body in the fiducial run. This does not develop in the higher resolution comparison simulations because the non-axisymmetric parasitic instabilities are more effective at breaking

up nascent channel flows. With this minor difference, the similarity in the evolution and saturation of the turbulence between the three simulations indicates that our fiducial run is adequately resolved.

In all, we can be confident in the convergence of our model. By standard measures the simulation is adequately resolved and has reached a level of saturated turbulence. The quality factors are slightly lower than what has been deemed well-resolved by prior convergence studies (i.e. Hawley et al., 2011, 2013; Sorathia et al., 2012), but the similarities between Θ_B in our long science run and those of our two shorter, high-resolution comparison simulations demonstrate the turbulence has reached a saturated level.

2.3 Turbulence and the Effective α Description of the Model Disk

2.3.1 Fluctuating Effective α

We will now look at the behavior of the effective α in the disk. Of particular interest is the variable behavior of the effective α as this is required to drive fluctuations in $\dot{M}$. Using Equation 2.1, we calculate the effective α by restricting the domain over which we average to the disk midplane, $\theta = [\pi/2 \pm h]$, where h is one disk scale height. For each data output from our simulation ($\Delta t = 123.2GM/c^3$) we calculate the average stress and pressure within one scale height across the entire azimuthal domain for each radial bin. The ratio of the stress to pressure was then taken to provide the effective α as a function of radius and time.

Figure 2.5 shows the time variability of the effective α parameter in the disk

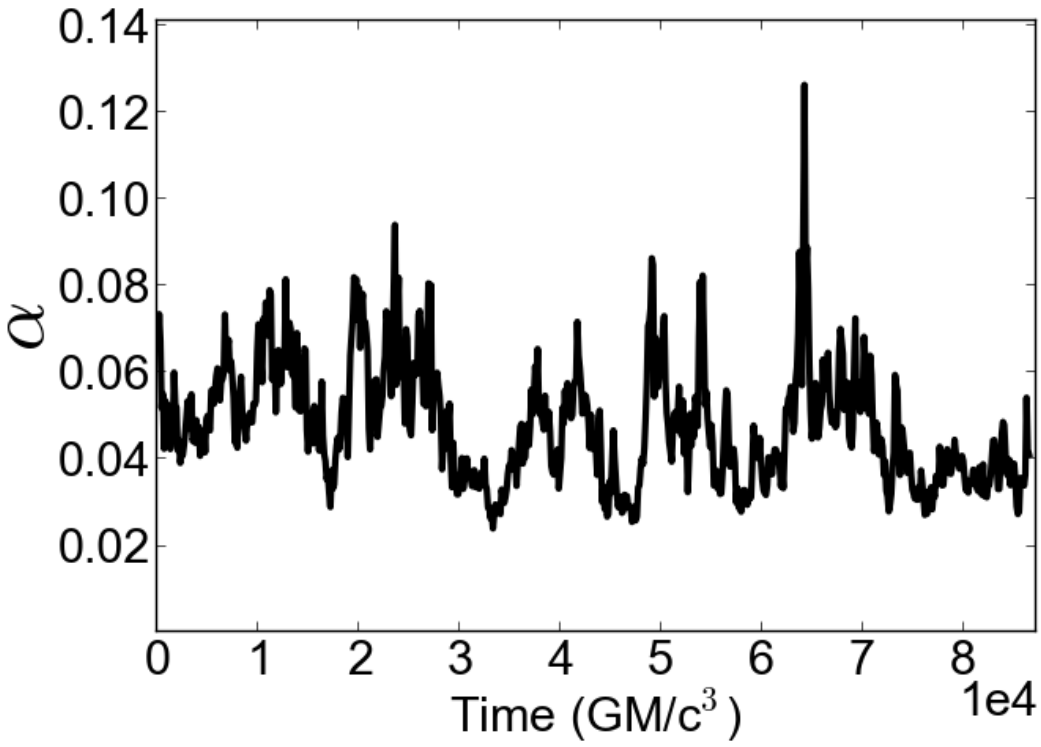

Figure 2.5: Time trace of the effective α parameter in the disk after averaging over radius. The α parameter is highly variable and fluctuates between $\alpha \approx 0.04$ and $\alpha \approx 0.08$ in a quasi-periodic manner.

after averaging over radius. Large variability occurs on an intermediate timescale, longer than a dynamical time and shorter than a viscous time. The value of the effective α in the disk typically fluctuates between $\alpha \approx 0.03$ and $\alpha \approx 0.08$ in a quasi-periodic manner. On the lower end of the fluctuating range, $\alpha \approx 0.03$ seemingly acts as a floor where the minima consistently returns. The upper range on the effective α is less well-defined with maxima found at different levels as low as $\alpha = 0.07$ and as high as $\alpha = 0.13$.

Figure 2.6 shows the histogram of effective α with normal (Gaussian) and log-normal fits to the probability density function (PDF). Statistically, the PDF of the

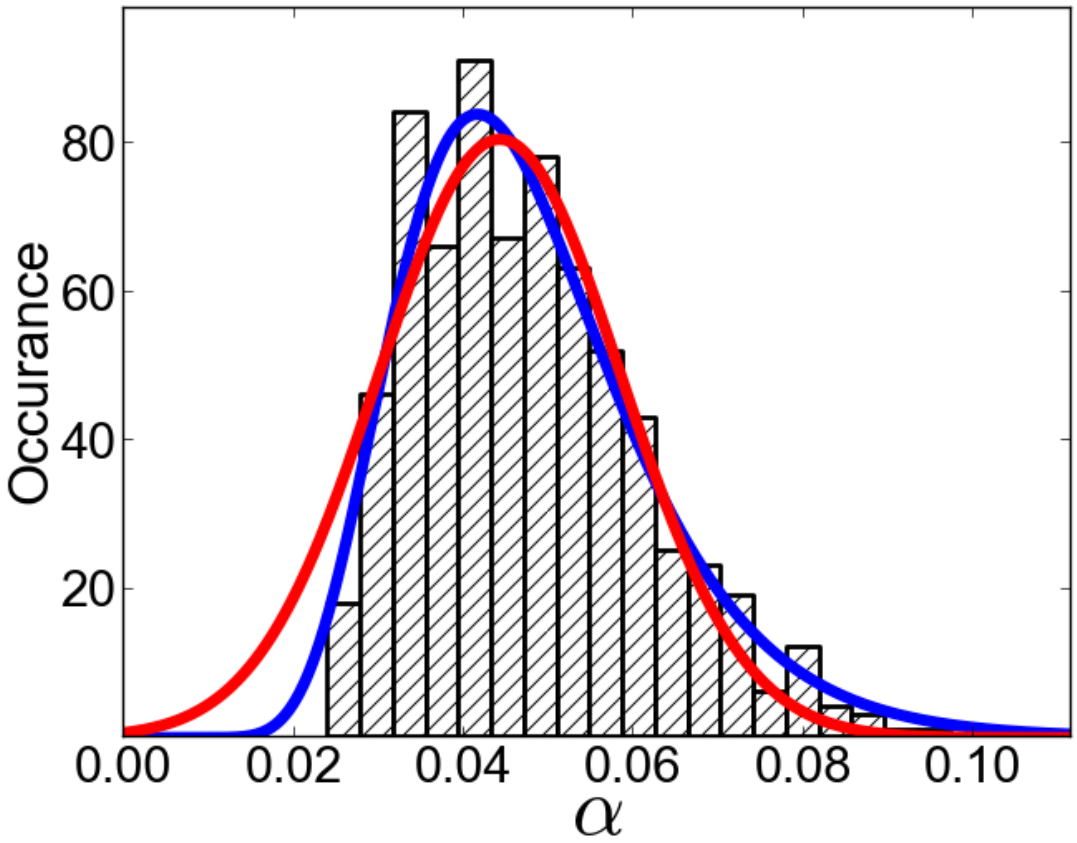

Figure 2.6: Histogram of α fit with a normal distribution (red line) and log-normal distribution (blue-line). The distribution is best fit by a log-normal distribution.

effective α is better fit by a log-normal distribution. The best fit with a normal distribution has $\chi^2/D.o.F = 44.7/24 = 1.9$ and the best fit with a log-normal distribution has $\chi^2/D.o.F = 29.6/24 = 1.2$.

2.3.2 Characterizing Velocity and Length Scales of the Turbulence

Let us now characterize the velocity and length scales of the turbulence. Given the range of time- and length-scales involved in a global disk simulation, we choose to perform this exercise over a limited range of radii; we select the region $R \in [15\mathrm{r_g}, 18\mathrm{r_g}], \theta \in [\pi/2 - 0.35, \pi/2 + 0.35], \phi \in [0, \pi/3)$. In physical coordinates, this domain spans $\Delta R = 3r_g, R\Delta\theta = 10.5r_g, R\Delta\phi = 5\pi r_g$. The size of the subdomain was chosen such that any localized turbulent structure would be well contained within the box, but also so that any medium-scale structure would be captured by our analysis if it is present.

2.3.2.1 Measuring Turbulent Velocity

Within this region, we first calculated the ratio of the turbulent speed to the sound speed within the disk midplane as a function of time. The turbulent velocity is defined as

$$|v| = \sqrt{v_r^2 + v_\theta^2 + (v_\phi - \langle v_\phi \rangle)^2} \tag{2.19}$$

and the sound is defined in its usual form

$$c_s = \sqrt{\frac{\gamma P}{\rho}}. \tag{2.20}$$

For each data dump, we calculated the volume weighted spatial average of $|v|/c_s$ to serve as a diagnostic for the average velocity of the turbulence within the disk.

Figure 2.7 shows the time variability of $\langle|v|/c_s\rangle$. This ratio is highly variable and fluctuates within a range of $|v|/c_s \approx 0.3$ to $|v|/c_s \approx 0.5$. Comparing with the time variability of α in Figure 2.5, the correlation between α and $|v|/c_s$ can be readily observed. The average value is $\langle|v|/c_s\rangle = 0.37$.

2.3.2.2 Measuring Turbulent Scales

Measuring the spatial scales of the turbulence is significantly more involved than measuring the turbulent velocity, but, nevertheless, provides a method for characterizing the turbulence in simple terms. The spatial scales of the density, magnetic field components and Maxwell stress of the turbulence were measured in our $r = 15 - 18r_g$ subdomain using the autocorrelation the method of Guan et al. (2009) & Beckwith et al. (2011) with some modifications. For each data dump after the initialization of the simulation, the two-point autocorrelation of a given quantity of interest, $F(r, \theta, \phi, t)$, was calculated within this subdomain in the following way. First, large-scale structure of $F(r, \theta, \phi, t)$ was removed. For a given time step, t, the average over $\Delta T = 1232$ GM/c^3 (11 data dumps) for each cell in the subdomain was calculated. The time average was centered on the timestep of interest such that the average for a single cell included its values 5 data dumps before and after. This was then subtracted off of the present cell value:

$$F_{sub}(r, \theta, \phi, t) = F(r, \theta, \phi, t) - \frac{1}{\Delta T} \int_{t-0.5\Delta T}^{t+0.5\Delta T} F_{norm}(r, \theta, \phi, t) dt \tag{2.21}$$

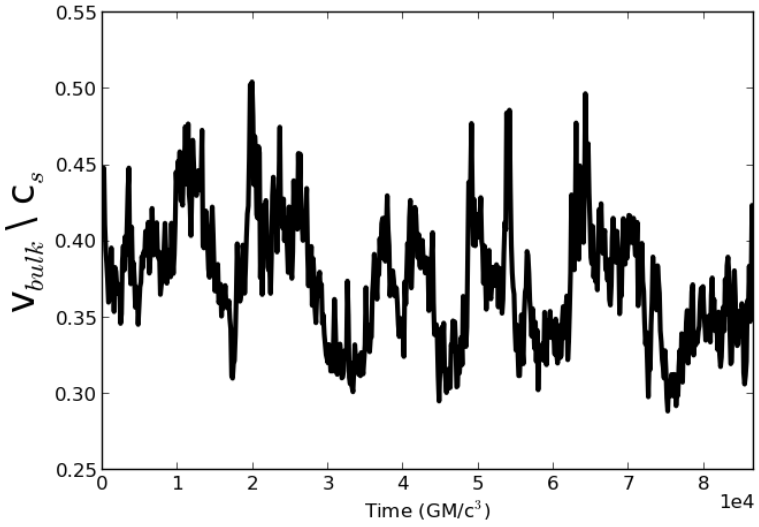

(a) Gas Velocity

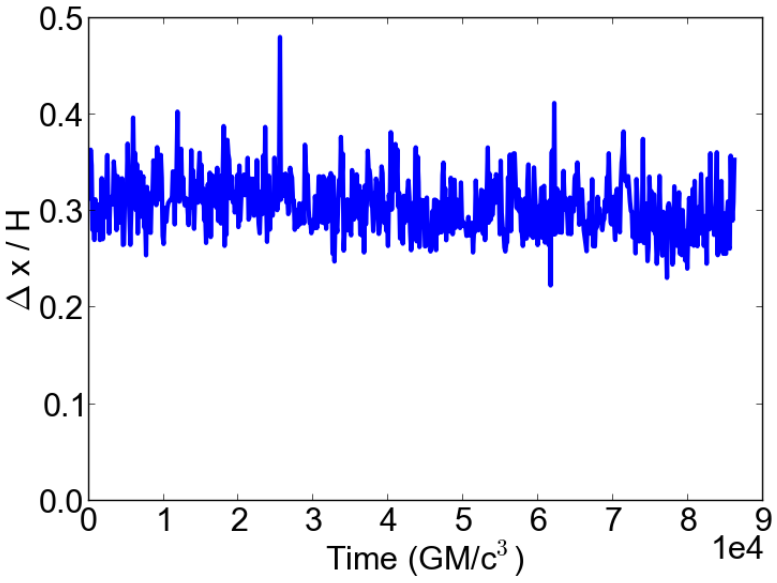

(b) Radial Correlation Length

Figure 2.7: Instantaneous values of v_{turb}/c_s. The fluctuations in v_{turb}/c_s are correlated with the changes in α seen in Figure 2.5 indicating that as the stress increases in the disk the gas is accelerated. Instantaneous values of $\Delta x/h$. $\Delta x/h$ fluctuates stochastically around $l = 0.32$ and is not correlated with α. The turbulent spatial scales are independent of the disk stress at all times.

leaving only the high-frequency perturbation. Since the average was determined for an individual cell, this also removes vertical gradients.

Next, the physical coordinates were normalized by the local scale height to express the turbulent scales in terms of h. This converts the wedge geometry into a rectangular geometry and allows for easier comparison with prior work. In this normalized geometry, r maps to x, ϕ maps to y, and θ maps to z.

After the normalization of the coordinates, the three-dimensional Fourier transform was then taken of F_{sub}:

$$\mathcal{F}(k_x, k_z, k_y, t) = \iiint F(x, z, y) e^{i(k_x x + k_z z + k_y y)} dx dz dy. \tag{2.22}$$

From this, the autocorrelation, $C_{\mathcal{F}}(\Delta x, \Delta z, \Delta y)$, was calculated according to:

$$C_{\mathcal{F}}(\Delta x, \Delta z, \Delta y) = \iiint |\mathcal{F}(k_x, k_z, k_y, t)|^2 \quad \times e^{i(k_x x + k_z z + k_y y)} dk_x dk_z dk_y. \tag{2.23}$$

For the first part of our analysis into the spatial scales, we fit the time average three-dimensional autocorrelations. Two-dimensional slices through the origin along the x-y, x-z, and y-z planes are shown in Figure 2.8. To measure the shape of the three-dimensional autocorrelations, we defined three surfaces corresponding to where the value of the autocorrelation falls to $C_{\mathcal{F}}(\Delta x, \Delta z, \Delta y) = 0.5$, e^{-1}, and e^{-2}. The standard definition of the correlation length is the full-width, half-max of the autocorrelation which is where the autocorrelation falls to 0.5. However, other works use different definitions of the correlation length, so we present those values to aid in comparing the turbulent scales between simulations.

A least-squares minimization was used to fit these surfaces with an ellipsoid

Table 2.3: Ellipsoid Fit Parameters

Variable	θ^{a}	Fit Parameters	Fit Parameters	Fit Parameters
		0.5	e^{-1}	e^{-2}
ρ	16.7°	a - 0.32 b - 1.17 c - 0.24	a - 0.41 b - 1.67 c - 0.42	a - 0.66 b - 3.49 c - 1.08
B_R	30.2°	a - 0.29 b - 0.75 c - 0.07	a - 0.38 b - 0.97 c - 0.10	a - 0.60 b - 1.79 c - 0.17
B_θ	14.8°	a - 0.20 b - 0.56 c - 0.14	a - 0.24 b - 0.74 c - 0.21	a - 0.36 b - 1.20 c - 0.38
B_ϕ	22.2°	a - 0.27 b - 0.97 c - 0.10	a - 0.35 b -1.31 c - 0.14	a - 0.58 b - 2.52 c - 0.24
B^2	22.2°	a - 0.20 b - 0.78 c - 0.07	a - 0.28 b - 1.03 c - 0.10	a - 0.47 b - 2.03 c - 0.21
$B_R B_\phi$	26.4°	a - 0.23 b - 0.70 c - 0.07	a - 0.30 b - 0.92 c - 0.10	a - 0.53 b - 1.64 c - 0.17

[a]Inclination of autocorrelation with respect to the azimuthal direction.

Ellipsoid fit parameters to autocorrelations shown in Figure 2.8 of turbulent quantities at $C_{\mathcal{F}} = 0.5, e^{-1}, e^{-2}$. From the autocorrelations, we find that the turbulent components of the magnetic field are coherent on spatial scales smaller than the gas density (ρ).

of the form:

$$1 = \frac{[x\cos(\theta) - y\sin(\theta]^2}{a^2} + \frac{[y\cos(\theta) - x\sin(\theta)]^2}{b^2} + \frac{z^2}{c^2}. \tag{2.24}$$

where θ is the tilt angle introduced by the disk shear and a, b, and c are the axes corresponding to the x, y, and z directions, respectively. The tilt angle and best fits for the three different correlation lengths are given in Table 2.3.

The radial correlation length of the gas density, ρ, provides an estimate for the characteristic length scale, l, of the turbulence. In the Shakura & Sunyaev α-prescription the turbulent scales are less than the disk scale height. This requirement does not strictly hold for the y- and z-directions, but it does hold for the x-direction, which is the important direction for the angular momentum transport. Figure 2.7 shows the time variability of l calculated at individual data dumps. Unlike $|v|/c_s$, the variability of l is stochastic and lacks the structure seen in the time variability of v_{turb}/c_s. Instead of varying in lock step with α, the time trace of l is flat and simply fluctuates around $l = 0.32$. This means that increases in stress act to drive the turbulence more quickly, rather than injecting energy at a larger scale and allowing it to cascade down to smaller scales and that the turbulent eddy scales are preserved regardless of the magnitude of the stress in the disk.

2.4 Disk Dynamo and Intermediate Timescale α Variability

We now turn to the disk dynamo and its influence on the variability of the effective α in the simulation. The cyclical magnetic dynamo is a well-established phenomenon in accretion disks and is seen in both local (Bodo et al., 2015; Branden-

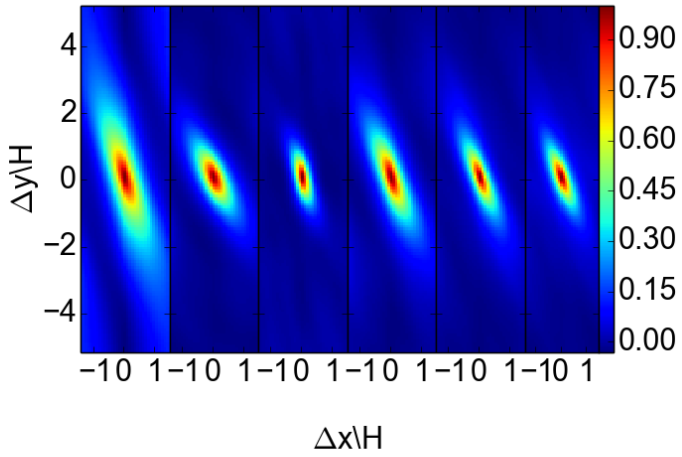

(a) $C_{\mathcal{F}}(\Delta x, \Delta z, \Delta y)$ in x-y plane

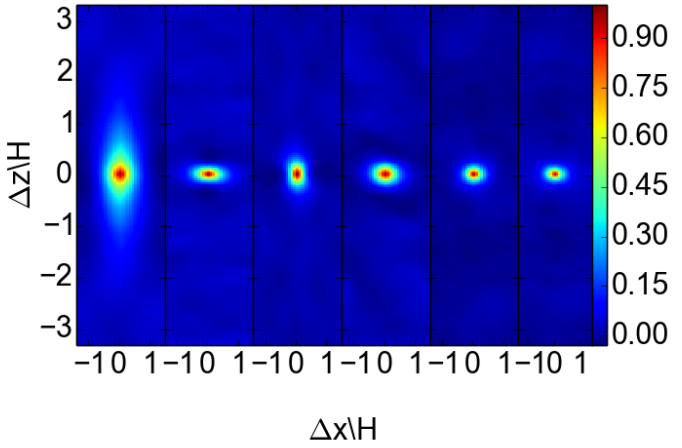

(b) $C_{\mathcal{F}}(\Delta x, \Delta z, \Delta y)$ in x-z plane

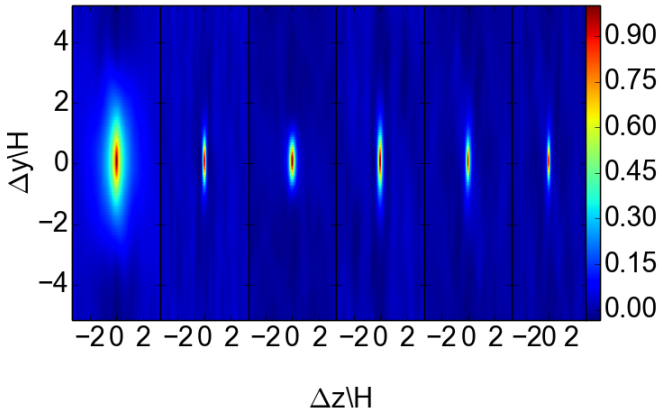

(c) $C_{\mathcal{F}}(\Delta x, \Delta z, \Delta y)$ in y-z plane

Figure 2.8: Slices of 3D autocorrelation function along x-y, x-z, and y-z planes for ρ, B_r, B_θ, B_ϕ, B^2, and $B_R B_\phi$.

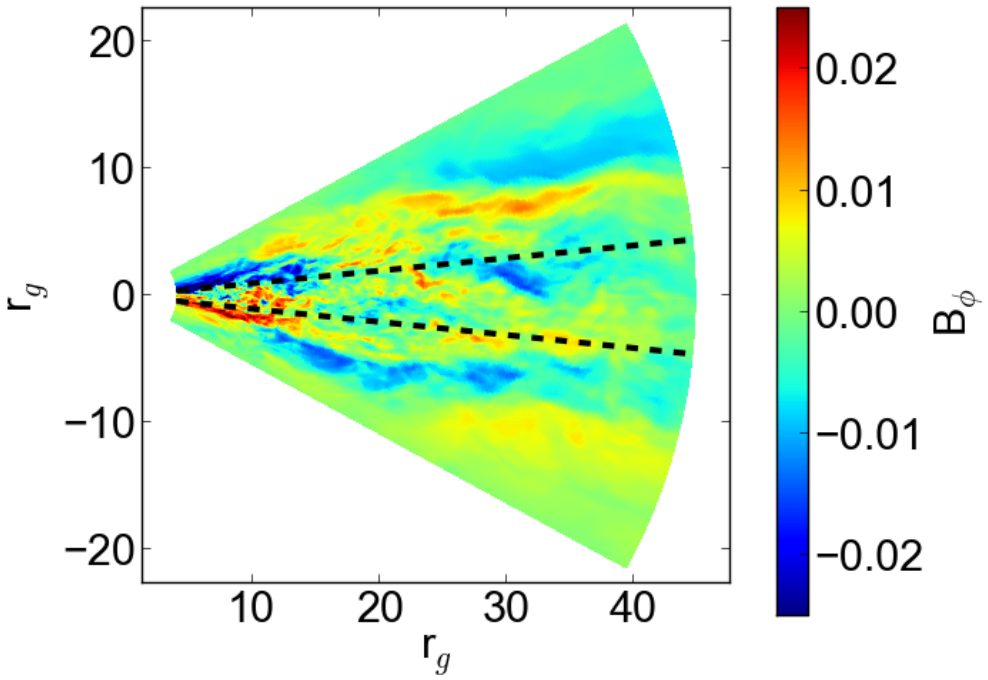

Figure 2.9: Azimuthally averaged B_ϕ at $t = 3.7 \times 10^4\ GM/c^3$. Within the disk midplane the fluctuations in B_ϕ are largely random. Large, stratified regions of coherent magnetic field develop in the corona as buoyancy lifts highly magnetized gas vertically and regions of similar polarity grow through magnetic reconnection. The coronal regions are symmetric across the midplane, but have opposite polarity.

burg et al., 1995; Davis et al., 2010; Hawley et al., 1996; Johansen et al., 2009; Stone et al., 1996; Suzuki & Inutsuka, 2009; Turner, 2004) and global (Beckwith et al., 2011; Flock et al., 2012; O'Neill et al., 2011; Parkin & Bicknell, 2013) MHD simulations. It is characterized by rising bundles of toroidal magnetic field in which the toroidal field flips polarity between two such events. The dynamo is quasi-periodic in nature with $\omega \sim 10^{-1}\,\omega_{dyn}$, where ω_{dyn} is the local dynamical frequency.

The influence the dynamo has on the disk is not fully understood. Since the Maxwell stress and, thus, turbulent injection from the MRI is proportional to $B_R B_\phi$, we might imagine that the stress would be modulated by the large-scale toroidal magnetic field generated by the dynamo. Indeed, a correlation between stress and toroidal magnetic field has been found (Davis et al., 2010; Flock et al., 2012), however, the coupling of Maxwell stress to the low-frequency, periodic fluctuations of the dynamo has not been well-investigated.

2.4.1 General Dynamo Behavior

We begin with an overview of the spatio-temporal properties of the magnetic field in the disk. After the intialization of the simulation, a stratified magnetic field geometry developed and was sustained. Figure 2.9 shows a snapshot of the azimuthal average of B_ϕ at an arbitrary time ($t = 3.7 \times 10^4\ GM/c^3$). Correlated regions of field in the corona are seen spanning large portions of the disk. Like other simulations, the large-scale magnetic field is generated in the disk and is then slowly lifted by magnetic buoyancy (Davis et al., 2010; O'Neill et al., 2011).

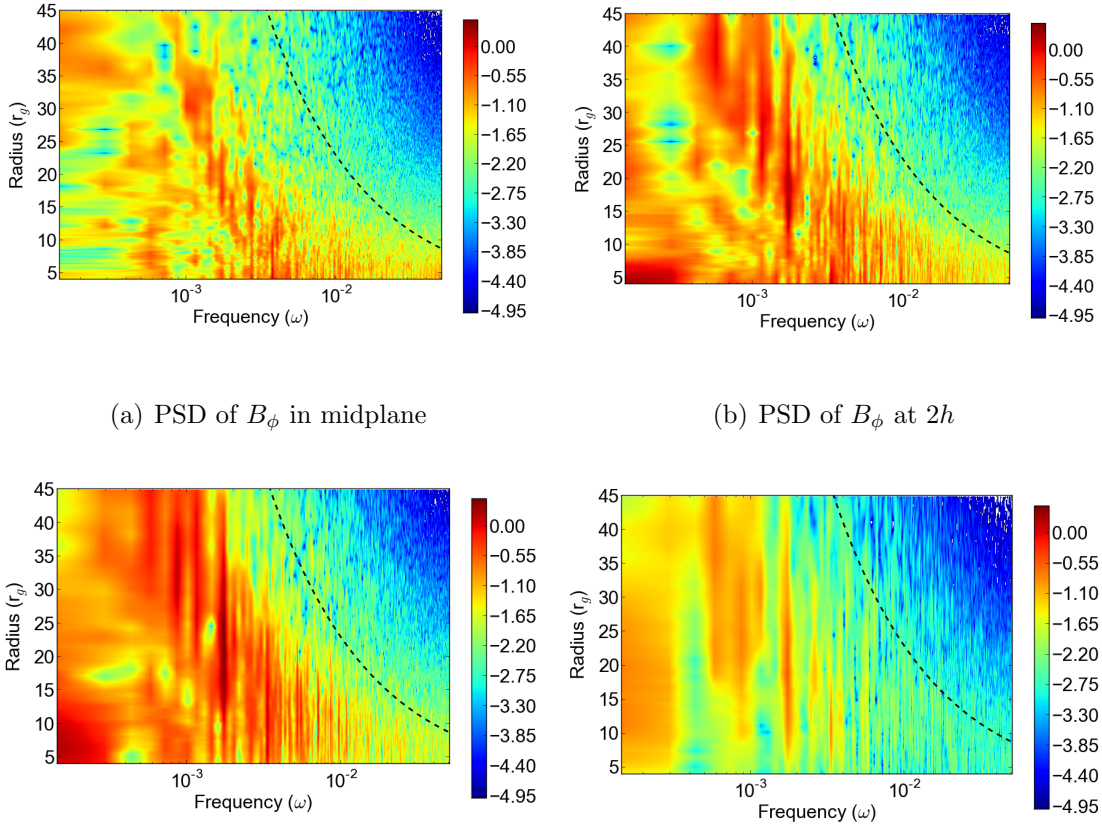

(a) PSD of B_ϕ in midplane

(b) PSD of B_ϕ at $2h$

(c) PSD of B_ϕ at $3h$

(d) PSD of B_ϕ at $4h$

Figure 2.10: PSDs of B_ϕ at different elevations above the disk with the orbital frequency overlaid as the black, dashed line. Within the midplane the standard $\alpha\Omega$ dynamo behavior is seen. A band of power vertically spanning ≈ 10 r_g follows the shape of the orbital frequency at $10\times$ lower frequency. The radial correlation of B_ϕ increases with increasing height above the disk due to the stratification that develops in the corona.

This growth can be seen in the PSDs of the azimuthally averaged B_ϕ. Shown in Figure 2.10 are the PSDs of B_ϕ as a function of radius for the midplane and 2h, 3h, and 4h above the disk midplane. The PSDs were calculated similarly to Reynolds & Miller (2009) and are defined as $P(\nu) = |\widetilde{f}(\nu)|^2$ where $\widetilde{f}(\nu)$ is the Fourier transform of the time sequence of the variable of interest,

$$\widetilde{f}(\nu) = \int f(t) e^{-2\pi i \nu t} dt. \tag{2.25}$$

In our case, the time sequence is the time variability of the azimuthal average of B_ϕ in the disk mid-plane. The Fourier transform was calculated for each point on the radial grid. The large gas reservoir supplies additional material to the disk during the simulation which protected from secular changes due to the draining from accretion. Therefore, there was no need "pre-whiten" before taking Fourier transforms of the basic fluid variability, as Reynolds & Miller (2009) discuss the need for in the case of significant secular evolution.

In the disk midplane the dynamo behaves similarly to the dynamo in Davis et al. (2010). Rather than having a single characteristic frequency, a band of enhanced power parallels the orbital frequency at frequencies $\approx 0.1\Omega$. For a given frequency, a band of power extends 10-15 r_g, highlighting the radial coherence of the dynamo action pointed out by O'Neill et al. (2011). For a given radius, the band of power spans approximately a factor of three.

The PSDs of the azimuthal magnetic field above the disk show a larger radial range of enhanced power. As the the height above the disk midplane increases, the vertical bands of power at a given frequency stretches to smaller radii. At $4h$,

power at the lowest frequencies is enhanced along the entire radial domain of the simulation. All the while, the high frequency envelope seen in the PSD of the disk midplane is preserved.

2.4.2 Modulation of Stress By Dynamo

Figure 2.11 shows the spatio-temporal evolution of the dynamo (probed by the azimuthal average of B_ϕ) compared with the Maxwell stress for three distinct radii (15 r_g, 20 r_g, & 25 r_g). We will refer to these three radii in order to provide a comparison of different properties related to the magnetic field throughout the disk. As we saw in the previous section, the dynamo plays a central role in the disk's magnetic field evolution and, as we can see from the butterfly diagrams, this translates into modulation of the Maxwell stress — when the magnetic field is stronger at the maxima and minima of the dynamo cycle, the stress is largest. This behavior is quite similar to that seen in the stratified shearing boxes of Davis et al. (2010). Since the polarity of the global field flips during the dynamo cycle, the stress is always positive. It is also worth noting that while the dynamo defines the trend within a given cycle, the fluctuations in the stress are dominated by high-frequency variability.

Shown in Figure 2.12 are the frequency-weighted PSDs of B_ϕ and $B_R B_\phi$ for 15 , 20, and 25 r_g. The modulation of the Maxwell stress by the dynamo is more clearly seen in the strong, multi-peaked bands of power in the PSDs of both B_ϕ and $B_R B_\phi$ corresponding to oscillations of the low-frequency dynamo. However, the PSDs of

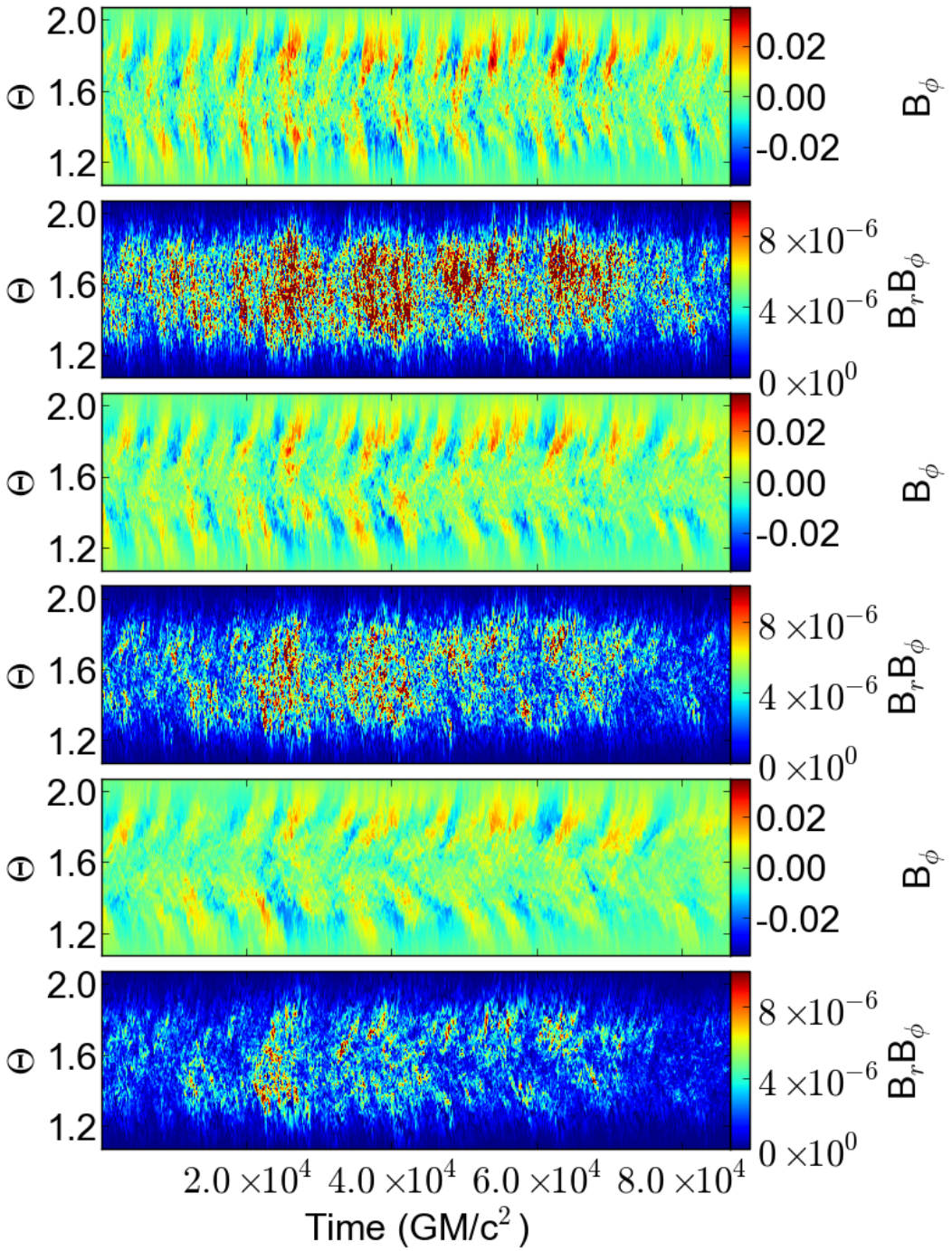

Figure 2.11: Spacetime diagrams of azimuthally averaged B_ϕ and $B_R B_\phi$ for 15, 20, and 25 r_g. The characteristic "butterfly" pattern is seen in the spacetime diagrams of B_ϕ. When B_ϕ is stronger, $B_R B_\phi$ is stronger, although the variability is mostly dominated by high-frequency variability.

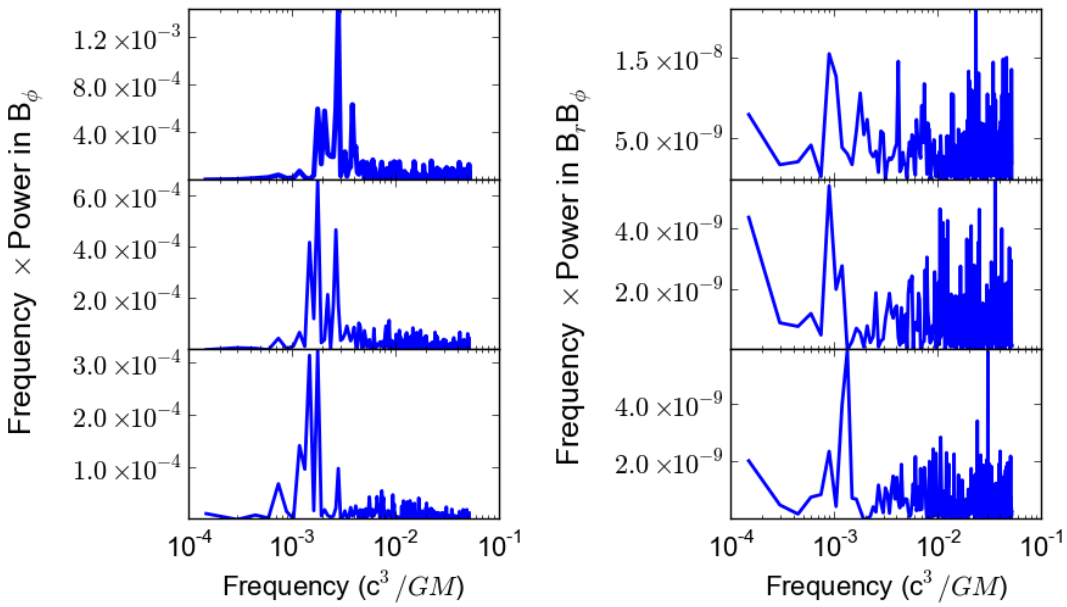

Figure 2.12: Frequency-weighted PSDs (νP) of B_ϕ (left panel) and $B_R B_\phi$ (right panel) for 15 (top), 20 (middle), and 25 (bottom) r_g. The strong, multi-peaked bands of power correspond to the oscillations seen in Figure 2.11. A noticeable difference between the frequency-weighted PSDs of B_ϕ and $B_R B_\phi$ is the strong power at high-frequencies in $B_R B_\phi$.

$B_R B_\phi$ also have an additional high-frequency component to its variability from fluctuations due to MRI-driven turbulence. This component is much more significant than the high-frequency variability in B_ϕ. Interestingly, the bands of low-frequency variability in the frequency-weighted PSDs of $B_R B_\phi$ are found around the local dynamo frequency, but the frequency of the variability is constant across the radii we probe. The strong band of power in the PSDs of B_ϕ shows the expected shift to lower frequency with increasing radii due to the decrease in orbital frequency. This discrepancy seems to indicate that while the dynamo does introduce the low frequency variability in α needed to drive the propagating fluctuations, the frequency at which the effective α-parameter is modulated is subject to a more global interaction of the magnetic field.

Fluctuations of the effective α-parameter on the viscous time were *a priori* assumed by Lyubarskii (1997) and Cowperthwaite & Reynolds (2014). The frequencies at which the Maxwell stress fluctuates in our simulation are higher than that assumed in those previous models of propagating fluctuations in mass accretion rate. Even though the frequency is a bit higher than previously assumed, the dynamo frequency is only a factor of a few longer than the inflow timescale, providing the required "low"-frequency oscillations for this model.

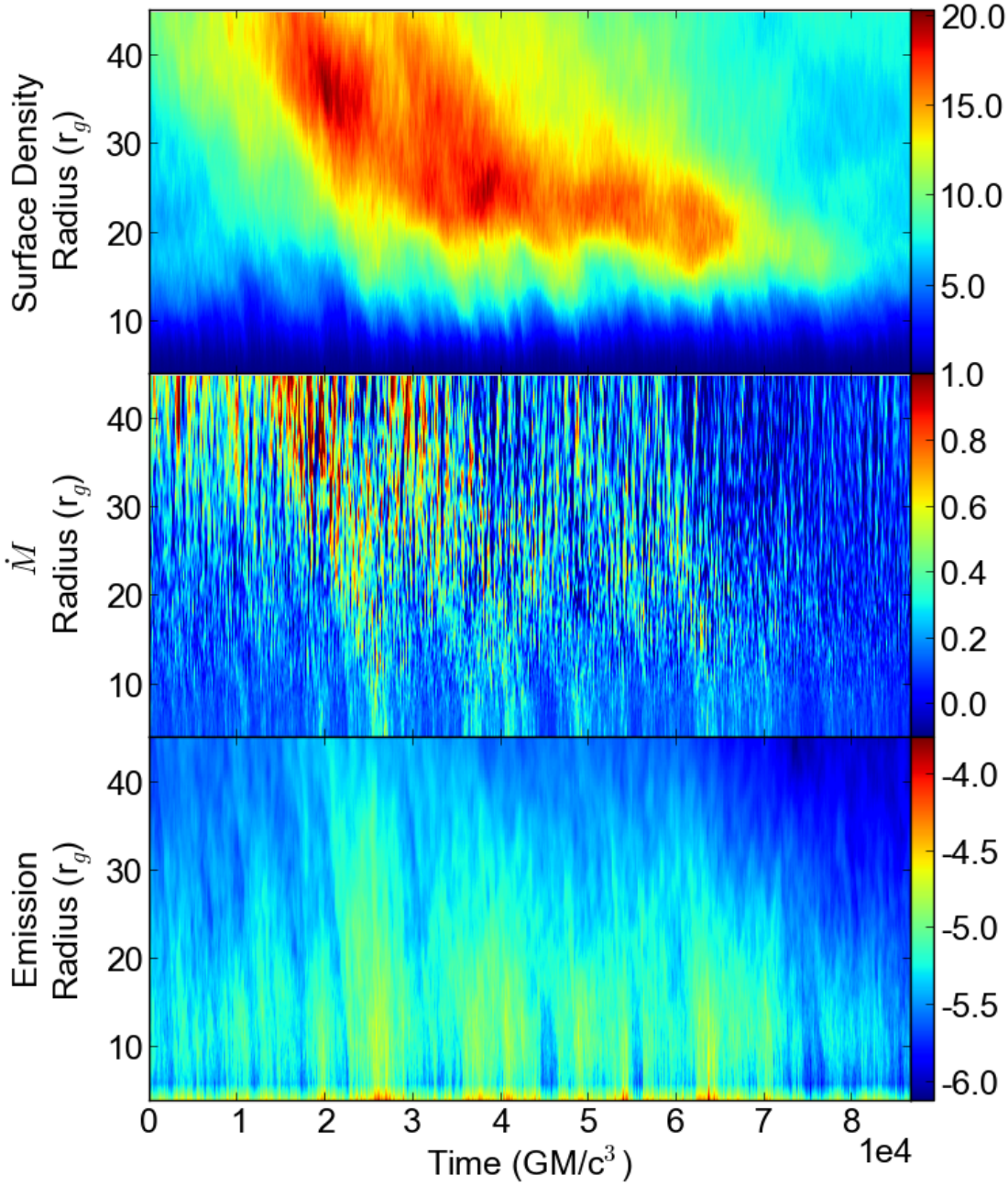

Figure 2.13: Spacetime diagrams of Σ (top panel), $\dot{M}$ (middle panel), and logarithm of the synthetic emission (bottom panel). Given the scale-free nature of the simulation, units are arbitrary and dimensionless. The preservation of fluctuations in the accretion flow that gives the appearance of "propagating fluctuations" is readily observed in the spacetime diagram of Σ and $\dot{M}$. While a simple estimate of the radiation, our emission proxy does track the other two quantities well, demonstrating that the behavior of the accretion flow will be observable.

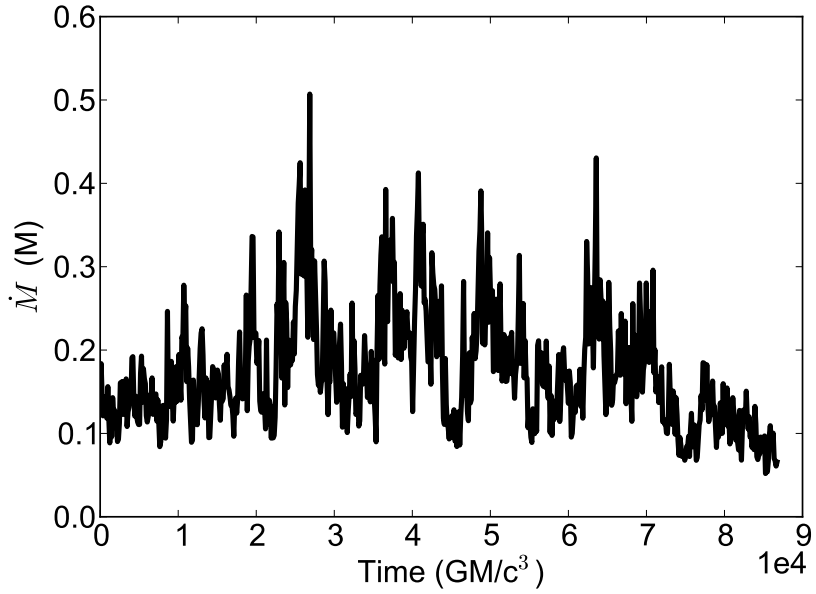

(a) $\dot{M}$ at ISCO

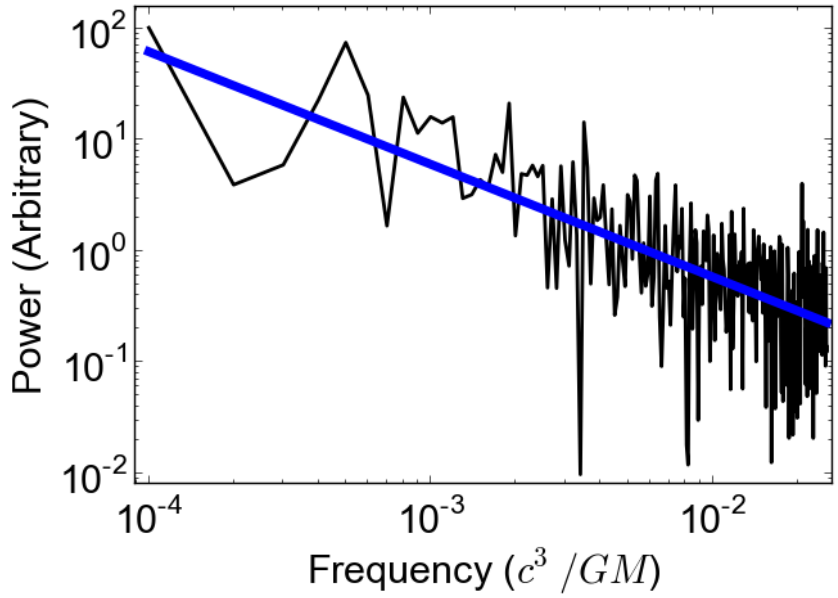

(b) PSD of $\dot{M}$ at ISCO

Figure 2.14: $\dot{M}$ at the ISCO (top panel) and its PSD (bottom panel). The PSD is best fit by a single power law with a slope of $\Gamma = -1$, shown by the blue line.

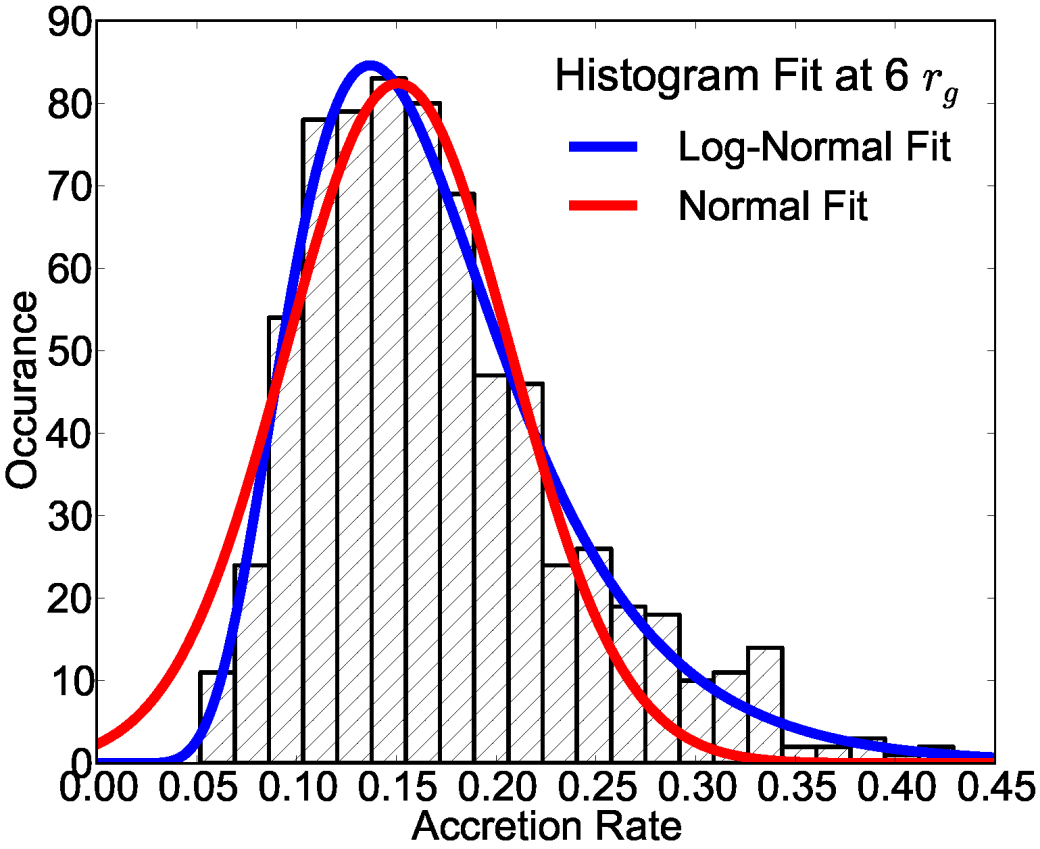

Figure 2.15: Histogram of $\dot{M}$ at the ISCO fit with a normal (red line) and log-normal (blue line) distribution. The log-normal distribution provides a superior fit.

2.5 Propagating Fluctuations in the Model Disk

2.5.1 Overview of Global Behavior

In studying the behavior of propagating fluctuations, we are interested in the relationship between the instantaneous mass accretion rate,

$$\dot{M}(R) = \int \rho v_R R \sin(\theta) d\phi d\theta, \tag{2.26}$$

and other local disk variables, specifically the surface density and the effective α-parameter. Additionally, we are interested in how evolution of the accretion disk might appear if we could observe our simulated disk. If ZEUS was an energy conserving code, we could use the simulation's cooling function as a measure of the radiated energy. However, it is not, which means the turbulent losses are not fully transferred into heat and captured by the cooling function. Therefore, we employ a dissipation proxy to generate a synthetic, time-dependent measure of the disk luminosity. In accretion disks, the outward transport of angular momentum liberates gravitational potential energy from the disk gas. This is then converted to thermal energy through the turbulent cascade of MRI driven turbulence and removed from the system through radiative processes. Assuming the disk is radiatively-efficient, the magnetic stress can be used as a tracer of energy dissipation since the energy injected by the stress is quickly radiated away. Adopting Eqn 9 from Hubeny & Hubeny (1998), the local flux at the photosphere of the disk (at one scaleheight)

due to dissipation is given by

$$F = \sqrt{\frac{GM}{r^3}} \left(\frac{A}{B} \right) \int_0^h B_r B_\phi dz \tag{2.27}$$

where A and B are relativistic correction factors given by

$$A = 1 - \frac{2GM}{rc^2} \tag{2.28}$$

and

$$B = 1 - \frac{3GM}{rc^2}. \tag{2.29}$$

This approach has been used to produce synthetic light curves in other studies of global accretion disks, e.g. Hawley & Krolik (2001) and Armitage & Reynolds (2003).

Shown in Figure 2.13 are the spacetime diagrams of Σ, $\dot{M}$ and the emission proxy. As can be seen in the figure, periods and regions of enhanced accretion (higher $\dot{M}$) are coincident with higher Σ. The correlation of $\dot{M}$ with surface density acts to (partially) preserve the pattern of fluctuations in surface density as disk material loses angular momentum and moves to smaller radii. Additionally, when $\dot{M}$ is greater at a given radii, there is a corresponding increase in the emission proxy. It is worth noting that the name "propagating fluctuations" is a slight misnomer as there is no real propagation mechanism at play in the disk. Rather, the mass accretion is a diffusive process that scales with Σ, providing the qualitative appearance of "propagating" to smaller radii.

Figure 2.14 shows the time trace and PSD of $\dot{M}$ at the ISCO (6 r_g). As expected, there are stochastic accretion events when $\dot{M}$ dramatically increases (by

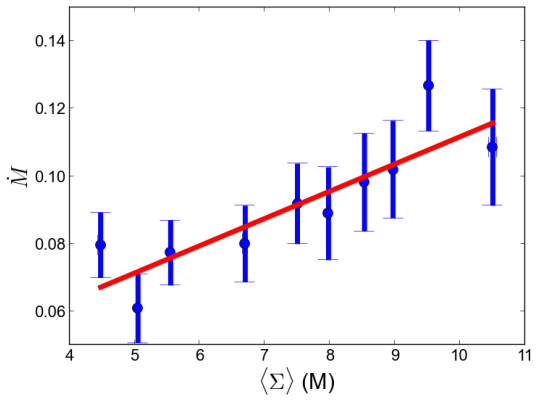

(a) Σ vs. $\dot{M}$

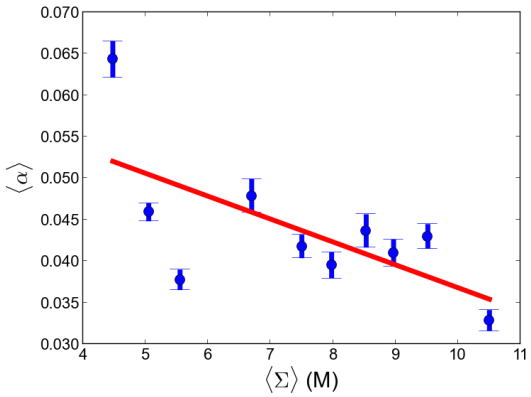

(b) Σ vs α

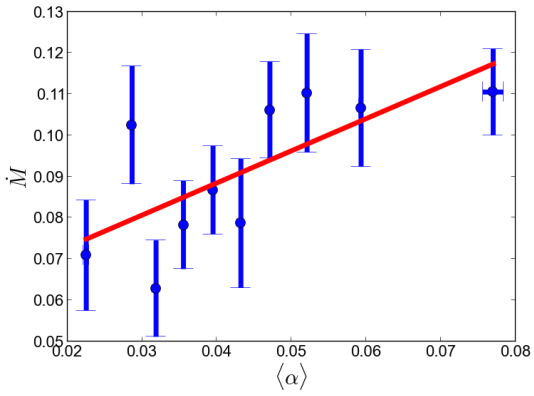

(c) α vs $\dot{M}$

Figure 2.16: Correlations between $\dot{M} - \Sigma$ (top left panel), $\alpha - \Sigma$ (top right panel), and $\dot{M} - \alpha$ (bottom panel) at $r = 15\ r_g$ in the simulation. There is a clear positive, linear trend in the $\dot{M}$ dependence on both α and Σ. Surprisingly, there is a negative trend in the Σ-α relationship which we believe is a caused by magnetic buoyancy of more strongly magnetized gas in the disk.

a factor of 3-5), and then returns to a stationary baseline value, a value of 0.1. The PSD is featureless and is best fit with a powerlaw with index of $\Gamma = -1.01 \pm 0.07$, corresponding to flicker-type noise.

2.5.2 Log-normal $\dot{M}$ Distribution

The histogram of the instantaneous mass accretion rate at the ISCO in our simulation is shown in Figure 2.15. The shape of the distribution resembles the distribution of GBHB systems like Cygnus X-1 (Uttley et al., 2005) and is, similarly, very well fit by a log-normal distribution of the form

$$f(x;\mu,\sigma) = P_0 \exp\Big[-\frac{(\ln x - \mu)^2}{2\sigma^2}\Big], \tag{2.30}$$

where P_0 is the normalization, μ is the log of the mean, and σ is the standard deviation. The best-fitting model parameters for the probability density function (PDF) of the mass accretion rate at $6r_g$ are $\mu = -1.84$ and $\sigma = -0.38$ and gives a $\chi^2/D.O.F$ of 17.9/24. For comparison, the best fit with a normal distribution has a $\chi^2/D.O.F$ of 79.8/24. Statistically, the log-normal distribution is overwhelmingly favored ($\Delta\chi^2 = 62$) and, visually, we can see the normal distribution fails to reproduce the fast rise of the distribution at low $\dot{M}$ values and shallower tail of the distribution at higher $\dot{M}$ values. The implication of this distribution is, hence, that fluctuations in $\dot{M}$ combine multiplicatively, rather than additively in our MHD disk.

We can also quantify the asymmetry of the distribution by measuring skewness. Skewness is the third momentum of the distribution and is given by,

$$\gamma_1 = \frac{\sum_{i=1}^{N}(X_i - \mu)^3/N}{\sigma^3} \tag{2.31}$$

where μ is the mean, σ is the standard deviation, and N is the number of data points. The distribution of $\dot{M}$ at the ISCO has a value of $\gamma_1 = 1.08$, indicating a strongly positively skewed distribution.

2.5.3 Correlations Between α, $\dot{M}$, & Σ

We will now look at the correlations in α, $\dot{M}$, & Σ to verify that $\dot{M}$ does indeed scale with both α and Σ. It is typically assumed α is independent of Σ thus, according the canonical disk equation, $\dot{M}$ is expected to be higher when α and Σ are larger. However, there is a degeneracy between these three parameters and we must remove the stochasticity of the third in order to tease out relationships between any two quantities. The easiest way to find the underlying trend is to simply bin the data, which essentially averages out the stochasticity of the variable we are not interested in. Since there are radial gradients in the disk, we focused on the behavior at $r = 15\ r_g$. Ten bins were used with 70 data points per bin. The bars indicate the standard deviation of the bin.

Figure 2.16 shows the $\dot{M} - \Sigma$, $\alpha - \Sigma$, and $\dot{M} - \alpha$ correlations. We find that, indeed, the mass accretion rate scales with both α and Σ, validating the *a priori* assumptions that went into the phenomenological motivation of the propagating fluctuations model. The Pearson correlation coefficient between Σ and $\dot{M}$ is 0.87 and between α and $\dot{M}$ it is 0.70, indicating these are both statistically strong correlations. Additionally, the correlation coefficient of α with Σ is $r = -0.66$, which is considered a moderately strong anti-correlation. While the strong positive correlations of $\dot{M}$

with α and Σ confirm the underlying assumptions of the propagating fluctuations model, the negative α-Σ correlation is a slightly different than expected. We believe the anti-correlation between α and Σ can be attributed to the magnetic buoyancy in the disk. In the higher density regions, pressure balance in the disk displaces magnetically dominated (lower β) gas upwards, decreasing the local field strength, thereby decreasing α and causing the negative trend.

2.5.4 Radial Coherence

The strongest evidence for propagating fluctuations in our simulation comes from radial coherence and frequency dependent phase shifts of the $\dot{M}$ variability. At the heart of the propagating fluctuations model is the predication that modulations in the accretion rate at larger radii will be seen at the inner radii with a time-lag set by the viscous inflow time. The coherence function provides the cleanest way to assess the causal connection in the disk.

Adopting the convention of Nowak et al. (1999a), we will consider $\dot{M}$ at two radii, $s_1(t)$ and $s_2(t)$, with Fourier transforms $S_1(f)$ and $S_2(f)$, respectively. The coherence of these two signals, given by

$$\gamma^2 = \frac{|\langle S_1^*(f) S_2(f) \rangle|^2}{\langle |S_1(f)|^2 \rangle \langle |S_2(f)|^2 \rangle}, \tag{2.32}$$

is a real-valued positive function that has a maximum of unity if and only if $s_2(t)$ is related to $s_1(t)$ via simple a linear transfer function,

$$s_2(t) = \int_{-\infty}^{\infty} \mathcal{T}_r(t-\tau) s_1(\tau) d\tau \tag{2.33}$$

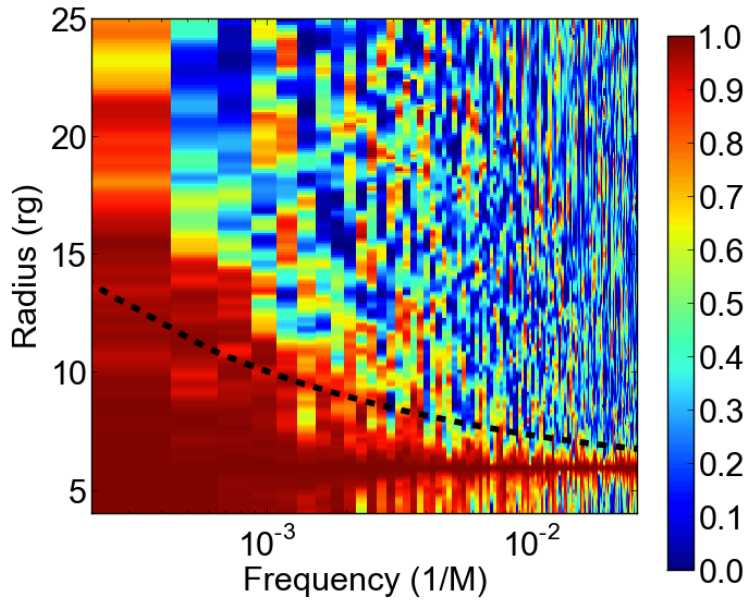

(a) Coherence

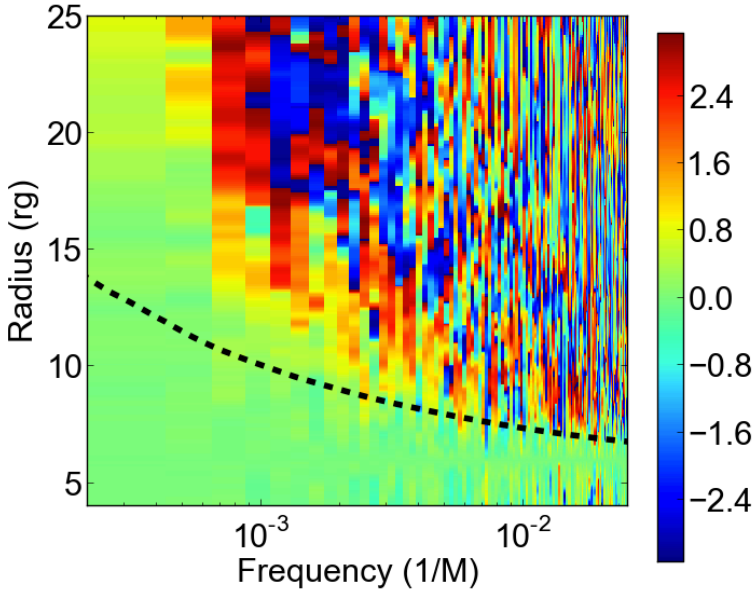

(b) Phase

Figure 2.17: Coherence (top panel) and phase (bottom panel) maps. The black dotted line indicates the local viscous frequency calculated from the average radial velocity of the gas. The region of high coherence and net phase shift is enveloped by the viscous frequency indicating fluctuations above the viscous frequency at a given radii are quickly damped out while fluctuations below the viscous frequency are preserved.

where $\mathcal{T}_r$ is some transfer function. In the other extreme, $\gamma^2 = 0$ implies no linear relationship between $s_1(t)$ and $s_2(t)$. In general, γ^2 can be considered a measure of the fraction of variability in $s_2(t)$ that is coherently related to $s_1(t)$ and has values between 0 (completely incoherent) and 1 (perfectly coherent). For non-zero coherence, we can compute the cross-spectrum $S_1^*(f)S_2(f)$. The complex phase $\Phi(f)$ of the cross spectrum gives the frequency-dependent phase shift of the coherent parts of $s_1(t)$ and $s_2(t)$.

The coherence function and phase shifts are shown in Figure 2.17. The coherence function was calculated with the ISCO taken to be the inner, reference radii. The $\dot{M}$ "signal" was broken into three segments for averaging and the coherence function was calculated with each radial bin. Similar to Cowperthwaite & Reynolds (2014), we find the coherent regions are found at frequencies below that of the local viscous frequency,

$$\omega_{visc}(R) = \frac{2\pi(R - 6r_g)}{\langle v_R(R) \rangle}. \tag{2.34}$$

The viscous time can hence be interpreted as a minimum timescale on which inward communication of flow fluctuations can occur.

From the average phases, time-lags can be determined. The frequency-dependent time lag at a given radii is $\tau(f) = \Phi(f)/2\pi f$. Figure 2.18 shows the coherence function calculated between $\dot{M}$ at the ISCO and 10 r_g. Given the length of our simulation, only the inner regions have been run for a viscous time, so we only show the structure of the phases and time lags calculated at these two radii. From the two plots we can see fluctuations in $\dot{M}$ have phase shifts that increase with

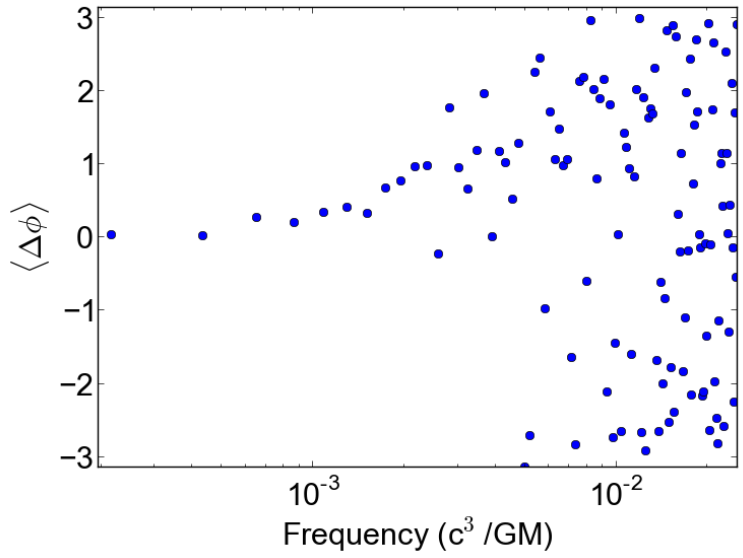

(a) Phase Difference

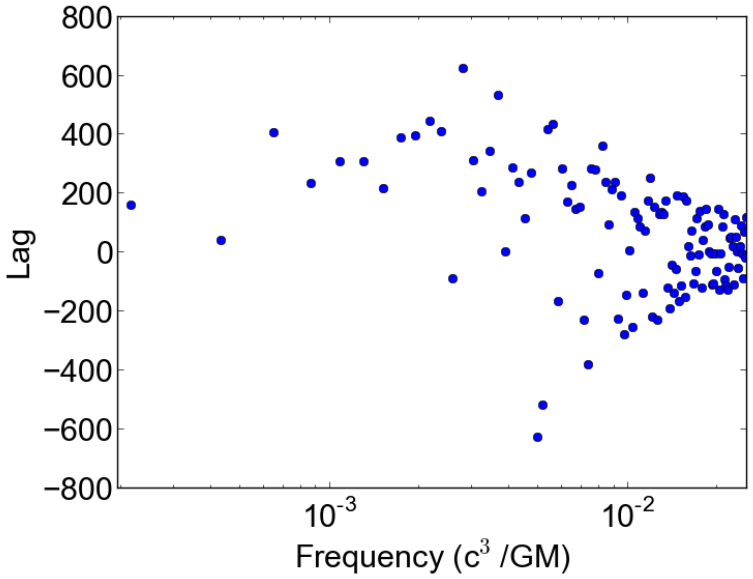

(b) Time Lags

Figure 2.18: Frequency dependent phase differences and time lags between $\dot{M}$ at $6\,r_g$ and $10\,rg$. At frequencies greater than $\omega \approx 3 \times 10^{-3}$ the coherence breaks down, as can be seen by the large scatter in the two plots.

frequency, but a constant time lag up until the fluctuations become incoherent at $\omega \approx 3 \times 10^{-3}$. The constant time lags of the fluctuation in $\dot{M}$ at different radii was seen in the semi-analytic model of Cowperthwaite & Reynolds (2014). This implies that the behavior of the propagating fluctuations in our MHD simulation is consistent with those of the one-dimensional viscous disk.

2.5.5 RMS-Flux Relationship

We finish our analysis of $\dot{M}$ by looking at the RMS-flux relationship. While the RMS-flux relationship is a staple of broadband variability (Heil et al., 2012), its physical origins remain uncertain. This relationship is of great interest because it appears to be an intrinsic property of the accretion process and, possibly, even more fundamental than the PSD of the variability. Uttley & McHardy (2001) originally hypothesized the RMS-flux relationship is evidence of Lyubarskii (1997) type propagating fluctuations in $\dot{M}$ since the RMS-flux relationship is a ubiquitous property from all black holes, regardless of mass.

If the RMS-flux relationship in the photometric variability is truly due to the propagating fluctuations in the accretion disks of these sources, it should be seen in the $\dot{M}$ of our simulation. To test this we calculated the mean,

$$\overline{\dot{M}} = \frac{1}{N} \sum_{i=1}^{N} \dot{M}_i, \tag{2.35}$$

and RMS

$$\sigma_{\dot{M}} = \sqrt{\frac{1}{N} \sum_{i=1}^{N} \left(\dot{M}_i - \overline{\dot{M}} \right)^2}, \tag{2.36}$$

of the mass accretion rate at the ISCO over a sliding window of 40 ISCO orbits

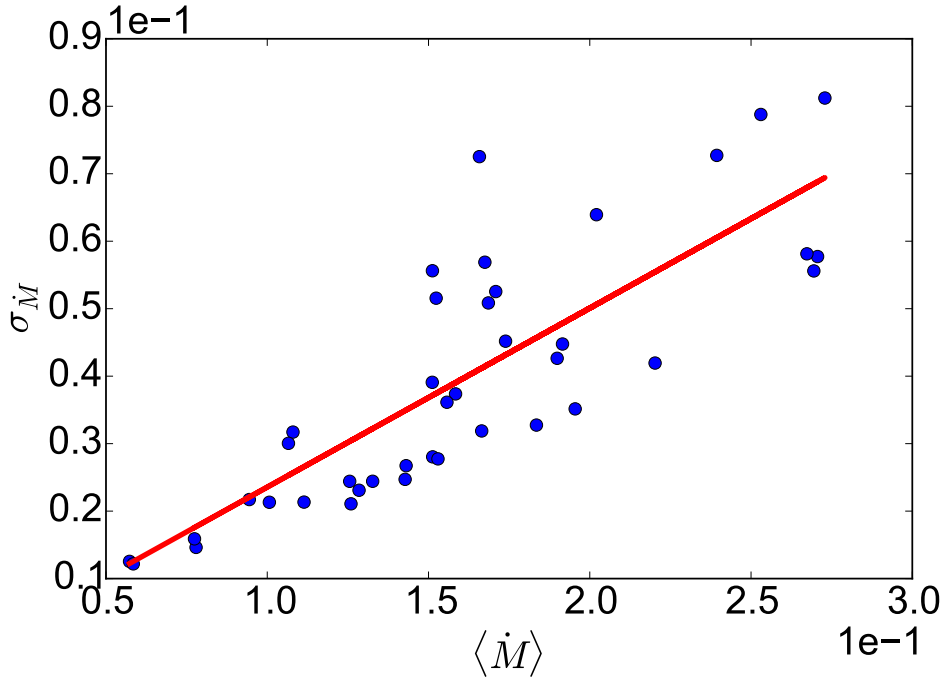

Figure 2.19: Relationship between the RMS of $\dot{M}$ vs its average value at the ISCO calculated over 40 ISCO orbit periods of the simulation. A strong linear dependence is present in the variability, consistent with the RMS-flux relationship observed from astrophysical black hole systems.

(N=20 data dumps). Shown in Figure 2.19 is a plot of the raw $\langle \dot{M} \rangle$ vs $\sigma_{\dot{M}}$ scatter plot. The relationship was fit using a Bayesian, MCMC method with a linear function of the form

$$\hat{\sigma} = k(\langle \dot{M} \rangle + C) \tag{2.37}$$

with best fitting parameters of $k = 0.30 \pm 0.03$ and $C = (-3 \pm 3) \times 10^{-3}$.

The linear correspondence of the RMS to the average mass accretion rate is expected, as well as the intercept passing through the origin, i.e. when there is no flux there should be no variability. However, the observed RMS-flux relationships are typically offset and best described by a model with a constant baseline flux, $F_{obs}(t) = F_{const} + F_{var}(t)$ (Gleissner et al., 2004), that varies with black hole spectral state. Our results suggest the variable component is related to the underlying MHD turbulence of the disk and the flux offset can be attributed to disk processes not captured by our simulation.

2.6 Proxy Light Curve Analysis

We now discuss the global behavior of our emission proxy and how the propagating fluctuations in $\dot{M}$ might appear as photometric variability. The full details of the radiation produced through the interaction of the accretion flow with the various emission mechanisms can only be captured by including more realistic radiation physics, which our simulation lacks. Nevertheless, we can use our emission proxy to explore the emission variability in a broad sense. In particular, we want to determine if the structure of the $\dot{M}$ variability can be easily observed when the emission

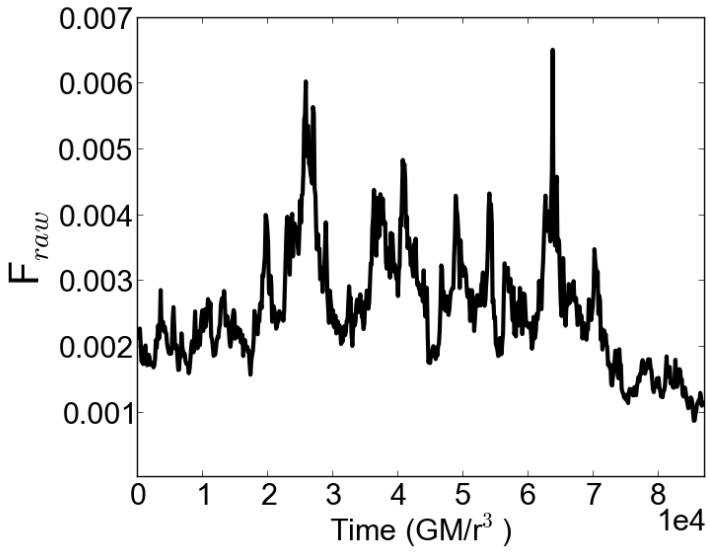

(a) Synthetic Light Curve

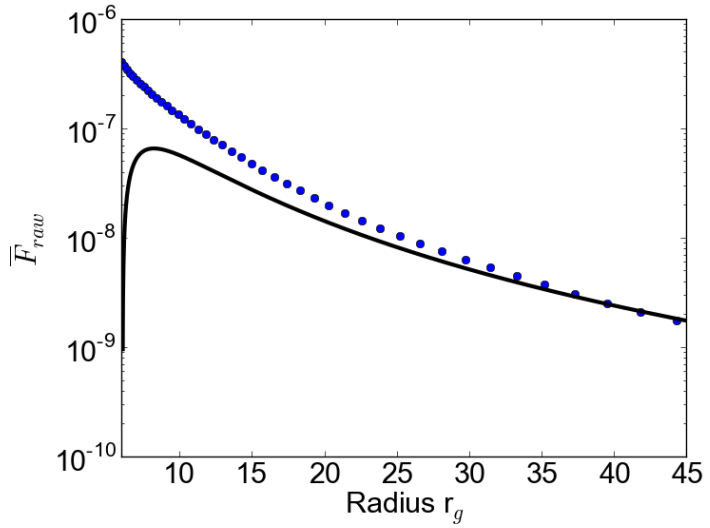

(b) Average Disk Emission Profile

Figure 2.20: Synthetic light curve (top panel) and disk emission profile (bottom panel, blue dots). The integrated synthetic emission from the disk displays large, rapid fluctuations and behaves similarly to $\dot{M}$ across the ISCO. Qualitatively, the variability is quite similar to the variability of real astrophysical black hole systems. The rapid variability indicates the inner regions of the disk have the largest contribution to the variability, which is confirmed by the radial profile of the synthetic emission proxy.

is integrated over the entire disk. The flux we observe from GBHBs and AGNs is, in effect, the integrated emission from a range of radii that evolve on timescales proportional to their dynamical times. Consequently, there is the possibility some of the variability could be smoothed out as lower-frequency variability from larger radii can wash-out higher-frequency variability. Given how clear the nonlinear signal is in astrophysical sources, we want to check it is reproduced by the variability of the emission proxy from our simulation.

Figure 2.20 shows the synthetic light curve and radial profile of the average emission for our disk. We created the light curve by integrating the dissipation from the emission proxy over the well-resolved region of the simulation ($4 - 45\, r_g$). Given our radial range, the synthetic light curve is composed of signals from radii with dynamical times that vary by a factor of 37.5, imitating observation with a broad-band filter. Several aspects of the disk emission are apparent. First, the light curve is similar to the time trace of $\dot{M}$ at the ISCO. The signal is aperiodic and flares in the light curve correspond to large accretion events. Second, any flares in the light curve quickly decay down to a well-defined, stationary average. The property of mean-reversion is of statistical interest as a way to model its behavior. Finally, and worth the most discussion, is the dominate role emission from the inner region plays in driving variability. This is more clearly seen in the radial profile of the emission per unit area of the disk, but can also be inferred by the high-frequency flares. In Figure 2.20 the disk profile of Shakura & Sunyaev (1973) is shown for comparison. The two profiles trace each other well at larger radii, but diverge in the innermost regions. In the canonical α-disk the energy flux goes to zero at the

ISCO because it was believed at the time that no torques could be felt from the gas in the inner plunging region. MHD simulations have shown that, in fact, torques can be felt across the ISCO and radiation can originate from closer to the black hole than the ISCO (Hawley & Krolik, 2001, 2002; Krolik & Hawley, 2002). In addition to the physical effect of torques spanning the ISCO region, there may also be a nonphysical contribution to our profile because we assume any energy from stresses is immediately converted into radiated energy. In reality, there is a time delay between the injection and the dissipation as the energy is transported through the turbulent cascade. In the inner regions near the black hole the material could be rapidly swept into the hole before it has had time to completely radiate the injected energy. This would lead to an overestimation of the emission from the inner regions by our emission proxy due to this advection of energy.

2.6.1 Signatures of Propagating Fluctuations

In our analysis of the mass accretion rate in the simulation we found the variability of $\dot{M}$ had near-identical structure to the universally observed flux variability from black hole systems. Real disk emission is much more complicated than what is captured by our emission proxy, however, the following analysis serves to provide a proof of concept demonstration that the $\dot{M}$ fluctuations in our simulation will translate into fluctuations in disk luminosity. While rudimentary, we will analyze the synthetic emission using the diagnostics used in Section 2.5.

Figure 2.21 (upper and middle panels) shows the flux histogram and RMS-

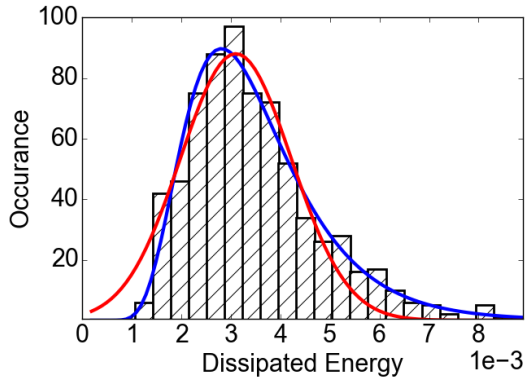

(a) Histogram of Light Curve

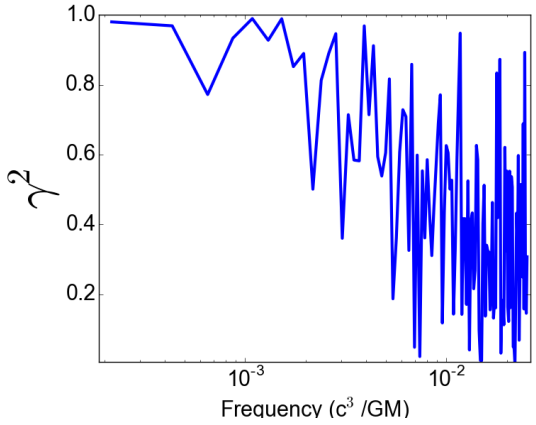

(b) Light Curve Coherence

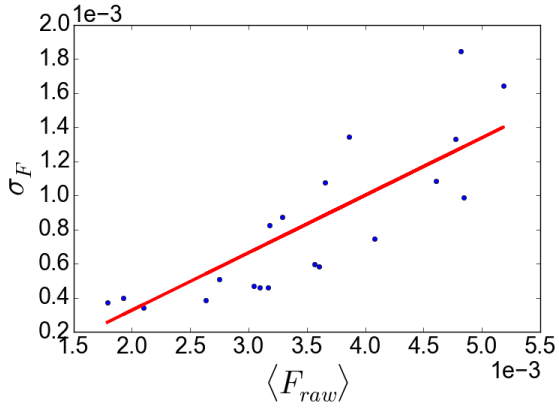

(c) RMS-Flux Relationship

Figure 2.21: Histogram of light curve (top left), light curve coherence (top right), and RMS-flux relationship (bottom). The structure of the synthetic light curve variability is similar to that of $\dot{M}$ at the ISCO, as is seen in Figures 2.15, 2.17, and 2.19.

flux relationship for the total ("broad-band") proxy light curve shown in Fig. 2.20. The preferred fit to the flux histogram is a log-normal distribution with parameters $\mu = -5.7$ and $\sigma = -0.39$. The $\chi^2/D.O.F$ of this fit is 18.1/24 which is statistically well-fit and much better than that of a normal distribution with $\chi^2/D.O.F$ of this fit is 98.9/24. The skewness of this distribution is $\gamma_1 = 1.28$, indicating the histogram of the light curve is more highly skewed than the histogram of the $\dot{M}$ and the log-normal distribution is more pronounced. Naively, the increased skewness is surprising given that the light curve is integrated over the disk and presumably additively combining many random processes. According to the central limit theorem, this should drive the distribution to be more Gaussian. However, since $\dot{M}$ is radially coherent, the fluctuations of the emission proxy are not independent, as is assumed in a Gaussian process.

The full synthetic light curve also has a linear relationship between the RMS of the variability and the average flux value. As we did with $\dot{M}$, the light curve was broken into 20 sections and the standard deviation and mean values were calculated for each. The distribution is well fit by a linear function with $k = 0.34 \pm 0.07$ and $C = (-3 \pm 3) \times 10^{-4}$.

Examination of radial coherence in the emission proxy requires that we first create two light curves to imitate observation in different energy bands (in a loose sense this can be thought of as observing an accreting stellar mass black hole in the hard and soft X-rays). The light curves we use were generated by integrating the emission proxy in the regions spanning $4 - 10r_g$ and $10 - 15r_g$. Then, as we did with $\dot{M}$, the coherence function was calculated by dividing the light curves

into three sections, resulting in the coherence function shown in Fig. 2.21 (bottom panel). The coherence shows the same behavior as found for the mass accretion rate, with highly-coherent signals at low-frequencies, and a falling coherence at higher-frequencies. De-coherence is seen at $\omega \approx 300\ c^3/GM$ which, while a relatively high-frequency, agrees with the coherence and phase plots of $\dot{M}$ fluctuations with the ISCO in Figure 2.17.

2.6.2 Timing Properties

Having established the signatures of propagating fluctuations in $\dot{M}$ are present in the variability of our emission proxy, we will now look at the PSD and the statistical behavior of the variability by fitting a simple Ornstein-Uhlenbeck (OU) process.

Shown in Figure 2.22 is the PSD of the synthetic light curve fit with a broken power law. The last 512 data points of our light curve were used to calculate the PSD which ensures no phase dependencies were present. Following the method described in Reynolds & Miller (2009), the PSD was fit with a power law plus white-noise component and broken power law plus white-noise component of the form

$$A(\omega) = \begin{cases} K\omega^{-\Gamma_1} & \text{if } \omega < \omega_{brk} \\ K\omega_{brk}^{\Gamma_2-\Gamma_1}\omega^{\Gamma_2} & \text{if } \omega > \omega_{brk} \end{cases} \tag{2.38}$$

where K is a normalization constant, Γ_1 is the low frequency slope, Γ_2 is the high frequency slope, and ω_{brk} is the break frequency, to determine which model provides the best description of the PSD. The power density was assumed to have an exponential probability distribution with the probability of measuring a given power

between p and $p + dp$ expressed by,

$$P(p)dp = \frac{1}{p_0} e^{-p/p_0} dp, \tag{2.39}$$

where p_0 is the mean power. For an individual bin, the likelihood of a measuring power $p_{obs,i}$ is

$$\mathcal{L}_i = (1/p_{mod,i}) \exp(p_{obs,i}/p_{mod,i}). \tag{2.40}$$

For the entire PSD, the likelihood is the product of the individual likelihoods. Since this can often be very large or very small, the standard statistic used is the log likelihood,

$$\ln \mathcal{L} = \sum_i [-\ln p_{mod,i} - p_{obs,i}/p_{mod,i}]. \tag{2.41}$$

A Markov Chain Monte Carlo (MCMC) algorithm was used to conduct the fitting and find the parameters that maximize the log likelihood of each PSD model.

The PSD is well fit by both a broken power law with $\Gamma_1 = 0.5 \pm 0.3$, $\Gamma_2 = 1.8 \pm 0.2$, and $\omega_{brk} = (2.9 \pm 1.4) \times 10^{-4}$ and a single power law with $\Gamma = 1.38 \pm 0.18$. However, the broken power law provides a much better statistical fit with $\Delta \ln \mathcal{L} = 5.08$ at the expense of two degrees of freedom. This translates into a $\Delta\chi^2 = 10.16$.

Hence, while the underlying PSD of $\dot{M}$ at the ISCO in our simulation has $\Gamma = 1$, the integrated emission proxy has a steeper PSD. This is simply due to the integrated contributions from across the accretion disk, with additional low frequency power from large radii being added to the PSD. It is not immediately clear what physics sets the break frequency, which corresponds to a timescale of $2000 - 6500\ r_g/c$. It is faster than the nominal viscous time and approximately matches the cooling/thermal timescale out to approximately $r = 20\ r_g$ in the disk.

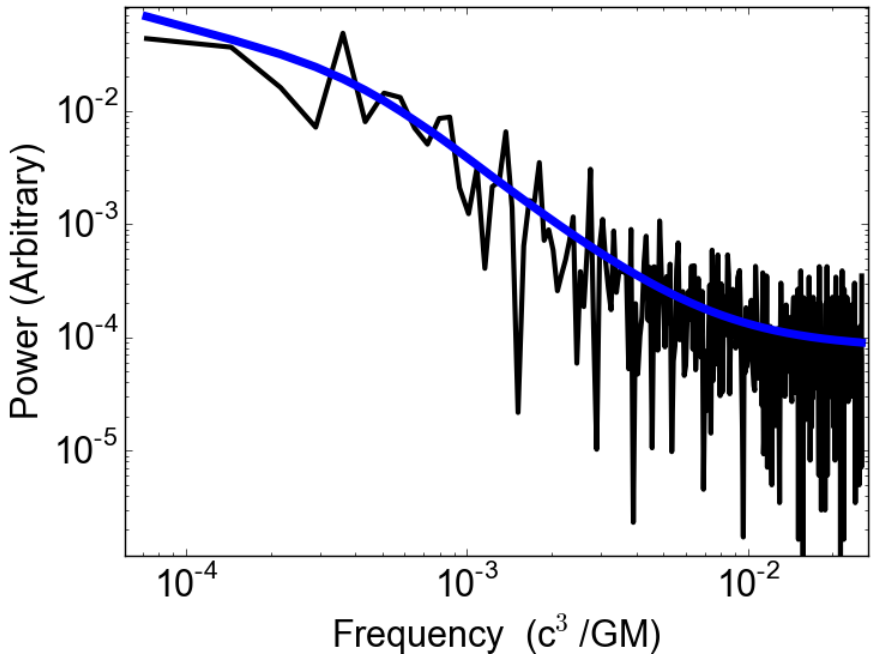

Figure 2.22: Synthetic light curve PSD with broken power law fit (blue line).

In order to ensure that the low-frequency break is not imposed by the truncation of our emission proxy at $r = 45r_g$, we generated light curves and the corresponding PDSs truncating at $r = 20, 30, 40r_g$. In all cases, the break persisted and the frequency was unchanged.

In addition to the PSD, the statistical properties of the variability provide an additional method of characterizing the synthetic light curve. Some recent work has shown a damped random-walk, and more specifically an Ornstein-Uhlenbeck (OU) process, provides a very good statistical model of GBHB and AGN variability (Kelly et al., 2009, 2011; Kozłowski et al., 2010; MacLeod et al., 2010), although there are others which suggest this may not be the case (Kasliwal et al., 2015; Kozłowski, 2017). The OU process is part of a class of statistical models called *continuous*

time, first order autoregressive, CAR(1), processes. CAR(1) processes can take many forms and behave very different depending on their model parameters. The OU process describes a noisy relaxation process where a system is stochastically perturbed from a stationary mean and decays back to the mean with a relaxation time τ (Gillespie, 1996). The stochastic differential equation describing such a process is:

$$dX(t) = \lambda(\mu - X(t))dt + \sigma dW_t \tag{2.42}$$

where $\lambda = 1/\tau$, μ is the mean and σ is a measure of the average magnitude of volatility per $\sqrt{dt}$. This equation has the following direct solution:

$$X_{i+1} = X_i e^{-\lambda t} + \mu(1 - e^{-\lambda\delta}) + \sigma\sqrt{\frac{1 - e^{-2\lambda\delta}}{2\lambda}}N_{0,1} \tag{2.43}$$

where δ is the time step and $N_{0,1}$ is a zero-centered, Gaussian distribution with a variance of 1.

The even sampling of our light curve provides some simplicity in fitting the OU process. X_{i+1} is linearly dependent on X_i and takes the form:

$$X_{i+1} = AX_i + b + \epsilon, \tag{2.44}$$

where ϵ is a normal-random term that is independent and identically distributed. From a simple linear fit, we can solve for λ, μ, and σ where

$$\lambda = \frac{-\ln a}{\delta}, \tag{2.45}$$

$$\mu = \frac{b}{1 - a}, \& \tag{2.46}$$

$$\sigma = sd(\epsilon)\sqrt{\frac{-2\ln a}{\delta(1 - a^2)}}. \tag{2.47}$$

Since the OU process is inherently a Gaussian process we must therefore perform the fit to the synthetic light curve in log-space since our "flux" distribution is log-normally distributed. Thinking in terms of real observations, this is equivalent to fitting in magnitude space. For our light curve, the best fit parameters are $\lambda = (3.5 \pm 1.2) \times 10^{-3}$, $\mu = (3.3 \pm 0.6) \times 10^{-3}$ and $\sigma = (6 \pm 3) \times 10^{-5}$. The λ parameter corresponds to a decay time of $t_{decay} = 286\, GM/c^3$.

2.7 Discussion

In our simulation we find that Lyubarskii (1997) type "propagating fluctuations" quickly develop and are sustained throughout the entire simulation. The multiplicative manner by which fluctuations in $\dot{M}$ combine and grow defines the behavior and subsequent evolution of the disk. The most significant consequence from the multiplicative combination of $\dot{M}$ fluctuations is that the accretion history of a given parcel of gas is retained, allowing for the apparent propagation of fluctuations on a viscous time. The $\dot{M}$ variability at the ISCO in our simulation bears striking resemblance to variability observed from astrophysical black holes and shares the same phenomenological properties. In particular, it reproduces the log-normal flux distributions, RMS-flux relationship, and radial coherence ubiquitously observed from GBHBs and AGNs. These nonlinear features have typically been difficult for variability models to account for, but are a consequence of a scenario where the mass accretion rate is proportional to the multiplicative product of a stochastically varying viscosity and the local surface density. In our simulated disk they develop

naturally from the MRI driven turbulence.

Additionally, we use an emission proxy to generate a disk-integrated synthetic light curve to verify that the nonlinear characteristics of the $\dot{M}$ variability will actually translate into observable features in the disk emission. While rudimentary, our emission proxy follows the turbulent energy injected to the gas, which we assume is quickly radiated away since we are considering a radiatively efficient disk. We find that, indeed, the nonlinear features of $\dot{M}$ are present when the entire disk integrated emission is considered and are not lost with the addition of low-frequency variability originating from gas at large radii.

Our work was able to address several issues raised by Cowperthwaite & Reynolds (2014) regarding the timescale on which the effective α parameter of the disk fluctuates and how well an MHD disk can really be described by a strictly viscous disk on long time scales. The previous efforts to model propagating fluctuations in mass accretion rate of Lyubarskii (1997) using a linearized model and Cowperthwaite & Reynolds (2014) using a one dimensional viscous disk model relied on the *a priori* assumption that the low-frequency fluctuations in effective α occurred on a viscous time. However, this is very long for the magnetic field to vary. When Cowperthwaite & Reynolds (2014) allowed α to vary on a dynamical time, the typically assumed evolutionary timescale for the MRI, they found that the fluctuations were too rapid and propagating fluctuations did not develop. We find the disk dynamo can provide the necessary intermediate timescale modulation of the effective α to drive propagating fluctuations in mass accretion rate. Dynamo action is universally observed in modern accretion disk simulations and seems to be intimately tied to

the MHD physics of a differentially rotating plasma. Thus, the dynamo can provide a natural mechanism to introduce variability in the effective α. While the ubiquity of the dynamo has been established, its presence is typically neglected when considering accretion disk evolution. Our results highlight the significant impact the dynamo can have on the disk and that it is a fundamental ingredient in the driving of propagating fluctuations.

The properties of the $\dot{M}$ and light curve variability from our global, *ab initio* MHD simulation are very similar to those from the simple viscous disk with stochastic viscosity parameter of Cowperthwaite & Reynolds (2014). From this similarity, we can conclude that on long timescales our MHD disk acts in a viscous manner. This is not surprising, but there is not a trivial connection between the internal MHD stresses that transport angular momentum and the expected viscous behavior of the disk, even though it has largely been intuited from empirical results.

Our MHD simulation captures gross aspects of real disk variability, but it is not without limitations. In particular, we use simple prescriptions to approximate the affects of general relativity and radiative physics. As a first effort at modeling propagating fluctuations in mass accretion rate in an MHD disk we are mainly concerned with capturing the dynamics of the disk and the interplay of the accretion flow with the stochastically fluctuating effective α. To do this, a long, high-resolution simulation is required. Therefore, the priority of where computational resources are used shifts away from more complex physics and into the duration and resolution of the simulation.

While the focus of our analysis has been on understanding the signatures of

propagating fluctuations around black holes, we do not expect the effects of general relativity and radiation physics to have a significant impact on the characteristics of the disk evolution are primarily concerned with. In fact, the phenomenology we seek to understand is also readily observed in cataclysmic variable (CV) systems (Scaringi et al., 2012a,b, 2014) and young stellar objects (YSOs, Scaringi et al., 2015). These systems are non-relativistic and not hot enough to be largely affected by radiation pressure in the disk. The similarity of the broad-band variability between YSOs, CVs, GBHBs, and AGNs implies that propagating fluctuations are a generic feature of highly ionized accretion disks. The fluctuations resulting from the underlying accretion processes behave consistently across many orders of magnitude of mass, temperature and evolutionary time implying that the growth of propagating fluctuations is not unique to a specific class of system, but rather intrinsically tied to the angular momentum transport resulting from MHD turbulence. Therefore, we believe that the results from this simulation are robust enough to provide a qualitative description the accretion mechanism for highly ionized accretion disks.

2.8 Conclusions

In this chapter we have performed the first examination of the propagating fluctuation picture using *ab initio* MHD turbulent models of disk accretion. The propagating fluctuations model has served to explain the universally observed non-linear features of photometric variability from accreting black holes of all masses. In our simulation, propagating fluctuations in $\dot{M}$ form and behave in a manner con-

sistent with those of the viscous disk model of Cowperthwaite & Reynolds (2014). The main results are summarized here:

1. The effective α-parameter in our simulated disk is highly variable. The variability has two components: a high-frequency component due to local fluctuations from the MRI and a lower frequency component due to modulation of the stress by the disk dynamo.

2. The lower frequency variability in the effective α-parameter from the disk dynamo drives fluctuations in $\dot{M}$ by modulating the internal disk stress on an intermediate timescale. As was shown in Cowperthwaite & Reynolds (2014), if fluctuations in α are too rapid, fluctuations will be damped out and propagating fluctuations will not grow. The dynamo frequency is low enough that propagating fluctuations can easily grow. Previous efforts directed at understanding the role of propagating fluctuations in $\dot{M}$ relied on *ad hoc* prescriptions for the variability timescale. We show, for the first time, that the dynamo fills this role and provides a natural driver for fluctuations in $\dot{M}$.

3. The $\dot{M}$ in our simulation is positively correlated with Σ and the effective α. In the analytic disk equations the mass accretion rate is proportional to the product of the local surface density and the local viscosity. These correlations are found in our *ab initio* simulation, suggesting that they naturally result from the interaction of the MRI with accretion flow.

4. The $\dot{M}$ variability at the ISCO of our simulation resembles the photometric variability observed from GBHBs and AGNs. The $\dot{M}$ variability is log-

normally distributed, has a linear RMS-flux relationship, and displays radial coherence. These features are empirically observed and have been attributed to propagating fluctuations in $\dot{M}$. We find that they are, in fact, properties of accretion flow when propagating fluctuations in $\dot{M}$ are present.

5. Using an emission proxy to generate a disk integrated, synthetic light curve, we find that the qualitative properties of the accretion flow are reflected in the observable emission. While the nonlinear signatures are preserved in the light curve, integrating over the disk adds additional low-frequency power from more distant radii. However, since the inner region of the disk is brightest, the high frequency variability is preferentially weighted and the nonlinear properties of $\dot{M}$ are preserved.

Chapter 3: Truncated Accretion Disks In Hydrodynamics

3.1 Introduction

One of the most dramatic examples of variable behavior seen from black hole binaries (BHBs) is the spectral state changes during outburst and the associated hysteresis. BHBs are relatively rare, but the several dozen that have been identified are found to have common evolutionary properties during their state transitions (e.g. Cygnus X-1, 4U 1543-47, H1743-332, GRO J1655-40, GX 339-4).

Much uncertainty surrounds this behavior, but spectral timing studies find that, in a broad sense, there are two primary BHB accretion states, low and high, with distinct properties and additional transitionary intermediate states with composite properties (Remillard & McClintock, 2006). Of the two main states, the low state is less luminous and the BHB X-ray spectrum is dominated by a power law with index ~ 1.7. A thermal spectral component is present, but typically contributes around 20% of the $2 - 20$ keV flux. Radio emission originating from a jet is usually observed and, in some objects with high luminosities, an outflowing wind can be found (Homan et al., 2016), too. In the high state, a BHB is more luminous. Thermal, blackbody emission dominates the X-ray spectrum and accounts for $> 75\%$ of the unobscured $2 - 20$ keV flux. The peak of this thermal

emission is around 1 keV, which is taken as evidence the geometrically thin disk extends close to the inner-most stable circular orbit (ISCO). In this state, a jet is absent, but signatures of outflowing winds are usually found in the X-ray spectrum. Additionally, quasiperiodic oscillations (QPOs) are observed during accretion state transitions, with high-frequency QPOs observed in certain intermediate states and low-frequency QPOs found in some low-states.

While these common behaviors exist, every outbursting BHB is unique and has its own peculiarities. Nevertheless, the gross differences between the low and high state properties seem to naturally be explained with a model where the accretion occurs through either a hot or cold mode. These different modes are associated with different accretion flow structures and varying degrees of inner disk truncation (for review see Done et al., 2007; McClintock & Remillard, 2006; Zdziarski & Gierliński, 2004). The preferred mode depends on the cooling efficiency of the inner region of the accretion flow as the accretion rate evolves; specifically, the flow is in a radiatively inefficient mode in the low state and a radiatively efficient mode in the high state. In the low state, the inefficient cooling in the inner region effectively truncates the cold, thin disk since the thermal energy of the gas cannot be radiated away. The inner disk is replaced by a hot, diffuse flow, hence, the accretion flow should inflate and be geometrically thick and optically thin. In the high state, radiation can efficiently remove thermal energy, allowing the disk to take on an optically thick and geometrically thin configuration like the α-disk of Shakura & Sunyaev (1973). Since the disk can cool efficiently, there is no disk truncation and the thin disk extends down to the ISCO.

The bifurcation of accretion states in active galactic nuclei (AGNs) is less clear, but there is evidence that accretion in low-luminosity AGN (LLAGN), including Sgr A* in our galactic center, is dominated by a hot mode (Narayan & Yi, 1995a; Rees et al., 1982). In AGNs whose accretion rate is sufficiently low, less than 1% of their Eddington limit, hot mode accretion (Ho, 2008; Yuan & Narayan, 2014) and inner disk truncation (Nemmen et al., 2014; Trump et al., 2011; Yu et al., 2011) seems to be common. Qualitatively, the properties of LLAGN resemble the BHB hard state. The SED of a standard, unobscured, luminous Seyfert ($1-30\%$ Eddington), on the other hand, typically has a large thermal component peaking in the far-UV, analogous to the soft state of BHBs. The prevalence with which thick-to-thin disk transitions are invoked to explain the phenomenology of both BHBs and AGNs warrants a rigorous investigation of the behavior of the accretion flow at this interface to solidify the theoretical underpinnings of the truncation model.

For gas to accrete onto the central black hole, it must lose angular momentum. The seminal work of Shakura & Sunyaev (1973) parameterized the strength of the internal stress relative to the gas pressure in the thin disk through the so-called "α-parameter," described in Chapter 1. The source of this anomalous viscosity was assumed to be turbulence, but the driving mechanism was not elucidated until the magnetorotational instability (MRI) was proposed as a viable instability (Balbus & Hawley, 1991). The connection between MRI-driven turbulence and the α-parameter has since been well-studied in global MHD accretion disk simulations (e.g. Armitage, 1998; Beckwith et al., 2011; Flock et al., 2011; Hawley, 2000) and thin disks have been shown to behave viscously.

The behavior, energetics, and dynamics of the hot phase accretion, on the other hand, are not well constrained. Many types of hot flows have been suggested to fill this role including advection dominated accretion flows (ADAFs; Narayan & Yi, 1994, 1995a,b) and convection dominated accretion flows (CDAFs; Quataert & Gruzinov, 2000). Simulations of non radiative, thick disks with varying levels of sophistication have been used to shed light on the behavior of hot accretion flows. Both HD (Igumenshchev & Abramowicz, 1999; Igumenshchev et al., 2000; Proga & Begelman, 2003; Stone & Balbus, 1996; Yuan & Bu, 2010) and MHD (Hawley & Balbus, 2002; Hawley et al., 2001; Igumenshchev et al., 2003; Stone & Pringle, 2001) numerical models ubiquitously develop outflows. In the HD cases, and some early MHD models, circulation often developed within the outflow and is interpreted as convection. In more recent MHD models, though, the convection is found to be stabilized (e.g. Narayan et al., 2012; Yuan et al., 2012, 2015).

Despite the thoroughness with which numerical models have investigated the thin and thick disk configurations separately, the details of how the hot and cold flow coexist are not understood. Several global accretion models have been proposed and either explored analytically or with simple numerical models to determine how a truncated disk might develop. For instance, a truncated disk could exist because the inner disk evaporates due to the cool, Keplerian disk being heated by a hot corona (Liu et al., 1999; Meyer & Meyer-Hofmeister, 1994; Narayan et al., 1996; RóżaŃska & Czerny, 2000). Alternatively, the diffusion of energy from the interior of the disk could also heat the gas beyond the viral temperature, thereby driving the inner disk to a hot accretion solution and truncating the disk (Honma, 1996;

Manmoto & Kato, 2000; Manmoto et al., 2000). Local thermal instability can also develop if the α-parameter is proportional to the magnetic Prandtl number (Potter & Balbus, 2014, 2017). However, there is still much uncertainty underlying the trigger mechanism.

Still, headway can be made in characterizing the flow dynamics of a truncated disk. Of the outstanding issues, there is a particular need to understand the structure of the transition from the assumed thin disk to the thick disk and the influence the truncation has on the disk evolution. For instance, how does the flow conserve mass, angular momentum, and energy when it passes through an abrupt transition zone? Can a steady-state configuration develop, or is time-variability a necessary ingredient? On these fronts, numerical models provide a valuable tool and way to glean insight into the properties of truncated disks.

Radiation HD (RHD; Das & Sharma, 2013; Wu et al., 2016a) simulations have tried to directly address the viability of the state transitions of BHBs. They find that when realistic radiation prescriptions which account for bremsstrahlung, synchrotron, and synchrotron self-Comptionization are included in the models, disks that are qualitatively similar to the BHB state transition model readily develop. These models naturally form truncated, thin, cold disks embedded in a hot, diffuse medium. Recently, Takahashi et al. (2016) used a simulation which accounted for general relativity, radiation and MHD (GRRMHD) and found a truncated disk developed where gas resided in a two-phase medium configuration. In the inner region of their simulations, the gas is radiatively inefficient and the viscous time is shorter than the cooling time. While it was not explicitly stated, this presumably

sets up an ADAF-like flow. Evidence for thermal, and possibly viscous instability, has also been found in the GRRMHD simulations in Mishra et al. (2016).

The truncated disks found in the RHD and GRRMHD simulations suggest these transitions can naturally happen, but relying on computationally intensive algorithms comes at the sacrifice of resolution and simulation time. A pervasive issue in these works is that the cold disk cools to the scale of the grid and the internal dynamics are unresolved. This poses a problem because the defining evolution of the accretion flow can occur on small scales and on long times, which makes a proper simulation of a truncated accretion disk very difficult to do with current computational capabilities. Thus, to conduct a detailed study of the accretion flow itself and get a handle on how a truncated accretion disk will evolve, we must make the problem tractable by forgoing some of the more computationally expensive physics, like a full treatment of the radiation physics and the general relativistic effects which may impact the evolution of the disk in the very inner region close to the black hole. Here, we assume the truncation found in the simulations of Das & Sharma (2013), Wu et al. (2016a), Takahashi et al. (2016), and Mishra et al. (2016) can naturally occur and seek to fully characterize the accretion flow of a truncated α-type viscous disk and understand the observational consequences.

In this chapter we discuss the behavior of the first sustained truncated accretion disk that has been produced, i.e. a truncation that can be studied for thousands of dynamical times. The simulation is well-resolved and allows for a detailed study of the dynamics, energetics, and angular momentum transport in the disk. We do not use a full prescription for the radiation, but rather use an *ad hoc*, bistable cool-

ing function to drive a thermal instability interior to some radius, thereby creating a transition between a cold and hot disk that can be characterized. *We emphasize that the aim of this work is not to reproduce the state transitions observed in BH systems, instead it is to study the putative truncated disk found in hard state BHBs and LLAGNs.* To isolate the behavior of the transition zone, we study the most ideal scenario possible, an axisymmetric viscous HD accretion disk in a Newtonian potential. The work presented here is a precursor to a study using a 3D high-resolution MHD simulation with the same bi-stable cooling function that is presented in Chapter 4.

The viscous formalism used here gives the freedom to set the viscosity and balance the heating rate to the cooling rate according to an α-parameter. To better match the accompanying MHD truncated disk simulation, we set $\alpha = 0.065$. This value was determined through a calibration MHD simulation, described in Chapter 4. In setting the HD α-parameter to that of an effective α-parameter from an MHD model, we can provide a more direct association of the disk behaviors between the HD and MHD regime.

By first establishing a benchmark with a simple α-disk, we hope to gain a better understanding of the more complex disk model set in MHD, where heating and angular momentum transport occur solely thorough MRI-driven turbulence, and more honestly assess the viability of truncated disk models in the literature. Much of the previous theoretical work is developed in HD, so the simplified model considered here will help bridge the gap between expectations of models developed in the literature and the more physical MHD model.

This chapter is organized as follows. In Section 3.2 we discuss our numerical model, simulation setup, and bistable cooling function. In Section 3.3 we discuss our analysis of dynamics, angular momentum transport, and energetics of the truncated disk. In Section 3.4 we discuss the implications of our results and the caveats associated with the simulation. In Section 3.5 we provide a summary and closing remarks.

3.2 Numerical Model

The goal here is to emulate a truncated accretion disk and perform a detailed study of its dynamics, angular momentum transport, and energetics. We therefore idealize our test problem so that we can direct our computational resources to the physics necessary to capture the hot-cold flow boundaries, run the model at high resolution, and run for many evolutionary times. In this work, we consider a two-dimensional, axisymmetric, viscous disk. The simulation is divided into two phases: an initialization period before the switch to the bistable cooling function and the latter portion used in our analysis where the bistable cooling function drives thermal instability and creates a sustained truncation. For numerical reasons that become especially important in the MHD case, we initially evolve the simulation as a thin disk with constant aspect ratio $h/r = 0.1$ where the disk thickness is maintained by a cooling function with a single target disk thickness. Once a quasi-steady state develops, the cooling is switched to a bistable cooling function where the gas can cool efficiently with a target scale height $h/r = 0.1$ or inefficiently with a target scale

height of $h/r = 0.4$, depending on its temperature. If the gas temperature is above the transition temperature, T_T, it cools according to the inefficient prescription; if it is below it cools according the the efficient prescription. The analysis focuses on the truncated disk.

The additional computational expense of accounting for full GR in this hydrodynamic simulation is manageable; however, it would be very restrictive for our follow-up simulation in MHD and hinder our ability to achieve the goal of performing a detailed study of the flow behavior. Therefore, we opt to consider the simplified Newtonian case here to aid in comparing between the HD and MHD scenarios. Additionally, these transitions are expected to occur at $30 - 100\ r_g$ (Nemmen et al., 2014), which is far enough from the black hole that relativistic effects are minimal, so there is observational motivation for neglecting GR as well.

3.2.1 Simulation Code

For this study we use the second-order accurate PLUTO *v4.2* code (Mignone et al., 2007) to model the gas dynamics. The equations of hydrodynamics are evolved,

$$\frac{\partial \rho}{\partial t} + \nabla \cdot (\rho \mathbf{v}) = 0, \tag{3.1}$$

$$\frac{\partial}{\partial t}(\rho \mathbf{v}) + \nabla \cdot (\rho \mathbf{v}\mathbf{v} + P\mathcal{I}) = -\rho \nabla \Phi + \nabla \cdot \sigma, \tag{3.2}$$

$$\frac{\partial}{\partial t}(E + \rho\Phi) + \nabla \cdot [(E + P + \rho\Phi)\mathbf{v}] = \nabla \cdot (\sigma : \mathbf{v}) - \Lambda, \tag{3.3}$$

where ρ is the gas density, $\mathbf{v}$ is the fluid velocity, P is the gas pressure, $\mathcal{I}$ is the unit rank-two tensor, $\boldsymbol{\sigma}$ is the viscous stress tensor, E is the total energy density of the fluid,

$$E = u + \frac{1}{2}\rho|\mathbf{v}|^2, \tag{3.4}$$

and Λ accounts for radiative losses through cooling. PLUTO was used in the dimensionally-unsplit mode with the `hllc` Riemann solver (a three-wave, four state solver) with piecewise linear spatial interpolation and second-order Runge-Kutta time integration. Since the Godunov scheme conserves the total energy of simulation to machine accuracy, the only energy losses come from outflow across the domain boundary and the cooling function of the simulation.

3.2.2 Simulation Setup

In our simulation we adopt an axisymmetric, two-dimensional, spherical coordinate system (r, θ, ϕ) for our computational grid. The domain spans $r \in [10r_g, 1000r_g]$ and $\theta \in [\pi/2 - 1.0, \pi/2 + 1.0]$ with $N_R \times N_\theta = 512 \times 512 = 2.62 \times 10^5$ zones. The radial spacing of the grid increases logarithmically so that $\Delta r/r$ is constant. In the θ-direction, the simulation uses 320 uniformly grid zones in the midplane region from $\theta = \pi/2 \pm 0.5$ and 96 geometrically stretched grid zones in each of the coronal upper regions ($\pi/2 + 0.5 \leq |\theta| \leq \pi/2 + 1.0$).

Outflowing boundary conditions are used for the inner and outer r-boundaries and the $\pm\theta$ boundaries, but were modified to prevent the inflow of material. Periodic boundary conditions are used for the axisymmetric ϕ-direction. A density and

pressure floor is implemented to protect against values becoming artificially small or negative. All fluid variables (e.g. ρ, p, T) are reported in normalized units from the simulation.

We consider an ideal gas with a $\gamma = 5/3$ adiabatic equation of state in a Newtonian gravitational potential where,

$$\Phi = -\frac{GM}{r}. \tag{3.5}$$

Initially, the simulated disk is thin ($h/r = 0.1$) and in vertical hydrostatic equilibrium. The steady state α-disk solution is used for initialization:

$$\rho(R,\theta) = \rho_0 R^{-3/2} \exp\left(-\frac{z^2}{2c_s^2 R^3}\right)\left[1-\left(\frac{R_*}{R}\right)^{\frac{1}{2}}\right] \tag{3.6}$$

where ρ_0 is a normalization constant to set the maximum disk density to unity, R is the cylindrical radius ($R = r\cos\theta$), z is the vertical disk height ($z = r\sin\theta$), and c_s is the sound speed ($c_s = \sqrt{P/\rho} = (h/r)v_K$). R_* is taken to be just inside the inner simulation domain ($R_* = 11\,GM/c^2$) to account for the torque-free inner boundary condition.

In astrophysical accretion disks, the effective viscosity originates from MRI driven turbulence. In our hydrodynamic simulation, however, we approximate this by treating the angular momentum transport with an α-type viscosity according to Shakura & Sunyaev (1973). We set the shear viscosity term to be,

$$\nu = \frac{2}{3}\alpha P \Omega_K^{-1} = \frac{2}{3}\alpha\rho T \Omega_K^{-1}, \tag{3.7}$$

where Ω_K is the Keplerian angular velocity. A dimensionless α-parameter is set to $\alpha = 0.065$ to match the test MHD run discussed in Chapter 4, as we described in

Section 3.1.

3.2.3 Cooling Function

Our goal is to construct a model accretion disk that undergoes a radial transition from a geometrically-thin radiatively-efficient state to a geometrically-thick inefficient state as the matter flows inwards. Once such a state has been constructed, we can then characterize the dynamics of this transition region. Here, we describe the toy optically-thin cooling function that we use to achieve this goal.

The volumetric heating due to the $r-\phi$ shear stresses is

$$\mathcal{H} = \frac{3}{2}\alpha\mathcal{R}\rho T\Omega_K, \tag{3.8}$$

where Ω_K is the Keplerian angular velocity, and $\mathcal{R}$ is the gas constant. In a steady-state, radiatively efficient disk we will have $\mathcal{H} = \Lambda$. We seek to construct a cooling function $\Lambda(\rho, T, r)$ that (i) is positive-definite everywhere (in contrast to many of the "target thickness" cooling functions employed in previous work; Noble et al. 2009), (ii) yields a disk model that is viscously stable, (iii) produces a hot, geometrically-thick solution at small radii, (iv) produces a cool, geometrically-thin solution at large radii. We adopt a cooling function of the form,

$$\Lambda = \Lambda_0(T)\rho T^2 f(r), \tag{3.9}$$

where $f(r)$ shall be specified later to maximize convenience. The linear dependence on density ensures that the thermal balance is independent of density, removing the possibility of viscous instability. Noting that $c_s^2 = \mathcal{R}T = (h/r)^2\Omega_K^2$, we see that the

condition $\mathcal{H} = \Lambda$ gives

$$\frac{h}{r} = \sqrt{\frac{3\alpha\mathcal{R}^2}{2\Lambda_0(T) r^2 \Omega_K f(r)}}. \tag{3.10}$$

We choose $f(r) = \mathcal{R}^2 r^{-2} \Omega_K^{-1} \propto r^{-1/2}$ so that

$$\frac{h}{r} = \sqrt{\frac{3\alpha}{2\Lambda_0(T)}}, \tag{3.11}$$

and, by construction, the disk has a constant aspect ratio (i.e., fixed h/r) if Λ_0 is a constant.

We induce thermal instability and hence a radial transition into the flow by introducing an abrupt decrease in $\Lambda_0(T)$ at a prescribed transition temperature T_T,

$$\Lambda_0(T) = \begin{cases} \Lambda_c & (T < T_T) \\ \\ \Lambda_h & (T \geq T_T) \end{cases} \tag{3.12}$$

where Λ_c and Λ_h are constants, and we will assume here that $\Lambda_c > \Lambda_h$. With Λ_0 so defined, the thermal balance condition $\mathcal{H} = \Lambda$ delineates three radial regions within the disk. Inside of a radius $r_{tr,i} = 3\alpha GM/2\Lambda_c \mathcal{R}^2 T_T$ (the inner transition radius), local thermal balance requires that the flow is hot with geometric thickness

$$\left(\frac{h}{r}\right)_{\text{hot}} = \sqrt{\frac{3\alpha}{2\Lambda_h}} \quad \text{for} \quad r < r_{tr,i} := \frac{3\alpha GM}{\Lambda_c \mathcal{R}^2 T_T} \tag{3.13}$$

Outside of a radius $r_{tr,o} = 3\alpha GM/2\Lambda_h \mathcal{R}^2 T_T$ (the outer transition radius), thermal balance requires that the flow is cold with geometric thickness

$$\left(\frac{h}{r}\right)_{\text{cold}} = \sqrt{\frac{3\alpha}{2\Lambda_c}} \quad \text{for} \quad r > r_{tr,o} := \frac{3\alpha GM}{\Lambda_h \mathcal{R}^2 T_T} \tag{3.14}$$

Between these two transition radii, the flow is bistable and thermal balance can be achieved either in the cold or the hot branch with geometric thickness

$$\left(\frac{h}{r}\right)_{\text{cold}} \quad \text{or} \quad \left(\frac{h}{r}\right)_{\text{hot}} \quad \text{for} \quad r_{tr,i} < r < r_{tr,o}. \tag{3.15}$$

Note that, due to the form of our cooling law, the ratio of the cold/hot geometric thickness is related to the ratio of the inner/outer transition radii,

$$\frac{r_{tr,o}}{r_{tr,i}} = \left[\frac{(h/r)_{\rm hot}}{(h/r)_{\rm cold}}\right]^2 \tag{3.16}$$

In this work, we set

$$\left(\frac{h}{r}\right)_{\rm cold} = 0.1 \tag{3.17}$$

$$\left(\frac{h}{r}\right)_{\rm hot} = 0.4 \tag{3.18}$$

$$r_{tr,i} = 100 r_g. \tag{3.19}$$

which implies $r_{tr,o} = 1600 r_g$. As we shall see, this toy cooling function results in a successful transition from a cold/thin to a hot/thicker disk close to the inner transition radius. Interestingly, the flow in the bistable region remains predominantly in the cold/thin state.

3.3 Results

We will now discuss our analysis of the hydrodynamic disk simulation. We show that a truncated disk does indeed develop and investigate the dynamics, energetics, and angular momentum transport associated with the accretion flow in the truncated state. Interestingly, we find that a sustained stream of sub-Keplarian gas flows inwards from the thick-to-thin disk transition and undergoes delayed heating. As the gas heats to T_T and beyond, pockets of hot gas form in the dense disk which buoyantly rise and cool, inducing a circular flow in the coronal regions of the disk and CDAF-like behavior. As the disk refills at the transition radius, the cycle

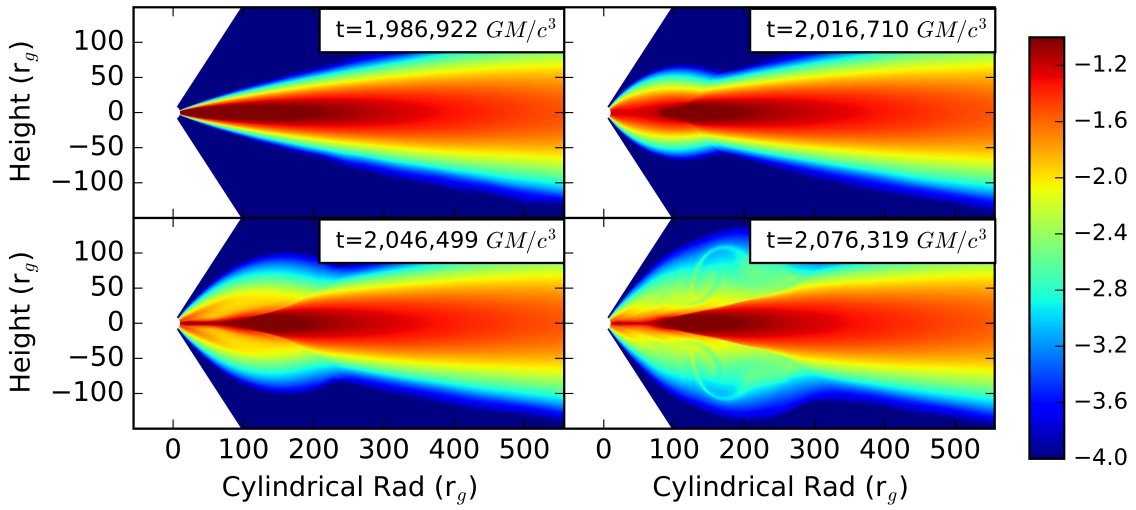

Figure 3.1: Snapshots of the gas density during transient heating event at the end of the disk initialization. The top left panel shows the simulation when the cooling is switched to the bistable cooling function at $t = 1.99 \times 10^6\ GM/c^3$ $(10,000th$ inner orbit). The following three panels show the simulation evolution at a $3.0 \times 10^4\ GM/c^3$ (150 inner orbit times) interval.

repeats quasi-periodically.

3.3.1 The Truncated Disk

We begin by discussing the initial development of the truncated disk in the final phase of the initialization and the general properties of the truncated disk. As discussed in Section 3.2.3, the simulation is first evolved with constant $h/r = 0.1$, from $t = 0\ GM/c^3$ to $t = 1.98 \times 10^6\ GM/c^3$ (the first $10,000$ inner orbits) before the cooling is switched to include both a hot and a cold branch. Immediately after the switch, there is a large, transient heating event within $r \approx 200\, r_g$ that lasts roughly $\Delta t = 1.4 \times 10^4\ GM/c^3$ and then cools over $\Delta t = 8.6 \times 10^4\ GM/c^3$. At 100 r_g, $t_{dyn} \sim 6.3 \times 10^3 GM/c^3$ so the heating event lasts approximately 2.5 dynamical

times and the cooling event occurrs on roughly the thermal time of the inner disk. Figure 3.1 shows four snapshots of ρ during the heating event.

The gas in the inner region of the disk responds to the change in cooling by inflating since it is beyond T_T and has an excess of thermal energy which it cannot rapidly dissipate on the inefficient cooling branch. Additionally, viscous stresses continue to do work on the gas, further increasing the temperature. A thin, dense stream of material plunges into the inner region between $t = 2.01 \times 10^6\, GM/c^3$ and $t = 2.04 \times 10^6\, GM/c^3$. Since this gas is near T_T, it ablates away, ultimately leaving a truncated disk. The final remnants of the transient can be seen in a very thin stream of dense gas in the inner region of the disk at $t = 2.01 \times 10^6\, GM/c^3$ and large, buoyant bubbles rising away from the transition radius.

The abrupt change in the cooling law is, obviously, unphysical and the heating event is the reaction of the gas to the sudden switch. Following this, however, the disk quickly settles into a new, sustained configuration with a "transition zone" from $r = 80 - 100\, r_g$. In this transition zone, the region is cyclically filled with material through accretion, but then evacuated as the gas heats to T_T. *Unless explicitly stated, the analysis we detail is conducted following the implementation of the bistable cooling function.*

Figure 3.2 shows two representative snapshots of the gas density and scale height temperature during initialization and during the analysis. Before the change in cooling function, the disk has a uniform scale height ratio and very little hot gas is present in the simulation. In the density and temperature maps of the truncated disk, wispy regions of cold, dense gas are seen surrounding diffuse, hot bubbles. The

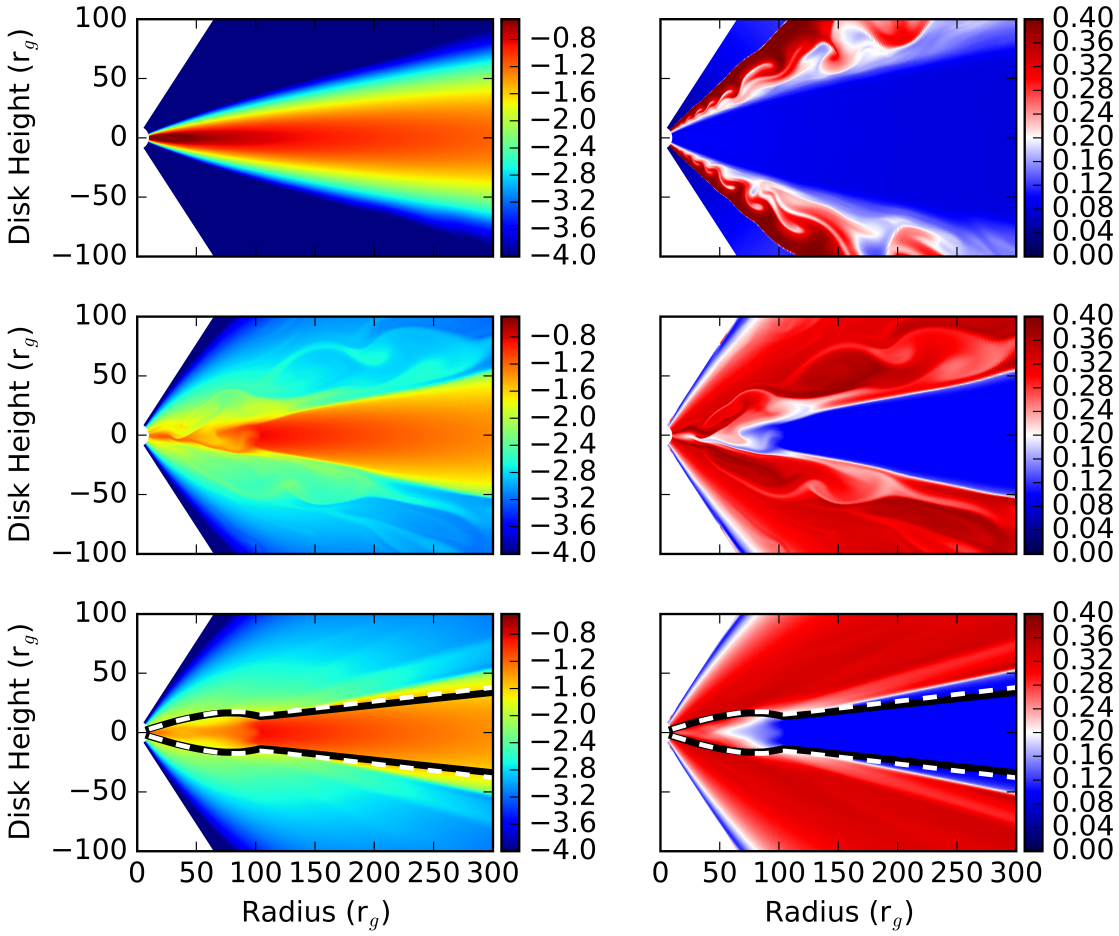

Figure 3.2: Density and temperature structure of the disk. In the top two rows, the logarithm of the instantaneous density (left column) and temperature scale height (right column) are shown of the inner simulation region during the initialization at the switch to the bistable cooling function $t = 1.99 \times 10^6\, GM/c^3$ and at an arbitrary time when the disk is truncated ($t = 5.96 \times 10^5\, GM/c^3$). In the bottom row, the time-averaged density and temperature maps are shown of the portion of the simulation over which we the used in our analysis ($t > 1.99 \times 10^6\ GM/c^3$). Overlaid is the average geometric scale height (h_g/r, black line) and the temperature scale height (h_T/r, white dashed line).

cold features are very dynamic and short lived, as they are close to the transition temperature and can spontaneously transition to the hot phase.

Figure 3.2 also shows the time averaged density of the disk with two measures of the characteristic disk scale height overlaid. The first measure is that of the geometric scale height ratio,

$$\frac{h_g(r)}{r} = \left\langle \sqrt{\frac{\int (\theta(r) - \bar{\theta}(r))^2 \rho d\Omega}{\int \rho d\Omega}} \right\rangle, \tag{3.20}$$

where $d\Omega = \sin\theta d\theta d\phi$ is the solid angle element in spherical coordinates and ,

$$\bar{\theta}(r) = \frac{\int \theta(r) \rho d\Omega}{\int \rho d\Omega} \tag{3.21}$$

is the average polar angle of the gas. The second measure is the density weighted, temperature scale height ratio,

$$\frac{h_T(r)}{r} = \left\langle \frac{\int \sqrt{Tr} \rho d\Omega}{\int \rho d\Omega} \right\rangle, \tag{3.22}$$

where T is the gas temperature, $T = P/\rho$. The values of h_g/r and h_T/r were calculated for every data dump and time averaged, denoted by the angled brackets. *Throughout this chapter we take gas in the "hot phase" to be that with $T > T_T$ and gas in the "cold phase" to have $T < T_T$.*

Spatially, the time-averaged gas density shows a distinct truncation at $r = 100$ r_g, which also corresponds to location where the disk becomes thicker, as shown by h_g/r and h_T/r. In the inner region of the disk ρ is lower than the disk body by approximately an order of magnitude. The averaged scale height ratio of the inner disk is only twice as thick as the rest of the disk and does not reach the "thick" scale height target of $h_h/r = 0.4$ due to a significant amount of advective cooling.

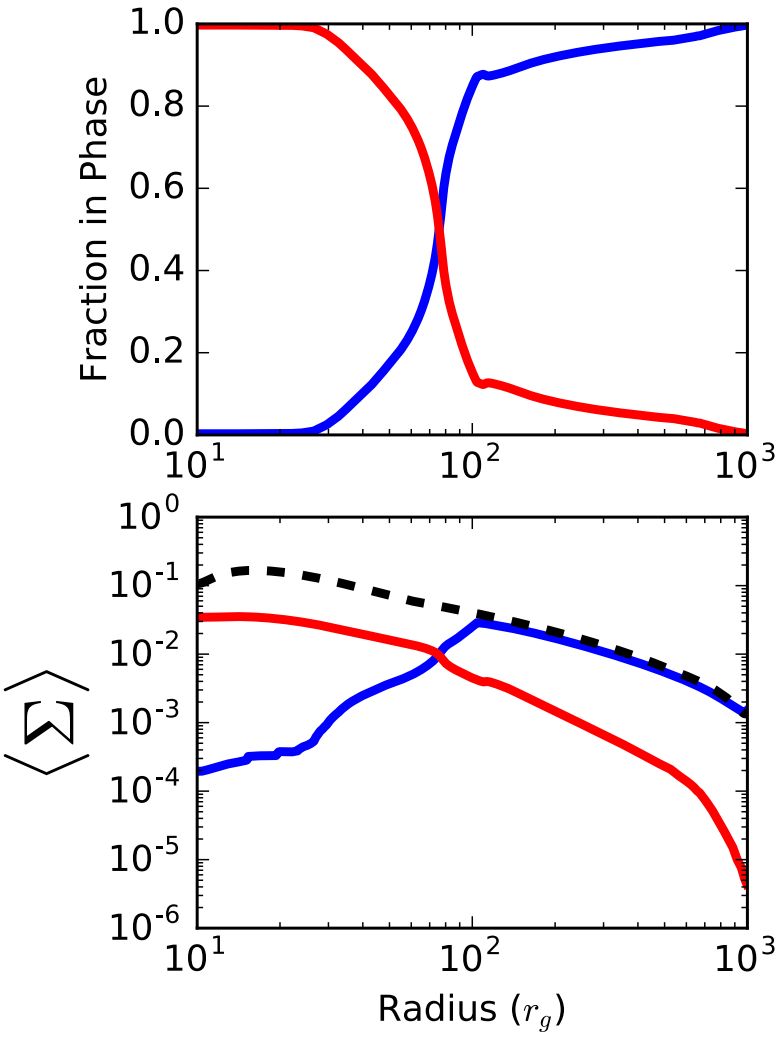

Figure 3.3: Top panel- Radial profiles of the time-averaged f_c (blue line) and f_h (red line). Bottom panel- Radial profiles of time-averaged Σ_c (blue line) and Σ_h (red line). The surface density at the end of the initialization prior to the switch to the bistable cooling function is shown as the black dashed line.

The signature of the thick-to-thin transition is also present in the thermal profile of the disk. Figure 3.3 shows the time averaged radial profile of the fraction of gas in the hot and cold phases. The fractions do vary in time, but, nevertheless, from this profile, we can see hot phase gas typically resides in the inner region of the disk and cold phase gas resides beyond the density transition. It is also worth noting that the transition from a predominately hot to cold phase, i.e. where the fraction gas in the hot phase equals the fraction of gas in the cold phase, does not occur at $r = 100\, r_g$ as we would expect from the cooling function, but rather just inwards of this radius at $r = 80\, r_g$. In brief, this is due to delayed heating as the gas is close to, but not yet at, T_T as it crosses $r = 100\, r_g$. At the hot/cold flow interface it moves inwards and then makes the transition within the expected transition radius.

The truncation is also present in the time averaged surface density,

$$\Sigma = \frac{1}{2\pi r} \int \rho r^2 d\Omega. \tag{3.23}$$

The hot and cold gas phases as a function of radius are also shown in Figure 3.3. Compared to the surface density at the end of the initialization, the inner disk surface density is lower by a factor of five. Further out, beyond the transition radius where the gas is predominantly in the cold phase, the overall surface density is very near the intialization level. Thus, through the launching of the convective cells by the transitioning gas, there is essentially an evacuation of the inner disk relative to the untruncated disk.

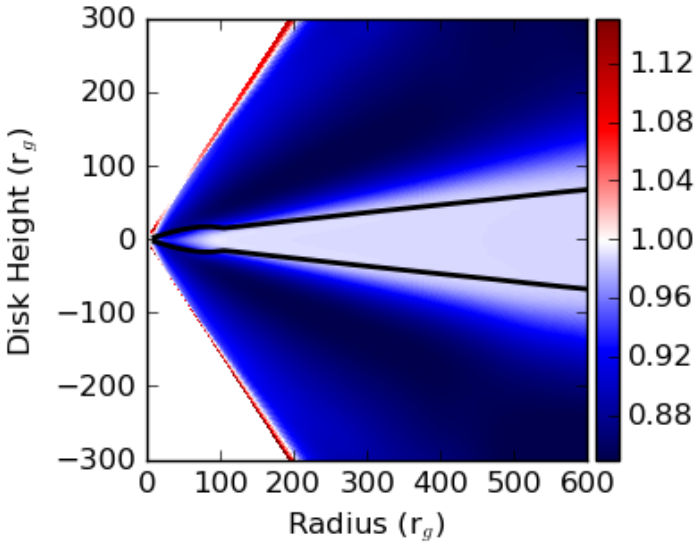

(a) $\langle v_\phi \rangle / v_K$

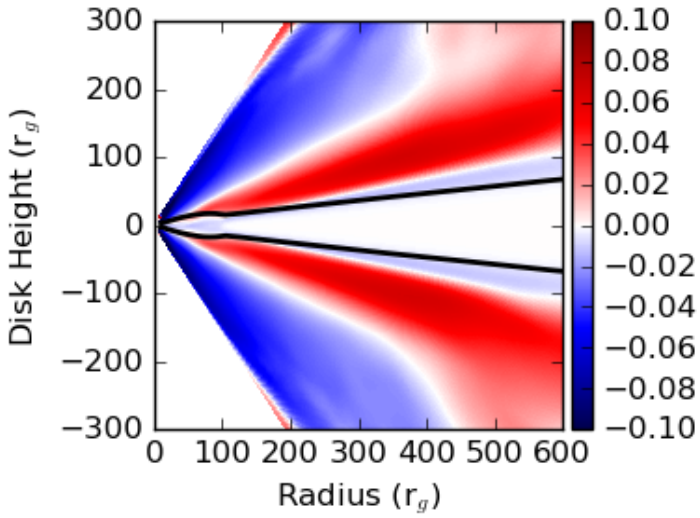

(b) $\langle v_r \rangle / v_K$

Figure 3.4: Maps of $\langle v_\phi \rangle / v_k$ and $\langle v_r \rangle / v_k$. For reference, h_g/r is overlaid. The $\langle v_\phi \rangle / v_k$ map shows the gas in the coronal regions of the disk and within the transition radius is sub-Keplerian. The stratified radial velocity structure of the gas is seen in the $\langle v_r \rangle / v_k$ map. Within the cold disk body, the gas has very little radial motion. The inflowing gas is seen as a thin boundary layer at the geometric scale height. Large convective cells are found the coronal regions of the disk, which are seen here as alternating positive velocities at lower altitudes and negative velocities at higher altitudes.

3.3.2 Disk Dynamics

The disk dynamics in a truncated disk are of interest since hot and cold accretion flows should behave quite differently, but the truncated disk model used to explain astrophysical sources expects the two flows to exist in close proximity. In the canonical thin accretion disk, the disk is rotationally supported and thermal motions are a small component of the overall velocities, i.e. $h/r = c_s/v_K$ where v_K is the Keplarian velocity (Shakura & Sunyaev, 1973).

In Figure 3.4 the time averaged ratios of $\langle v_\phi \rangle / v_K$ and $\langle v_r \rangle / v_K$ are shown as a function of position in the simulation domain. In the normalized simulation units (i.e. $G = M = c = 1$), the Keplerian velocity is:

$$v_K = \frac{1}{\sqrt{r}}. \tag{3.24}$$

The disk establishes four dynamically distinct regions. First is the outer disk body where the gas follows Keplerian orbits with very small radial velocity, as in a standard thin accretion disk. Second, are the coronal regions, where the gas is sub-Keplerian with an average azimuthal velocity of $\approx 15\%$ below v_K. For comparison, previous hydrodynamic studies of hydrodynamic CDAF-like flows (e.g. Stone et al., 1999), typically find that the azimuthal velocities are nearly-Keplerian and greater than we find here. Additionally, as can be seen in the plot of $\langle v_r \rangle / v_K$, there is a substantial outflow with $v_r \approx 10\%$ of the local v_K immediately above and below the disk, and a comparable fallback velocity at higher altitude. This is due to a single convective cell that occupies each of the coronal regions. Third is the inner disk

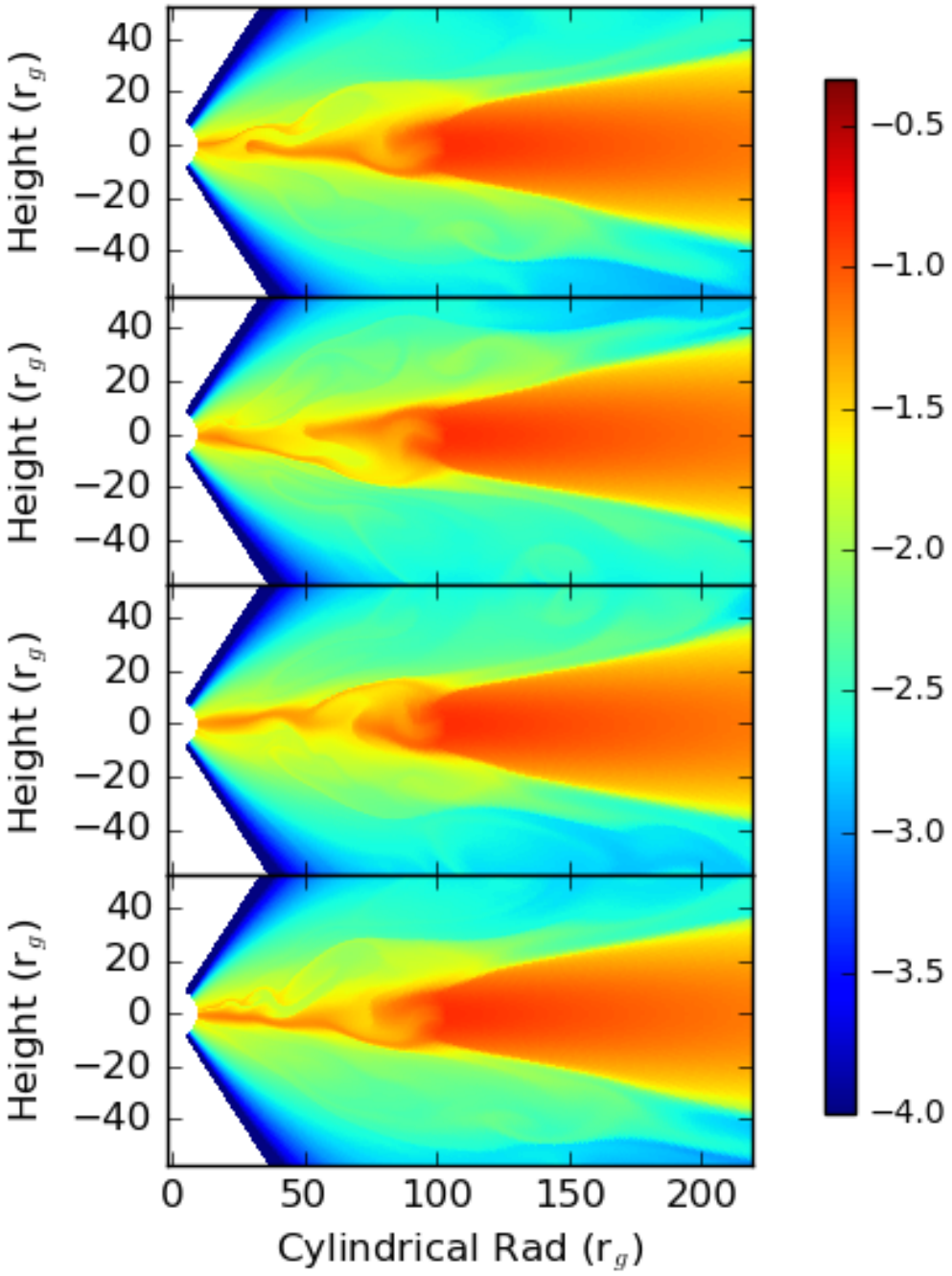

Figure 3.5: Launching of outflow as pockets of hot gas spontaneously transition to the hot phase. This sequence of images shows the gas density in the inner region at $t = 2.48 \times 10^6\, GM/c^3$ (12,500 inner orbits), $2.50 \times 10^6\, GM/c^3$ (12,600 inner orbits), $2.52 \times 10^6\, GM/c^3$ (12,700 inner orbits), and $2.54 \times 10^6\, GM/c^3$ (12,800 inner orbits) and is representative of the general behavior observed in the simulation.

body found within $r = 100\, r_g$ and one scale height above and below the disk. In Figure 3.2 we saw that this region was less dense, but contained a fair amount of cold gas. In Figure 3.4 we can see that this cooler region is modestly sub-Keplerian and inflowing at 1% of v_K. Finally, there is a thin layer of gas enveloping the disk at one scale height where the $\langle v_r \rangle / v_K$ map reveals that there is a prominent inflow directly on the disk body. It is in this region that the bulk of the mass accretion from the outer disk occurs.

The launching mechanism is interesting, especially considering this is a simple hydrodynamic simulation so a magnetocentrifugally driven wind (Blandford & Payne, 1982) or a radiation driven wind (Proga & Kallman, 2004; Proga et al., 2000) cannot form. Here, we find the outflow in the simulation is launched by pockets of hot gas that spontaneously undergo a transition from the cold phase to the hot phase in the cool stream. As the gas expands, it becomes less dense and, thus, buoyantly unstable according to the the Solberg-Høiland criterion describing the stability of a rotating fluid. When the gas is launched, there is already an angular momentum deficit, so it has little rotational support at a large radius. Unlike a pure CDAF, the gas accretes when it falls back because, while the cooling of the hot gas is inefficient, it is not zero and Bernoulli parameter is not conserved.

The launching processes is shown in a sequence of images in Figure 3.5. The cold, sub-Keplerian stream can be seen in the dense gas. As the gas spontaneously transitions to the inefficient cooling branch, it heats and expands. In doing so, these pockets of newly heated gas are surrounded by denser, cooler material so they buoyantly rise which disrupts the cold stream and disturbs the flow. Once the gas

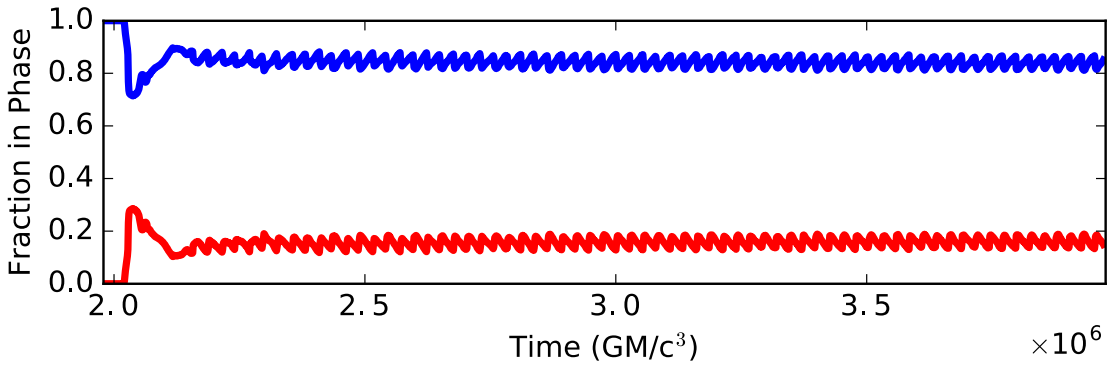

Figure 3.6: Gas fractions (f_c and f_h) at $r = 100\, r_g$ following the switch to the bistable cooling function. The initial heating event is seen as a spike in the hot gas fraction and subsequent decay at early times. The gas fraction oscillations are found after this transient behavior dies away.

reaches a low density region, at approximately one density scale height, it moves radially against the temperature-gravity gradient.

Figure 3.6 shows a time trace of the fraction of the gas in the hot phase, f_h, and the fraction of gas in the cold phase, f_c, at $r = 100\, r_g$. The transient heating event is seen at early times in time traces of f_h and f_c. Once the disk relaxes into its truncated configuration, f_h and f_c oscillate as heating events quasi-periodically occur in the cold streaming material and hot gas bubbles rise. These fluctuations are relatively small, but rapid with the fluctuations on average taking $t = 2.65 \times 10^4\, GM/c^3$, or four thermal times. At $r = 100\, r_g$ the average gas fractions in each phase are $f_c = 0.84$ and $f_h = 0.15$. The oscillations in the gas fraction are asymmetric and have a standard deviation of 0.03. As the oscillations occur, f_h rises rapidly and then experiences a slower decay. Consequently, f_c decreases sharply and gradually increases before the cycle repeats.

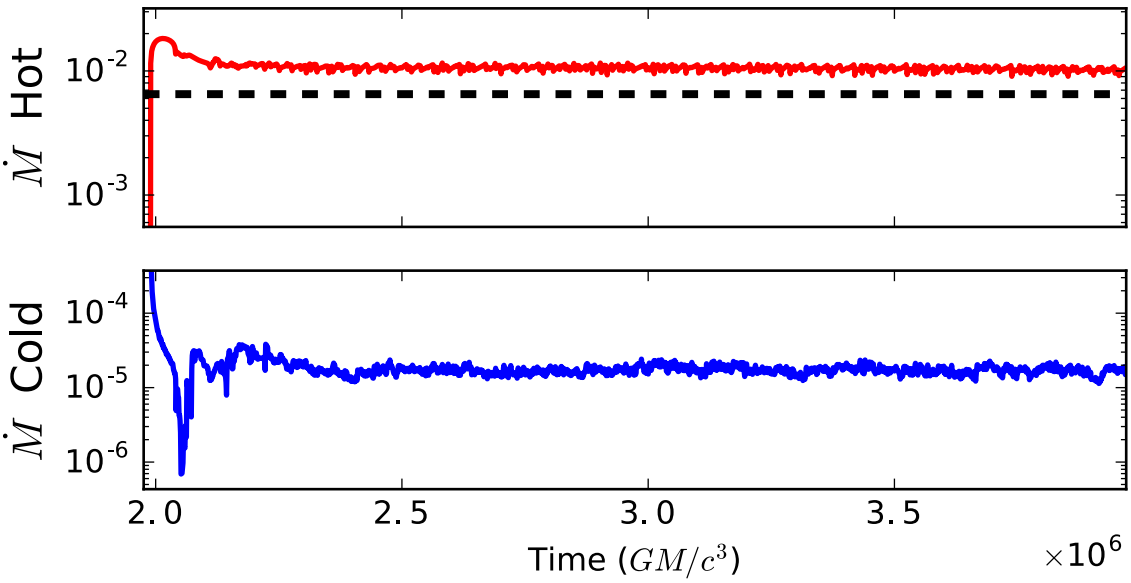

Figure 3.7: $\dot{M}_h$ (top panel) and $\dot{M}_c$ (bottom panel).

3.3.3 Mass Accretion and Angular Momentum Transport

Previous numerical studies of convective-like, hydrodynamic accretion flows have found that very little gas actually accretes onto the black hole (Igumenshchev & Abramowicz, 1999, 2000; Narayan et al., 2000; Stone et al., 1999). Here, we report conflicting results, as we find that the hot gas does indeed accrete in our simulation. One possibility for this divergence from previous studies of hot flows is that the convective cells in our simulation are continually fed at the truncation of the thin disk so the gas originates from deeper in the the gravitational potential, rather than being a hot flow throughout the entire domain and overall being less gravitationally bound.

In our 2D, axisymmetric disk, the instantaneous mass accretion rate in the

simulation is given by,

$$\dot{M}(R) = \int -\rho v_r r^2 d\Omega. \tag{3.25}$$

Using our definition of the gas phases from Section 3.3.1, we show the time trace of the accretion rate for the hot ($\dot{M}_H$) and cold phase ($\dot{M}_C$) gas at the inner boundary of our simulation in Figure 3.7. The pre-analysis disk mass accretion rate of cold gas, $\langle \dot{M}_{pre} \rangle = 6.65 \times 10^{-3}$, is also shown for reference.

We find, somewhat surprisingly, the mass flux across the inner boundary is slightly higher in the truncated disk than in the initialization phase. Additionally, there is a striking disparity between the $\dot{M}_h$ and $\dot{M}_c$. Overwhelmingly, by approximately three orders of magnitude, hot gas is accreted rather than cold gas. Initially, the overall mass accretion rate is higher during the transient phase of the heating event, but it settles into a sustained accretion rate of $\langle \dot{M} \rangle = 1.0 \times 10^{-2}$ for the remaining length of the simulation.

Since an appreciable amount of gas is accreted, there must be efficient angular momentum transport in the simulation. In our disk, the angular momentum can be transported three ways: through advection, stresses arising from the radial shear of the disk, and stresses from shear in the atmosphere of the disk as it rotates within the sub-Keplerian convective outflow. The conservation of angular momentum equation takes the following form,

$$\frac{\partial}{\partial t}\left(\rho r v_\phi\right) = \nabla \cdot \left(\eta r^2 \frac{\partial}{\partial r}\left(\frac{v_\phi}{r \sin\theta}\right)\hat{\mathbf{e}}_r + \eta \sin\theta \frac{\partial}{\partial \theta}\left(\frac{v_\phi}{\sin\theta}\right)\hat{\mathbf{e}}_\theta - \rho r v_\phi \mathbf{v}\right),$$

where the three components appearing in the divergence term are, respectively, the advection term, the $r - \phi$ viscous stress term, and the $\theta - \phi$ stress term. The

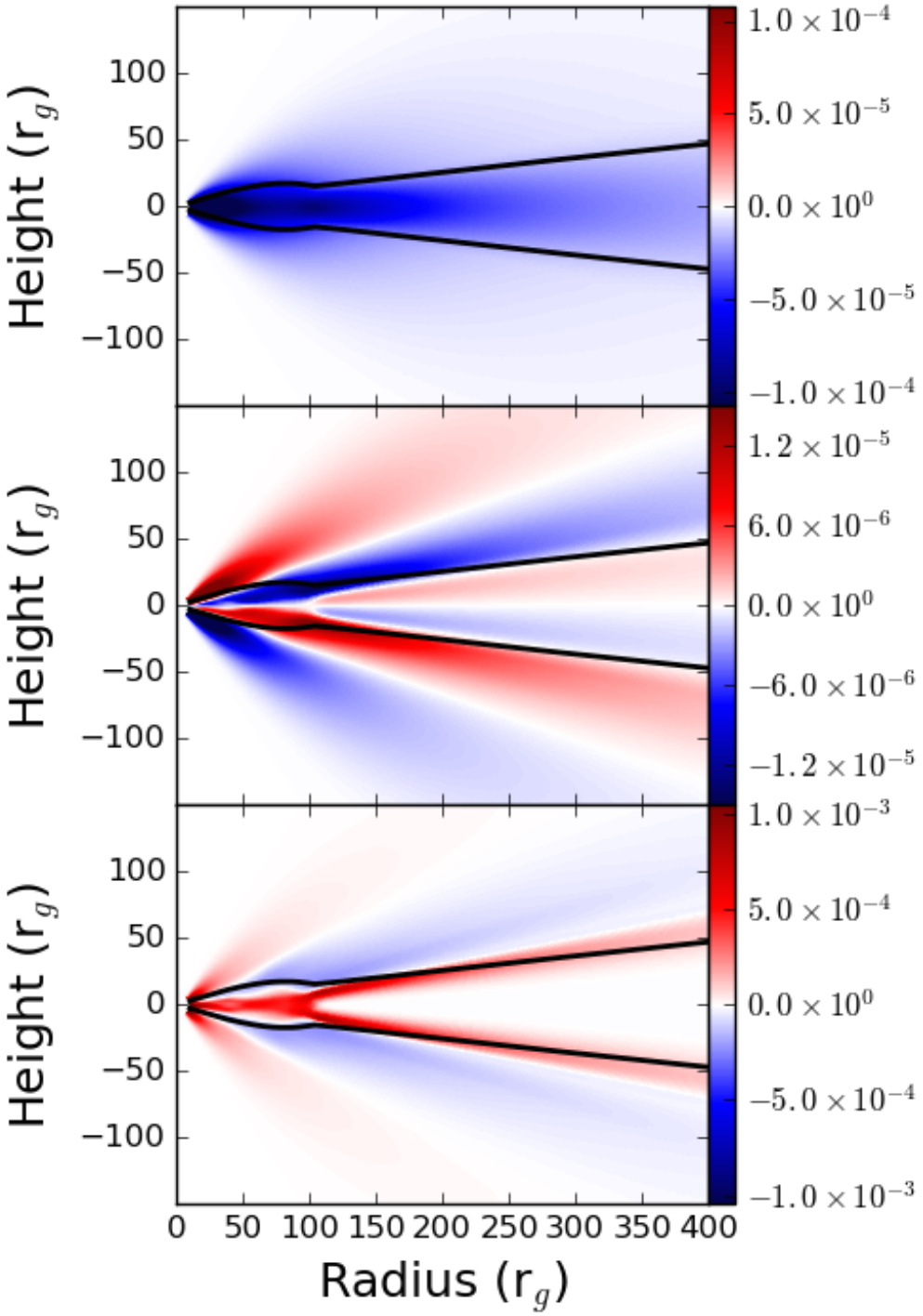

Figure 3.8: Maps of $r-\phi$ viscous stress (top panel), $\theta-\phi$ viscous stress (middle panel), and advection of angular momentum (bottom panel). Overlaid is the average geometric scale height (black solid line).

time-averaged maps of these terms shown in Figure 3.8.

The importance of the transport terms at different locations in the disk is quite clear. The $r-\phi$ viscous stress is negative everywhere and largest within the disk body, closer in towards the inner domain. This structure is expected since we consider an α-type viscosity where the viscous stress is proportional to the gas pressure and ϕ-shear and the pressure is largest in the inner regions of the disk. Above and below the disk, at approximately one scale height, there are localized layers of $\theta-\phi$ stress where the Keplerian disk interacts with the sub-Keplerian outflow. Also, within the very inner regions, the sign of the stress in each respective hemisphere reverses where the convective cell closes, reflecting the opposite signs of the vertical $v_\phi/\sin(\theta)$ gradient. The largest $\theta-\phi$ stresses occur on the upper and lower edges of the truncated disk where the cold, dense disk is buffeted by the outflowing, hot, buoyant gas. The stress gradually decreases at larger radii as the strength of the interaction between the disk and outflow decreases.

The time averaged map of the angular momentum advection terms is also stratified, reflecting the structure seen in Figure 3.4 of the radial velocities. It is worth noting that within the disk body meridional circulation establishes a very small, but positive, net radial velocity at the disk midplane. This behavior was originally predicted by Kippenhahn & Thomas (1982) and Urpin (1984) and has since been reproduced numerically for viscous accretion disks (Kley & Lin, 1992; Rozyczka et al., 1994). Moving away from the disk midplane to higher latitude, the circulation reverses the flow and gas moves inwards.

The radial profiles of the time averaged angular momentum fluxes resulting

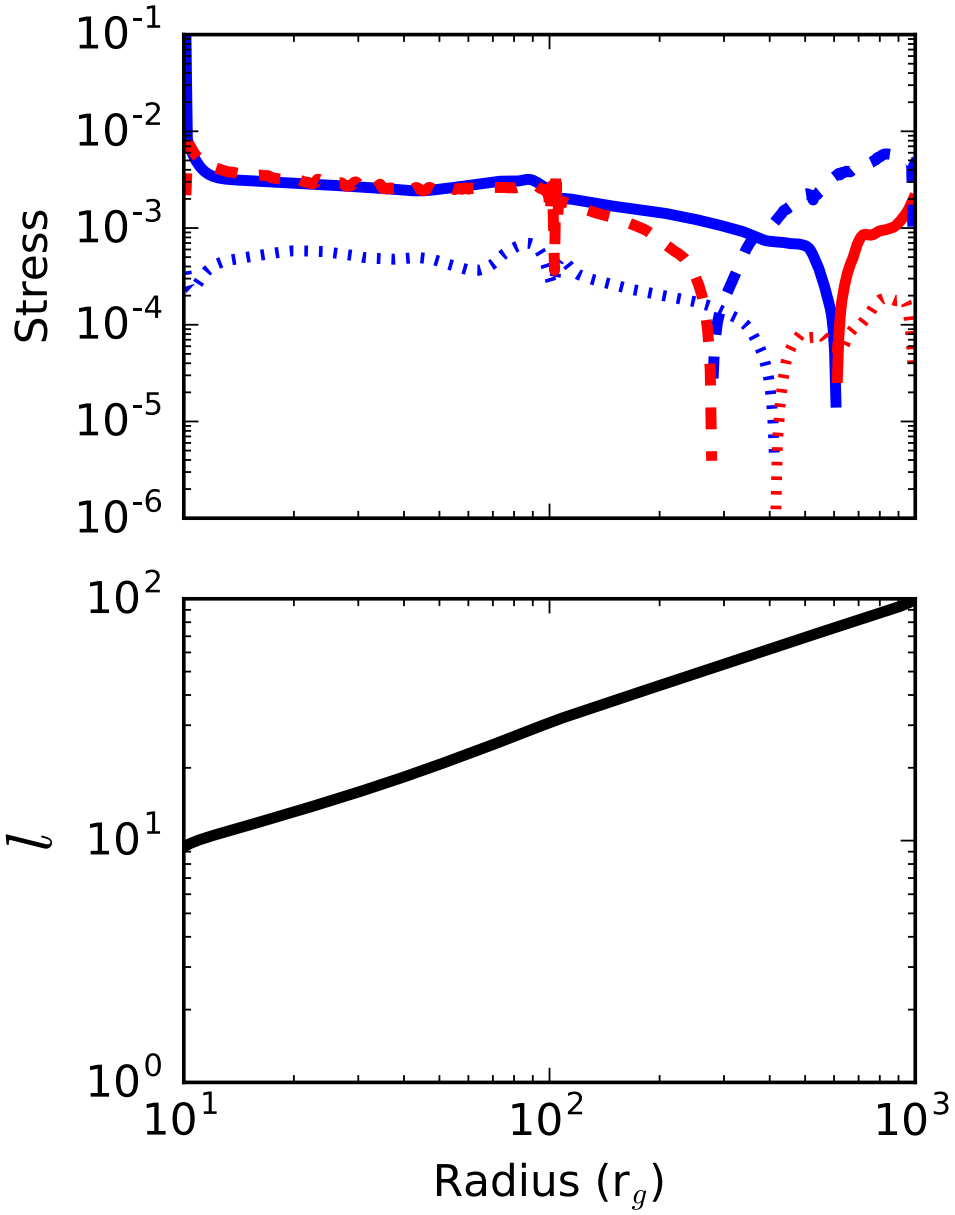

Figure 3.9: Top panel- Radial profiles of angular momentum advection (dashed line), $r-\phi$ viscous stress term (solid line), and $\theta-\phi$ term (dotted line) integrated through a shell at a given radius. Blue indicates a negative quantity and red indicates a positive quantity. Bottom Panel- Radial profile of time averaged specific angular momentum.

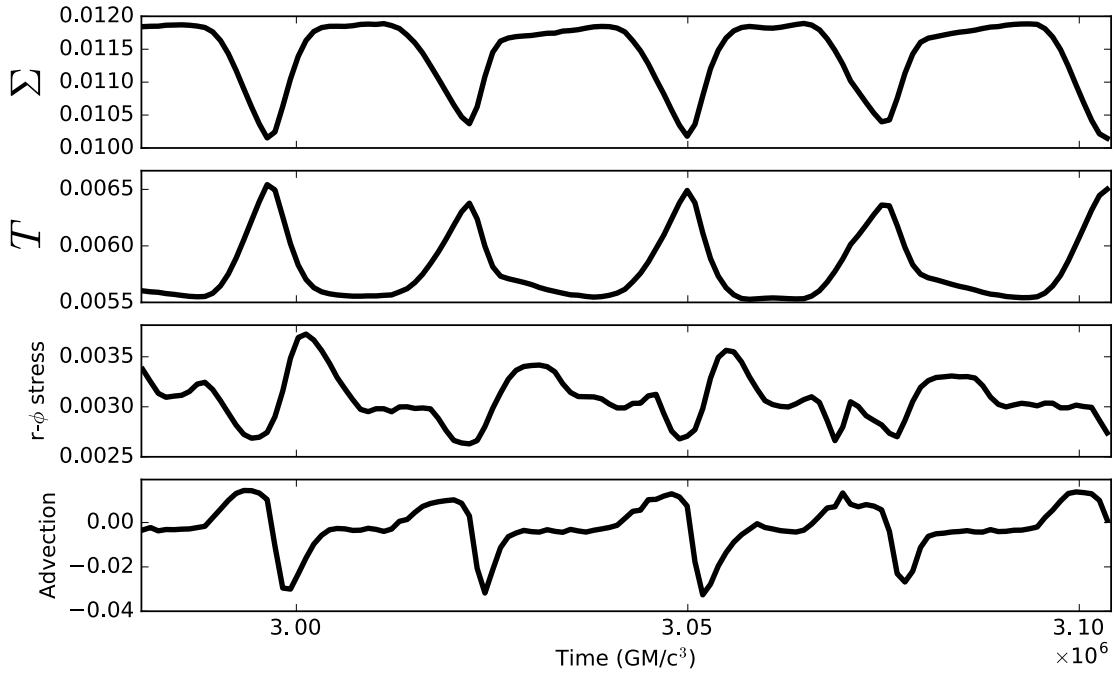

Figure 3.10: Time variability of Σ (top panel), T (second panel), $r-\phi$ stress (third panel), and advection (bottom panel) at $r = 80\,r_g$.

from the terms in Equation 3.26 are shown in Figure 3.9. On average, the viscous $r-\phi$ stress is balanced by advection, at least within the region that has established a quasi-steady state and viscous equilibrium (out to $\approx 500\,r_g$). In a purely convective flow, angular momentum is advected inwards, rather than transported outward (Ryu & Goodman, 1992; Stone & Balbus, 1996). However, in this model, the viscous stresses continually act on the gas, allowing for the loss of angular momentum. Consistent with the removal of angular momentum by viscous torques, the specific angular momentum profile, also shown in Figure 3.9, is Keplerian, $l \propto r^{1/2}$, when averaged over the duration of the simulation.

The angular momentum transport at the hot-cold phase interface is complex and depends on the time variability of Σ, T, the $r-\phi$ stress component, and the

advective stress component. Figure 3.10 shows these quantities at $r = 80r_g$, in the heart of the transition zone, over several of the bubble launching cycles. In Figure 3.10, Σ, T, the $r - \phi$ stress, and advective stress have been averaged over one thin-disk scale height ($h = \pi/2 \pm 0.1$).

At the truncation, a cyclical building and expulsion of material occurs with a period of $t \approx 2.65 \times 10^4\, GM/c^3$. In this cycle, peaks in T occur when the density is lowest and vice versa. The angular momentum terms vary with Σ and T, but there is a slight delay, $\Delta t \approx 2.05 \times 10^3\, GM/c^3$, in the maxima and minima. For the majority of the cycle, approximately 80%, the surface density increases. Eventually, a critical threshold is reached when the heating rate exceeds the cooling rate, causing the temperature to increase and the cooling to become inefficient as pockets of gas reach T_c. This causes a runaway heating event, seen in the rapid increase of T, and the outflow to be launched which can be seen as turn over in the advection term to positive values.

A key feature throughout this cycle is that the gas pressure remains relatively constant as the gas expands to maintain a pressure equilibrium, a facet which is discussed to greater depth in Section 3.3.4. This, in turn, means that the specific angular momentum of the lower density, transitioning gas at the truncation is more rapidly lost to the neighboring dense gas of the disk body through the $r - \phi$ viscous stress since the amplitude of the viscosity is proportional to the pressure. Additionally, as seen in Figure 3.5, the hot transitioning gas is in contact with the dense gas of the cooler stream which cannot lose angular momentum as well. As the specific angular momenta of these two regions changes due to the differences in the viscous

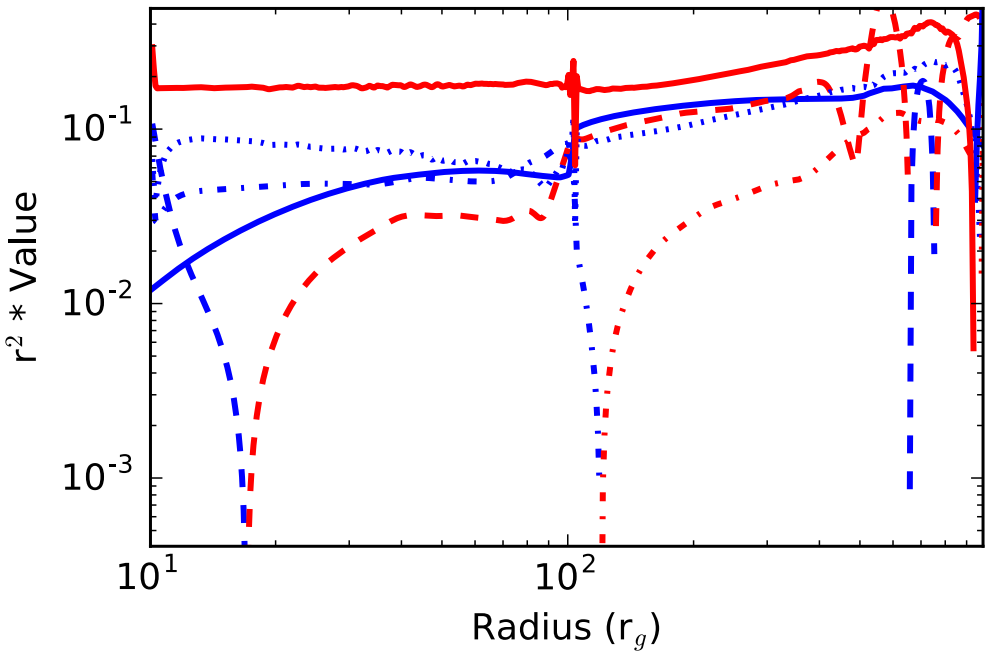

Figure 3.11: Radial profiles of terms in energy equation. Blue indicates negative values, red indicates positive values. The combined viscous dissipation ($\mathcal{W}$, $\theta - \phi$ and $r - \phi$ terms) are shown by the dashed line, the advection of kinetic energy ($\mathcal{A}_\mathcal{K}$) is shown by the dotted line, and the advection of thermal energy ($\mathcal{A}_\mathcal{T}$) is shown by the dot-dashed line. Since the cooling term ($\mathcal{C}$) is positive everywhere in our notation and the change in gravitational potential energy ($\mathcal{G}$) is negative everywhere, both are shown as solid lines.

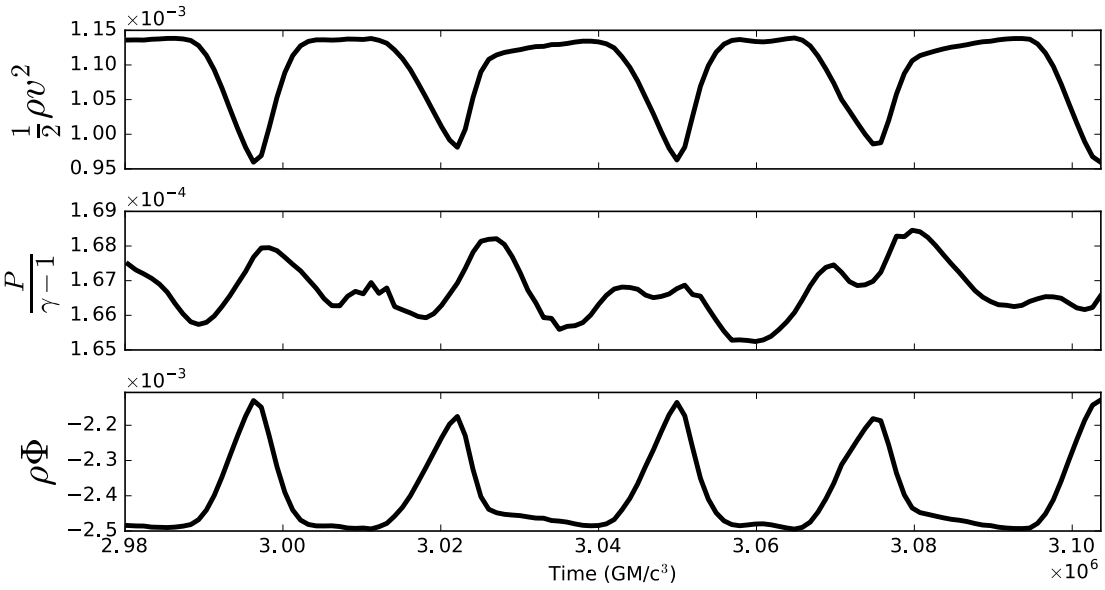

Figure 3.12: Time variability of $\mathcal{E}_K$ (top panel), $\mathcal{E}_I$ (middle panel), and $\mathcal{E}_G$ (bottom panel) at $r = 80\, r_g$.

efficiency, a vertical shear is introduced. This shear allows the $\theta - \phi$ viscous stress to transfer angular momentum from the dense gas in the stream to the diffuse, outflowing bubble where it is carried away. This changes the shear rate of the dense gas, resulting in a spike in the $r - \phi$ stress component. This rapid exchange of angular momentum drives the angular momentum transport in the stream which then flows to smaller radii, as evidenced by the sharp negative dip in the advective angular momentum transport term corresponding to the peak in the $r - \phi$ stress term.

After this involved transitory event, the disk refills and the cycle repeats.

3.3.4 Disk Energetics

3.3.4.1 Energy Terms

In our hydrodynamic model, the conservation of energy equation is,

$$\frac{\partial \mathcal{E}}{\partial t} + \mathcal{C} + \mathcal{A}_{\mathcal{K}} + \mathcal{A}_{\mathcal{T}} + \mathcal{G} - \mathcal{W} = 0, \tag{3.26}$$

where $\mathcal{E}$ is the total disk energy, $\mathcal{C}$ is the "radiative" cooling done by the cooling function, $\mathcal{A}_{\mathcal{K}}$ is the advection of kinetic energy, $\mathcal{A}_{\mathcal{T}}$ is the advection of thermal energy, $\mathcal{G}$ is the advection of gravitational potential energy, and $\mathcal{W}$ is the work done by viscous torques. We will consider these terms in a spherical shell integrated form, such that they are

$$\frac{\partial \mathcal{E}}{\partial t} = \frac{\partial}{\partial t}\left[\int d\Omega\left(\frac{1}{2}\rho v^2 + \frac{P}{\gamma - 1} + \rho\Phi\right)\right], \tag{3.27}$$

$$\mathcal{C} = \int d\Omega \Lambda, \tag{3.28}$$

$$\mathcal{A}_{\mathcal{K}} = \frac{1}{r^2}\frac{\partial}{\partial r}\left[r^2 \int d\Omega\left(\frac{1}{2}\rho v^2\right) v_r\right], \tag{3.29}$$

$$\mathcal{A}_{\mathcal{T}} = \frac{1}{r^2}\frac{\partial}{\partial r}\left[r^2 \int d\Omega\left(\frac{P}{\gamma - 1}\right) v_r\right], \tag{3.30}$$

$$\mathcal{G} = \frac{1}{r^2}\frac{\partial}{\partial r}\left[r^2 \int d\Omega\left(\rho\Phi\right) v_r\right], \tag{3.31}$$

$$\mathcal{W} = \frac{1}{r^2}\frac{\partial}{\partial r}\left\{r^2 \int d\Omega \eta v_\phi \left[r\frac{\partial}{\partial r}\left(\frac{v_\phi}{\sin\theta}\right) + \sin\theta \frac{\partial}{\partial \theta}\left(\frac{v_\phi}{\sin\theta}\right)\right]\right\}. \tag{3.32}$$

The time averaged, radial profiles of these terms are shown in Figure 3.11. The presence of a truncated disk influences every energy term, with the exception of $\mathcal{G}$. Given that there is sustained accretion and the average specific angular momentum profile is Keplerian, this is not necessarily surprising in the time average profile. Es-

sentially, the smooth, time averaged $\mathcal{G}$ indicates that, globally, material is accreting and there is no mass build-up anywhere in the disk. Even though material may temporarily be caught in convective cells, it is eventually accreted so gravitational potential energy is liberated.

In the outer disk the $\mathcal{A}_{\mathcal{T}}$ term, which is positive, is suppressed and accounts for very little of the overall energy transport of the gas. This changes within $r < R_T$, however, as $\mathcal{A}_{\mathcal{T}}$ and $\mathcal{A}_{\mathcal{K}}$ become major contributors in the truncated disk region. Advection plays a dominate role in the energy transport within the transition radius, overtaking the cooling. The dynamical influence of the convective cells acts to advect energy across the inner boundary as material gets swept inwards.

There is a slight deficit in the $\mathcal{A}_{\mathcal{K}}$ term and a significant deficit in the $\mathcal{W}$ term inside of $r < R_t$ because of the disk truncation. The impact on the $\mathcal{A}_{\mathcal{K}}$ term is twofold. In the inner disk the density is lower and the flow is sub-Keplerian, thus overall advection of kinetic energy in this region is slightly less what it might otherwise be. Regardless, the sign does not change as the bulk of the kinetic energy is swept inwards in the dense gas that streams inwards through the viscous interaction of the hot outflow. In a general, time averaged sense, the energy dissipation of the $\mathcal{W}$ term is suppressed because the density is lower and the fluid motions are more chaotic in this region. However, as seen in the variability of the viscous stress components, there are brief periods of enhanced viscous stress and, therefore, heating. Nevertheless, the disruption of the flow by the hot gas bubbles makes it more difficult to establish the *sustained* radial and vertical gradients in v_ϕ that generate the viscous stresses and heating in the outer disk, thereby diminishing the contribution

of the $\mathcal{W}$ term in the inner region of the disk.

The transition has the strongest affect on the $\mathcal{A}_{\mathcal{T}}$ term, as its sign actually flips at the disk transition. Within the inner disk, material is generally swept inwards, either in the streaming material or through the return of the convective cells. The sign of $\mathcal{A}_{\mathcal{T}}$ flips at the transition, however, because the majority of the thermal energy resides in the buoyant, outflowing gas. The apparent suppression of this term is somewhat artificial because it accounts for two competing components; the net inflow of thermal energy through the accretion in the dense, thin disk and the outflow of the diffuse, hot gas.

Further insight into the periodic launching of the buoyant bubbles can be gained from examining the individual components of $\mathcal{E}$, i.e. the kinetic energy ($\mathcal{E}_K = 1/2\rho\mathbf{v}$), the internal energy ($\mathcal{E}_I = P/(\gamma - 1)$), and the gravitational potential energy ($\mathcal{E}_G = \rho\Phi$) of the gas. The variability of these energy components at $r = 80 r_g$ is shown in Figure 3.12. Similar to Figure 3.10, these terms have been averaged over $h = \pi/2 \pm 0.1$.

The cyclical behavior observed in Σ, T, the $r - \phi$ stress, and the angular momentum advection is also seen in the gas energy. Unlike the involved angular momentum transport interaction observed in this region, the temporal variability of the gas energy terms is simply due to the removal of gas in the buoyant bubbles, which can be seen in the corresponding dips in Σ in Figure 3.10 and in the variability of $\mathcal{E}_G$ since Φ is a constant at $r = 80 r_g$. The removal of the gas is tied to an increase in the gas energy as it heats (i.e. increased $\mathcal{E}_I$). Throughout the launching of the hot bubbles, the internal energy and gas pressure have very little variability ($\approx 2\%$).

When gas transitions in the flow, the bubble expands adiabatically as it buoyantly rises vertically along the density gradient.

3.3.4.2 Bound Outflow

Throughout the simulation, the Bernoulli parameter,

$$Be = \frac{1}{2}\mathbf{v}^2 + \Phi + W, \tag{3.33}$$

where W is the specific enthalpy

$$W = \frac{\gamma c_s^2}{\gamma - 1} \tag{3.34}$$

of the gas, is negative. When Be is negative, the kinetic and thermal energy of the gas is less than the gravitational potential energy, so the gas is bound and cannot escape.

Shown in Figure 3.13 is the distribution of outflowing mass fraction ($\dot{M}_{out}$), i.e. gas with $v_r > 0$, at $r = 100\, r_g$ as a function of Be. On the surface, it looks like $\dot{M}_{out}$ is nearly independent of Be. When we dig deeper into the distribution, we find that, in fact, there are two components to the outflow: one component that is diffuse gas with high velocities and other that is dense gas with low radial velocity. Also shown in Figure 3.13 are the average density of the outflow and velocity as a function of Be. When a bubble of hot gas is launched from the inner region of the disk, the gas has a large, positive radial velocity, but low density. As it rises, higher density gas gets entrained in the wake of the bubble and pulled along to larger radius, although at a lower velocity.

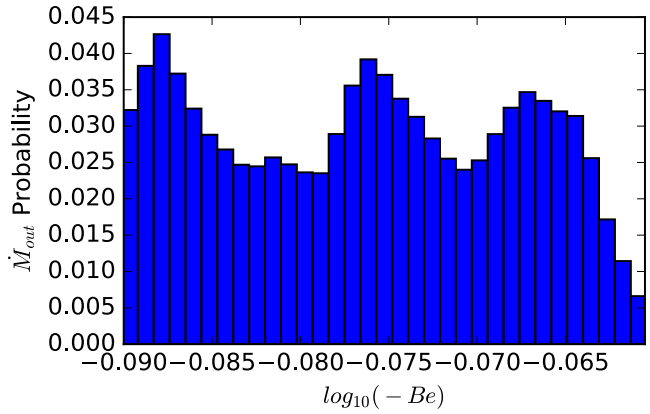

(a) Histogram of Be of Outflowing Gas at $100\,r_g$

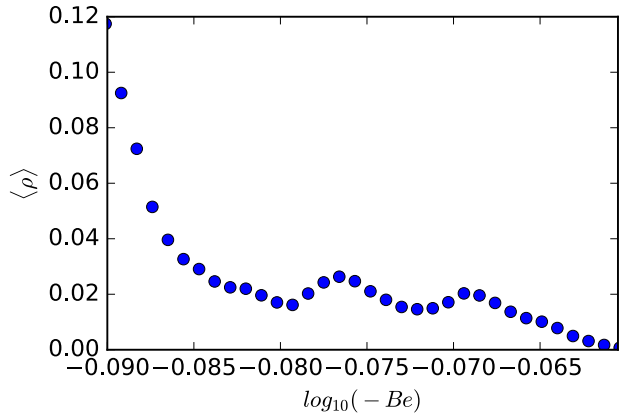

(b) Be vs. ρ of Outflowing Gas at $100\,r_g$

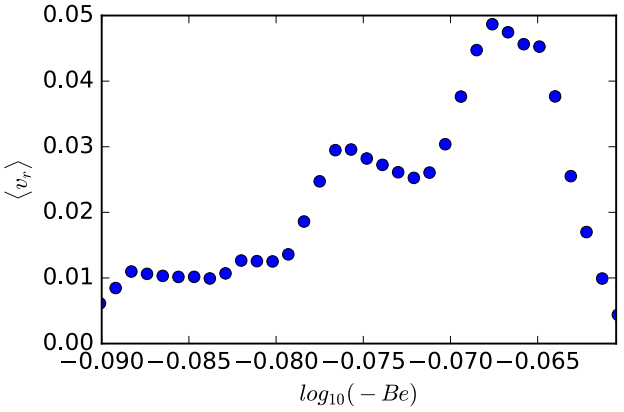

(c) Be vs. v_r of Outflowing Gas at $100\,r_g$

Figure 3.13: Histogram of the outflowing gas's Be at $r = 100\,r_g$ during the analysis portion of the simulation. This is decomposed into the average density of the outflow as a function of Be and the average velocity as a function of Be.

3.3.4.3 Synthetic Light Curves

To finish our analysis, we use the cooling in our simulation to generate a synthetic light curve. Since PLUTO conserves total energy in the simulation, the "radiative losses" our cooling function imitates can be used as a proxy for the broadband emission. There are obvious caveats to this exercise, namely that we use an *ad hoc* cooling function to approximate the real, detailed radiation physics of the disk. Regardless, it will provide a sense of what type of photometric variability could originate from this disk.

Observationally, in astrophysical black hole systems, the higher energy emission is attributed to the hot, radiatively inefficient gas. The lower energy, blackbody emission is attributed to the cooler, radiatively efficient, dense gas. Following this paradigm, we use our previously defined temperature criteria to generate "hard," L_h, and "soft," L_s, band light curves, shown with the volume integrated cooling as a function of time of the hot and cold gas, respectively, in Figure 3.14.

During the initialization, the large heating event causes an immediate spike in L_h that decays down to a level of $L_h = 3.0 \times 10^{-3}$ which it maintains for the rest of the simulation. This is higher than the total pre-analysis emission level, L_p, of 2.8×10^{-3}. L_s is approximately a quarter less than the L_h, due in part to the fact that the hot gas fills a large portion of the simulation volume. Interestingly, there is very little sign of the oscillatory behavior seen Figure 3.3 of the gas fraction at r_{trans}. Instead, the light curves of each gas phase qualitatively resemble the the time trace of the respective mass accretion rates, shown in Figure 3.7.

3.4 Discussion

By introducing a bistable cooling law to a simple hydrodynamic viscous disk, we find that gas transitioning from the hot phase to the cold phase develops significant time variability which affects the evolution of the disk. The transition between efficient and inefficient gas cooling leads to disk truncation and causes large, convective cells to develop in the inner region of the disk. The presence of sub-Keplerian, outflowing gas in close proximity to the accretion disk generates a large $\theta - \phi$ viscous stress which has previously been neglected, but is influential here. The inner, truncated region of the disk is occupied by hot gas that cools inefficiently. Beyond the transition, the bulk of the gas resides in the cool phase in a configuration similar to a standard Shakura & Sunyaev thin disk. In general, the truncated disk in our simulation is qualitatively similar to the phenomenological model invoked to explain the spectral properties of BHBs in the low/hard and intermediate states like Cygnus X-1 (Done & Zycki, 1999), XTE J1650-500 (Done & Gierliński, 2006), H1743-322, (Sriram et al., 2009), MAXI J1543-564 (Rapisarda et al., 2014), and GX 339-5 (Plant et al., 2015), which was expected by construction. There are several notable differences between the simulation and the standard truncated disk model, which could manifest as observable signatures in BHB and LLAGN systems.

In the canonical HD truncated disk model, the inner accretion flow is assumed to be an ADAF and many of the observational results are interpreted with this assumption (e.g. Gammie et al., 1999; Ho et al., 2000; McClintock et al., 2003; Shields et al., 2000; Ulvestad & Ho, 2001; Yuan et al., 2005). Hence, it is interesting

that a flow which closely resembles a CDAF naturally forms. Even though there are qualitative similarities, the convective flow is ultimately distinct from the standard CDAF. The primary way in which it differs is that the gas does not stay in the convective flow indefinitely as it is constantly cooling. Once it is launched, the gas rises to larger radii, but then stalls and falls back. The accretion rate is higher following the transition because of the interaction of the outflowing gas and the thin disk body. It is, in fact, primarily the gas in the hot phase that accretes with very little cold gas making it to the inner boundary of the simulation.

One might hope the oscillatory gas fraction could be connected to observable variability, like a QPO, but that is not currently supported by our simulation. QPOs are present in the intermediate states between the low-hard state and the high-soft states when the disk is assumed to be truncated, similar to what we modeled. However, neither the mass accretion rate nor our simple cooling prescription show appreciable variability. If the buoyant bubbles we capture in our simulation can be physically realized and related to QPO behavior, their signature must ultimately arise from more complex radiative processes than we have included.

Despite the obvious issues with connecting this HD accretion disk model to real black hole disks, it still plays an important role in providing a needed benchmark against which future MHD models of truncated disks can be compared, as we originally motivated. In particular, the surprising complexity in the disk structure, angular momentum transport, and energetics demonstrate how poorly the behavior of disks in this state is understood, even in what should be a simple case. The results from this simulation help to provide a bridge between the simple disk model

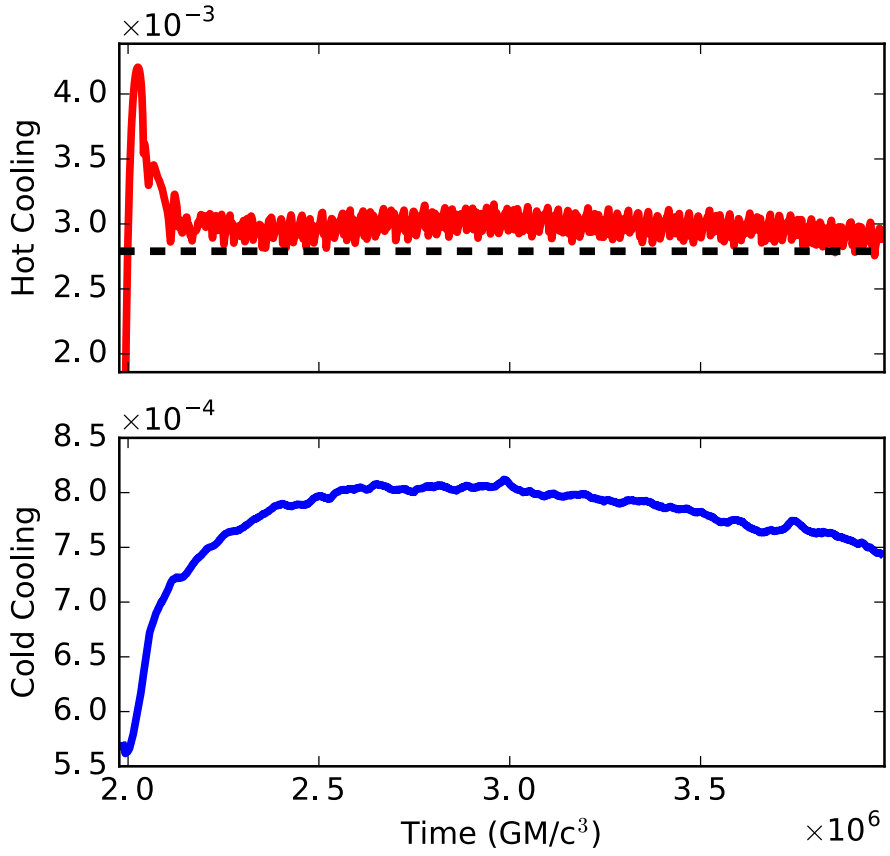

Figure 3.14: Disk integrated synthetic light curve from the hot gas cooling (L_h, top panel) and cool gas cooling (L_s, blue line). The cooling level during initialization of $L_p = 2.8 \times 10^{-3}$ is shown as the black dashed line for reference.

currently used to understand state transitions in BHBs and LLAGNs and the more complex MHD physics that actually govern their evolution.

Of the many caveats and pitfalls associated with using an HD model to describe a real accretion disk, we will briefly discuss two. The first concern is that the behavior is sensitive to the strength of the anomalous viscosity. As the viscosity of the disk changes, the ability of the fluid to develop small scale structure and buoyantly rise also changes, which has been shown to affect the size and behavior of hydrodynamic, convective accretion flows (Igumenshchev & Abramowicz, 1999). To test the sensitivity of this model we reran the full simulation with $\alpha = 0.04$. The development of this low α-parameter was similar. Granted, the amplitudes of the stress, $\dot{M}$, etc. changed because of the lower viscosity, but the distinguishing flow properties like the rapid inflow of gas along the skin of the disk, a single large convective eddy in the atmosphere, and the quasi-periodic development of buoyant bubbles at the truncation were all reproduced. In all, we can be confident that the behavior we present in this chapter is robust for reasonable α-parameter values.

The biggest concern is the role MHD will play in altering the behavior of the disk. One of the most conspicuous features of our simulation is the presence of a "cold" stream of gas extending from the transition radius down to near the inner boundary. Observationally, there is evidence that cool gas may be present near the black hole, even when the disk is thought to be truncated (Miller et al., 2002a,b). While it is tempting to make a connection between what develops in our simulation and what is empirically observed, this must be done cautiously. In an astrophysical accretion disk the gas motions are dominated by vigorous, MHD turbulence with

correlation lengths of order the disk scale height (Beckwith et al., 2011; Guan et al., 2009; Hogg & Reynolds, 2016). The stream of material in this simulation is smaller than that nominal scale, hence, it is reasonable to expect that even if this stream could form, it would quickly be disrupted by the turbulence and unable to exist in the way it does in our simulation.

3.5 Conclusions

Using a viscous, hydrodynamic simulation of an accretion disk with a bistable cooling function, we conduct a detailed analysis of the dynamics, angular momentum transport and energetics. We find that a truncated configuration develops and that convective cells are launched from the evacuated region as cold gas flows inwards and undergoes delayed heating. Pockets of hot gas form within the cold gas stream and buoyantly rise along the surface of the cooler disk which introduces a $\theta - \phi$ viscous stress component through a vertical shear between the coronal atmosphere and the disk itself. This viscous stress component has been neglected in previous hydrodynamic treatments of accretion disks, but it plays in important role in the evolution of the disk by transferring additional angular momentum from the dense disk to the outflow and enhancing accretion in a thin layer long the surface of the disk. In this truncated disk, the bulk of the accreted material is in the hot phase, rather than the cold phase, and the accretion rate is slightly elevated compared to that of the thin disk during the initialization. The spontaneous transition of gas to the hot phase in the cold stream of material causes a quasi-periodic oscillation

in the hot/cold gas fraction at the transition radius, but this does not translate in any appreciable fluctuations in the mass accretion rate, nor the volume integrated cooling ratio. With this baseline hydrodynamic model of a truncated disk, we can begin to understand more complex future MHD models.

Chapter 4: Truncated Accretion Disks In Magnetohydrodynamics

4.1 Introduction

Accreting stellar mass black hole systems in black hole binaries (BHBs) display a characteristic hysteresis during outburst as they undergo state changes (Done et al., 2007; Remillard & McClintock, 2006; Zdziarski & Gierliński, 2004). In the low/hard state the system is less luminous and the spectrum is harder, while in the high/soft state the luminosity is dramatically increased and the spectrum is dominated by soft emission from thermal, black body emission with a peak around ≈ 1 keV. Accreting supermassive black holes in active galactic nuclei (AGNs) seem to similarly fall into spectral classes like the BHB states, although interpreting them as true analogs is treacherous because the long evolutionary time scales prevents the direct observation of any possible hysteresis cycle. Low-luminosity AGNs (LLAGNs) are observed to have low accretion rates, low luminosities, and hard spectra which is interpreted as evidence of accretion through a hot, diffuse flow (Ho, 2008; Narayan & Yi, 1995a; Rees et al., 1982; Yuan & Narayan, 2014). The standard Seyfert or quasar, on the other hand, has a higher accretion rate, higher luminosity, and a softer spectra dominated by a thermal continuum which peaks in the ultraviolet.

The canonical model behind the two accretion state paradigm in BHBs and

AGNs attributes the distinct properties to varying degrees of disk truncation (Esin et al., 1997; Nemmen et al., 2014; Trump et al., 2011; Yu et al., 2011). The putative truncation is believed to arise as the gas transitions from a radiatively-efficient, geometrically-thin flow in the outer regions of the disk to a radiately-inefficient, geometrically-thick flow in the inner region. When the disk is truncated and the inner region of the disk is occupied by gas in the hot phase, the system should be less luminous and have a harder spectrum as free-free emission and Comptonization dominates the radiation. When the optically-thick, geometrically-thin accretion disk extends down to the innermost stable circular orbit (ISCO), the system should be more luminous and the spectrum should be dominated by quasi-blackbody thermal radiation.

Additional evidence for disk truncation in BHBs in the high/soft state and LLAGNs comes from X-ray monitoring of the 6.4 keV Fe $K\alpha$ line. In BHB systems like GX 339-4 (Tomsick et al., 2009) and H1743-322 (Shidatsu et al., 2014), the line profile is seen to evolve as the outburst evolves. In the low/hard state, the line is narrower and is best fit if the line originates from large radii, while in the high/soft state, the line is broader and best fit if the bulk of the emission originates close to the central black hole. Narrow Fe Kα lines are also observed from LLAGNs and associated with a truncated accretion disk in systems like M81 (Dewangan et al., 2004), NGC 4579 (Dewangan et al., 2004), NGC 4593 (Brenneman et al., 2007; Markowitz & Reeves, 2009; Reynolds et al., 2004), and NGC 4258 (Reynolds et al., 2009). This seemingly direct evidence of truncation lends credibility to the model, but it is not quite so clear. In fact, broadened Fe $K\alpha$ lines from relativistic blurring

have been reported in a number of sources when they are in the (luminous) hard state, including GRS 1739-278 (Miller et al., 2015), Cygnus X-1 (Parker et al., 2015) and even GX 339-4 (Miller et al., 2006), suggesting the optically-thick disk extends to the ISCO even in the hard state.

A transition in the radiative efficiency makes it particularly challenging to understand the flow dynamics. Separately, much effort has gone into studying cooler accretion flows in radiatively-efficient, geometrically-thin disks and hot flows in non-radiative, geometrically-thick disks. However, merging the two models is not straightforward and has a strong dependence on whether the disk is considered in a hydrodynamic (HD) or magnetohydrodynamic (MHD) regime.

Computational and algorithmic advances have recently enabled the numerical exploration of BHB state transitions. HD models (Das & Sharma, 2013; Wu et al., 2016b) which self-consistently account for radiation from bremsstrahlung, synchrotron and synchrotron self-Comptonization demonstrate one of the basic tenets of the current state transition model: that a cold, dense disk forms out of the hot, diffuse medium once the accretion rate exceeds a critical threshold. As the accretion rate and density increase, cooling becomes more efficient in the inner region of the disk, thereby decreasing the radius of the truncation. Using a three-dimensional MHD simulation which accounts for general relativity and radiation, Takahashi et al. (2016) corroborate this finding.

Despite the success simulations have had in demonstrating the viability of the truncated disk model to explain the phenomenology observed from BHB and AGN systems, they have yet to yield a detailed understanding of the gas dynamics

and disk evolution in a truncated disk system. Properly modeling a truncated disk requires a simulation grid capable of resolving the internal dynamics of the thin-disk, a large computational volume, and a long enough integration that global processes can develop over several viscous timescales. Fundamentally, these requirements are at odds with each other, requiring sacrifices in various aspects of the simulation. This chapter is a continuation of the work in Chapter 3 where we implemented an *ad hoc* bistable cooling prescription to force a truncation in a two-dimensional, axisymmetric, HD, viscous accretion disk. Here, we extended the model to a three-dimensional, MHD accretion disk, which better represents a physical system since MRI driven turbulence provides an effective viscosity and heats the gas.

In both of these simulations, we prioritize resolution and evolutionary time over less influential physics. For instance, we simulate both disks with non-relativistic physics in a Newtonian potential since empirical measurements place the truncation at large radii where GR effects should be negligible. Additionally, the cooling function used in these simulations is computationally simple, but still captures the essence of the true radiative physics, albeit in an approximate manner.

The HD case provides a benchmark against which we can compare the behavior of the MHD accretion disk. In Chapter 3, several HD features significantly affect the evolution. The launching of buoyant bubbles within the flow as gas transitioned from the efficient cooling branch to the inefficient cooling branch was crucial in shaping the global disk dynamics. This cyclical process involved the interplay of the gas density and temperature, and introduced time variability to the angular momentum transport efficiency and energetics. Buoyant bubbles drove an outflow,

leading to a circulation pattern in the disk atmosphere. Gas was expelled from the inner disk, but fell back and was eventually accreted. Additionally, a thin stream of cooler gas reached from the disk body into the truncated region, almost to the inner boundary. Since we considered a full viscous prescription with an isotropic viscous stress tensor, the $\theta-\phi$ stress component was influential where vertical velocity shears were present, for instance between the Keplerian disk body and the sub-Keplerian outflow in the disk atmosphere.

Considering an MHD accretion disk introduces additional complexity, most notably the role of turbulence and the large-scale magnetic dynamo. The chaotic disk turbulence, by its nature, acts to disrupt coherent structure on small scales. Much of the behavior in the HD accretion disk that developed on large scales originated on much smaller scales. The large-scale magnetic dynamo induces low-frequency variability in the accretion disk. Dynamos, in some form, seem to be a natural occurrence in rotating plasmas. While magnetic activity cycles with long periods have been known to exist in stars for many decades (Wilson, 1978), we have only just begun to uncover the role dynamos play in moderating the evolution and time variability of black hole accretion disks. Numerically, dynamos are ubiquitously observed in shearing box and global simulations of MRI driven turbulence. The large-scale dynamo is characterized by oscillation of the global magnetic field orientation and amplitude. Except for extreme circumstances, like a strong magnetic field (Salvesen et al., 2016), the dynamo frequency is regularly found to be $\Omega_d \approx 5-20\Omega_K$, where Ω_K is the orbital frequency. This becomes important because the dynamo modulates the local Maxwell stress (Davis et al., 2010; Flock et al., 2012; Hogg &

Reynolds, 2016), which consequently influences variability in the angular momentum transport and, presumably, gas heating.

In this chapter we begin with a summary of the numerical model in Section 5.2 and present an overview of the initial setup, bistable cooling function, a test simulation and a resolution assessment. In Section 5.3 we present our analysis of the truncated disk's dynamics, angular momentum transport, energetics, and magnetic field properties. We summarize our analysis and discuss the implications of our results in Section 5.5 and provide closing remarks in Section 5.6.

4.2 Numerical Model

In this chapter we consider a three-dimensional, semi-global accretion disk with a bistable cooling curve. The disk was constructed to match the HD model, but extended to MHD and three dimensions. An overview of the bistable cooling function we used is given here, as a more rigorous discussion and motivation is presented in Chapter 3. The cooling prescription is calibrated through a pre-chosen effective α-parameter, which we determined with a calibration simulation. The fiducial model is evolved in two stages. The first stage is an initialization where the model is evolved with a constant disk aspect ratio ($h/r = 0.1$) for $1.99 \times 10^5\, GM/c^3$ to allow the MRI driven turbulence to fully develop in the simulation volume. At the inner-edge of the simulated disk ($r = 10\, r_g$), this is 1000 orbital timescales where $t_{orb,10} = 199\, GM/c^3$. Then the cooling function is switched to the bistable cooling function described below and the model evolves for an additional $1.99 \times 10^5\, GM/c^3$

to allow the truncated disk to fully develop and the unphysical transient behavior to die away before we begin our analysis. The second stage is the portion of the simulation used in our analysis and lasts $t = 8.14 \times 10^5\, GM/c^3$ ($4096\ t_{orb,10}$).

4.2.1 Simulation Code

We use the second-order accurate PLUTO *v4.2* code (Mignone et al., 2007) to solve the equations of ideal MHD,

$$\frac{\partial \rho}{\partial t} + \nabla \cdot (\rho \mathbf{v}) = 0, \tag{4.1}$$

$$\frac{\partial}{\partial t}(\rho \mathbf{v}) + \nabla \cdot (\rho \mathbf{v}\mathbf{v} - \mathbf{B}\mathbf{B} + P\mathcal{I}) = -\rho \nabla \Phi, \tag{4.2}$$

$$\frac{\partial}{\partial t}(E + \rho\Phi) + \nabla \cdot [(E + P + \rho\Phi)\mathbf{v} - \mathbf{B}(\mathbf{v} \cdot \mathbf{B})] = -\Lambda, \tag{4.3}$$

$$\frac{\partial \mathbf{B}}{\partial t} = \nabla \times (\mathbf{v} \times \mathbf{B}),$$

where ρ is the gas density, $\mathbf{v}$ is the fluid velocity, P is the gas pressure, $\boldsymbol{B}$ is the magnetic field, $\mathcal{I}$ is the unit rank-two tensor, E is the total energy density of the fluid,

$$E = u + \frac{1}{2}\rho |\mathbf{v}|^2 + \frac{\mathbf{B^2}}{2}, \tag{4.4}$$

and Λ accounts for radiative losses through cooling. The equations were solved using the `hlld` Riemann solver with the code in the dimensionally unspilt mode. A piecewise parabolic reconstruction is used in space and time integration is done with a second-order Runge Kutta algorithm. PLUTO is a Godunov code, so the total energy in the simulation is conserved except for losses across the boundary and energy removed through our cooling function. The method of constrained transport is used to enforce the $\nabla \cdot \mathbf{B} = 0$ condition.

4.2.2 Simulation Setup

The simulation grid is the same as in the HD model, but expanded in the ϕ-direction, rather than being treated axisymmetrically. Spherical coordinates are used in a computational domain that spans $r \in [10r_g, 1000r_g]$, $\theta \in [\pi/2 - 1.0, \pi/2 + 1.0]$, and $\phi \in [0.0, \pi/2]$ with $N_R \times N_\theta \times N_\phi = 512 \times 512 \times 128 = 3.35 \times 10^7$ zones. Logarithmic spacing is used in the radial coordinate so that $\Delta r/r$ is constant. In the θ-direction, the simulation uses 320 uniformly grid zones in the midplane region from $\theta = \pi/2 \pm 0.5$ and 96 geometrically stretched grid zones in each of the coronal regions (i.e. $\pi/2 - 1.0 \leq \theta \leq \pi/2 - 0.5$ and $\pi/2 + 0.5 \leq \theta \leq \pi/2 + 1.0$). Outflow is allowed through the r and θ boundaries while the the ϕ boundaries are periodic. To prevent artificially low or negative values, floors are imposed on density and pressure.

Since the truncation is expected to occur at $30 - 100\, r_g$ (Nemmen et al., 2014), we can consider a scale free Newtonian potential,

$$\Phi = -\frac{GM}{r}. \tag{4.5}$$

Similarly, all fluid variables (e.g. ρ, p, T) are considered and reported in a normalized, scale free form. The gas is considered ideal with a $\gamma = 5/3$ adiabatic equation of state.

To initialize the simulation, we use the steady state α-disk solution:

$$\rho(R, \theta) = \rho_0 R^{-3/2} \exp\left(-\frac{z^2}{2c_s^2 R^3}\right)\left[1 - \left(\frac{R_*}{R}\right)^{\frac{1}{2}}\right] \tag{4.6}$$

where ρ_0 is a normalization constant to set the maximum disk density to unity, R

is the cylindrical radius ($R = r\cos\theta$), z is the vertical disk height ($z = R\sin\theta$), and c_s is the isothermal sound speed ($c_s = \sqrt{P/\rho} = hv_K$). R_* accounts for the torque-free inner boundary condition and is set just inside the inner simulation domain ($R_* = 11\,GM/c^2$).

The gas starts with a purely azimuthal velocity that is set such that the effective centripetal force balances the gravitational force. The initial magnetic field is weak ($\langle 8\pi p_{gas}/B^2\rangle = 200$) and set from a vector potential,

$$A_r = 0, \tag{4.7}$$

$$A_\theta = 0, \tag{4.8}$$

$$A_\phi = A_0 p^{\frac{1}{2}} e^{-(z/h)^4} R\sin\left(\frac{\pi\log(R/2)}{h}\right), \tag{4.9}$$

where A_0 is a normalization constant. Beyond $|z| = 2.5h$ and within $r = 15\,r_g$, A_ϕ is set to zero. Because of these field loops, the gas is unstable to the MRI.

To help manage the data volume, simulation data was dumped every 2 $t_{orb,10}$ ($\Delta t = 397.4\,GM/c^3$).

4.2.3 Test Simulation

The bistable cooling function used in the simulation assumes a balance between the global heating and cooling and requires an effective α-parameter be known *a priori*. To determine this value, we ran a test simulation using the same grid and initial conditions that are used in our fiducial MHD model. Instead of the bistable cooling function, a simple Noble et al. (2009) style cooling function enforces a target scale height ratio, $h/r = 0.1$ in this case, such that $P_{targ} = \rho v_\phi^2 (h/r)^2/\gamma$. In terms of

pressure the cooling function is, $\Lambda = f(P - P_{targ})/\tau_{cool}$, where f is a switch function ($f = 0.5[(P - P_{targ})/|P - P_{targ}| + 1]$) and τ_{cool} is the cooling time. We take τ_{cool} to be the orbital time to strictly enforce the scale height ratio.

The simulation was run for $t = 1.01 \times 10^5 GM/c^3$ ($512\ t_{orb,10}$) to allow the MRI driven turbulence to fully develop and saturate in the inner third of the simulation domain. Averaged over the final 50 orbits of the simulation, we find $\langle\alpha\rangle = 0.065$ which we use to set the cooling rates of the bistable HD and MHD simulations.

4.2.4 Cooling Function

Our overarching goal is to characterize the dynamics of a truncated accretion disk. To this end, a thermodynamic transition between an efficient cooling state and an inefficient cooling state must arise at some radius to produce the truncation. We accomplish this by treating the gas cooling with an *ad hoc* optically-thin cooling function with two branches reflecting the efficient and inefficient cooling, a similar technique to that employed by Fragile et al. (2012) to study how accretion disk geometry influences jet power. Starting from the simple, viscous formalism of Shakura & Sunyaev (1973), the volumetric heating rate is

$$\mathcal{H} = \frac{3}{2}\alpha\mathcal{R}\rho T\Omega_K, \tag{4.10}$$

where $\mathcal{R}$ is the gas constant. In a steady-state disk, $\mathcal{H} = \Lambda$. Taking as an *ansatz* that the cooling function has the form,

$$\Lambda = \Lambda_0(T)\rho T^2 f(r), \tag{4.11}$$

we can construct a cooling law that is positive-definite everywhere, viscously stable, and produces a geometrically-thick solution at small radii and a geometrically-thin solution at large radii.

We seek to cool to a local equilibrium temperature. This is related to a target scale height ratio by $c_s^2 = \mathcal{R}T = (h/r)^2\Omega_K^2$. The $\mathcal{H} = \Lambda$ condition gives

$$\frac{h}{r} = \sqrt{\frac{3\alpha\mathcal{R}^2}{2\Lambda_0(T)r^2\Omega_K f(r)}}. \tag{4.12}$$

For convenience, we take $f(r) = \mathcal{R}^2 r^{-2}\Omega_K^{-1} \propto r^{-1/2}$ so that

$$\frac{h}{r} = \sqrt{\frac{3\alpha}{2\Lambda_0(T)}}. \tag{4.13}$$

The disk will have a constant aspect ratio if Λ_0 is constant. If there is an abrupt decrease in $\Lambda_0(T)$ at a prescribed temperature T_T,

$$\Lambda_0(T) = \begin{cases} \Lambda_c & (T < T_T) \\ \\ \Lambda_h & (T \geq T_T) \end{cases} \tag{4.14}$$

where Λ_c, Λ_h are constants and $\Lambda_c > \Lambda_h$, we can induce a thermal instability and consequently a radial transition into the flow.

In this formulation, the $\mathcal{H} = \Lambda$ condition dictates three regions exist in our disk. An inner truncation radius occurs at $r_{tr,i} = 3\alpha GM/2\Lambda_c\mathcal{R}^2T_T$ inside of which thermal balance requires the flow to be hot with geometric thickness

$$\left(\frac{h}{r}\right)_{\text{hot}} = \sqrt{\frac{3\alpha}{2\Lambda_h}} \quad \text{for} \quad r < r_{tr,i} := \frac{3\alpha GM}{\Lambda_c\mathcal{R}^2T_T} \tag{4.15}$$

Outside of $r_{tr,o} = 3\alpha GM/2\Lambda_h\mathcal{R}^2T_T$ the flow will be cold with geometric thickness

$$\left(\frac{h}{r}\right)_{\text{cold}} = \sqrt{\frac{3\alpha}{2\Lambda_c}} \quad \text{for} \quad r > r_{tr,o} := \frac{3\alpha GM}{\Lambda_h\mathcal{R}^2T_T} \tag{4.16}$$

The flow is bistable in between these two radii and thermal balance is satisfied on either the hot or cold branch with geometric scale height

$$\left(\frac{h}{r}\right)_{\rm cold} \quad \text{or} \quad \left(\frac{h}{r}\right)_{\rm hot} \quad \text{for} \quad r_{tr,i} < r < r_{tr,o}. \tag{4.17}$$

The ratio of the cold/hot geometric thickness is related to the ratio of the inner/outer transition radii,

$$\frac{r_{tr,o}}{r_{tr,i}} = \left[\frac{(h/r)_{\rm hot}}{(h/r)_{\rm cold}}\right]^2 \tag{4.18}$$

In this work, we set

$$\left(\tfrac{h}{r}\right)_{\rm cold} = 0.1 \tag{4.19}$$

$$\left(\tfrac{h}{r}\right)_{\rm hot} = 0.4 \tag{4.20}$$

$$r_{tr,i} = 100 r_g. \tag{4.21}$$

which implies $r_{tr,o} = 1600 r_g$. As we shall see, this toy cooling function results in a successful transition from a cold/thin to a hot/thicker disk close to the inner transition radius. Interestingly, the flow in the bistable region remains predominantly in the cold/thin state.

4.2.5 Resolution Diagnostics

When interpreting results from numerical MHD accretion disk models, the issues of convergence and resolvability are paramount. As a result, much effort has gone into developing criteria and diagnostics to judge the fidelity of these models. Here, we apply a standard suite of tools to demonstrate that this model is adequately

resolved. All measurements are averaged over time and volume. Time averages are taken during the first initialization stage before the change in the cooling law from $t = 1.79 - 1.99 \times 10^5\ GM/c^3$ (900-1000 $t_{orb,10}$). Volume averages are taken within the main disk body ($h/r < 0.1$) and within the region where the MRI turbulence has saturated ($r < 500\ r_g$) during this time. These can be taken as lower bounds on the resolution because the disk inflates in the analysis stage of the simulation to $h/r > 0.1$ and the effective disk resolution increases.

At the minimum target scale height ratio of $h/r = 0.1$, the simulation grid covers one disk scale height with 32 zones. This value has been shown to be a crude threshold where the macroscopic disk behavior and simulation results converge (Hawley et al., 2013; Sorathia et al., 2012). Quality factors provide a way to assess resolvability of the simulation by comparing the characteristic MRI wavelength in each direction, $\lambda_{MRI} = 2\pi v_A/\Omega$, where v_A is the Alfvén speed, to the grid zone size, i.e. the θ component in the vertical direction and ϕ component in the azimuthal direction (Hawley et al., 2011). Strictly speaking, they only measure the linear MRI amplitude, but they serve as a probe of the fully nonlinear turbulence. The quality factors are,

$$Q_\theta = \frac{\lambda_{MRI,\theta}}{R\Delta\theta} \tag{4.22}$$

and

$$Q_\phi = \frac{\lambda_{MRI,\phi}}{R\Delta\phi}. \tag{4.23}$$

We find that $\langle Q_\theta \rangle = 16.5$ and $\langle Q_\phi \rangle = 19.5$. This is considered "well-resolved" as $Q_\theta > 6 - 8$ has been shown to properly capture the growth rate of the MRI (Flock

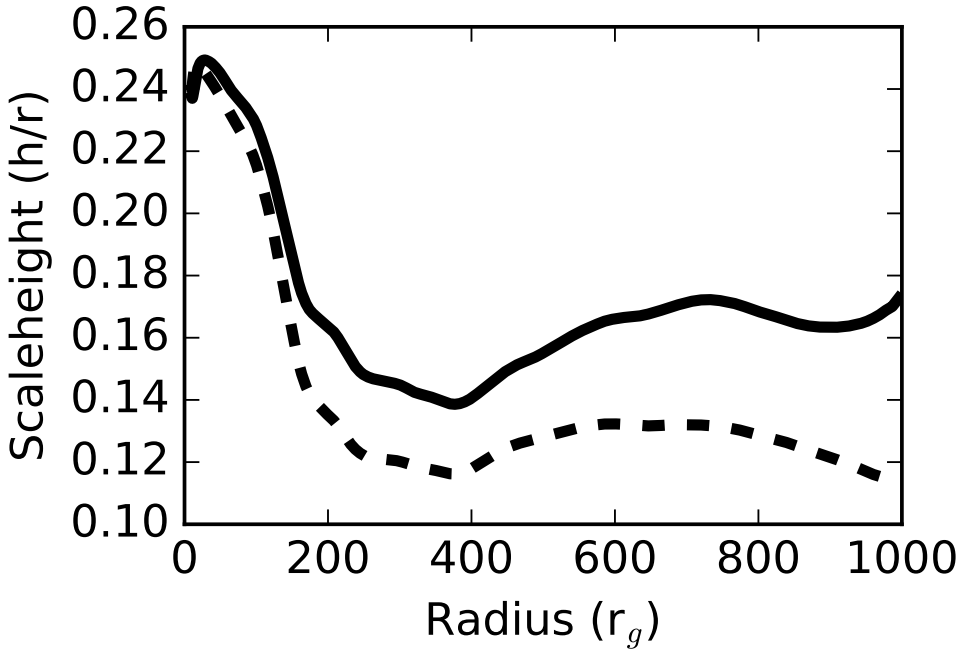

Figure 4.1: Average $h_g(r)/r$ (solid line) and $h_T(r)/r$ (dashed line). Averaging has been done over time as described in the text.

et al., 2010; Hawley & Stone, 1995; Sano et al., 2004). The resolvability criteria for capturing the nonlinear behavior of the MRI driven turbulence is somewhat stricter, $Q_\theta > 10$ and $Q_\phi > 20$ (Hawley et al., 2011, 2013; Sorathia et al., 2012), although they are not independent of each other. Nevertheless, we either meet or exceed these guidelines.

The saturation level of the anisotropic turbulence can be measured through the characteristic orientation of the magnetic field, given by the average in-plane magnetic tilt angle,

$$\Theta_B = -\arctan\left(\left\langle \frac{B_r}{B_\phi} \right\rangle\right). \tag{4.24}$$

Theoretical estimates predict $\Theta_B \approx 15^\circ$ (Guan et al., 2009; Pessah, 2010) and it is

empirically found to be between $\Theta_B \approx 11 - 13^\circ$ in high resolution simulations of local (Hawley et al., 2011) and global (Hawley et al., 2013; Hogg & Reynolds, 2016; Sorathia et al., 2012) MRI driven turbulence. We measure $\langle \Theta_B \rangle = 12.3^\circ$, which is within the bounds of previously measured saturated turbulence.

4.3 Results

In our analysis we are primarily focused on the dynamics of the truncated disk and any sources of variability that could potentially be observable. We strive to understand the drivers behind the disk behaviors and aim to dissect the details of the angular momentum transport and disk energetics. To this end, we take a broad approach and consider all aspects of the accretion flow by investigating how properties like the gas temperature, motions, magnetic field strength, and density vary in both space and time and their interdependencies. The analysis is specifically interested in understanding how the presence of the truncation alters the components of the accretion flow interior to, in, and beyond the truncation. In many cases the analysis considers both the average and instantaneous properties to develop the most complete understand of the truncated disk behavior.

4.3.1 The Truncated Disk

We begin our analysis with an overview of the truncated disk in the simulation. The truncated disk we study has hot, diffuse gas in the inner region and a cooler, Keplerian main disk body. The inner region thickens since it is hot and the gas has

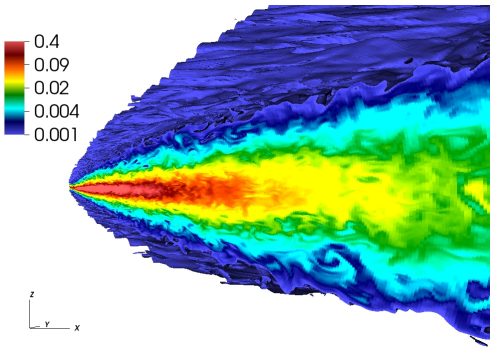

(a) ρ at $t = 1.99 \times 10^5\, GM/c^3$

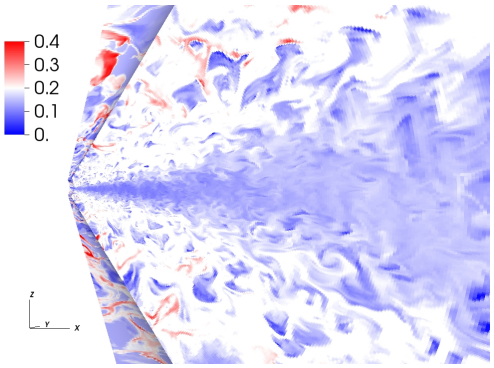

(b) h_T/r at $t = 1.99 \times 10^5\, GM/c^3$

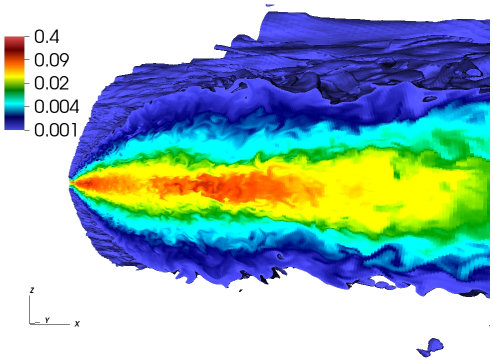

(c) ρ at $t = 3.98 \times 10^5\, GM/c^3$

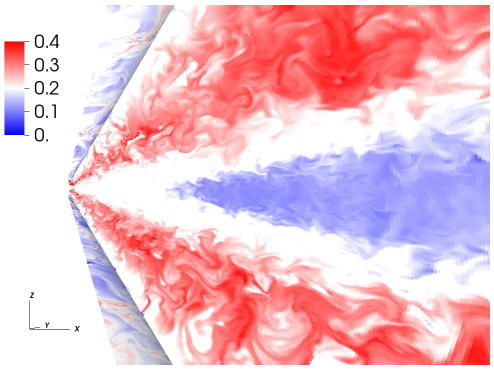

(d) h_T/r at $t = 3.98 \times 10^5\, GM/c^3$

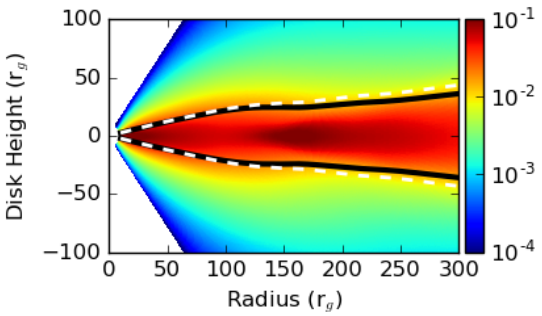

(e) $\langle\rho\rangle$

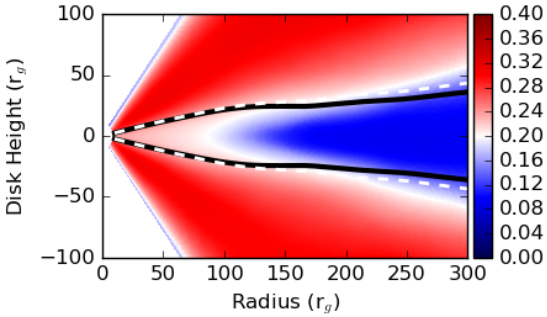

(f) $\langle h_T/r\rangle$

Figure 4.2: Top row- 3D renderings of density (left) and h_T/r (right) at $t = 1.99 \times 10^5\, GM/c^3$ (1000 $t_{orb,10}$). The upper surface of the density rendering is set by the $\rho = 0.001$ contour. Middle row- 3D renderings of density (left) and h_T/r (right) at $t = 3.98 \times 10^5 GM/c^3$ (2000 $t_{orb,10}$). The upper surface of the density rendering is set by the $\rho = 0.001$ contour. Bottom row- Density (right) and h_T/r (left) averaged over azimuth and time. Both $\langle h_g/r\rangle$ (white dashed line) and $\langle h_T/r\rangle$ (black solid line)is overlaid in for reference.

additional thermal support. Figure 4.1 shows two diagnostics of the time averaged scale height ratio. The first measure is the geometric scale height,

$$\frac{h_g(r)}{r} = \left\langle \sqrt{\frac{\int (\theta(r) - \bar{\theta}(r))^2 \rho d\Omega}{\int \rho d\Omega}} \right\rangle, \tag{4.25}$$

where $d\Omega = \sin\theta d\theta d\phi$ is the solid angle element in spherical coordinates and,

$$\bar{\theta}(r) = \frac{\int \theta(r) \rho d\Omega}{\int \rho d\Omega} \tag{4.26}$$

is the average polar angle of the gas. Second, is the density weighted, temperature scale height ratio,

$$\frac{h_T(r)}{r} = \left\langle \frac{\int \sqrt{Tr} \rho d\Omega}{\int \rho d\Omega} \right\rangle \tag{4.27}$$

(where we have taken $\mathcal{R} = GM = 1$). For each data dump, h_g/r and h_T/r were calculated and the time average was taken, denoted by the angled brackets. At small radii, $r < 50\, r_g$, h_g/r and h_T/r are ≈ 0.25. This is below the target scale height of the upper branch of the cooling law ($h/r = 0.4$) and similar to the peak of the average disk scale height in the HD model. Like the HD model, advection acts as a non-radiative cooling term which helps to keep the disk thinner than the hot phase h/r target. At larger radii, the gas resides on the efficient cooling branch and maintains a thin geometry.

Figure 4.2 shows 3D volume renderings of ρ and the local scale height temperature at $t = 1.98 \times 10^5\, GM/c^3$ and $t = 8.94 \times 10^5\, GM/c^3$, to highlight the changes the bistable cooling function introduces from the untruncated disk in the initialization. Of the general differences, the decreased density and increased temperature of the gas in the inner disk are most evident. While the inner region is evacuated,

the density in the coronal regions increases. Additionally, the gas in the atmosphere is significantly hotter and entirely in the hot phase, with temperature scale heights at or above $h_T/r = 0.4$. Throughout the simulation chaotic turbulence dominates the disk and at no point do coherent, small scale structures form. Qualitatively, the truncation resembles the phenomenological model invoked to explain the spectral features from putative truncated accretion disks in BHB and AGN systems, e.g. the schematics in Zdziarski & Gierliński (2004) and Done et al. (2007), albeit with a hotter atmosphere.

Time and azimuthal averages of ρ and the local h_T/r are also shown in Figure 4.2. The gas density peaks in the disk midplane between $r = 150 - 200\,r_g$. In the truncated region the gas density is appreciably lower, but the disk is inflated so the density is enhanced vertically for a given radius. Buoyancy introduces a stratified temperature structure in the outer disk. The thickness of the cold, intermediate, and hot layers changes based on the radial heating profile. The cold gas layer thins with decreasing radius as the gas interior to the truncation zone has $h_T/r \geq 0.2$.

Figure 4.3 shows profiles of the time averaged fraction of gas in each phase as a function of radius. The hot gas is taken to have $T > T_T$. In the inner disk ($r < 100\,r_g$), the gas is entirely above T_T. In the outer disk ($r > 300\,r_g$), $\approx 10\%$ of the gas resides in the hot phase. The gas fractions gradually change in between these two regions as fluctuations allow varying amounts of the disk to reach T_T. Quantitatively we take the "truncation" to be at $r = 170\,r_g$ where the two gas fractions are equal, but the region between $130 - 200\,r_g$ should really be considered a truncation zone between the outer, cold thin disk and the inner, hot thick disk.

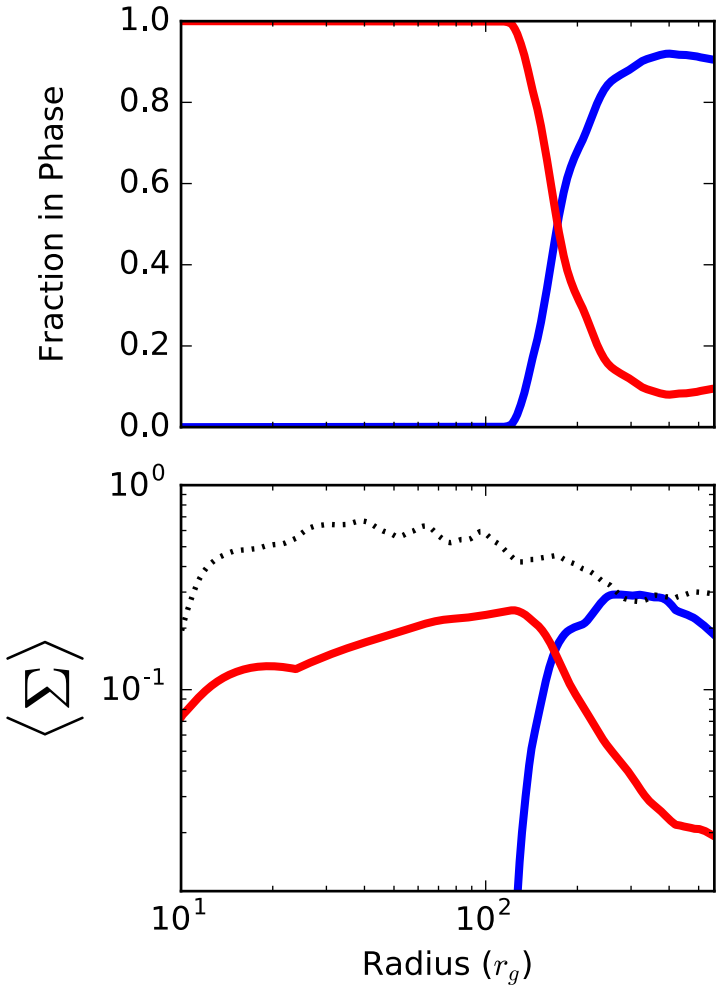

Figure 4.3: Top panel- Radial profiles of the time-averaged f_c (blue line) and f_h (red line). Bottom panel- Radial profiles of time-averaged Σ_c (blue line) and Σ_h (red line). The surface density during the initialization immediately prior to the switch to the bistable cooling function is shown for reference as the black dotted line. In the inner regions of the disk $\Sigma_c \approx 1 \times 10^{-7}$ and is off the plot axes.

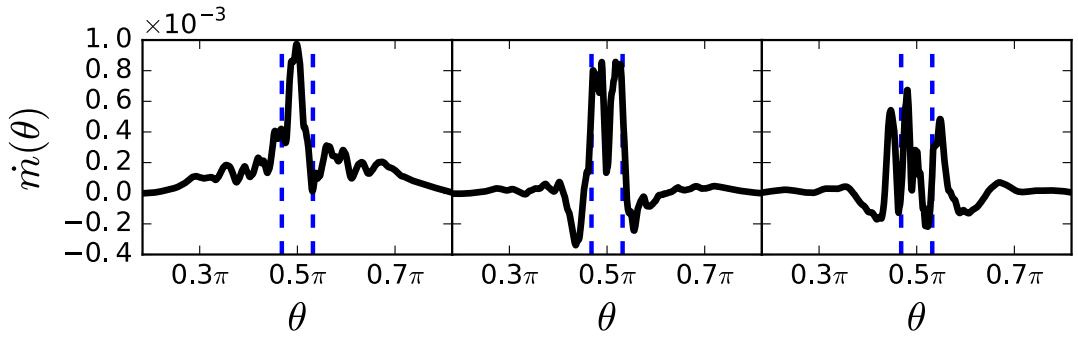

Figure 4.4: Time averaged mass flux ($\dot{m}$) profiles along the polar angle (θ) at $r = 100\,r_g$ (left), $r = 200\,r_g$ (middle), and $r = 300\,r_g$ (right). The blue dashed lines mark one disk scaleheight above and below the disk. We adopt the convention that inflow is positive and outflow is negative.

This region corresponds to the tapering of the cold gas seen in the averaged ρ and h_T/r in Figure 4.2. The surface density,

$$\Sigma(r) = \frac{1}{2\pi r} \int \rho r^2 d\Omega, \tag{4.28}$$

of each respective gas phase is also shown in Figure 4.3. The integration has been done over the entire θ and ϕ domain at each radius. In the inner disk Σ is reduced by $70 - 80\%$ compared to the thin disk in the initialization stage.

4.3.2 Disk Dynamics and Variability

Three dynamically distinct regions develop in the simulation's global flow pattern. The first is the thin, rotationally supported main disk body. Radial motions are dominated by the chaotic flow, but are slightly negative on average as material slowly sinks deeper into the gravitational potential and accretes. Inside of the transition zone, the flow behavior is slightly modified and v_ϕ is modestly sub-Keplerian

(by 10%) because thermal support becomes more influential to the dynamics. The radial velocity is greater than the slow diffusive drift found in the main disk body, but v_r still remains less than a few fractions of a percent of the local Keplerian velocity. In the hot gas filled disk atmosphere, however, the dynamics are quite different from the other two regions. There, thermal support plays its biggest role and the gas is $10-15\%$ below the local Keplerian velocity. The real distinguishing feature of this region, and most dynamically interesting, is a thermally driven outflow that underlies the turbulent fluctuations.

The vertical structure of the bulk gas dynamics is revealed through the mass flux as a function of polar angle

$$\dot{m}(\theta)_r = -\int \rho v_r r \sin\theta d\phi, \tag{4.29}$$

where r is the radius of interest where the mass flux is calculated. Figure 4.4 shows the averaged mass flux at $r = 100,\ 200,\ \&\ 400\ r_g$. At $r = 100\ r_g$, there is a time-averaged inflow as material and thermal energy is advected into the inner boundary, similar to an ADAF. The profiles at $r = 200\ \&\ 400\ r_g$ show that this changes beyond the truncation. Accretion still occurs in the main disk body where the mass is concentrated, but directly above and below the cold disk, starting at one disk scaleheight on either side, $\dot{m}$ is negative, indicating a net outflow of material. This outflow is not a persistent, laminar wind. Rather, it is a bulk motion in the highly turbulent gas from the thermal instability (compared to the strong wind in weak turbulence seen in Yuan et al. (2015), for instance). Figure 4.5 shows the spacetime diagram of the azimuthally averaged radial velocity at $r = 300\ r_g$.

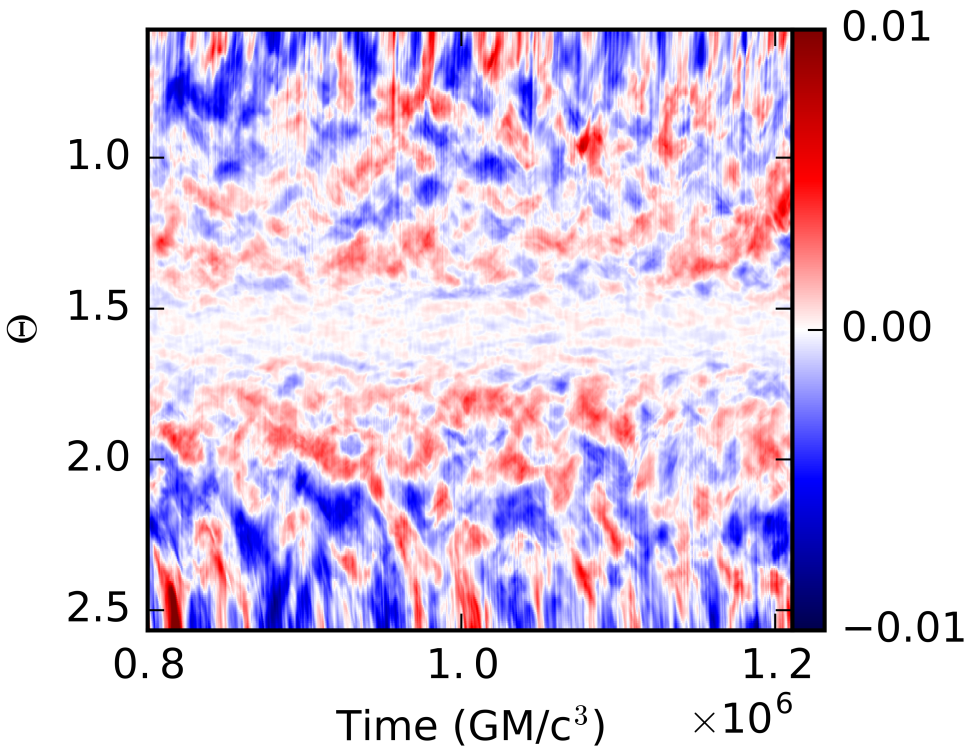

Figure 4.5: Spacetime diagram of v_r at $r = 300\,r_g$. Red denotes positive radial velocities and blue denotes negative radial velocities. The disk midplane is found at $\theta = \pi/2$.

Consistent with the mass flux profiles, the outflow appears as the typically positive v_r values directly above the main disk body, which is seen as the smaller amplitude fluctuations within $\theta = \pi/2 \pm 0.1$. Moving away from the disk to higher altitudes, the fluctuations become more stochastic as the outflow strength diminishes.

The radial structure of the inflow in the inner disk and the outflow beyond the truncation zone is shown in the time averaged profiles of T, v_r, and ρ in Figure 4.6. We have taken a slice along the heart of the outflow from $\theta = \pi/2 - 0.3$ to $\theta = \pi/2 - 0.325$. The temperature profile reveals a near perfect powerlaw scaling with index $\Gamma = -0.992 \pm 0.003$, consistent with the $T \propto r^{-1}$ solution proposed

by Narayan & Yi (1995a). The profiles of v_r and ρ display different behaviors on either side of transition zone. In the inner disk the gas velocities are negative and accelerating inwards as material advects, and the density profile from $r = 20-100\,r_g$ is described by a $\Gamma = 0.69 \pm 0.01$ powerlaw. In the transition zone the average radial velocity is $v_r = 0$ and the density profile rolls over. Beyond the transition, the radial velocity of the outflow is positive and the gas feels a positive acceleration away from the black hole. The acceleration of the outflow is due to buoyant forces and not the magnetic forces, which are quite small (a 10% contribution). The density profile steepens and falls off with a powerlaw index of $\Gamma = -2.13 \pm 0.01$.

The turbulent dynamics of the disk also display differences in the inner disk, transition zone, and outer disk. A simple diagnostic of the turbulent density fluctuations is the turbulent intensity. This is the time averaged, fractional standard deviation of the density as a function of radius, $\overline{\delta(r)}$, shown in Figure 4.7. For each data dump, we calculate,

$$\delta(r) = \frac{\sqrt{\langle |\rho_{mid}(r) - \langle \rho_{mid}(r) \rangle|^2 \rangle}}{\langle \rho_{mid} \rangle}, \tag{4.30}$$

with $\langle \cdot \rangle$ representing azimuthal averages and subscripts denoting that we only consider the disk midplane. Considering the turbulent intensity offers several advantages for comparing the global behavior of the turbulence in the disk. First, this essentially normalizes away any long-term variability in the density. Second, turbulence is inherently a multiplicative process (Kowal et al., 2007; Passot & Vázquez-Semadeni, 1998) and, under constant conditions, the amplitude of fluctuations scales with the density so we need to remove effects from radial density gradients in the

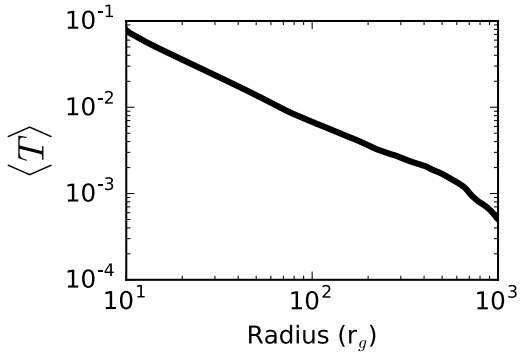

(a) $\langle T(r) \rangle$ of Outflow

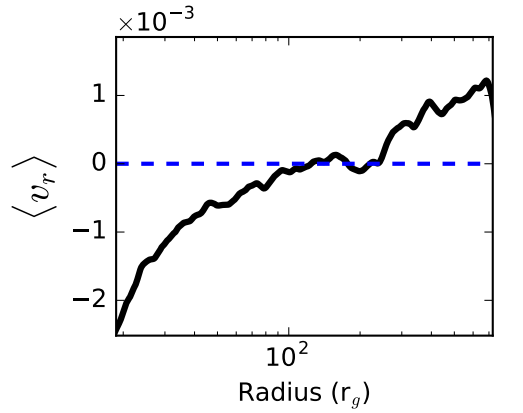

(b) $\langle v_r(r) \rangle$ of Outflow

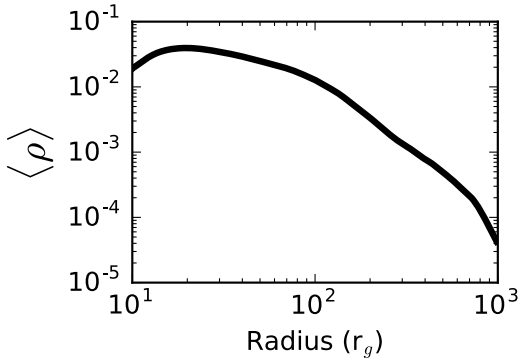

(c) $\langle \rho(r) \rangle$ of Outflow

Figure 4.6: Radial profiles of the average gas temperature (a), radial velocity (b), and density (c) along the outflow ($\theta = \pi/2 - 0.3$ to $\theta = \pi/2 - 0.325$). The profiles have been averaged over azimuth, height, and the duration of the simulation. The blue-dashed line marks $v = 0$, for reference.

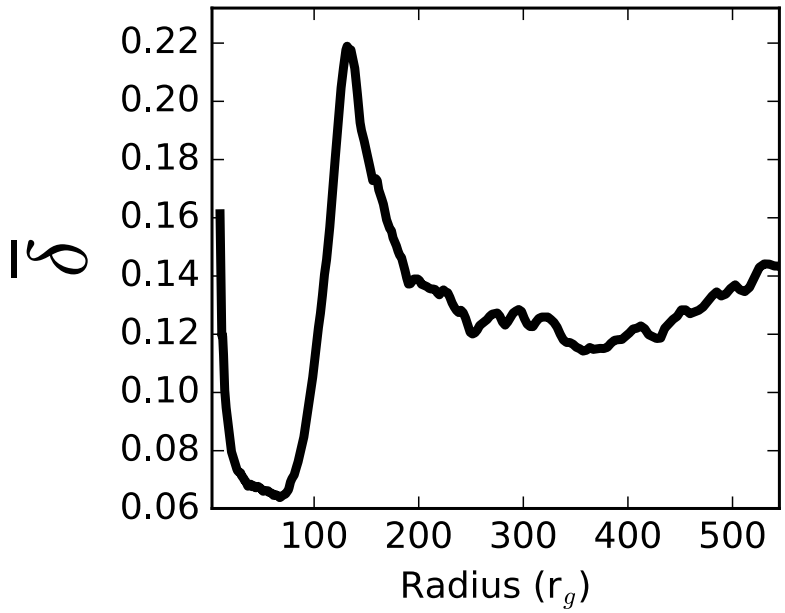

Figure 4.7: Radial profile of the average turbulent intensity, $\overline{\delta(r)}$, measured in the density fluctuations in the ϕ-direction at the disk midplane.

disk.

Throughout most of the disk, $\overline{\delta} = 0.13$, meaning that density fluctuations are on average 13% of the mean. As gas reaches the temperature transition in the truncation zone, $\overline{\delta}$ dramatically increases from 0.14 at $r = 200\, r_g$ to 0.22 at $r = 130\, r_g$. There is then a precipitous drop in the inner disk and δ falls to $\overline{\delta} \approx 0.06$ as the turbulence is suppressed. Close to the inner boundary ($r < 30\, r_g$), the turbulence increases again and approaches the intensity of the main disk body.

Searching for time variability is a goal of our analysis because it could offer a way to observationally probe the accretion flow and test the model predictions. One key source of variability in a truncated accretion disk on timescales longer than the turbulent fluctuations is from appreciable changes in the gas fraction. If this

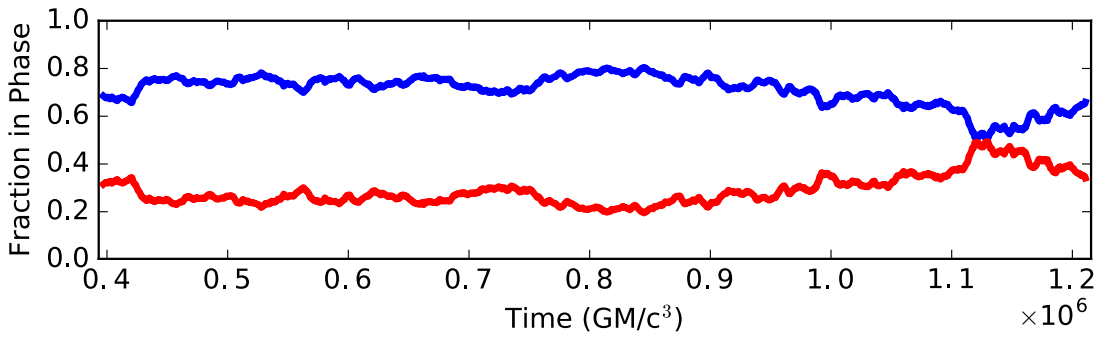

Figure 4.8: Gas fractions f_c (blue line) and f_h (red line) at $r = 200\,r_g$, just beyond the truncation.

results from large changes in the thermal instability, it should appear on the local thermal time and potentially be observable. Figure 4.8 shows the time evolution of the gas fraction in the hot phase, f_h, and the cold phase, f_c, at $r = 200\,r_g$. Both f_h and f_c are featureless and meander around their average values of 0.29 and 0.71, respectively. There is no obvious indication of an instability occurring on a thermal time in this simulation, where $t_{th} \approx 2\times10^3 GM/c^3$ at $r = 200 r_g$. The only prominent behavior is a gradual heating event in the latter half of the simulation. At the peak of the heating event f_h and f_c are equivalent, but then the disk begins to cool and f_h decreases. Small amplitude, high frequency variability from turbulent fluctuations are superimposed on top of the long term trend.

4.3.3 Mass Accretion and Angular Momentum Transport

The mass accretion rate,

$$\dot{M}(r) = \int \rho v_r r^2 d\Omega, \tag{4.31}$$

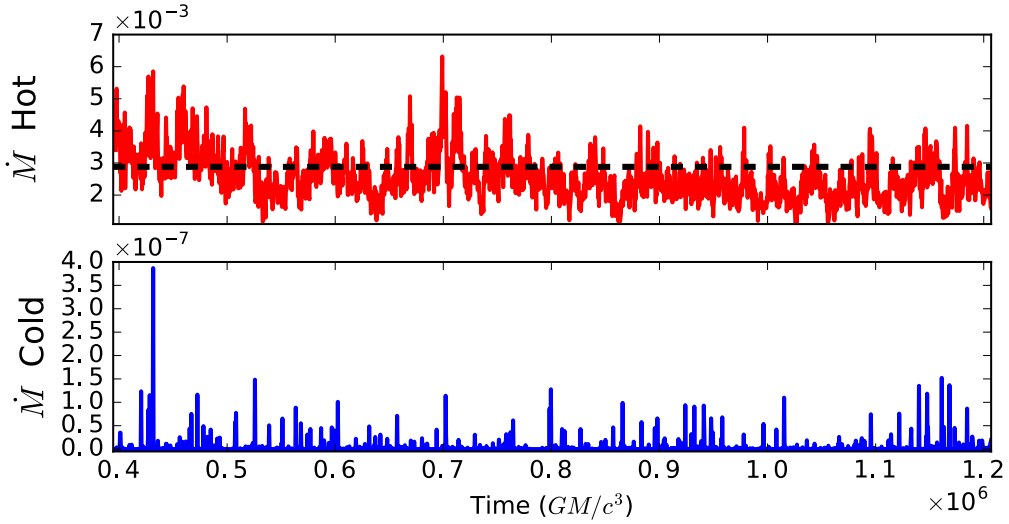

Figure 4.9: $\dot{M}_h$ (top panel) and $\dot{M}_c$ (bottom panel) at the inner boundary over the course of the simulation. The $\dot{M}_{ini}$ at the inner boundary is shown as the black dashed line in the top panel for reference.

is highly variable on short timescales. The variability in the simulation is from rapid fluctuations due to the disk turbulence, and there is a marked absence of any long-term, coherent variability that might be tied other accretion processes. Figure 4.9 shows $\dot{M}$ at the inner boundary separated into the hot phase gas and cold phase components. The hot gas is accreted at a rate of $\langle \dot{M}_h \rangle = 2.5 \times 10^{-3}$ with a characteristic variability of $\sigma_{\dot{M}} = 7.0 \times 10^{-4}$, or 28%. The cold gas accretion rate is negligible at $\langle \dot{M} \rangle = 3.4 \times 10^{-9}$. There are brief excursions from this very low value, but it rarely exceeds more than a 1×10^{-7}. For reference, the mass accretion rate of the thin disk during initialization was $\langle \dot{M}_{init} \rangle = 2.8 \times 10^{-3}$ is also shown. The slight suppression in the truncated disk mass accretion is from the removal of a small amount of material by the weak outflow, which prevents it from reaching the inner boundary.

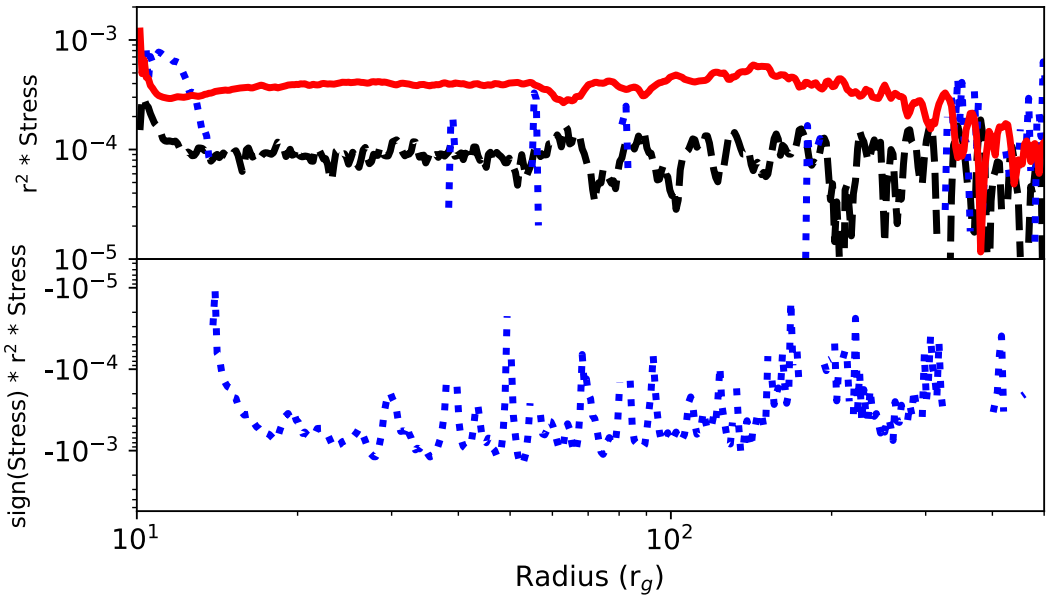

Figure 4.10: Radial profiles of the shell integrated angular momentum advection (blue dotted line), Maxwell stress (solid red line), and the Reynolds stress (dashed black line). The profiles are shown as the logarithm of the absolute value with the original sign of the stress, i.e. $\text{sign}(x)\log(|x|)$. Additionally, they have been scaled by r^2.

The transport of angular momentum enabling the mass accretion has three components: the Maxwell stress, the Reynolds stress, and advection. Conservation of angular momentum is given by,

$$\frac{\partial}{\partial t}(\rho r v_\phi) + \nabla \cdot (\rho r v_\phi \mathbf{v} - r B_\phi \mathbf{B}) = 0. \tag{4.32}$$

The dominant torque, rB_rB_ϕ, is exerted by the Maxwell stress. The $\rho r v_\phi \mathbf{v}$ term can be further separated into an average velocity term representing the advection of angular momentum, $\rho r v_\phi \langle v_r \rangle$, and its fluctuating component, $\rho r v_\phi \delta v_r$, which accounts for torques from the Reynolds stress. The radial profiles of the three terms are shown in Figure 4.10 after summing over shells and taking the time average.

Throughout the disk the Maxwell and Reynolds stress transport angular mo-

mentum outwards to larger radii. The Maxwell stress is $\approx 5\times$ larger than the Reynolds stress and provides the majority of the angular momentum transport. This is consistent with the 4-5:1 ratio broadly seen in other numerical models of MHD accretion disks (Blackman et al., 2008; Hawley et al., 1995; Pessah et al., 2006). Interior to the transition zone all of the angular momentum transport terms are enhanced by factors of 2 over what they are in the outer disk.

Spatially, there is a partitioning of the Reynolds and Maxwell stress enhancements and the increased stresses occur in discrete zones. Figure 4.11 shows the two-dimensional structure of the average Reynolds stress, Maxwell stress, and advection. The Reynolds stress is more intense within the disk body where transitioning gas causes the disk to taper. This region coincides with the larger turbulent intensity, δ. Together, this indicates that the turbulent fluctuations not only have a larger amplitude, but they are also correlated.

The Maxwell stress enhancement forms an envelope around the truncation zone. Given that it occurs where the outflow originates and flows along the disk, it seems the outflow amplifies the field. The likely mechanism behind this amplification is the conversion of kinetic energy into magnetic energy by nonlocal energy transfers through shells in Fourier space. For a wavenumber of the velocity field k_v, and wavenumber in the magnetic field, k_m in a turbulent flow, the magnetic field will receive energy from the velocity field for all shells with $k_v < k_m$ (Mininni, 2011; Moffatt, 1978). Comparing the small turbulent scales in this region to the outflowing gas scale, the flow meets this criterion. As the gentle outflow moves through the turbulent accretion flow, field lines are stretched and the field is amplified. This

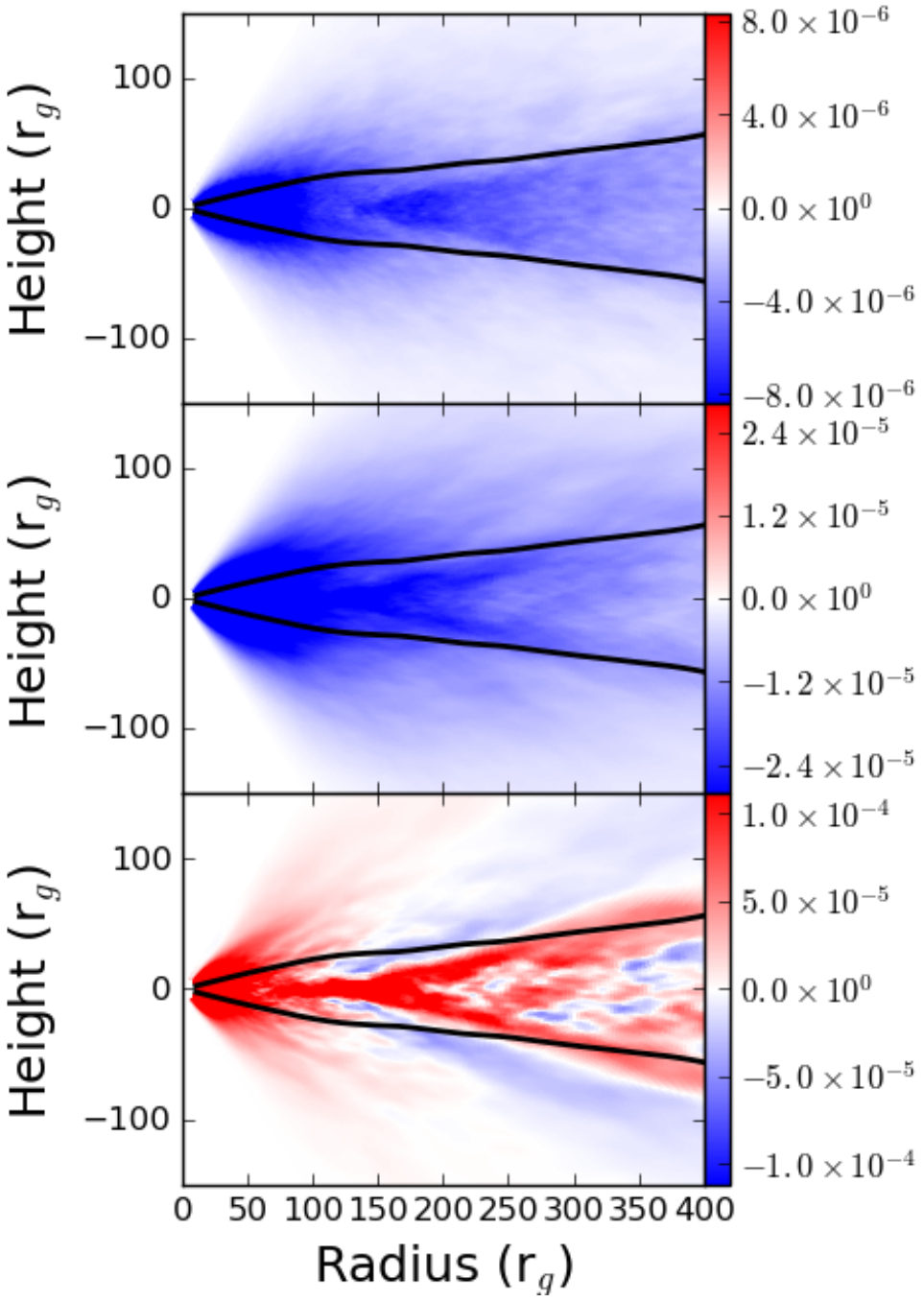

Figure 4.11: Maps of $\rho r v_\phi \delta v_r$ (top panel), $-rB_rB_\phi$ (middle panel), and $\rho r v_\phi \langle v_r \rangle$ (bottom panel). Overlaid is the average geometric scale height (black solid line).

phenomenon has been invoked in a number of contexts, including geophysical dynamo action of the terrestrial magnetic field (Peña et al., 2016), but is less well studied in accretion flows. Lesur & Longaretti (2011) showed that these non-local transfers in spectral space operate in MRI-driven turbulence, but there has yet be an investigation into the global energy transfer properties of an accretion disk.

Several distinct regions form in the advective term. The greatest inwards advection of angular momentum occurs on the surface of the disk, coincident with the largest Maxwell stresses. Disk material typically accretes along the skin of the disk and then in a channel like region in the disk midplane stemming from the truncation. It is important to bear in mind that the appearance of this channel-like region is simply the average advection and that entire region is turbulent, despite it being suppressed relative to the rest of the disk. The inwards drift of material is still very slow and the gas dynamics are dominated by the turbulent velocity. Above this inflowing region, the outflowing gas is launched in the transition zone as hotter gas rises to larger radii. Interior to this region ($r < 100\, r_g$), all of the gas is in the hot phase and the Maxwell and Reynolds stresses are large which drives material inwards to the inner boundary.

4.3.4 Disk Energetics

In this MHD accretion flow, the conservation of energy equation is,

$$\frac{\partial \mathcal{E}}{\partial t} + \mathcal{C} + \mathcal{A}_{\mathcal{K}} + \mathcal{A}_{\mathcal{T}} + \mathcal{A}_{\mathcal{M}} + \mathcal{G} - \mathcal{W} = 0, \tag{4.33}$$

where $\mathcal{E}$ is the total disk energy, $\mathcal{C}$ is the "radiative" cooling done by the cooling function, $\mathcal{A}_\mathcal{K}$ is the advection of kinetic energy, $\mathcal{A}_\mathcal{T}$ is the advection of thermal energy, $\mathcal{A}_\mathcal{M}$ is the advection of magnetic energy, $\mathcal{G}$ is the advection of gravitational potential energy, and $\mathcal{W}$ is the work done by magnetic torques. Here, we will consider a spherical shell integrated form of the terms, such that they are

$$\frac{\partial \mathcal{E}}{\partial t} = \frac{\partial}{\partial t}\left[\int d\Omega\left(\frac{1}{2}\rho v^2 + \frac{P}{\gamma-1} + \rho\Phi + \frac{B^2}{2}\right)\right], \tag{4.34}$$

$$\mathcal{C} = \int d\Omega\Lambda, \tag{4.35}$$

$$\mathcal{A}_\mathcal{K} = \frac{1}{r^2}\frac{\partial}{\partial r}\left[r^2\int d\Omega\left(\frac{1}{2}\rho v^2\right)v_r\right], \tag{4.36}$$

$$\mathcal{A}_\mathcal{T} = \frac{1}{r^2}\frac{\partial}{\partial r}\left[r^2\int d\Omega\left(\frac{P}{\gamma-1}\right)v_r\right], \tag{4.37}$$

$$\mathcal{A}_\mathcal{M} = \frac{1}{r^2}\frac{\partial}{\partial r}\left[r^2\int d\Omega\left(\frac{B^2}{2}\right)v_r\right], \tag{4.38}$$

$$\mathcal{G} = \frac{1}{r^2}\frac{\partial}{\partial r}\left[r^2\int d\Omega\left(\rho\Phi\right)v_r\right], \tag{4.39}$$

$$\mathcal{W} = \frac{1}{r^2}\frac{\partial}{\partial r}\left[r^2\int d\Omega v_\phi B_\phi B_r\right]. \tag{4.40}$$

The time averaged radial profiles of $\mathcal{C}$, $\mathcal{A}_\mathcal{K}$, $\mathcal{A}_\mathcal{T}$, $\mathcal{A}_\mathcal{M}$, $\mathcal{G}$, and $\mathcal{W}$ are shown in Figure 4.12.

In the inner disk the kinetic, thermal, and magnetic energy fluxes are negative, indicating there is an inwards advection with the accretion flow. Most of the advection is in $\mathcal{A}_\mathcal{K}$, followed by thermal energy ($\mathcal{A}_\mathcal{T} \approx 0.5\,\mathcal{A}_\mathcal{K}$) and finally the magnetic energy ($\mathcal{A}_\mathcal{M} \approx 0.03\,\mathcal{A}_\mathcal{K}$). Beyond the truncation in the thin disk, $\mathcal{A}_\mathcal{K}$ remains constant, but $\mathcal{A}_\mathcal{T}$ actually switches sign as the hot gas in the outflow dominates this energy term. $\mathcal{A}_\mathcal{T}$ is slightly suppressed since there is competition between the inwards flow of cooler gas in the disk body and the hot gas with positive radial velocity, but ultimately the hot gas is main contributor. Additionally, the $\mathcal{A}_\mathcal{M}$ term

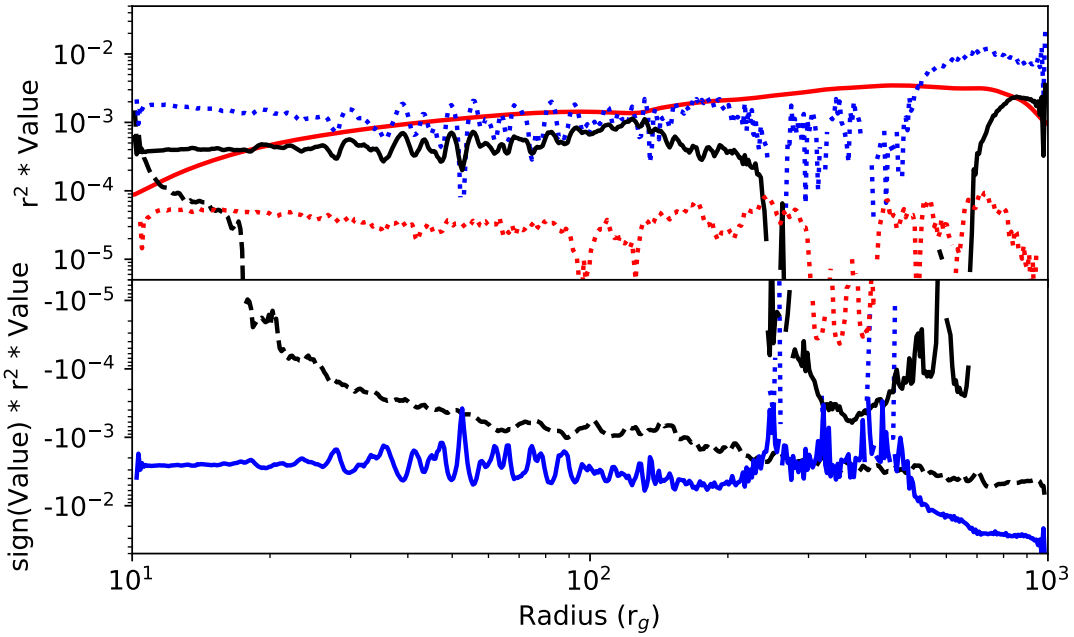

Figure 4.12: Radial profiles of terms in the energy equation. The profiles are shown as the logarithm of the absolute value with the original sign of the energy, i.e. $\text{sign}(x)\log(|x|)$. Additionally, they have been scaled by r^2. The work done by magnetic torques ($\mathcal{W}$) is shown by the black dashed line, the advection of kinetic energy ($\mathcal{A}_\mathcal{K}$) is shown by the blue dotted line, the advection of thermal energy ($\mathcal{A}_\mathcal{T}$) is shown by the black solid line, the advection of magnetic energy $\mathcal{A}_\mathcal{M}$ is shown by the red dotted line, the cooling term ($\mathcal{C}$) is shown as the red solid line, and the change in gravitational potential energy ($\mathcal{G}$) is shown by the blue solid line.

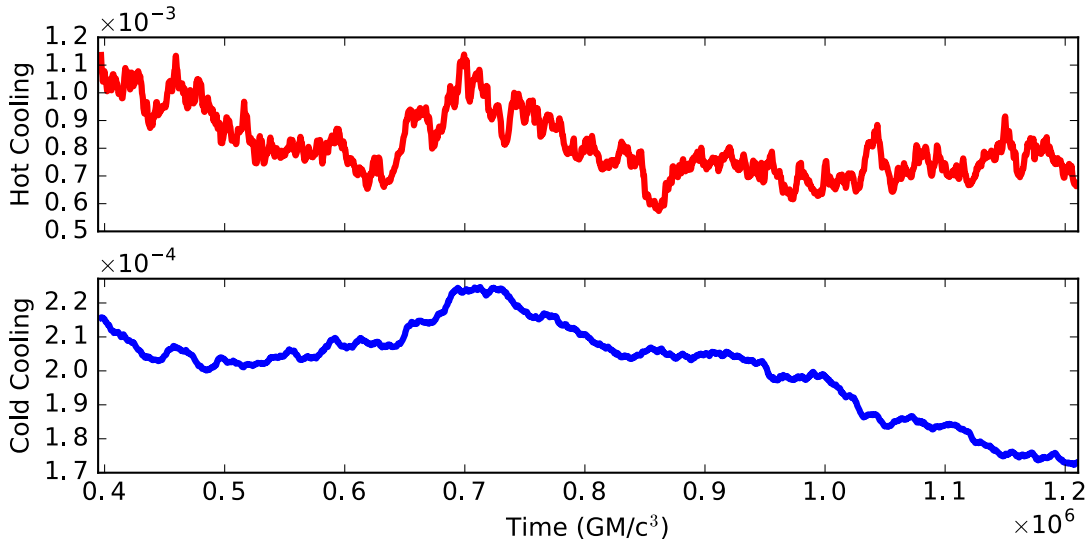

Figure 4.13: Disk integrated synthetic light curve from the hot gas cooling (top panel) and cool gas cooling (bottom panel).

switches sign because buoyancy lifts organized patches of overmagnetized gas as the disk dynamo cyclically builds magnetic field in the outer disk. The role of magnetic buoyancy is minimal in the inner disk because the dynamo is suppressed, an aspect of the simulation discussed on Section 4.3.5. The contribution of $\mathcal{C}$ to the energy budget increases further out in the disk, reflecting the change in gas fraction and cooling efficiency. In the inner disk, $\mathcal{C} \approx 0.3\,\mathcal{G}$. In the outer region, though, the disk approaches the standard thin disk ratio of $\mathcal{C} \approx 1.5\,\mathcal{G}$.

Using the *ad hoc* cooling as a proxy for emitted radiation, we create synthetic light curves, shown in Figure 4.13. The cooling is separated into that from the hot and cold gas phases, which can loosely be considered "hard"-band and "soft"-band emission, following observational convention. The cool gas light curve has been renormalized to correct for the draining of cool gas from the simulation. Over the course of the simulation, the cool gas depletes by $\approx 20\%$. We scale the density by

the ratio of cool gas mass at the beginning of our analysis to the current cool gas mass at each point. This scaling was not applied to the hot gas because we have reached an approximate inflow equilibrium so the rate at which it is accreted is the same rate at which cold gas transitions. This keeps the total hot gas mass roughly constant throughout the analysis portion of the simulation.

The variability in these light curves predominately occurs on long timescales, i.e. longer than a dynamical or thermal time. The main feature is a brightening event that peaks in both light curves at $t = 7 \times 10^5 \, GM/c^3$. This event increases the cool gas light curve by only 10%, but the hot gas light curve by 50%. The variability of the gas fraction near the transition zone seen in Figure 4.8 does not translate to the light curve. The amplitude of stochastic fluctuations is much greater in the hot gas light curve. Several flaring events occur when the hot gas light curve rapidly increases by 30% and then decays to the lower trend level. These events occur randomly and do not have any distinguishing periodicity or even a characteristic shape.

4.3.5 Disk Dynamo

The importance of the magnetic dynamo action on the evolution of a black hole accretion disk cannot be overstated. On small scales an effective MHD dynamo is essential for sustaining the MRI driven turbulence because it provides a continual source of the magnetic field regeneration against dissipation and reconnection (first shown by Hawley et al., 1995). On larger scales, spacetime diagrams of B_ϕ in

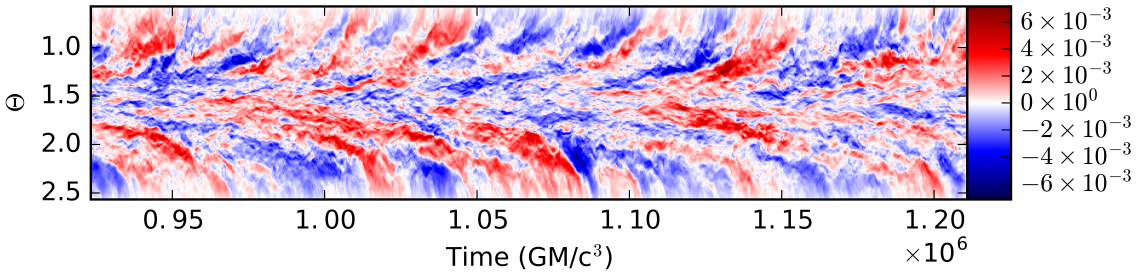

(a) $\langle B_\phi \rangle$ at $r = 100\,rg$

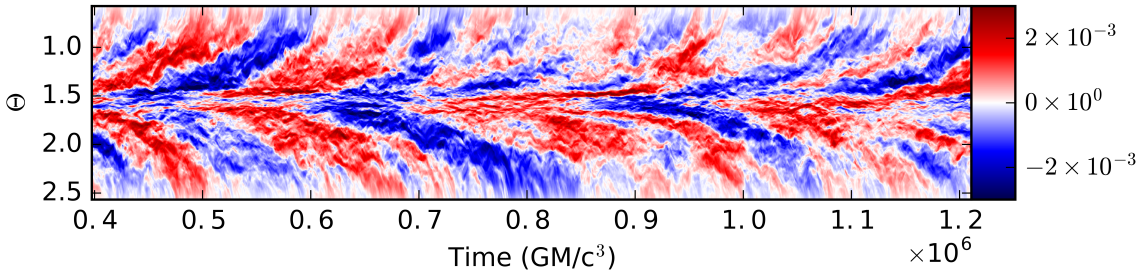

(b) $\langle B_\phi \rangle$ at $r = 200\,rg$

Figure 4.14: Spacetime diagrams of the azimuthally averaged B_ϕ at $r = 100r_g$ (top panel) and $r = 200r_g$ (bottom panel). The time axis in the top panel has been rescaled to show $r_{100}^{1.5}/r_{200}^{1.5}$ of the time to better match the differences in the evolutionary timescales of the dynamo process and aid in the direct comparison of B_ϕ at each radius. These two disk locations were chosen to represent the more general behavior on either side of the truncation zone.

numerical simulations reveal a quasiperiodic reversal of the magnetic field orientation and lifting of the field which forms the so-called "butterfly" pattern. Global PSDs show that, in fact, the organization of the field is a large-scale phenomenon and bands of power in the oscillation span several radii (O'Neill et al., 2011). Nominally, the frequency of the oscillation, Ω_d, is taken to be one tenth of Ω_K.

Figure 4.14 shows the spacetime diagram of the azimuthally average magnetic field on either side of the truncation zone at $r = 100r_g$ and $r = 200r_g$. The time axis of the $r = 100\,r_g$ butterfly diagram has been rescaled to show a similar evolutionary

time (i.e. only a portion corresponding to $r_{100}^{1.5}/r_{200}^{1.5}$ of the analysis time). Beyond the transition zone, the B_ϕ pattern is organized with a coherent, quasi periodic oscillation at a frequency of $f = 3.7 \times 10^{-6}\, c^3/GM$ (15× the orbital frequency). At the midplane the field strengthens, diminishes, alternates sign, strengthens and the cycle repeats. The region is dominated by field of similar polarity spanning the midplane. A cycle is present inside the truncation, but the pattern is disturbed and stochastic fluctuations account for much of the variability. Additionally, the magnetic field is less ordered and the field oscillations are intermittent, thus preventing the development of strong field throughout the entire midplane. Rather than sustained values that are typically near the maximum amplitude, weak B_ϕ is common. Nevertheless, this does not lower the average Maxwell stress which is actually higher within the truncation zone, as we saw in Figure 4.10. At higher altitudes above and below the disk the cycle recovers and is more clearly defined.

A consequence of disrupting the dynamo is that the net field strength is lower than it would be otherwise. Coupled with the increased gas pressure from the transitioning gas, the ratio of the gas pressure to the magnetic pressure,

$$\beta = \frac{P_g}{P_m}, \tag{4.41}$$

is high in the inner disk and the transition zone. Figure 4.15 shows β averaged over time and azimuth. The increase in β is most prominent in the inner region of the disk body where thermal pressure inflates the disk. Extending away from the inner regions are wings of high-β gas that trace the outflow.

The increased gas pressure also acts to decrease the effective α-parameter in

the inner disk. Figure 4.15 shows the time averaged radial profile of the effective α. For each data dump we calculated the volume averaged stress and volume averaged pressure within the geometric scale height (h_g/r) and took the ratio, according to Eqn 2.1. Beyond the transition in the region that has reached a quasi-steady state, the effective α parameter is $\alpha = 0.055$. This is 15% below the average effective α in our calibration due to the additional gas pressure support from small patches of transitioning gas triggered by turbulent fluctuations. Moving inwards from the truncation zone, the effective α-parameter decreases from 200 r_g to 110 r_g which corresponds spatially with the tapering of the cold disk body seen in Figure 4.2. In the very inner regions where the gas is entirely in the hot phase, the effective α-parameter settles to a value of $\alpha \approx 0.02$. There is a rapid recovery in the effective α at the inner edge of the simulation which could be due to boundary effects and thus artificial.

The Fourier transform of the Maxwell stress,

$$\widetilde{M_{r\phi}}(f) = \int M_{r\phi}(t) e^{-2\pi i f t} dt. \tag{4.42}$$

reveals periodicity in its variability. Shown in Figure 4.16 is the power spectrum of the integrated Maxwell stress in the truncation zone between $r = 130\, r_g$ and $r = 200\, r_g$. The total stress has been summed over $\theta = \frac{\pi}{2} \pm 0.2$. Overall, the power spectrum scales as f^{-1} and $f\widetilde{M_{r\phi}}(f)$ is flat. On top of the powerlaw spectrum, though, there is a band of power where the variability is strongly periodic. This feature is centered at $f = 4.0 \times 10^{-5}\, c^3/GM$, coherently spans five spectral bins, and is $\approx 4\times$ greater than the noise spectrum. Given its strength and relatively low

frequency, this develops from an interaction with the disk dynamo. Interestingly, it is five times faster than the local dynamo frequency at $f = 7.2 \times 10^{-6}\, c^3/GM$ for $r = 170\, r_g$.

4.4 Discussion

The MHD model presented here and the viscous HD model in are targeted to study the dynamics of truncated accretion disks. Compared to the rich literature on hot, geometrically thick accretion flows and cool, geometrically thin accretion flows, the truncated disk model is poorly explored, despite the frequency with which this flow configuration is invoked to explain the spectral properties of hard state BHBs and LLAGNs. This work has characterized the general flow properties, but further work is required to fully capture the subtleties of flow at the transition zone. Broadly, the HD and MHD models were similar even though they were set in very different fluid regimes. Both models preferred a cool solution until near the imposed r_T, launched some sort of thermally driven outflow, and formed a thin layer of enhanced stress as the hot gas moved along the surface of the main disk body. In the viscous HD model the enhanced stress was due to the $\theta - \phi$ viscosity component and in the MHD model this arose through the stretching of field lines which intensified the Maxwell stress. These are two fundamentally distinct origins, but they ultimately have the same effect. Furthermore, the inner disk regions in both models are evacuated, which is seen as deficits in the surface density profiles interior to r_T compared to what it would be as a standard thin, cold disk. This is

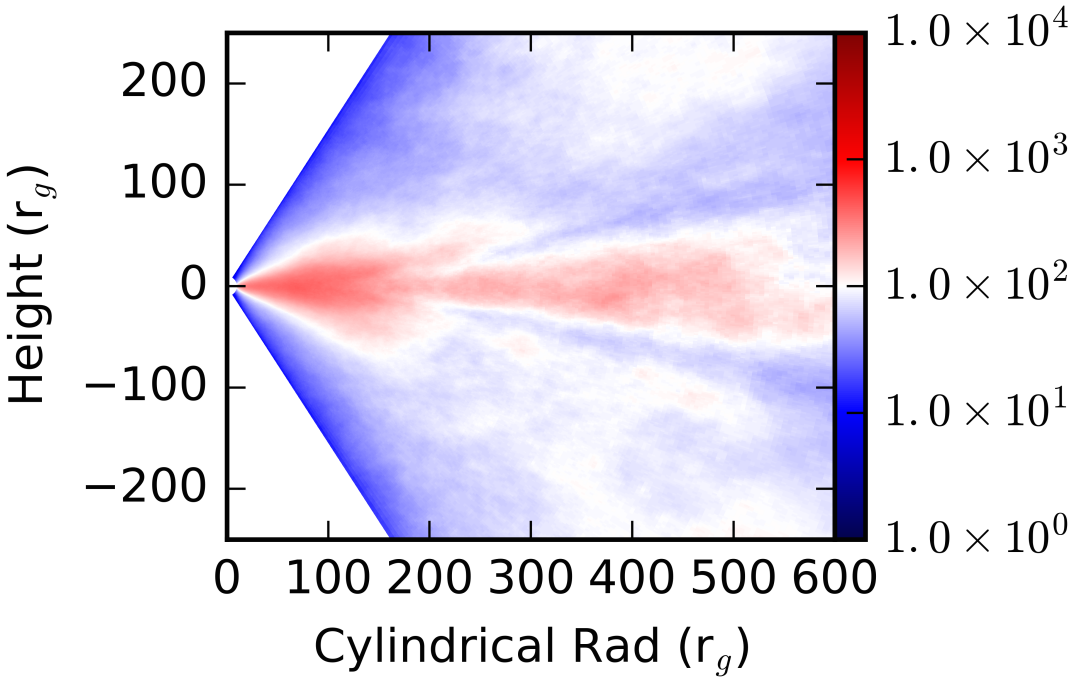

(a) $r - \theta$ map of $\langle\beta\rangle$

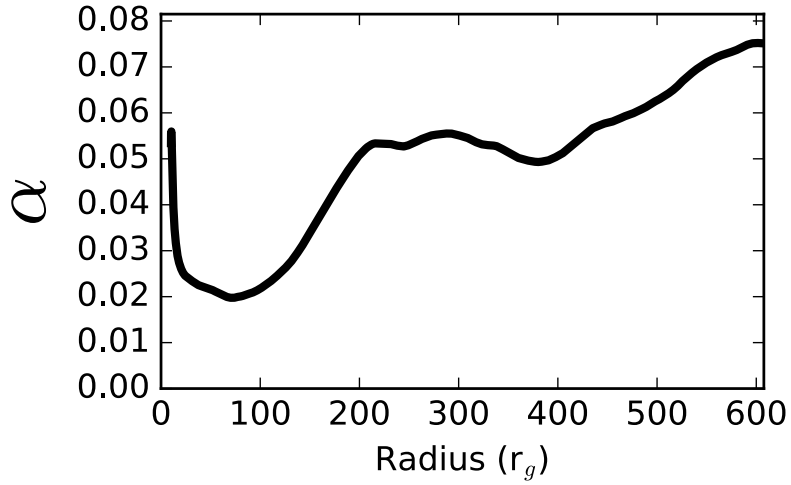

(b) Radial $\langle\alpha\rangle$ profile

Figure 4.15: $r - \theta$ map of $\langle\beta\rangle$ (a) and the radial $\langle\alpha\rangle$ profile (b). The $r - \theta$ map of $\langle\beta\rangle$ has been averaged over azimuth and time. The radial $\langle\alpha\rangle$ profile is the time averaged effective α value calculated within the local geometric scale height (h_g).

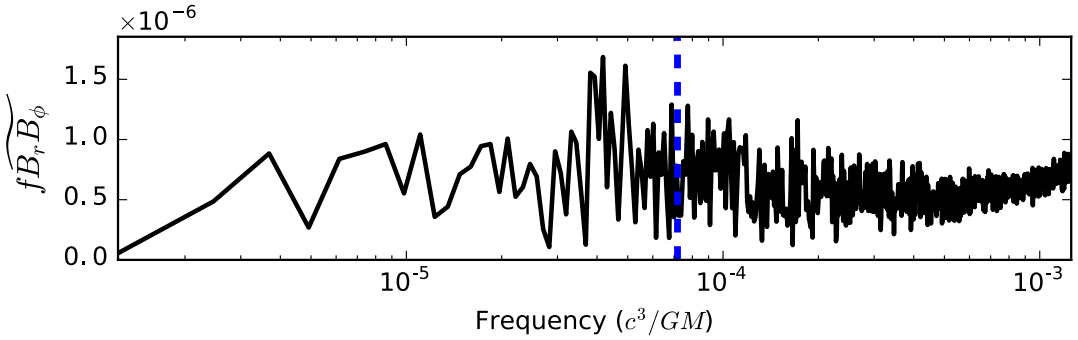

Figure 4.16: Power spectrum of the Maxwell stress, $f\widetilde{M_{r\phi}}$, in the truncation zone. The local dynamical frequency at $r = 170\,r_g$ is shown as the dashed blue line.

generally consistent with observational results where the inner regions of hard state BHBs and LLAGNs are measured to be less dense.

In the HD and MHD models the flow takes on a configuration where the cooler thin disk is embedded within the hot gas. Typically, phenomenological models of truncated disks envision the hot gas occupying the inner region of the disk in a spherical bulge whose extent is roughly the truncation radius (e.g. Shapiro et al., 1976). Our results, along with other numerical models of truncated disks (e.g. Mishra et al., 2016; Takahashi et al., 2016), suggest that the hot gas may fill the entire region surrounding the black hole and take on a structure akin to that presented in Cui et al. (1997); Esin et al. (1997); Liang & Nolan (1984). Additional scattering resulting from "sandwiching" a disk between between the two hot coronal regions can produce telling observational signatures in the X-ray spectrum (Takahashi et al., 2016) and in polarization (Schnittman & Krolik, 2010).

While the presence of an outflow is shared between the HD and MHD truncated disk models, the manifestations are distinct. In the HD model convection appears in

the flow atmosphere, reminiscent of a CDAF-type flow, except that the gas in these convective eddies eventually fell back and was accreted. In the MHD model convection is stabilized and, even though the instantaneous gas motions are dominated by MHD turbulence, there is a thermally driven bulk outflow. Scaling the system to physical values, there appears to be only limited promise in observing the outflow. Taking a characteristic inner disk temperature to be virial at $T = 10^{12}\ K$ (Shapiro et al., 1976), the outflow would have temperatures between $T \approx 5 \times 10^{9} - 10^{12}\ K$. Scaling the dimensionless velocity by the speed of light, c, we find that the velocity range spans $v_r \approx 0 - 300$ km/s. The velocity is in the range of empirically measured outflows, but its observational prospects may be hindered by the high temperature and the large turbulent broadening since the turbulent velocity is three times greater than the bulk flow ($\Delta v \approx 1,000$ km/s).

Considering the truncated disk in MHD has elucidated several unique disk features that have not previously been considered. First is the interplay between stochastic temperature fluctuations and the thermal instability. MHD turbulence driven by the MRI has been understood as a key way to transport angular momentum and heat the disk through turbulent dissipation, and we find it is also important in triggering the thermal instability. At a given radius, the gas has a range of temperatures with some fraction of the distribution lying beyond the transition condition. This can impact the disk geometry because local pockets of gas can transition at radii which would otherwise be too cool to satisfy the thermodynamic criterion. As gas sinks to smaller radii, the fraction of gas on the inefficient cooling branch will increase. The natural result of this radial variation is a disk tapering

in a transition zone like that produced in our simulation, rather than a transition edge. Measurements of truncation radii from spectral fits may benefit from fitting a smoother transition rather than a sharp inner disk cutoff, as is often used.

The details of the transition rests on the precise transition mechanism. Here, we treated the cooling with a simple threshold, but a more physical prescription is needed before a complete understanding of the dynamics in a truncated disk can be achieved. This demands that the theory underlying the thermal instability be developed. So far, several global accretion models have been proposed as candidates to fill this role. Inner disk evaporation of the cool, Keplerian disk by heating from a hot corona (Liu et al., 1999; Meyer & Meyer-Hofmeister, 1994; Narayan et al., 1996; RóżaŃska & Czerny, 2000) could lead to disk truncation. The interior of the disk could also heat the gas beyond the virial temperature because of the diffusion of energy from through the disk (Honma, 1996; Manmoto & Kato, 2000; Manmoto et al., 2000). Alternatively, local thermal instability can develop if the α-parameter is proportional to the magnetic Prandtl number (Potter & Balbus, 2014, 2017). Work has gone into understanding these mechanisms analytically and with simple numerical models, but their viability in a global MHD accretion disk is untested. Numerical models must rigorously test these mechanisms to determine which are the most feasible and to tie them to observational signatures that could originate at the transition. The latter goal could provide a fruitful avenue for informing the large, time-domain surveys scheduled for the near future.

The second unique insight that comes from studying the MHD truncated disk is the interaction with the magnetic dynamo; specifically, that the dynamo was

disrupted in the truncated disk region and that the outflow strengthened the field surrounding the cooler disk body. Some form of low-frequency magnetic dynamo is universally observed in three-dimensional MHD accretion disk models. Usually, the dynamo appears as quasi-periodic oscillations of the large-scale magnetic field in a standard thin accretion disk. However, there is a developing narrative that certain conditions can hinder the organization of the large-scale field by the dynamo and impede the regular strengthening of the dynamo cycle. A few instances from numerical models include quenching in a magnetically dominated disk (Bai & Stone, 2013; Salvesen et al., 2016) and the mixing of field from hydrodynamic convection (Coleman et al., 2017). Global simulations of super-Eddington flows that include radiative effects find that the dynamo period remains regular, but is slower when than what it should normal be (Jiang et al., 2014). Nonphysical causes like resolution effects from sensitivities to the simulation domain aspect ratio have also been shown to quench the dynamo (Walker & Boldyrev, 2017). The sporadic dynamo oscillations in the inner regions of the truncated disk provide another example of how the dynamo behavior can be modified, which we expand on in Chapter 5.

Interior to the transition the magnetic field might have been expected to scale with the increase in gas pressure. Instead, we find that β increases and there is a steep drop in the effective α-parameter to $\alpha = 0.02$, or $\approx 35\%$ of its pretransition value. The inability of the magnetic field to adjust and increase to maintain the higher α-parameter is most likely due to the outflow launched from the gas transitioning between the two cooling branches in the transition zone. This modifies the flow dynamics and disrupts the organization of the large-scale field.

Oddly enough, the same outflow that suppresses the dynamo in the inner disk produces a thin layer of enhanced magnetic field that envelopes the transition zone. This occurs as the outflowing gas stretches the magnetic field when it flows over the tapered disk body, which converts kinetic energy into magnetic energy. In addition to demonstrating a secondary pathway that can amplify field, this feature is interesting because of its observational prospects. In particular, it could appear as a quasiperiodic oscillation (QPO). QPO phenomenology is rich and complex, but generally low-frequency QPOs appear in the PSDs of hard-state BHB light curves as strong and narrow peaks whose central frequency can evolve with the black hole outburst. The magnetic dynamo has been suggested as a driver of this peculiar behavior (Begelman et al., 2015; O'Neill et al., 2011) and our results offer an extension to this model that may bolster its theoretical underpinnings. Specifically, the additional field strengthening occurs at the innermost part of the truncated disk, which is already the most luminous region of the disk. Given that this emission is quite localized, it will preferentially weight a small range of frequencies and could explain the high quality factors that are typically observed. Frequency evolution in the signal is naturally accounted for in this model because the QPO frequency is tied to the orbital and dynamo frequencies, and will therefore change as the secular changes in the mass accretion rate change the truncation radius of the disk.

Headway can be made in more accurately modeling the dynamics of truncated accretion disks by including a more realistic radiation prescription, which we have purposefully treated with a simple optically thin approximation. The accretion flow and transition zone behavior could be altered from the model analyzed here because

radiation pressure could modify the flow dynamics and the thermal transition could evolve differently. Our aim was to conduct a generalized investigation that is applicable to black holes across the mass scale. Uniquely targeting truncated accretion disks in either outbursting stellar mass black holes in the hard-state or LLAGNs requires accounting for the detailed thermodynamics, which are quite different between the two regimes. The ability of the radiation field to impart momentum to the gas and help launch an outflow (Proga, 2000) is likely to be a significant contributor to the thermal acceleration we find here. In AGNs, line driving could also lead to truncation (Laor & Davis, 2014) and iron opacity may be important to the disk structure (Jiang et al., 2016).

4.5 Conclusions

We investigate the dynamics of a truncated accretion disk around a black hole using a well-resolved, semi-global MHD model. An *ad hoc* bistable cooling function is implemented to mimic the radiative transitions thought to be responsible for the distinct spectral states in stellar mass and supermassive black hole systems. This cooling function produces a truncated accretion disk where the outer disk cools efficiently and resembles the standard Shakura & Sunyaev thin disk. Within the truncation the gas is hot and diffuse, and the disk thickens. Between these two regions lies a "transition zone" from $r = 130 - 200\, r_g$ where the cool, Keplerian gas disk tapers into the hot flow. A thermally driven outflow is launched from this region, slightly depleting the accretion flow. As the outflow buoyantly rises along

the disk body, we find it amplifies the magnetic field on the edge of the main disk body. The turbulent intensity ($\overline{\delta}$) is boosted in the transition zone as a result of the transitioning gas and the increase in the Maxwell stress from the outflow; in stark contrast to the inner disk where $\overline{\delta}$ is at a minimum. In addition to the gas temperature and density, we find that the inner accretion flow of the truncated disk is differentiated from the outer cool disk in other ways as well. In particular, the magnetic dynamo is suppressed and the effective α-parameter is greatly diminished. Despite these changes between the inner and outer disk, hot gas is able to efficiently accrete throughout the duration of the simulation. We do not find that the accretion is inhibited by the presence of the truncation, with the exception of a slight siphoning of gas by the outflow. The accretion rate through the inner simulation domain is essentially set by the feeding from the outer disk with the truncated region filling the role of an intermediary between the outer Shakura & Sunyaev-like thin disk and the black hole.

Two aspects of the simulation are worth highlighting because they are pertinent to the interpretation of spectra from systems with a truncated accretion disk: the effectiveness of the hot phase gas to fill the volume of the coronal regions above the cold, thin disk and the influence of turbulent fluctuations in introducing a radial taper. In this simulation, the upper atmosphere of the disk is full of hot, radiatively inefficient gas and the density is greater because of the mass loaded outflow. A large effort has gone into constraining the coronal geometry empirically and models typically assume the hot gas lies within the truncation. Our results, in conjunction with prior studies, suggest it may not be the case that hot gas is only confined to

a spherical region with a size set by the truncation radius. A configuration where the hot gas freely fills the volume around the black hole above and below the cold, thin disk may be more realistic. Additionally, consensus has been reached that MRI driven turbulence is the chief mediator of the angular momentum transport and disk heating. Incorporating the modification of the truncation from a sharp interface to a more gradual radial dependence with a vertical temperature stratification because of the turbulent fluctuations may lead to more accurate measurements of truncation radii in these systems. Since the truncation zone accounts for an appreciable portion of the disk, it is unclear where iron reflection measurements would place the truncation edge in such a system. Adding sophistication to a well-resolved, long-duration, global MHD truncated accretion disk model by including more accurate radiative physics will help alleviate outstanding uncertainty and advance the understanding of the dynamics of truncated accretion disks.

Chapter 5: Towards A More Complete Understanding Of The Large-scale Magnetic Dynamo

5.1 Introduction

The vigorous MRI-driven turbulence and shear expected in an accretion disk provide conditions that make it prime territory for the development of a magnetic dynamo (Tout & Pringle, 1992). Indeed, the self-organization of the magnetic field on large-scales has been universally observed in simulations of moderately mangetized, thin accretion disks. Despite the ubiquity with which dynamo behavior develops, the phenomenon remains an enigma and much of the fundamental theory behind its global growth remains undeveloped.

The large-scale dynamo often presents itself in simulations as a quasiperiodic reversal of the azimuthal field polarity. Bundles of field rise as the overmagnetized regions feel a buoyant force, and spacetime diagrams show a characteristic "butterfly pattern," akin to that observed in the migration of sunspots on the Sun. This behavior is often interpreted as the evolution of the mean field within the framework of the $\alpha\Omega$ dynamo model, which has two ingredients. First is the α effect which is sourced in the induction of azimuthal field from the movement of radial and the

vertical magnetic field in a helical fluid flow (Krause & Raedler, 1980). This acts to generate large-scale field from small-scale turbulent motions. Second is the Ω effect which arises through differential rotation and grows azimuthal magnetic field back from radial and vertical fields. This seeds the MRI from the large-scale field and further sustains turbulence allowing the cycle to continue. For the sake of clarity, we denote the α effect parameter as α_d henceforth to prevent confusion with the effective Shakura & Sunyaev α-parameter.

Shearing box simulations have been instrumental in allowing for the detailed exploration of the relation between the accretion flow and large-scale magnetic field, thus enabling the assembly of many of the pieces in the dynamo puzzle. Early simulations demonstrated the sensitivity of the magnetic stresses to the net field spanning the domain (Hawley et al., 1995; Pessah et al., 2007; Sano et al., 2004) and that large-scale magnetic cycles with periods of roughly ten times the orbital period readily develop (Brandenburg et al., 1995; Davis et al., 2010; Guan & Gammie, 2011; Lesur & Ogilvie, 2008; Oishi & Mac Low, 2011). Considering only a local patch of an accretion disk allows for the rigorous investigation of the structure of the turbulence, including its spectral properties (Gogichaishvili et al., 2017; Murphy & Pessah, 2015) and saturation (Bodo et al., 2008; Latter et al., 2009; Obergaulinger et al., 2009; Pessah, 2010; Pessah & Goodman, 2009), which is important because the large-scale field grows from turbulent fluctuations.

Ultimately, though, the disk dynamo is a global phenomenon which requires models with large domains that properly account for the vertical and radial gradients in the accretion flow, as well as the coupling of radii with different evolutionary

times. Like their local counterparts, global models find dynamo periods of $10-20\times$ the local orbital period (e.g. Beckwith et al., 2011; Flock et al., 2012; Hawley et al., 2013; Hogg & Reynolds, 2016; O'Neill et al., 2011; Parkin & Bicknell, 2013). These simulations are thin disks with typical thermal scaleheight ratios of $h/r = 0.07-0.1$. They find that the dynamo coherently spans roughly $\Delta r = 10 r_g$ in radius, modulates the accretion disk stresses, and collects into sheets of azimuthal magnetic field of the same orientation in the coronal region.

In this chapter, we aim to understand how the timing properties of the dynamo and large-scale magnetic field evolution depend on accretion disk geometry, i.e. the disk scaleheight ratio, and if there is a threshold of either large or small thickness beyond which the large-scale dynamo cannot be excited. Exploring this is crucial because dynamos have been directly invoked to explain time variability signatures from accreting black holes (King et al., 2004; Mayer & Pringle, 2006), as well as in several peripheral contexts. Examples include dynamo cycles as a source of the low-frequency quasi-periodic oscillation (QPO O'Neill et al., 2011), the driver of "propagating fluctuations" in mass accretion rate (Chapter 2), and as the trigger behind the secular evolution in the spectral state transitions (Begelman et al., 2015).

Furthermore, while numerical simulations have established the robustness of the dynamo in a standard thin accretion disk, several cases have been found where the well-ordered oscillations are altered or vanish in atypical disk conditions. For instance, using global simulations of a super-Eddington accretion flow, Jiang et al. (2014) found that the dynamo period is regular, but slower. The dynamo can be quenched in a magnetically dominated disk (Bai & Stone, 2013; Salvesen et al.,

2016) or if hydrodynamic convection acts to mix the field (Coleman et al., 2017). Additionally, the transition in the flow geometry of a truncated disk and its associated flow dynamics has been shown to impede the dynamo and lead to a sporadic, intermittent oscillation of the large-scale magnetic field in the inner hot disk (Chapter 2). Of course, a lingering concern is always that simulations are affected by nonphysical sensitivities like resolution and domain aspect ratios, which have also been shown to halt the dynamo (Walker & Boldyrev, 2017).

To delve into the scaleheight dependence of the magnetic dynamo, we constructed a suite of global, MHD disk models with varying scaleheight ratios. In Section 5.2 we describe the numerical simulation of these models including the code details, initial conditions, and resolution properties. In Section 5.3 we present an analysis of the large-scale dynamo properties, measure $\alpha_{\rm d}$ values for each simulation, briefly look at the evolution of the large-scale helicity in one of our simulations, and discuss potential observational characteristics of each simulation. We discuss our results and their broader implications in Section 5.5 and provide closing remarks in Section 5.6.

5.2 Numerical Model

In this chapter we consider four well-resolved MHD simulations of model accretion disks in a pseudo-Newtonian potential, Equation 5.5, with scaleheight ratios: $h/r = \{0.05, 0.1, 0.2, 0.4\}$. The goal of this chapter is to use these simulations to understand how the accretion disk geometry affects the properties of the large scale

magnetic field. Hence, we strive for consistency in our models and to evolve the models for long enough to fully sample the global dynamo for several cycles. To this end, these simulations were initialized with the same initial conditions and each were allowed for evolve for $t \approx 4 \times 10^4\, GM/c^3$, or roughly 650 ISCO orbits.

5.2.1 Simulation Code

This work uses the second-order accurate PLUTO *v4.2* code (Mignone et al., 2007) to solve the equations of ideal MHD,

$$\frac{\partial \rho}{\partial t} + \nabla \cdot (\rho \mathbf{v}) = 0, \tag{5.1}$$

$$\frac{\partial}{\partial t}(\rho \mathbf{v}) + \nabla \cdot (\rho \mathbf{v}\mathbf{v} - \mathbf{B}\mathbf{B} + \mathbf{P}\mathcal{I}) = -\rho \nabla \Phi, \tag{5.2}$$

$$\frac{\partial}{\partial t}(E + \rho\Phi) + \nabla \cdot [(E + P + \rho\Phi)\mathbf{v} - \mathbf{B}(\mathbf{v} \cdot \mathbf{B})] = -\Lambda, \tag{5.3}$$

$$\frac{\partial \mathbf{B}}{\partial t} = \nabla \times (\mathbf{v} \times \mathbf{B}),$$

where ρ is the gas density, $\mathbf{v}$ is the fluid velocity, P is the gas pressure, $\boldsymbol{B}$ is the magnetic field, $\mathcal{I}$ is the unit rank-two tensor, E is the total energy density of the fluid,

$$E = u + \frac{1}{2}\rho |\mathbf{v}|^2 + \frac{\mathbf{B^2}}{2}, \tag{5.4}$$

and Λ accounts for radiative losses through cooling. All fluid variables (e.g. ρ, P, T) are evolved and reported in a scale-free, normalized form. The `hlld` Riemann solver was used to solve the MHD equations in the dimensionally unsplit mode. Linear reconstruction is used in space and the second-order Runge Kutta algorithm is used to integrate forward in time. To enforce the $\nabla \cdot \mathbf{B} = 0$ condition, the method of constrained transport is used.

5.2.2 Simulation Setups

To remain as consistent as possible between models, the simulation grids are designed under the following strategy. Each model is set in spherical coordinates with $\theta \in [\pi/2 - 5h/r, \pi/2 + 5h/r]$. As we vary the scaleheight ratio, we keep the number of grid cells in this direction ($N_\theta = 248$) the same. Uniform grid spacing is used within $\pm 3\, h/r$ around the disk midplane with 28 zones per scaleheight. A stretched grid is used beyond $3h/r$ with 40 zones in each of the coronal regions where there is less small scale structure. The only exception being the thickest $h/r = 0.4$ disk, which we only model with $\theta \in [\pi/2 - 2.5\, h/r, \pi/2 + 2.5\, h/r]$ and halve the grid cells, accordingly. The radial range stays the same between models ($r \in [5r_g, 145r_g]$) and is divided into an inner well resolved region used for the analysis ($r \in [5r_g, 45r_g]$) and an outer less resolved region ($r \in (45\ r_g, 145\ r_g]$) that acts as a gas reservoir to mitigate artificial effects from draining of the disk material that could introduce secular changes in the accretion flows. Logarithmic spacing is used to keep $\Delta r/r$ constant along the grid. The azimuthal ($\phi \in [0, \pi/3]$) domain is also fixed between models and has uniform spacing in ϕ. When varying the scaleheight ratio by factors of 2 between models, we change the number of radial and azimuthal grid zones to preserve the cell aspect ratio ($\Delta r : \Delta r \sin\theta \Delta\theta : r\Delta\phi \approx 1 : 1 : 2$). This helps remove any resolution dependencies that could influence the results and adjusts the integration timestep, which is set by the Courant condition. The validity of restricting the ϕ-domain to $\phi \in [0, \pi/3]$ between our models rather than adjusting it in a similar manner to that used in the θ-domain is addressed in Section 5.4. The

Table 5.1: Simulation Parameters

Simulation	Total Duration	ISCO Orbits	N_r	N_θ	N_ϕ	$H/\Delta\theta$
`hr_005`	$3.58 \times 10^4\ GM/c^3$	581.5	1232	248	256	28
`hr_01`	$3.88 \times 10^4\ GM/c^3$	630.5	616	248	128	28
`hr_02`	$4.19 \times 10^4\ GM/c^3$	680	308	248	64	28
`hr_04`	$4.15 \times 10^4\ GM/c^3$	675.5	154	248	32	28

full details of the simulation grids are given in Table 5.1. Outflow is allowed through the r and θ boundaries while the ϕ boundaries are periodic. Density and pressure floors are imposed to prevent artificially low or negative values.

A psuedo-Newtonian potential of the form,

$$\Phi = -\frac{GM}{R - 2r_{\rm g}}, \qquad r_{\rm g} \equiv \frac{GM}{c^2} \tag{5.5}$$

is used to approximate the dynamics of a general relativistic flow around a non-rotating black hole. This captures features like the shear profile and the presence of an innermost stable circular orbit (ISCO) at $r = 6\,r_{\rm g}$ without the computational expense of fully including general relativity. A $\gamma = 5/3$ adiabatic equation of state is used for the gas; the internal energy density of the gas is hence given by $u = P/(\gamma - 1)$.

As the turbulence decays, it deposits energy in the gas in the form of heat so the disk would tend to become thicker. To enforce the target disk aspect ratio for each of the simulations, a Noble et al. (2009) style cooling function is used to emulate radiative losses. The local target gas pressure is set to,

$$P_{targ} = \frac{\rho v_{\rm K}^2 (h/r)^2}{\gamma}, \tag{5.6}$$

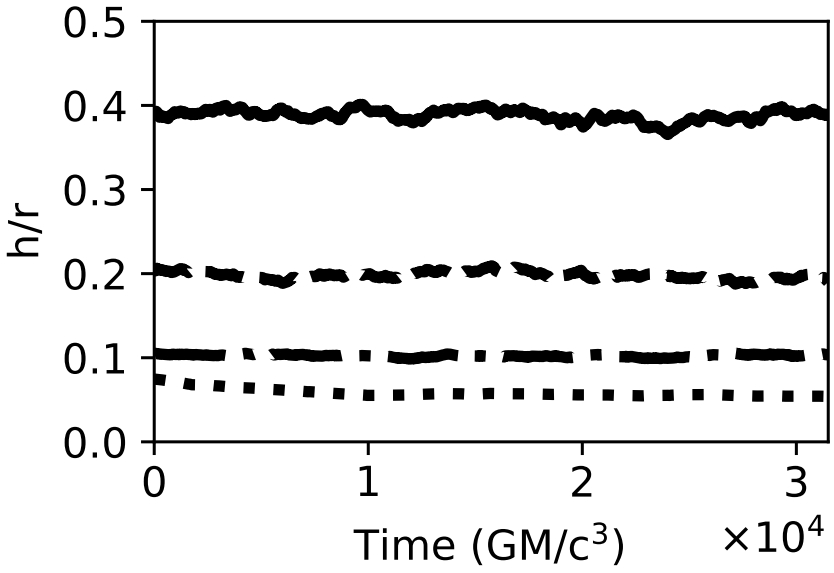

Figure 5.1: Time variability of disk scaleheight ratios for `hr_005` (dotted line), `hr_01` (dot-dash line), `hr_02` (dashed line), and `hr_04` (solid line).

where $v_{\rm K}$ is the local Keplerian velocity given by

$$v_{\rm K} = \frac{GM\sqrt{r}}{r - 2r_{\rm g}}. \tag{5.7}$$

The excess heat is cooled according to,

$$\Lambda = \frac{f(P - P_{targ})}{\tau_{cool}}, \tag{5.8}$$

where f is a switch function,$f = 0.5[(P - P_{targ})/|P - P_{targ}| + 1]$, and τ_{cool} is the cooling time which we set to the local orbital period.

The maintenance and stability of the target disk scaleheights is of paramount importance in our simulations so that we can clearly isolate any disk height dependences. Figure 5.1 shows the time variability in of average scaleheight ratio for the simulations. For each radial element in each data dump we calculate the geometric

scaleheight ratio

$$\frac{h(r)}{r} = \left\langle \sqrt{\frac{\int (\theta(r) - \bar{\theta}(r))^2 \rho d\Omega}{\int \rho d\Omega}} \right\rangle, \tag{5.9}$$

where $d\Omega = \sin\theta d\theta d\phi$ is the solid angle element in spherical coordinates and,

$$\bar{\theta}(r) = \frac{\int \theta(r) \rho d\Omega}{\int \rho d\Omega} \tag{5.10}$$

is the average polar angle of the gas. The total disk-averaged scaleheight is calculated for each instant by weighting every radial bin by its width to account for the nonuniform spacing of the grid in the r-coordinate. This shows the cooling function keeps our target scaleheight throughout the duration of each simulation. Turbulence introduces small fluctuations in the disk scaleheight ratio, but no worrisome trends are present in the `hr_01`, `hr_02`, and `hr_04` simulations. In the time trace of the `hr_005` simulation there is a residual transient from initialization artificially inflates the disk, but it decays quickly. It has no significant influence on our study, but does appear in synthetic light curves presented in Section 5.3.5 where we discuss it further.

5.2.3 Initial Conditions

The simulations are initialized to a steady-state α-disk like solution:

$$\rho(R, \theta) = \rho_0 R^{-3/2} \exp\left(- \frac{z^2}{2 c_s^2 R^3} \right) \tag{5.11}$$

where ρ_0 is a normalization, $R = r \sin\theta$ is the cylindrical radius, and $z = r\cos\theta$ is the vertical disk height. The gas pressure is set from the density, $P = c_s^2 \rho$. The velocity field is set such that the azimuthal velocity has the local Keplerian value (v_K) and $v_r = v_\theta = 0$.

We set a weak magnetic field ($\langle\beta\rangle = \langle P_{gas}/P_{mag}\rangle = 200$) from a vector potential to guarantee the divergence free condition is satisfied to machine level precision. The initial field configuration is set to be logarithmically spaced loops with a vertical taper function in the upper atmosphere with the form,

$$A_r = 0, \tag{5.12}$$

$$A_\theta = 0, \tag{5.13}$$

$$A_\phi = A_0 p^{\frac{1}{2}} e^{-(z/h)^4} R \sin\left(\frac{\pi \log(R/2)}{h}\right). \tag{5.14}$$

In the early evolution of each model, these field loops feel the radial shear of the disk and the gas is destabilized by the MRI, which goes nonlinear and drives turbulence.

5.2.4 Convergence

To assess the overall convergence and consistency between the models, we apply several resolvability and convergence metrics. The results of these diagnostics are presented in Table 5.2. All averages are taken over the portion of the simulations used the analysis and taken within the volume of the simulation domain contained within two scaleheights above and below the disk where the dynamo behavior originates.

The resolution of the grid in simulation zones per disk scaleheight provides the simplest measure of the resolvability. Several studies (e.g. Hawley et al., 2013; Sorathia et al., 2012) have shown around 30 vertical zones per disk scaleheight offers a crude threshold near where the turbulence is resolved well enough to capture the small-scale evolution, and hence motivated our grid design. We use the correspond-

ing "quality factors" to probe how well the simulation grid samples characteristic MRI wavelength, $\lambda_{MRI} = 2\pi v_A/\Omega$, where v_A is the Alfvén speed. For each simulation, we calculate the average quality factor in the θ and ϕ directions,

$$Q_\theta = \frac{\lambda_{MRI,\theta}}{R\Delta\theta} \tag{5.15}$$

and

$$Q_\phi = \frac{\lambda_{MRI,\phi}}{R\Delta\phi}. \tag{5.16}$$

Values of $Q_\theta > 6 - 8$ have been shown to properly capture the linear growth of the MRI (Flock et al., 2010; Hawley & Stone, 1995; Sano et al., 2004) and a stricter threshold of $Q_\theta > 10$ and $Q_\phi > 20$ (Hawley et al., 2011, 2013; Sorathia et al., 2012) has been established as adequate to capture the nonlinear growth of the instability. Finally, we measure the saturation of the anisotropic MRI driven turbulence through the average in-plane magnetic tilt angle,

$$\Theta_B = -\arctan\left(\left\langle \frac{B_r}{B_\phi} \right\rangle\right). \tag{5.17}$$

This quantifies the characteristic orientation of the magnetic field, a value that theoretical estimates predict to be near $\Theta_B \approx 15^\circ$ (Guan et al., 2009; Pessah, 2010). Measurements in prior accretion disk simulations (e.g. Hawley et al., 2011, 2013; Hogg & Reynolds, 2016; Sorathia et al., 2012) find the turbulence saturates at a somewhat lower tilt of $\Theta_B \approx 11 - 13^\circ$.

By all measures, our models are well-resolved and have similar properties, with the exception of the `hr_04` model. Given the remarkable consistency of the other models, it is difficult to attribute the sudden decrease in the quality factors,

Table 5.2: Resolution Diagnostics

Simulation	$\langle Q_\theta \rangle$	$\langle Q_\phi \rangle$	$\langle \Theta_B \rangle$	$\langle \alpha_{SS} \rangle$	$\langle \beta \rangle$
`hr_005`	15.9	37.7	12.3	0.065	9.1
`hr_01`	11.8	30.1	12.4	0.057	10.1
`hr_02`	11.9	28.7	12.4	0.052	10.4
`hr_04`	5.7	16.6	11.8	0.026	11.8

effective α-parameter, and increase in plasma β to the changes in the grid, although we are simulating half of the physical domain (i.e. only $\pm 2.5\, h/r$). One clue into the discrepancy is that the inconsistent diagnostics all depend on the strength of the magnetic field, which appears to be lower by roughly half compared to the thermal energy. The Θ_B value, on the other had, is similar to the other three models, suggesting the saturation of the turbulence is the same, but the field doesn't naturally grow to the same relative level. A key result of this chapter is that the organization of the dynamo in the thicker disks is impeded and less efficient, so the resolution metrics could be biased by this phenomenon. Nevertheless, when interpreting the following results, it is important to remain aware of what could be a decrease in the effective resolution of the `hr_04` model.

5.3 Results

The analysis we conduct is restricted to the final $\Delta t = 3.15 \times 10^4\, GM/c^3$ (512 ISCO orbits) of each simulation. By allowing the simulations to evolve for at least 100 ISCO orbits, we avoid transient nonphysical behaviors that only exist as the simulated disks relax into a quasisteady state. The simulation data is written out every $\Delta t = 30.7812 GM/c^3$, or every half of an orbital period at the ISCO, providing

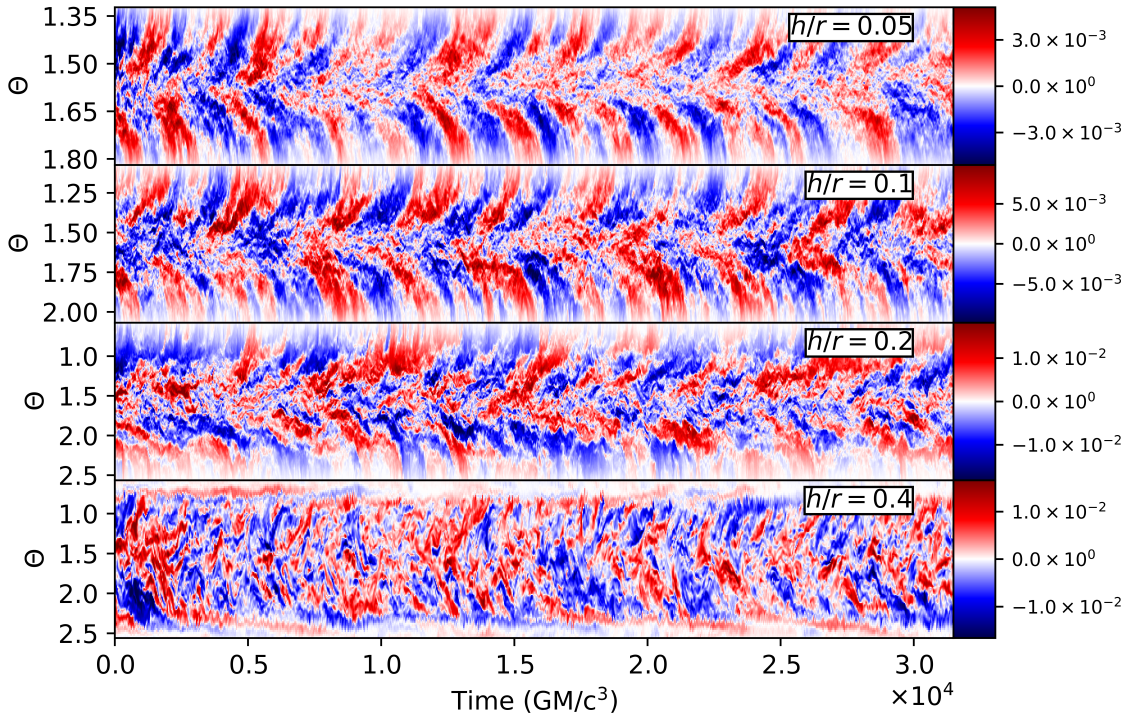

Figure 5.2: Spacetime diagrams of the azimuthally averaged B_ϕ at $r = 15\,r_g$ for `hr_005`(top), `hr_01` (second from top), `hr_02` (second from bottom), and `hr_04` (bottom). Positive values (red) indicate orientation of the field in the positive ϕ-direction while negative (blue) indicates an opposite orientation. Color intensity corresponds to the averaged magnitude.

1024 snapshots for the analysis.

5.3.1 The Global Dynamo

We begin by first presenting spacetime diagrams of the toroidal magnetic field in Figure 5.2. The spacetime diagrams were calculated by taking azimuthal averages of B_ϕ at each time step at $r = 15\,r_g$ in each of our four simulations. The large-scale dynamo organizes itself into global, vertically stratified sheets of field of similar polarity. These diagrams effectively trace the evolution of the cross section of this

pattern at a chosen radii, which typically reveals a vertically propagating pattern that has a characteristic acceleration, evidenced by the increasing slope. Snapshots of the normal pattern's structure are shwon in Figure 2.9.

The different behaviors between the models are immediately apparent with the most striking difference being the breakdown of the regular, periodic oscillation pattern with increasing disk thickness. The thinnest disk in the `hr_005` model shows a cyclical building of the field and decay with a reversal of the orientation. Near the midplane it is fairly stochastic, but in the atmosphere the organization develops as the overmagnetized regions buoyantly rise. In the `hr_01` model, a pattern is still present, but it is less well organized compared to the `hr_005` simulation. In `hr_02` and `hr_04` there are hints the organized oscillations attempt to develop, but patchy, chaotic fluctuations dominate the behavior. However, there is still field amplification and regeneration of the field throughout the simulation, despite the lack of a regular, ordered pattern.

Further inspection of the `hr_005` and `hr_01` models reveal other interesting features of the butterfly pattern. There are periods of the simulation where the dynamo seemingly fails to reverse, for instance $t = 1.5 \times 10^4\, GM/c^3$ and $t = 1.7 \times 10^4\, GM/c^3$ in `hr_005`. Additionally, the large-scale field generated by the dynamo can evolve independently in the upper and lower coronal regions of each disk. At some points in the simulations the magnetic fields are aligned in the upper atmospheres, like at $t = 6.0 \times 10^3 GM/c^3$ in the `hr_005` simulation, but then at a later time the fields are antialigned, like $t = 2.1 \times 10^4 GM/c^3$. This is the same change in parity observed in Flock et al. (2012). Several factors contribute to this, including irregularities in

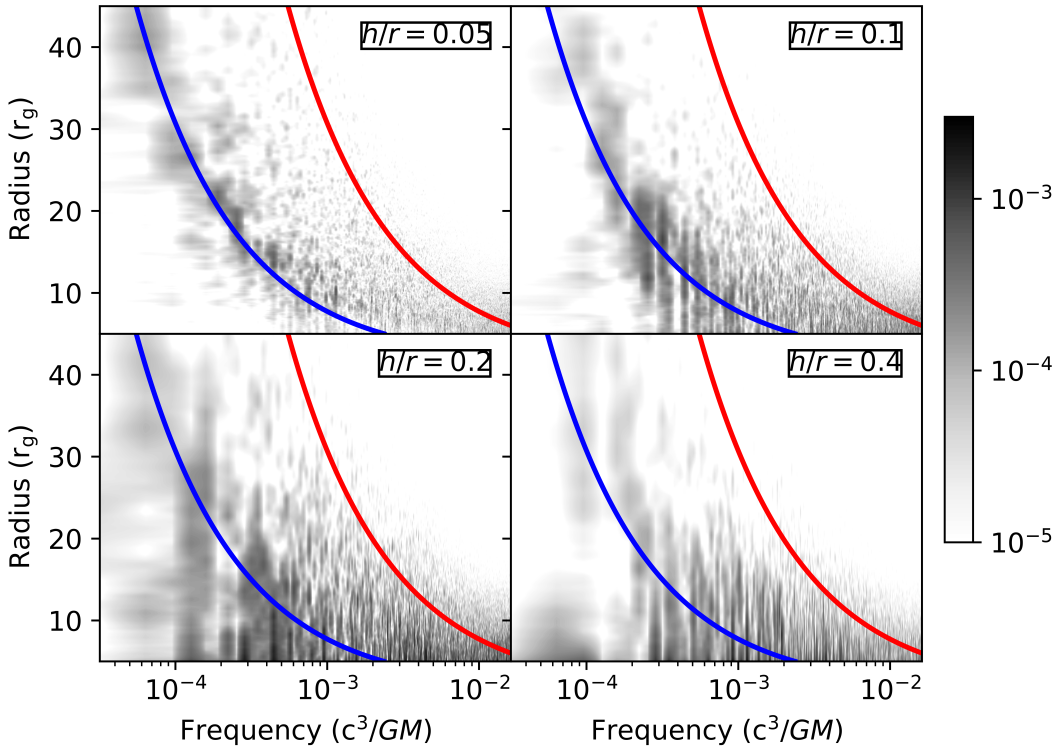

Figure 5.3: PSDs of B_ϕ at $1.5h$ above the disk midplane for `hr_005` (top left), `hr_01` (top right), `hr_02` (bottom left), and `hr_04` (bottom right). Darker colors (black) represents greater power in that frequency bin for a given radius. The orbital frequency is shown with the red line and one tenth the orbital frequency is shown with the blue line.

the local evolution of the dynamo cycle and a global influence from the coupling of field since the field buoyantly rises as coronal sheets of field with similar polarity (Beckwith et al., 2011; Hogg & Reynolds, 2016). These butterfly diagrams can be compared to those observed from local shearing box simulations, e.g. Davis et al. (2010) and Simon et al. (2012), which tend to have more more regular periods.

Turning to the thicker disks in the `hr_02` and `hr_04` models, we see the amplification of the field is typically localized. Enhanced regions of strong field form, but they are disrupted before they can collect in the midplane. In both of these simulations we see that even though the pockets of strengthened field do not trace out a butterfly pattern *per se*, they still typically originate near the midplane and are expelled into the disk atmosphere, presumably due to their magnetic buoyancy like before. In the `hr_02` model, there are periods when the butterfly pattern almost takes hold, but it often only in one hemisphere and then traces out an inconsistent rise.

The power spectral density (PSD) at one scaleheight above the disk midpane, shown in Figure 5.3, more clearly show the presence or absence of periodicity in the dynamo. The PSDs were calculated as $P(\nu) = \nu|\widetilde{f}(\nu)|^2$ where $\widetilde{f}(\nu)$ is the Fourier transform of the time sequence of the variable of interest,

$$\widetilde{f}(\nu) = \int f(t) e^{-2\pi i \nu t} dt. \tag{5.18}$$

Here, we consider the power spectra of the azimuthally averaged B_ϕ at each radial grid point. We also average B_ϕ over the θ direction from $\pi/2 - 1.25\, h/r$ to $\pi/2 - 0.75\, h/r$ to get a better sense of the dominating mean field.

The `hr_005` and `hr_01` simulations show a distinct band of power at one tenth of the orbital frequency. This band of enhanced power spans roughly a factor of three in frequency space and extends radially approximately $10\,r_g$, consistent with the PSDs seen in thin accretion simulations, like those presented in O'Neill et al. (2011) and Figure 2.10. At lower frequencies there is very little power and at higher frequencies there is residual power up to a dissipative scale.

The power spectra of the `hr_02` and `hr_04` simulations tell a different story, though. In these simulations there are no discernible bands of power indicating they lack any unique timescales where the field has significant oscillations. There is power at all frequencies below the orbital frequency, indicating the large-scale dynamo is operating; however, it is neither organized nor confined to a specific timescale. This confirms the seeming randomness and disorder seen in the respective butterfly diagrams, suggesting there is no single characteristic scale on which energy is injected, rather the disorder allows the flow to inject energy over a range of scales, which then decay.

5.3.2 Measuring $\alpha_{\rm d}$

Next, we seek to probe the heart of the dynamo mechanism by measuring the parameterization of the "α-effect." The large-scale dynamo is typically interpreted through a mean field theory. To produce the large scale toroidal field, there must be a net electromagnetic force (EMF) to induce a magnetic field in the azimuthal

direction, which is predominately governed by:

$$\langle \mathcal{E}'_{\phi} \rangle = \alpha_{d,\phi\phi} \langle B_{\phi} \rangle. \tag{5.19}$$

Like other works (e.g. the local shearing box simulations of Brandenburg et al. (1995), Brandenburg & Donner (1997), Ziegler & Rüdiger (2001), and Davis et al. (2010) and global disk model of Flock et al. (2012)), we neglect contributions to the α effect from the less influential $\alpha_{d,rr}$ component and also higher order derivatives of the magnetic field from the diffusivity tensor (usually denoted as $\tilde{\eta}$), thereby allowing us to approximate $\alpha_{\phi\phi}$ through a simple correlation between the turbulent EMF,

$$\mathcal{E}'_{\phi} = v'_r B'_{\theta} - v'_{\theta} B'_r, \tag{5.20}$$

where X' of a flow variable X indicates its fluctuating component taken by subtracting off its azimuthal average ($X' = X - \langle X \rangle$), and the average toroidal magnetic field.

We calculate the volume averaged $\mathcal{E}'_{\phi}$ and B_{ϕ} in the upper and lower hemispheres of each simulation for each data dump. The regions in which we take these averages spans the entire azimuthal domain, radially from $r = 15\ r_g$ to $r = 15 + 15(h/r)$, and poloidally from h to $2h$ in the upper hemisphere and $-h$ to $-2h$ in the lower hemisphere. The correlation of $\langle \mathcal{E}'_{\phi} \rangle$ and $\langle B_{\phi} \rangle$ is then measured by fitting a simple line of the form,

$$\langle \mathcal{E}'_{\phi} \rangle = \alpha_d \langle B_{\phi} \rangle + C, \tag{5.21}$$

where C is an allowed vertical offset. The fitting was done using a Bayesian MCMC method. Figure 5.4 shows the data, best fit, and parameter contour plots of the fit

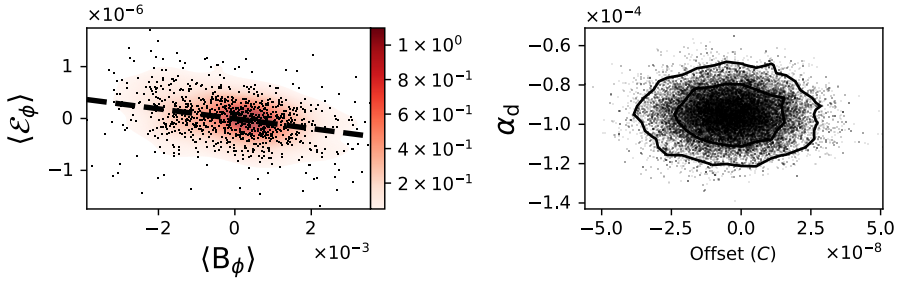

(a) Upper Hemisphere `hr_005`

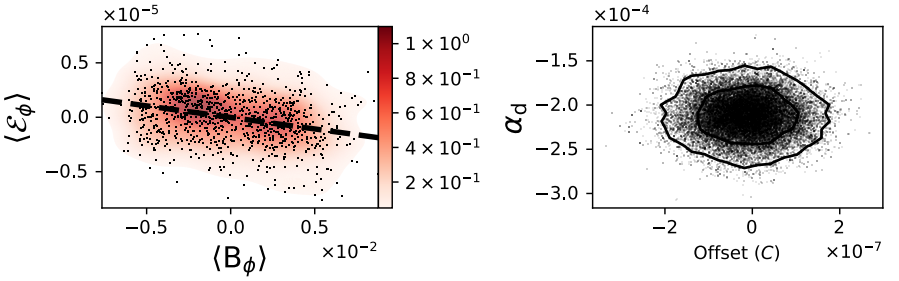

(b) Upper Hemisphere `hr_01`

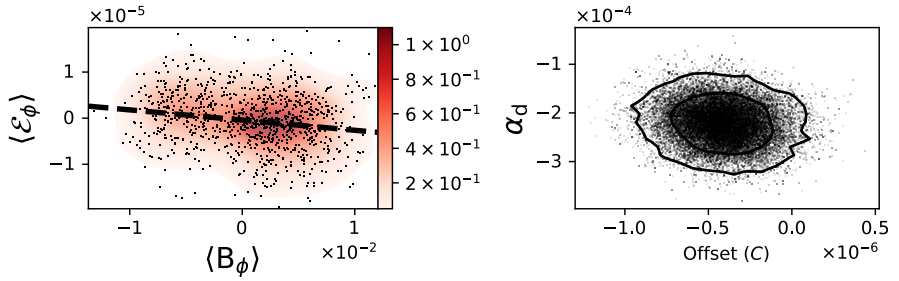

(c) Upper Hemisphere `hr_02`

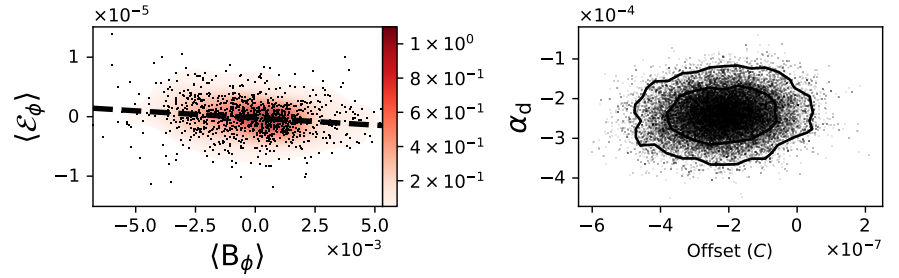

(d) Upper Hemisphere `hr_04`

Figure 5.4: Scatter plots of instantaneous values of $\langle B_\phi \rangle$ vs $\langle \mathcal{E}'_\phi \rangle$ in the upper coronal regions of the disks (black dots) with the best fitted lines (left column) and the best parameter fits from our MCMC modeling with 1σ and 2σ contours (right column). The color coding in the lefthand panels shows the density distribution of the points, estimated from a Gaussian kernel.

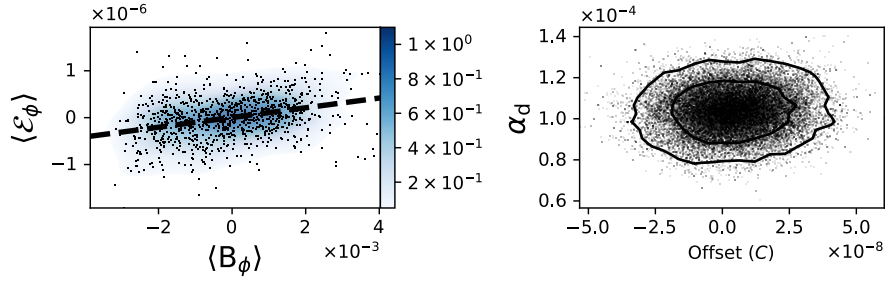

(a) Lower Hemisphere `hr_005`

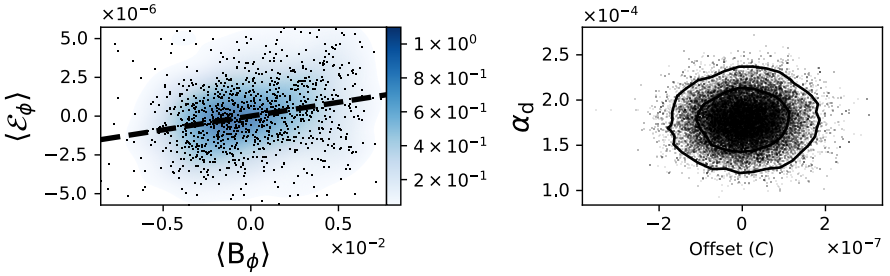

(b) Lower Hemisphere `hr_01`

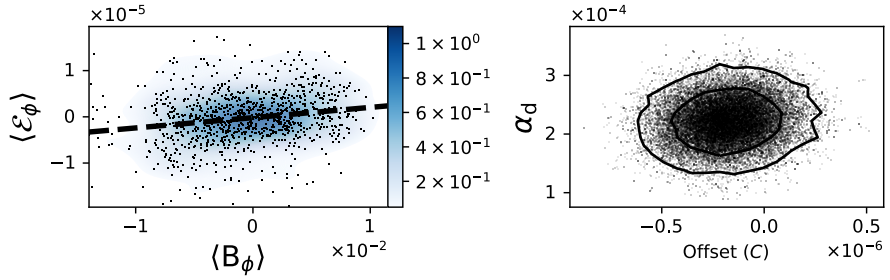

(c) Lower Hemisphere `hr_02`

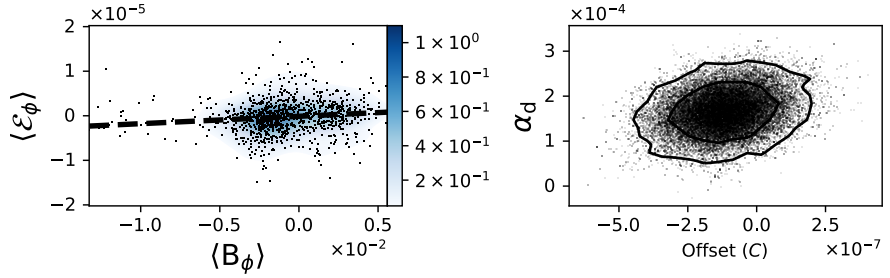

(d) Lower Hemisphere `hr_04`

Figure 5.5: Scatter plots of instantaneous values of $\langle B_\phi \rangle$ vs $\langle \mathcal{E}'_\phi \rangle$ in the lower coronal regions of the disks (black dots) with the best fitted lines (left column) and the best parameter fits from our MCMC modeling with 1σ and 2σ contours (right column). The color coding in the lefthand panels shows the density distribution of the points, estimated from a Gaussian kernel.

Table 5.3: Upper Hemisphere Dynamo Coefficient Fits

Simulation	$\alpha_{d,uh}$	Offset_{uh}
`hr_005`	$(-9.5 \pm 0.1) \times 10^{-5}$	$(-0.4 \pm 1.2) \times 10^{-8}$
`hr_01`	$(-2.1 \pm 0.2) \times 10^{-4}$	$(-1 \pm 7) \times 10^{-8}$
`hr_02`	$(-2.2 \pm 0.4) \times 10^{-4}$	$(-4 \pm 2) \times 10^{-7}$
`hr_04`	$(-2.3 \pm 0.5) \times 10^{-4}$	$(-2.1 \pm 1.0) \times 10^{-7}$

parameters for the upper hemisphere of the different models, and Figure 5.5 shows the corresponding results for the lower hemispheres. Tables 5.3 and 5.4 summarize the best fits.

We find that α_d consistently has an amplitude of $|\alpha_d| \approx 1 - 2 \times 10^{-4}$ in all of these disk simulations with the upper hemisphere having a negative sign and the lower hemisphere having a positive sign, similar to Brandenburg et al. (1995) and Davis et al. (2010), but different than other works. Furthermore, they are a slightly weaker than other values reported in the literature. The increase in the scatter of the $\langle \mathcal{E}'_\phi \rangle$ and $\langle B_\phi \rangle$ correlations with increased disk thickness indicates the diffusive term becomes a larger contributor.

5.3.3 Magnetic Helicity

As an exploratory exercise to bore into the organization, or lack thereof, in the dynamo pattern, we sought to measure the large- and small-scale magnetic helicities,

Table 5.4: Lower Hemisphere Dynamo Coefficient Fits

Simulation	$\alpha_{d,lh}$	Offset_{lh}
`hr_005`	$(1.0 \pm 0.1) \times 10^{-4}$	$(0.4 \pm 1.5) \times 10^{-8}$
`hr_01`	$(1.7 \pm 0.2) \times 10^{-4}$	$(-1 \pm 7) \times 10^{-8}$
`hr_02`	$(2.2 \pm 0.4) \times 10^{-4}$	$(-1.9 \pm 1.8) \times 10^{-7}$
`hr_04`	$(1.7 \pm 0.4) \times 10^{-4}$	$(-1.5 \pm 1.2) \times 10^{-7}$

current helicities, and kinetic helicities in the four simulations. Teasing out the time variability of these quantities from the chaotic turbulence ultimately proved not to be feasible with these models, and we were not able to overcome the inherent noise from differencing the stochastically fluctuating fluid variables. However, we were able to find a correlation between the large-scale magnetic helicity

$$\mathcal{H}_m = \langle \bar{\mathbf{A}} \cdot \bar{\mathbf{B}} \rangle \tag{5.22}$$

with the average $\langle B_\phi \rangle$ in the midplane of the `hr_005` simulation, shown in Figure 5.6. Since the large-scale helicity is a volume integrated quantity, it was calculated in a subdomain of the global simulation. We chose a reference radius, $r_{ref} = 15\, r_g$, and then defined the subdomain to span radially from r_{ref} to $r_{ref}(1+h/r)$, vertically from the midplane ($\theta = \pi/2$) to one disk scaleheight ($\theta = \pi/2 - h/r$), and in azimuth over the entire ϕ-domain. The subdomain was designed this way for several reasons. The radial location was selected to be far enough from the ISCO that turbulent

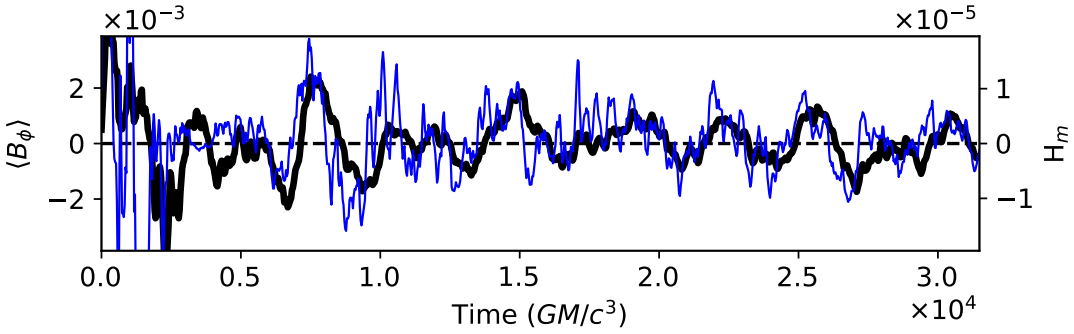

Figure 5.6: Average B_ϕ (dark black line) and $\mathcal{H}_m$ (thin blue line) for `hr_005` at $r = 15\,r_g$. The two time traces have a Pearson-r statistic of 0.4.

edge effects (Krolik & Hawley, 2002) are miniscule. Moving away from the inner boundary also has the additional benefit that the dynamo period is longer, so our effective time resolution is increased by approximately a factor of 4, but it is still short enough we can still study the behavior for many evolutionary times. We are primarily interested in where the dynamo pattern originates and first organizes itself, which drives us to the midplane of the disk. However, since the helicity production is roughly asymmetric about the midplane (Blackman, 2012), we must only sample one hemisphere so that there is not cancelation, and we choose the upper hemisphere by default. We tested several vertical extents and determined that the general trends held no matter where we placed the upper vertical boundary of the subdomain within one disk scaleheight above the midplane, but the noise was minimized at the upper limit.

Typically, $\mathcal{H}_m$ evolves with $\langle B_\phi \rangle$. When $\langle B_\phi \rangle$ oscillates and changes sign, $\mathcal{H}_m$ seems to vary with it. There are periods when the cycle seems to stall, like from

$t = 1.0 \times 10^4\, GM/c^3$ to $t = 1.3 \times 10^4\, GM/c^3$, where $\mathcal{H}_m$ similarly shows no real evolution. This is either because the helicity is not produced or because there is no *net* production due global effects like cancelation with neighboring radii. Noise dominates much of the signal, but the linear correlation of $\mathcal{H}_m$ and $\langle B_\phi \rangle$, as measured with the Pearson-r statistic, is $r = 0.38$ which indicated a moderate correlation. Over different periods of the simulation it changes, though. For instance, if the correlation coefficient is only calculated over the last half of the simulation, it is higher at $r = 0.58$.

This hint that the large-scale magnetic helicity is tied to the organization of the dynamo should help motivate further study of the role that the flow helicity plays in regulating the global dynamo in future investigations. There is a wealth of literature showing a connection between the dynamo and its quenching to the flow helicity from analytic studies (Blackman & Brandenburg, 2002; Brandenburg & Subramanian, 2005; Vishniac & Cho, 2001). Explaining the large-scale accretion disk dynamo through this lens offers great prospect and could yield a greater understanding of the global disk evolution. Of particular interest is how the helicity produced at different radii, and consequently on different timescales, interacts. Unlike the magnetic field which decays through turbulence to larger wave numbers, the magnetic helicity undergoes an inverse cascade and relaxes to smaller wave numbers, which could effectively couple radii as the helicities add or cancel, depending on the interference of the production patterns. Unraveling these connections may explain some of the radial coherence, as well as the intermittencies and irregularities observed in global dynamos.

5.3.4 Mass Accretion Rates

Having seen the role of organization on the magnetic field, we can begin to ask how it effects the disk evolution. One of the clearest ways to detect the dynamo influence is in the mass accretion rate

$$\dot{M} = \int \rho v_R R \sin(\theta) d\phi d\theta, \tag{5.23}$$

where we take R to be the inner simulation boundary, calculated from the instantaneous values of density and velocity for each data dump. In Chapter 2 we showed that the large-scale dynamo drove propagating fluctuations which appear as a telling log-normal distribution in the large-scale accretion rate due to the modulation of the effective disk viscosity. Figure 5.7 shows the histograms of $\dot{M}$ for each of the models. Note, that in the `hr_005` model, there is a residual transient in $\dot{M}$ from the initialization so the first 100 orbits of the analysis which has been removed to prevent contamination of the histogram. In all four of our models the histograms have a characteristic skewed distribution. We fit both normal

$$P(x)_N = P_0 e^{-(x-\mu)^2/2\sigma^2} \tag{5.24}$$

and log-normal,

$$P(x)_{LN} = \frac{P_0}{x} e^{-(lnx-\mu)^2/2\sigma^2} \tag{5.25}$$

functions to the $\dot{M}$ distributions, where x is the data count rate in each bin, σ is the distribution width, and μ is the peak. In every case they are better fit by the fast rise and slow decay in the high valued tail of the log-normal distribution. The normal distributions fail to match the shapes of the distributions at high and low

$\dot{M}$ and consistently are shifted to the right of the peak in the distribution. As a reminder, the simulations are evolved in a scale free form and the amplitude of the mass accretion rate is largely set by the density in the model. We are primarily interested in the consistent qualitative behavior here, since all of the models are initialized with the same density normalization. This means the integrated "mass" of the disk is larger with increasing scaleheight, which, when coupled with the shorter evolutionary timescales and shorter accretion timescales, should give higher $\dot{M}$ with progressively larger scaleheights.

5.3.5 Observational Signatures

On their own, the distinct dynamo behaviors we find are interesting, but greater physical meaning can be found by connecting the unique manifestations to observables. The rich photometric variability seen from accreting black holes encodes information about the accretion process, with the imprint of the dynamo being a likely component of this signal. Since we neglect detailed radiative physics in order to save computational resources, we explore this with an emission proxy. We use a scheme employed by other global accretion disk simulations (e.g. Hawley & Krolik (2001), Armitage & Reynolds (2003) & Hogg & Reynolds (2016)) based on the internal disk stress. Adopting Eqn 9 from Hubeny & Hubeny (1998), the local flux at the photosphere of the disk to dissipation is given by

$$F = \frac{3}{2}\sqrt{\frac{GM}{r^3}}\left(\frac{A}{B}\right)\int_0^h B_r B_\phi dz, \tag{5.26}$$

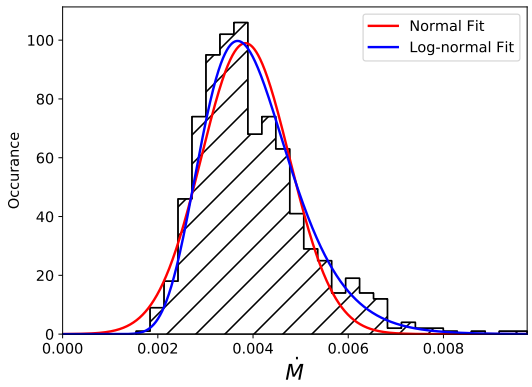

(a) `hr_005` $\dot{M}$ Distribution

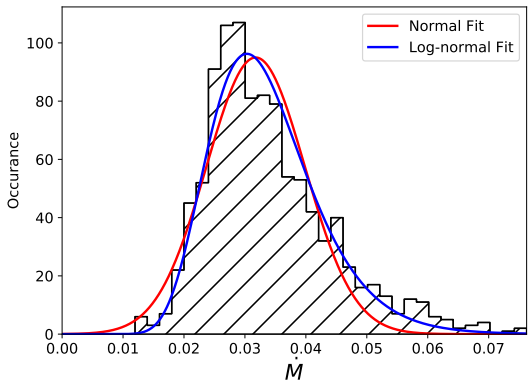

(b) `hr_01` $\dot{M}$ Distribution

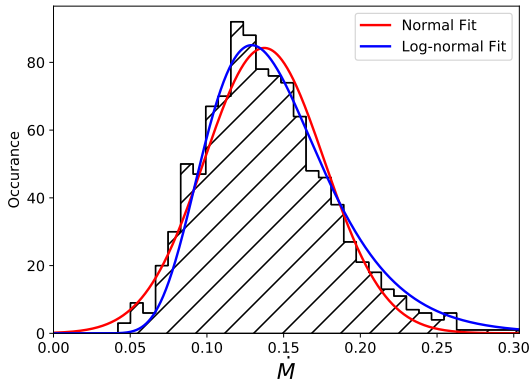

(c) `hr_02` $\dot{M}$ Distribution

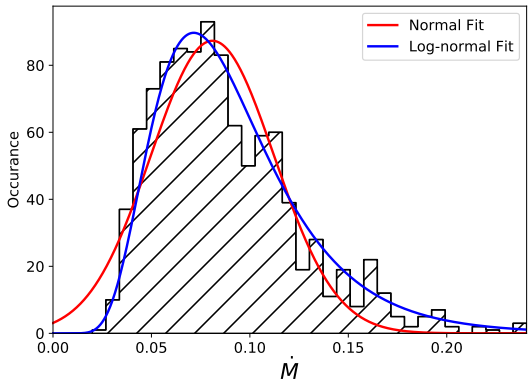

(d) `hr_04` $\dot{M}$ Distribution

Figure 5.7: Mass accretion rate distributions at the inner boundary of `hr_005` (a), `hr_01` (b), `hr_02` (c), and `hr_04` (d). The distributions have been fit by fit by a Gaussian function (red) and log-normal function (blue lines), and they are all better fit by a log-normal function. As noted in the text, we are primarily concerned with the qualitative shape rather than the quantitative amplitude since all simulations were initialed with the same density normalizations and the total disk "mass" scales increases with increasing thickness.

where A and B are relativistic correction factors given by

$$A = 1 - \frac{2GM}{rc^2} \tag{5.27}$$

and

$$B = 1 - \frac{3GM}{rc^2}. \tag{5.28}$$

For each data dump we integrate F within $r = 25\, r_g$ to calculate a bolometric "luminosity," L. The region beyond $r = 25\, r_g$ is excluded because of residual transient behavior from the initialization of the disk which affects the very early part of our analysis phase. This also contaminates the very early part of the `hr_005` lightcurve, which we ignore in our calculation of its standard deviation. We normalize by the mean luminosity to express the variability in a fractional form and because the models are evolved dimensionless, scale free form. The lightcurves are shown in Figure 5.8.

The most obvious difference in the synthetic light curves is the level of organization provided by the relative coherence of the dynamo. Prior numerical studies have shown the stress in the disk is modulated by the dynamo (Davis et al., 2010; Flock et al., 2012; Hogg & Reynolds, 2016), which provides a link to the disk heating as the energy injected by the dynamo is ultimately deposited as heat. In our simulations, we see that the thinner disks with a more organized dynamo display slower undulations and a smaller fractional amplitude. As measured by the standard deviation,

$$\sigma = \sqrt{\frac{1}{N}\sum_{i=1}^{N}\left(L_i - \overline{L}\right)^2}, \tag{5.29}$$

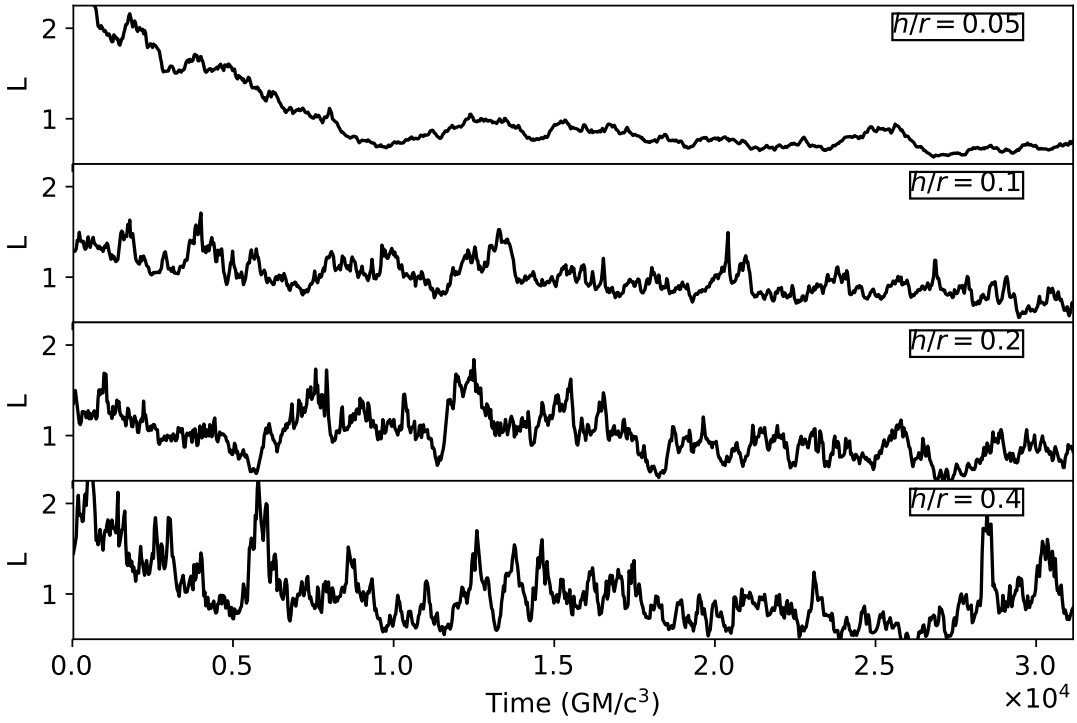

Figure 5.8: Synthetic light curves calculated from the disk cooling for `hr_005` (top), `hr_01` (second to top), `hr_02` (second to bottom), and `hr_04` (bottom). The cooling has been normalized to the mean value of the lightcurve to express the amplitude in terms of a fractional amplitude.

the typical fractional amplitude of the hr_005 model is $\sigma = 0.14$ and for the hr_01 model it is $\sigma = 0.20$.

The thicker disks display rapid, incoherent variability with a much larger fractional amplitude. In the hr_02 model, $\sigma = 0.24$ and in the h_04 model, $\sigma = 0.35$. In these models, the fluctuations are much more "flarey" and the light curves show rapid brightening episodes and subsequent troughs. For instance, in the hr_02 model from $t = 1.1 \times 10^4\, GM/c^3$ to $t = 1.3 \times 10^4\, GM/c^3$ when the disk luminosity would appear to diminish by 36%, only to quickly rebrighten by a factor of three. Later, from $t = 1.7 \times 10^4 GM/c^3$ to $t = 1.9 \times 10^4\, GM/c^3$, the disk dips to half its baseline value, only to return quickly. The hr_04 model shows less structure than the hr_02 model, with fast, stochastic fluctuations of roughly factors of 2.5, i.e. fluctuations between 0.6 and 1.5 on several occasions. At two points there are large excursions from the mean with flares that peak at over twice the mean value.

5.4 Extended Domain Tests

To confirm the results from our analysis, we ran two additional simulations of the thickest accretion disks, hr_02_pi and hr_04_pi. These simulations were constructed identically to their $\Delta\phi = \pi/3$ counterparts, but with a ϕ-domain extended to $\Delta\phi = \pi$. The resolution element is preserved by tripling the number of zones in the azimuthal direction so that hr_02_pi has $N_R \times N_\theta \times N_\phi = 308 \times 248 \times 192$ zones and hr_04_pi has $N_R \times N_\theta \times N_\phi = 154 \times 248 \times 96$ zones. The hr_02_pi model was integrated for 680 ISCO orbits, or $t = 4.19 \times 10^4\, GM/c^3$. The hr_02_pi model was

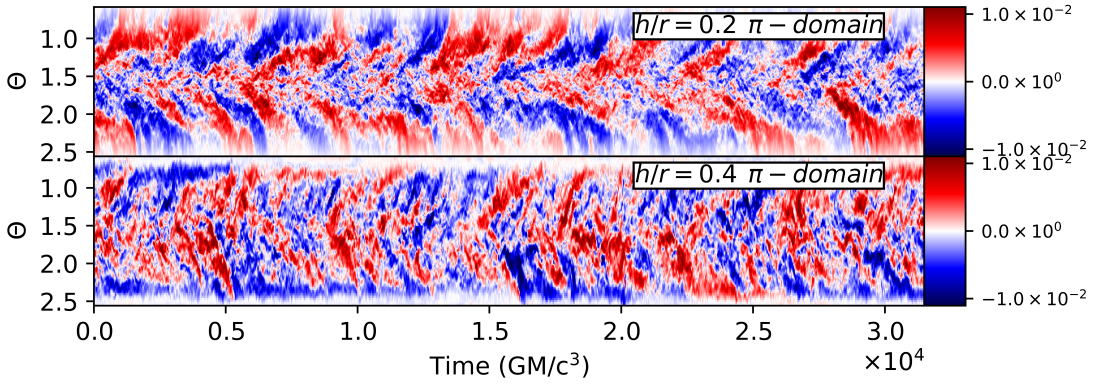

Figure 5.9: Spacetime diagrams of the azimuthally averaged B_ϕ at $r = 15\,r_g$ for the extended π-domain `hr_02` (top) and `hr_04` (bottom) tests. Positive values (red) indicate orientation of the field in the positive ϕ-direction while negative (blue) indicates an opposite orientation. Color intensity corresponds to the averaged magnitude.

also integrated for 680 ISCO orbits, or $t = 4.19 \times 10^4\,GM/c^3$. As before, only the final $\Delta t = 3.15 \times 10^4\,GM/c^3$ (512 ISCO orbits) is used in the analysis.

Extending the ϕ-domain places these models within a similar regime to `hr_005` and `hr_01` in terms of the number of disk scale heights per azimuthal expanse. Since the large-scale dynamo depends on the self-organization of the MRI-driven turbulence, a smaller domain might not fit the global flow structure that leads to this behavior. However, these models would allow similar butterfly patterns to develop in these thicker disk simulations if our previous results were solely due to a failure to capture the global modes.

Figure 5.9 shows spacetime diagrams of the azimuthally averaged B_ϕ of `hr_02_pi` and `hr_04_pi` at $r = 15\,r_g$. As seen in `hr_02`, the dynamo attempts to establish a butterfly pattern, but it is much more irregular and disorganized than that seen in the `hr_005` and `hr_01` models. Sometimes an organized field dominates for a long

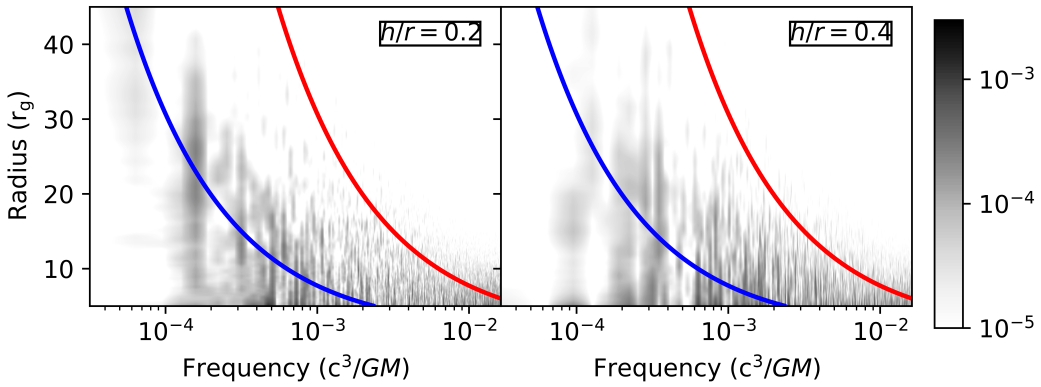

Figure 5.10: PSDs of B_ϕ at $1.5h$ above the disk midplane for the extended π-domain `hr_02` (left), and `hr_04` (right) tests. Darker colors (black) represents greater power in that frequency bin for a given radius. The orbital frequency is shown with the red line and ten times the orbital frequency is shown with the blue line.

portion of the simulation, i.e. $t = 1.3 - 1.5 \times 10^4\, GM/c^3$ in the upper hemisphere of the simulation, while at others it is only momentary present. The `hr_04_pi` simulations shows no organization, like `hr_04`. Fluctuations in the field are rapid, disorganized, and chaotic which resembles nothing more than turbulent fluctuations. Figure 5.10 shows the PSDs of `hr_02_pi` and `hr_04_pi`. Like Figure 5.3, the thick disks show broad bands of power with no evidence of the typical band of power found at one tenth the orbital frequency. The similarity between the PSDs offers secondary evidence the behavior of the magnetic field evolution does not depend on the domain size.

These $\Delta\phi = \pi$ simulations offer compelling evidence that the breakdown in the dynamo pattern with increasing disk scaleheight is a real effect and not a nuance that arises from the grid scheme. In Section 5.5 we offer several refinements for future studies that will help alleviate any remaining concern of numerical artifacts.

Incorporating these improvements with additional features, like a test-field method to probe the field evolution, will provide valuable insights into the dynamo process.

5.5 Discussion

The results from the suite of accretion disk simulations we present here highlight how poorly the dynamo mechanism in accretion disks is understood and the additional work that is needed to fully leverage this phenomenon as an observational probe. The crux of this work is that the large-scale dynamo can fail to organize into the low-frequency, quasiperiodic butterfly pattern typically seen in time traces of the vertical, azimuthally averaged toroidal magnetic field ($\langle B_\phi \rangle$). Instead, in the thicker accretion disks the field is amplified in a stochastic way and on small-scales with no obvious structure or order, but still at low frequencies. This challenges the ubiquity of a self-organized large-scale dynamo appearing as a feature of black hole disks. Consequently, this could translate into observable signatures as the synthetic lightcurves we generate reflect the degree of order in the magnetic field.

Unfortunately, we cannot pin down a detailed reason for why the dynamo fails to organize when the disk thickness is increased. However, these results suggest a separation between turbulent fluctuating scales and the dominant scale of the flow is needed for the dynamo organization. Considering the MHD turbulence spectrally has led to "shell" models of the interactions in Fourier space where it has been shown that the magnetic and velocity fluctuations both decay locally to larger wavenumber. However, the interactions between the two occur non-locally (Mininni, 2011;

Moffatt, 1978) as long wavelength velocity fluctuations are needed to stretch the magnetic field lines and long wavelength magnetic field fluctuations are needed to apply a net Lorentz force. Understanding the details of how the spectral behaviors and interactions of the turbulence depend on disk thickness may help to tie the development of the large-scale dynamo into this framework.

Related to this, the different turbulent scales may change the *effective* magnetic Prandtl number, Pr_m. This could be a viable explanation since the effective diffusivity changes because of the larger turbulent eddies, which we find evidence for here in the increased scatter of the $\langle \mathcal{E}'_\phi \rangle$ and $\langle B_\phi \rangle$ correlations. Guan & Gammie (2009) explored the role of the turbulent Pr_m in MHD accretion disks, and found it increased with increasing scaleheight. The excitation of the MRI has been shown to depend on Pr_m (Fromang & Papaloizou, 2007; Fromang et al., 2007), and simulations of forced turbulence have shown that the large-scale dynamo excitation also has a dependence on Pr_m, depending on how the turbulence is injected (Brandenburg, 2014). Since the effective viscosity, as measured by α_{ss}, is roughly constant, this could show the role of the larger eddies increasing the turbulent magnetic diffusivity and connect to disappearance of they dynamo cycle at low Pr_m (Riols et al., 2015).

Investigating the role of helicity in the disk may help in deciphering the differences between the thick and thin disks. The evolution and influence of the flow helicities is expected to be intimately linked to global field behavior, and could be important in the excitation and organization of a large scale dynamo (e.g. Blackman, 2012, 2015; Frick et al., 2006; Käpylä & Korpi, 2011). However, it is unclear the role

that it plays in the global behavior of an accretion disk. The clear case of a relation between the large-scale magnetic helicity with the azimuthally averaged toroidal field in the `hr_005` simulation offers a glimpse into the the behavior. Pursuing this connection more may help to explain the curious changes in the parity between the two disk hemispheres, as well as abnormal features like the intermittency and "failed reversals" in the field oscillations because they may be related to the ability of the disk to assemble the large-scale field into an ordered pattern and its ability to shed the helicity generated by the turbulence.

Fundamentally, all of these scenarios are related and could all be contributing to the disorganization of the dynamo on some level. Moving forward, there are several routes that could clarify why the large scale dynamo failed to organize. Using test field methods, first applied to the geodynamo (Schrinner et al., 2005, 2007), to measure the mean-field dynamo coefficients in these global runs is possibility the most important next step as it has been effectively used to characterize the dynamo in local shearing box simulations (Gressel, 2010; Gressel & Pessah, 2015). Additionally, expanding the simulations to encompass the full 2π azimuthal domain could be significant for fully capturing of the large scale structure. To run the simulations for our planned duration, we were restricted to a truncated azimuthal domain out of necessity. Our simulations were already very computational expensive, with `hr_01` requiring 2 million CPU hours and `hr_005` requiring over 7 million CPU hours, so extending the domain with proper resolution like we had in these models was impractical. A number of dedicated resolution studies have shown that the properties of the MRI turbulence can depend on the domain and it is possible we are simply

seeing an analogous sensitivity in the dynamo. In Section 5.4 we present two test simulations of `hr_02` and `hr_04` that have ϕ-domains extended to $\Delta\phi = \pi$. These simulations show identical behavior to their compliments used in this analysis, which offers encouraging evidence the grid design is not the root cause of the unstructured pattern. This bolsters these results, but subtle numerical effects remain a lingering concern. Guided by this first attempt to explore the scaleheight dependence of the dynamo, we can tailor our simulations to target the two interesting regimes. Furthermore, we were intentionally very conservative with the length of the initialization phase in these simulations to prevent transients from distorting our results, and it could likely be shorted to redirect computational resources in the future.

As a note, in Chapter 4 we studied an MHD model of a "truncated" accretion disk where there is believed to be a transition region between a hot, radiatively inner accretion flow and a cooler, radiatively efficient disk. In the outer thin disk ($h/r = 0.1$), we find the large scale dynamo readily develops and is sustained. However, in inner region where the disk thickens ($h/r > 0.2$), we find it fails to develop, similar to this study. In the truncated disk the flow had the added component of an outflow originating from the truncation zone, so it is not an isolated system like those presented here, but the failed organization of the dynamo in the thicker disk is reminiscent of that detailed in this chapter. The truncated disk scenario essentially provides a composite accretion flow and demonstrates that it truly is a scale height dependence since the two distinct flow behaviors develop in close proximity and can even interact.

The observational consequences of changing disk height are of great interest.

The lightcurves we present in Figure 5.8 show that the temporal behavior of the photometric variability from emission should be distinct, which meshes with empirical results. Accreting stellar mass black holes in black hole binaries (BHBs) and supermassive black holes in active galactic nuclei (AGNs) display a bifurcation in spectral states that is typically attributed to the radiative efficiency of the system. In the low-hard state of BHBs and in low-luminosity AGNs (LLAGNs) the accretion flow is presumed to be radiatively inefficient and hot. The accretion flow should, therefore, take on a thicker disk geometry since it cannot radiate away its thermal energy. High-soft state BHBs and the typical Seyfert-like AGNs and quasars, on the other hand, should be able to radiate efficiently, so the accretion is expected to occur through a thin disk.

Making a direct association between the lightcurves from our simulations to astrophysical black hole systems is not straightforward since the disk emission is produced by different processes and in different wavebands for the thin and thick disk cases, but it nevertheless seems to hold. Indeed, this scheme matches the trends from BHBs as they change states during outburst (Remillard & McClintock, 2006). Variability in AGNs is poorly understood, but the different timing properties of LLAGNs compared to Seyfert-like AGNs may be a clue about their ability to host a large-scale dynamo in the disk. LLAGNs typically have rapid variability e.g. NGC 4258 (Markowitz & Uttley, 2005) and NGC 3226 (Binder et al., 2009), but they are less well studied than their higher Eddington ratio counterparts. Extensive monitoring campaigns have been completed across the electromagnetic spectrum for Seyfert-like AGNs which show variability on a thermal time, $t_{therm} \approx 1/\alpha\Omega$,

(Kasliwal et al., 2017; Kelly et al., 2009; MacLeod et al., 2010), roughly the same timescale that the dynamo oscillations might present themselves.

The results we present here may have additional observational impacts as a number of other variable processes could stem from the presence of a well-ordered large scale dynamo. Features like dynamo driven low-frequency QPOs could be impacted by the departure from the assumed cyclical behavior, so it is prudent to revisit their utility as probes of the central black hole mass and spin (e.g. Gierliński et al., 2008; Pan et al., 2016; Pasham et al., 2014; Zhou et al., 2010) to verify the assumptions that serve as the foundation of the mass scaling remain valid since they will not appear if they dynamo is unordered.

In Chapter 2 we presented a detailed analysis of a simulated thin disk where propagating fluctuations in mass accretion rate naturally developed from the turbulence. At its core, the telling nonlinear signatures that are commonly observed, i.e. log-normal flux distribution, linear relations between the RMS and flux level of the variabiltiy, and interband coherence where the harder emission lags the softer emission, arise from the multiplicative combination of stochastic fluctuations in the mass accretion rate. As we emphasized the name "propagating fluctuations" is a misnomer since the phenomenon is fundamentally just the preservation of the fluctuation pattern as angular momentum is diffusively redistributed according to the canonical disk equation (Pringle, 1981),

$$\frac{\partial \Sigma}{\partial t} = \frac{3}{R}\frac{\partial}{\partial R}\Big[R^{\frac{1}{2}}\frac{\partial}{\partial R}(\nu\Sigma R^{\frac{1}{2}})\Big]. \tag{5.30}$$

A key component in the growth of propagating fluctuations in mass accretion rate

is that the effective viscosity must be modulated at low enough frequencies that turbulent fluctuations do not wipe out the growth of the structure in the accretion flow (Cowperthwaite & Reynolds, 2014). The results presented here show that this condition is met, even when the dynamo is not ordered into its standard cycle because low-frequency power is still seen in the 2D PSDs. The log-normal $\dot{M}$ distributions we find in these simulations further confirms that the growth of propagating fluctuations is hardy enough to occur in an accretion disk regardless of the dynamo organization, the dynamo just simply needs operate.

There has been a recent push to understand the dynamo beyond the standard thin accretion disk, and from these efforts a narrative is developing that it is possible to impede or alter the growth of the large-scale dynamo. Here, we present one more example of modification of the large-scale dynamo. Further investigation into the peculiarities of the dynamo are needed and warranted to get a better handle on when it is a reliable source of variability and when it cannot contribute to the observational signatures. This discussion is meant to highlight several ways in which commonly observed features could be impacted by the breakdown of the dynamo organization, but it is by no means complete. There are additional ramifications beyond these that could be significant for interpreting the accretion flow dynamics around a black hole.

5.6 Conclusion

With this study, we sought to clarify how the dynamo fits into the larger puzzle of black hole accretion. Using a suite of four global, MHD accretion disk simulations with scale height ratios $h/r = \{0.05, 0.1, 0.2, 0.4\}$, we expose a scaleheight dependence in the ability of an accretion disk to organize the large-scale dynamo. In summary, our top-line results from these simulations are:

1. Low-frequency, ordered oscillations in the azimuthal magnetic field from the large-scale dynamo are present in the `hr_005` ($h/r = 0.05$) and `hr_01` ($h/r = 0.1$) models, but are increasingly absent in the `hr_02` ($h/r = 0.2$) and `hr_04` ($h/r = 0.4$) models.

2. When the organized large-scale dynamo is present in the thinner disks, there is a coherent band of power in the PSD of azimuthally average toroidal magnetic field, $\langle B_\phi \rangle$, at approximately $10\times$ the local orbital period. In the thicker accretion disks where the large-scale dynamo is unorganized, the PSD is featureless with power on all timescales, down the the lowest frequencies we can probe with the duration of our simulations.

3. Calculation of α_d through correlations between $\langle B_\phi \rangle$ and the turbulent electromotive force, $\langle \mathcal{E}'_\phi \rangle$, in the coronal regions of the simulations yield similar values across our models. In the upper hemisphere of the simulations α_d is negative, while in the lower hemisphere it is positive.

4. In synthetic light curves produced through a proxy, the presence of a large-scale

dynamo is related to the level of order and amplitude of the fluctuations. The light curves of the thicker disks display large amplitude, stochastic fluctuations, which reflects the lack of organization in the accretion flow. The thinner disk simulations, in comparison, show a dearth of large amplitude variation and smaller-scale, slower undulations instead.

As we continue to assemble the accretion puzzle and interpret variability from accreting black holes, exploring the details of the underlying physics is an important pursuit. The spectrotemporal behavior provides a crucial window into these systems, but a first principles understanding of their origin remains elusive. This hinders the ability to leverage the observational signatures to their full potential and offers an opportunity for future advancement. The odd dynamo behavior we detail here has the immediate implication that the large-scale dynamo shows markedly different appearance in thicker accretion disks compared to its well characterized behavior in thin disks, which could have broader importance in the global accretion disk evolution.

Chapter 6: Conclusions

With this work, we sought to confront phenomenological models of black hole accretion with MHD theory. We investigated the growth of "propagating fluctuations" in mass accretion rate and how they lead to nonlinear variability, the dynamics of truncated accretion disks, and finally the development of dynamo action in thick and thin accretion disks. With minimal input, the simulations we conducted resemble the scenarios called upon in interpreting observations. This is encouraging and suggests the models commonly used in the literature are likely to be realized in nature. However, at each point in this dissertation research, we discovered important revisions to these models that better reflect the physical reality of black hole systems. To summarize each of the main areas of focus:

1. **Propagating Fluctuations In Mass Accretion Rate** - The main driver of angular momentum transport in a thin accretion disk around a black hole is MRI-driven turbulence. This turbulence causes an internal stress in the disk and also has the interesting property that fluctuations multiplicatively combine. If there is sufficiently slow modulation of the disk stress, fluctuations will grow hierarchically and be preserved as they accrete. This imparts a distinguishing nonlinear structure on the mass accretion rate fluctuations, and

subsequent variability of the emitted radiation, in the form of log-normal distributions, a linear relation between the RMS of fluctuations and the average level, and radial coherence. Analytic and semi-analytic studies demonstrated the feasibility of this variability model, but we show it naturally develops in MHD turbulence. Most significantly, we identify the large-scale magnetic dynamo as the source of the low-frequency stress modulation for the first time. Prior studies provisionally assumed the modulation occurred on a viscous timescale, but we were able to uncover the true physical driver.

2. **Truncated Accretion Disks** - Spectral evidence of a population of lower luminosity X-ray binaries and AGNs implies that the disks in these systems are truncated and the inner regions are evacuated. The current paradigm dictates that hot gas is confined to an inner region and the transition is sharp and well-defined. Here, we attempted to bridge the gap between this simple picture and a full MHD theory by initially running a hydrodynamic model and then following it up with a matched MHD model. These studies taught us that rather than the currently envisioned truncated disk model where gas gets to a certain radius and changes phase, it really should be considered more like a boiling. Because of turbulent fluctuations, there is a range of gas temperatures and a certain fraction of the distribution will be above the instability criterion at a given radius. As gas moves inwards, the temperature increases so the fraction above the instability threshold increases until eventually all of the gas occupies a hot phase. This leads to a "tapering" in the disk in a truncation

zone, rather than an edge. Like boiling a pot of water, once gas is in the hot phase, an outflow is launched as it buoyantly rises against gravity and fills the volume around it, rather than being confined to a small region. Schematics of the usually accepted disk configuration and our revised model are shown in Figure 6.1. Interestingly, this outflow amplifies the magnetic field and enhances the stress in a thin sheath enveloping the cool disk body. This interacts with the dynamo to introduce a periodicity that could conceivably appear as a strong quasiperiodic oscillation.

3. **Large-scale Magnetic Dynamo Action** - Dynamo activity is critical for maintaining magnetic field against dissipation in an accretion disk and also seems to be the puppet master behind many different forms of variability. To understand the dynamo activity better, we studied its dependence on the disk scaleheight. Despite the simplicity of our experiment, the dynamo showed puzzling behavior. At the outset, we naively hypothesized that changing the disk scaleheight might change the dynamo period. Instead, we found that in thin disks the period is the same and that in thick disks it fails to organize into its ordered pattern. Regardless of the pattern organization, the dynamo strength is consistent across disk thickness. In the thinnest disk simulation, we find tantalizing, yet inconclusive, evidence that the dynamo cycle may be tied to the flow helicity, but further investigation must be done before any firm claims can be made.

Looking forward, we find ourselves at an exciting time. Immense efforts are

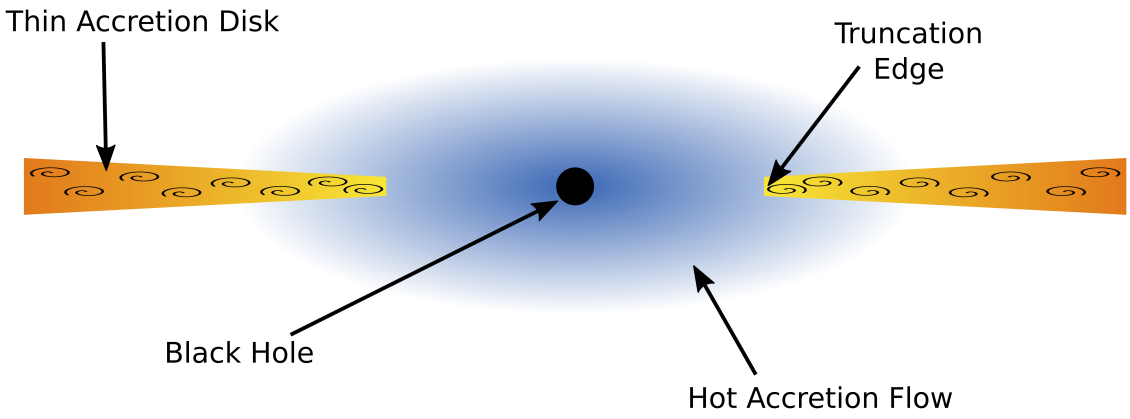

(a) Standard Truncated Disk Model

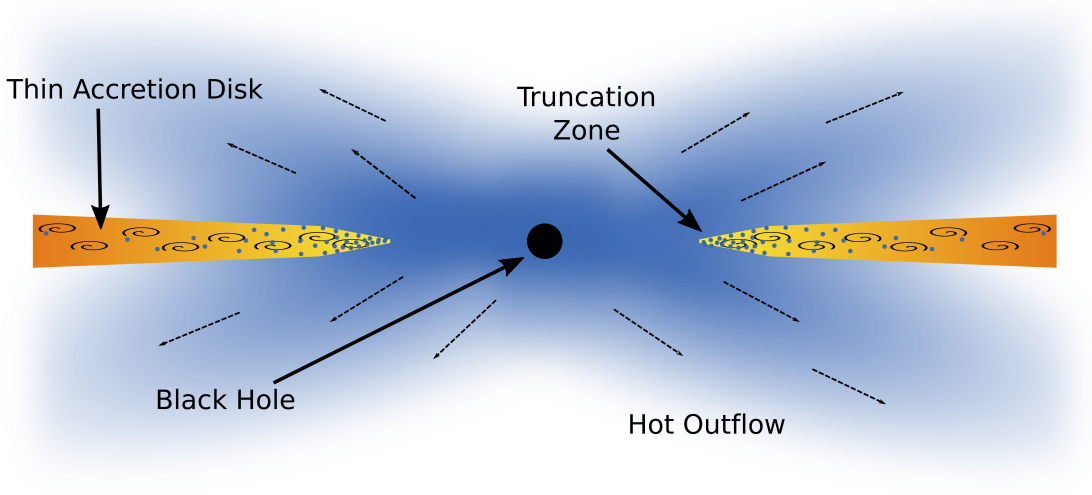

(b) Revised Truncated Disk Model

Figure 6.1: Illustrations of the current truncated disk configuration (a) and our revised model (b). In both drawings cooler gas is shown by redder colors an hotter gas is shown by bluer colors. Motivated by the results from our simulations, we advocate for a truncation zone rather than a sharp transition. Turbulent fluctuations allow for pockets of gas to enter the hot phase within the disk body, represented by the blue bubbles, which then buoyantly rise outflow, shown with the darker blue regions hugging the disk body. Our results suggest that hot gas more easily fills the volume surrounding the black hole instead of just being confined to radii within the truncation and is fed by the wind.

underway to understand black hole variability with the next-generation of ground- and space-based telescopes, and through massive simulation efforts. Since beginning this dissertation, there have been rapid advancements to bring theoretical predictions and observations together, which we have contributed to.

There are several technical ways to expand the work we have presented. Firstly, including radiative physics may be important, especially when it comes to driving the outflows from truncated disks. Including radiative physics is computationally expensive and should not dramatically change the disk dynamics that we have studied, but its inclusion could aid in connecting to observables. These methods have reached a point that they can be considered mature and robust enough to gain meaningful insight, so this is an important next step in adding realism to these simulations. Secondly, we could potentially rerun this work with recently released algorithms that have performance enhancements to run for longer duration. We were careful in identifying numerical transients and understanding how they could affect our results, but running simulations long enough that they are no longer issues may ensure they did not affect our work in subtle ways.

More fundamentally, pinning down the truncation mechanism is a pressing matter. The bistable cooling function used in studying truncated accretion disks was simply that, a bistable cooling law triggered by the gas temperature. Relating this to more physical properties of the flow could provide deeper insight and including a proper triggering mechanism in simulations will more faithfully reproduce the flow dynamics.

We are well-poised to unravel the curious dynamo behavior. Adding test-field

machinery to our simulation codes and rerunning models like those presented here will provide a deeper look into the dynamo mechanics. In Chapter 5 we speculate on what may be causing the dynamo pattern to not organize, but we do not have a satisfactory explanation. Being able to directly measure properties like the flow helicity in a global simulation, rather than trying to calculate them in post-processing, may be the key to make headway on this problem.

The future of accretion theory is bigger than just these topics, though. As mentioned in Chapter 1, the stabilization of an accretion disk against thermal and viscous instability in radiation dominated accretion disks like those expected to reside in the interiors of AGNs has not been resolved. Much work is needed to understand how they might be stabilized, or if they can be. If they cannot, it may explain the large variability this is observed and therefore be a useful accretion diagnostic if we can characterize it. Furthermore, understanding the peculiarities of black hole variability may come from including kinetic effects in simulations. The MRI has been demonstrated to work in a kinetic shearing box (Kunz et al., 2016), but much uncertainty surrounds the putative "corona" that dominates X-ray variability in AGNs. Allowing for particle-wave interactions opens numerous instabilities that can add additional heating and particle acceleration to drive variability. Also, as we are now in the era of gravitational wave astronomy and on the search for elusive SMBH binaries with optical surveys, modeling efforts are underway to simulate these systems. Taking variability as a marker for these systems is a tricky business (Vaughan et al., 2016), so using it as reliable probe requires the accretion physics and their signatures are reasonably well understood.

There is also ample room to learn about accretion by better leveraging observational data. The prevalence of advanced classification and regression algorithms in modern life has changed the way we shop, diagnose illness, and conduct business. Machine learning models have become so advanced they can even identify cancer cells far more accurately than expert epidemiologists and drive cars. This technology has begun to creep into the astrophysical community, but there is much more that could be done. As we are tasked with interpreting seemingly random events like stochastic variability and changing look AGNs where the emission from the disk "turns off," we have to take a more comprehensive look at the data and use all the tools at our disposal. Conceivably, there must be some sort of distinguishing signal from the accretion physics that projects its future actions. As large surveys like the *Large Synoptic Sky Telescope* come online, we will be inundated with information. If we can understand the complex relationships between the many parameters that impact the accretion behavior, we can get a handle on this difficult physical problem and perhaps even predict interesting phenomena rather than simply react.

Bibliography

Adams, S. M., Kochanek, C. S., Gerke, J. R., & Stanek, K. Z. 2017a, MNRAS, 469, 1445

Adams, S. M., Kochanek, C. S., Gerke, J. R., Stanek, K. Z., & Dai, X. 2017b, MNRAS, 468, 4968

Armitage, P. J. 1998, ApJL, 501, L189

Armitage, P. J., & Reynolds, C. S. 2003, MNRAS, 341, 1041

Armitage, P. J., Reynolds, C. S., & Chiang, J. 2001, ApJ, 548, 868

Bai, X.-N., & Stone, J. M. 2013, ApJ, 767, 30

Balbus, S. A., & Hawley, J. F. 1991, ApJ, 376, 214

Balbus, S. A., & Papaloizou, J. C. B. 1999, ApJ, 521, 650

Beckwith, K., Armitage, P. J., & Simon, J. B. 2011, MNRAS, 416, 361

Begelman, M. C., Armitage, P. J., & Reynolds, C. S. 2015, ApJ, 809, 118

Binder, B., Markowitz, A., & Rothschild, R. E. 2009, ApJ, 691, 431

Blackman, E. G. 2012, Phys. Scr, 86, 058202

—. 2015, Space Sci. Rev., 188, 59

Blackman, E. G., & Brandenburg, A. 2002, ApJ, 579, 359

Blackman, E. G., & Field, G. B. 2002, Physical Review Letters, 89, 265007

Blackman, E. G., Penna, R. F., & Varnière, P. 2008, New Ast., 13, 244

Blandford, R. D., & Payne, D. G. 1982, MNRAS, 199, 883

Bodo, G., Cattaneo, F., Mignone, A., & Rossi, P. 2015, ApJ, 799, 20

Bodo, G., Mignone, A., Cattaneo, F., Rossi, P., & Ferrari, A. 2008, A&A, 487, 1

Bolton, C. T. 1971, in , Vol. 3, Bulletin of the American Astronomical Society, 458

Bolton, C. T. 1972, Nature, 235, 271

Bondi, H. 1952, MNRAS, 112, 195

Brandenburg, A. 2014, ApJ, 791, 12

Brandenburg, A., & Donner, K. J. 1997, MNRAS, 288, L29

Brandenburg, A., Nordlund, A., Stein, R. F., & Torkelsson, U. 1995, ApJ, 446, 741

Brandenburg, A., & Subramanian, K. 2005, Phys. Rep., 417, 1

Brenneman, L. W., Reynolds, C. S., Wilms, J., & Kaiser, M. E. 2007, ApJ, 666, 817

Chandrasekhar, S. 1960, Proceedings of the National Academy of Science, 46, 253

Coleman, M. S. B., Yerger, E., Blaes, O., Salvesen, G., & Hirose, S. 2017, MNRAS, 467, 2625

Cowperthwaite, P. S., & Reynolds, C. S. 2014, ApJ, 791, 126

Cui, W., Heindl, W. A., Rothschild, R. E., et al. 1997, ApJL, 474, L57

Das, U., & Sharma, P. 2013, MNRAS, 435, 2431

Davis, S. W., Stone, J. M., & Pessah, M. E. 2010, ApJ, 713, 52

De Villiers, J.-P., Hawley, J. F., & Krolik, J. H. 2003, ApJ, 599, 1238

Dewangan, G. C., Griffiths, R. E., Di Matteo, T., & Schurch, N. J. 2004, ApJ, 607, 788

Done, C., & Gierliński, M. 2006, MNRAS, 367, 659

Done, C., Gierliński, M., & Kubota, A. 2007, A&A Rev., 15, 1

Done, C., & Zycki, P. T. 1999, MNRAS, 305, 457

Esin, A. A., McClintock, J. E., & Narayan, R. 1997, ApJ, 489, 865

Evans, C. R., & Hawley, J. F. 1988, ApJ, 332, 659

Flock, M., Dzyurkevich, N., Klahr, H., & Mignone, A. 2010, A&A, 516, A26

Flock, M., Dzyurkevich, N., Klahr, H., Turner, N., & Henning, T. 2012, ApJ, 744, 144

Flock, M., Dzyurkevich, N., Klahr, H., Turner, N. J., & Henning, T. 2011, ApJ, 735, 122

Fragile, P. C., Etheridge, S. M., Anninos, P., Mishra, B., & Kluźniak, W. 2018, ApJ, 857, 1

Fragile, P. C., Wilson, J., & Rodriguez, M. 2012, MNRAS, 424, 524

Frank, J., King, A., & Raine, D. J. 2002, Accretion Power in Astrophysics: Third Edition, 398

Frick, P., Stepanov, R., & Sokoloff, D. 2006, Phys. Rev. E, 74, 066310

Fromang, S., & Papaloizou, J. 2007, A&A, 476, 1113

Fromang, S., Papaloizou, J., Lesur, G., & Heinemann, T. 2007, A&A, 476, 1123

Gammie, C. F., McKinney, J. C., & Tóth, G. 2003, ApJ, 589, 444

Gammie, C. F., Narayan, R., & Blandford, R. 1999, ApJ, 516, 177

Gaskell, C. M. 2004, ApJL, 612, L21

Gerke, J. R., Kochanek, C. S., & Stanek, K. Z. 2015, MNRAS, 450, 3289

Gierliński, M., Middleton, M., Ward, M., & Done, C. 2008, Nature, 455, 369

Gillespie, D. T. 1996, American Journal of Physics, 64, 225

Gleissner, T., Wilms, J., Pottschmidt, K., et al. 2004, A&A, 414, 1091

Gogichaishvili, D., Mamatsashvili, G., Horton, W., Chagelishvili, G., & Bodo, G. 2017, ArXiv e-prints, arXiv:1707.07044

Goodman, J., & Xu, G. 1994, ApJ, 432, 213

Gressel, O. 2010, MNRAS, 405, 41

Gressel, O., & Pessah, M. E. 2015, ApJ, 810, 59

Guan, X., & Gammie, C. F. 2009, ApJ, 697, 1901

—. 2011, ApJ, 728, 130

Guan, X., Gammie, C. F., Simon, J. B., & Johnson, B. M. 2009, ApJ, 694, 1010

Hawley, J. F. 2000, ApJ, 528, 462

—. 2001, ApJ, 554, 534

Hawley, J. F., & Balbus, S. A. 1991, ApJ, 376, 223

—. 2002, ApJ, 573, 738

Hawley, J. F., Balbus, S. A., & Stone, J. M. 2001, ApJL, 554, L49

Hawley, J. F., Gammie, C. F., & Balbus, S. A. 1995, ApJ, 440, 742

—. 1996, ApJ, 464, 690

Hawley, J. F., Guan, X., & Krolik, J. H. 2011, ApJ, 738, 84

Hawley, J. F., & Krolik, J. H. 2001, ApJ, 548, 348

—. 2002, ApJ, 566, 164

Hawley, J. F., Richers, S. A., Guan, X., & Krolik, J. H. 2013, ApJ, 772, 102

Hawley, J. F., & Stone, J. M. 1995, Computer Physics Communications, 89, 127

Hayes, J. C., Norman, M. L., Fiedler, R. A., et al. 2006, ApJS, 165, 188

Heger, A., Fryer, C. L., Woosley, S. E., Langer, N., & Hartmann, D. H. 2003, ApJ, 591, 288

Heil, L. M., Vaughan, S., & Uttley, P. 2012, MNRAS, 422, 2620

Hirose, S., Krolik, J. H., & Blaes, O. 2009, ApJ, 691, 16

Ho, L. C. 2008, ARA&A, 46, 475

Ho, L. C., Rudnick, G., Rix, H.-W., et al. 2000, ApJ, 541, 120

Hogg, J. D., & Reynolds, C. S. 2016, ApJ, 826, 40

Homan, J., Neilsen, J., Allen, J. L., et al. 2016, ApJL, 830, L5

Honma, F. 1996, PASJ, 48, 77

Hubeny, I., & Hubeny, V. 1998, ApJ, 505, 558

Igumenshchev, I. V., & Abramowicz, M. A. 1999, MNRAS, 303, 309

—. 2000, ApJS, 130, 463

Igumenshchev, I. V., Abramowicz, M. A., & Narayan, R. 2000, ApJL, 537, L27

Igumenshchev, I. V., Narayan, R., & Abramowicz, M. A. 2003, ApJ, 592, 1042

Janiuk, A., & Misra, R. 2012, A&A, 540, A114

Jiang, Y.-F., Davis, S. W., & Stone, J. M. 2016, ApJ, 827, 10

Jiang, Y.-F., Stone, J. M., & Davis, S. W. 2013, ApJ, 778, 65

—. 2014, ApJ, 796, 106

Johansen, A., Youdin, A., & Klahr, H. 2009, ApJ, 697, 1269

Käpylä, P. J., & Korpi, M. J. 2011, MNRAS, 413, 901

Kasliwal, V. P., Vogeley, M. S., & Richards, G. T. 2015, MNRAS, 451, 4328

—. 2017, MNRAS, 470, 3027

Kato, S., & Yoshizawa, A. 1995, PASJ, 47, 629

Kelly, B. C., Bechtold, J., & Siemiginowska, A. 2009, ApJ, 698, 895

Kelly, B. C., Sobolewska, M., & Siemiginowska, A. 2011, ApJ, 730, 52

King, A. R., Pringle, J. E., West, R. G., & Livio, M. 2004, MNRAS, 348, 111

Kippenhahn, R., & Thomas, H.-C. 1982, A&A, 114, 77

Kley, W., & Lin, D. N. C. 1992, ApJ, 397, 600

Kowal, G., Lazarian, A., & Beresnyak, A. 2007, ApJ, 658, 423

Kozłowski, S. 2017, A&A, 597, A128

Kozłowski, S., Kochanek, C. S., Udalski, A., et al. 2010, ApJ, 708, 927

Krause, F., & Raedler, K. H. 1980, Mean-field magnetohydrodynamics and dynamo theory

Krolik, J. H., & Hawley, J. F. 2002, ApJ, 573, 754

Kunz, M. W., Stone, J. M., & Quataert, E. 2016, Physical Review Letters, 117, 235101

Laor, A., & Davis, S. W. 2014, MNRAS, 438, 3024

Latter, H. N., Lesaffre, P., & Balbus, S. A. 2009, MNRAS, 394, 715

Lesur, G., & Longaretti, P.-Y. 2011, A&A, 528, A17

Lesur, G., & Ogilvie, G. I. 2008, A&A, 488, 451

Liang, E. P., & Nolan, P. L. 1984, Space Sci. Rev., 38, 353

Lightman, A. P. 1974, ApJ, 194, 419

Lightman, A. P., & Eardley, D. M. 1974, ApJL, 187, L1

Liu, B. F., Yuan, W., Meyer, F., Meyer-Hofmeister, E., & Xie, G. Z. 1999, ApJL, 527, L17

Lyubarskii, Y. E. 1997, MNRAS, 292, 679

MacLeod, C. L., Ivezić, Ž., Kochanek, C. S., et al. 2010, ApJ, 721, 1014

Manmoto, T., & Kato, S. 2000, ApJ, 538, 295

Manmoto, T., Kato, S., Nakamura, K. E., & Narayan, R. 2000, ApJ, 529, 127

Markowitz, A., & Uttley, P. 2005, ApJL, 625, L39

Markowitz, A. G., & Reeves, J. N. 2009, ApJ, 705, 496

Matthews, T. A., & Sandage, A. R. 1963, ApJ, 138, 30

Mayer, M., & Pringle, J. E. 2006, MNRAS, 368, 379

McClintock, J. E., Narayan, R., Garcia, M. R., et al. 2003, ApJ, 593, 435

McClintock, J. E., & Remillard, R. A. 2006, Black hole binaries, ed. W. H. G. Lewin & M. van der Klis, 157–213

McKinney, J. C. 2006, MNRAS, 368, 1561

McKinney, J. C., Tchekhovskoy, A., Sadowski, A., & Narayan, R. 2014, MNRAS, 441, 3177

Meyer, F., & Meyer-Hofmeister, E. 1994, A&A, 288, 175

Mignone, A., Bodo, G., Massaglia, S., et al. 2007, ApJS, 170, 228

Miller, J. M., Fabian, A. C., in't Zand, J. J. M., et al. 2002a, ApJL, 577, L15

Miller, J. M., Homan, J., Steeghs, D., et al. 2006, ApJ, 653, 525

Miller, J. M., Fabian, A. C., Wijnands, R., et al. 2002b, ApJ, 578, 348

Miller, J. M., Tomsick, J. A., Bachetti, M., et al. 2015, ApJL, 799, L6

Mininni, P. D. 2011, Annual Review of Fluid Mechanics, 43, 377

Mishra, B., Fragile, P. C., Johnson, L. C., & Kluźniak, W. 2016, MNRAS, 463, 3437

Moffatt, H. K. 1978, Magnetic field generation in electrically conducting fluids

Murphy, G. C., & Pessah, M. E. 2015, ApJ, 802, 139

Narayan, R., Igumenshchev, I. V., & Abramowicz, M. A. 2000, ApJ, 539, 798

Narayan, R., McClintock, J. E., & Yi, I. 1996, ApJ, 457, 821

Narayan, R., SÄ dowski, A., Penna, R. F., & Kulkarni, A. K. 2012, MNRAS, 426, 3241

Narayan, R., & Yi, I. 1994, ApJL, 428, L13

—. 1995a, ApJ, 444, 231

—. 1995b, ApJ, 452, 710

Negoro, H., & Mineshige, S. 2002, PASJ, 54, L69

Nemmen, R. S., Storchi-Bergmann, T., & Eracleous, M. 2014, MNRAS, 438, 2804

Noble, S. C., Krolik, J. H., & Hawley, J. F. 2009, ApJ, 692, 411

—. 2010, ApJ, 711, 959

Nowak, M. A., Vaughan, B. A., Wilms, J., Dove, J. B., & Begelman, M. C. 1999a, ApJ, 510, 874

Nowak, M. A., Wilms, J., & Dove, J. B. 1999b, ApJ, 517, 355

Obergaulinger, M., Cerdá-Durán, P., Müller, E., & Aloy, M. A. 2009, A&A, 498, 241

Ogilvie, G. I. 2003, MNRAS, 340, 969

Oishi, J. S., & Mac Low, M.-M. 2011, ApJ, 740, 18

O'Neill, S. M., Reynolds, C. S., Miller, M. C., & Sorathia, K. A. 2011, ApJ, 736, 107

Paczyński, B., & Wiita, P. J. 1980, A&A, 88, 23

Pan, H.-W., Yuan, W., Yao, S., et al. 2016, ApJL, 819, L19

Parker, M. L., Tomsick, J. A., Miller, J. M., et al. 2015, ApJ, 808, 9

Parkin, E. R., & Bicknell, G. V. 2013, ApJ, 763, 99

Pasham, D. R., Strohmayer, T. E., & Mushotzky, R. F. 2014, Nature, 513, 74

Passot, T., & Vázquez-Semadeni, E. 1998, Phys. Rev. E, 58, 4501

Peña, D., Amit, H., & Pinheiro, K. J. 2016, Earth, Planets, and Space, 68, 78

Pessah, M. E. 2010, ApJ, 716, 1012

Pessah, M. E., Chan, C.-K., & Psaltis, D. 2006, MNRAS, 372, 183

Pessah, M. E., Chan, C.-k., & Psaltis, D. 2007, ApJL, 668, L51

Pessah, M. E., Chan, C.-K., & Psaltis, D. 2008, MNRAS, 383, 683

Pessah, M. E., & Goodman, J. 2009, ApJL, 698, L72

Piran, T. 1978, ApJ, 221, 652

Plant, D. S., Fender, R. P., Ponti, G., Muñoz-Darias, T., & Coriat, M. 2015, A&A, 573, A120

Potter, W. J., & Balbus, S. A. 2014, MNRAS, 441, 681

—. 2017, ArXiv e-prints, arXiv:1704.02485

Pringle, J. E. 1981, ARA&A, 19, 137

Pringle, J. E., Rees, M. J., & Pacholczyk, A. G. 1973, A&A, 29, 179

Proga, D. 2000, ApJ, 538, 684

Proga, D., & Begelman, M. C. 2003, ApJ, 582, 69

Proga, D., & Kallman, T. R. 2004, ApJ, 616, 688

Proga, D., Stone, J. M., & Kallman, T. R. 2000, ApJ, 543, 686

Quataert, E., & Gruzinov, A. 2000, ApJ, 539, 809

Rapisarda, S., Ingram, A., & van der Klis, M. 2014, MNRAS, 440, 2882

Rees, M. J., Begelman, M. C., Blandford, R. D., & Phinney, E. S. 1982, Nature, 295, 17

Remillard, R. A., & McClintock, J. E. 2006, ARA&A, 44, 49

Reynolds, C. S., Brenneman, L. W., Wilms, J., & Kaiser, M. E. 2004, MNRAS, 352, 205

Reynolds, C. S., & Miller, M. C. 2009, ApJ, 692, 869

Reynolds, C. S., Nowak, M. A., Markoff, S., et al. 2009, ApJ, 691, 1159

Riols, A., Rincon, F., Cossu, C., et al. 2015, A&A, 575, A14

Ross, J., Latter, H. N., & Tehranchi, M. 2017, MNRAS, 468, 2401

RóżaŃska, A., & Czerny, B. 2000, A&A, 360, 1170

Rozyczka, M., Bodenheimer, P., & Bell, K. R. 1994, ApJ, 423, 736

Ryu, D., & Goodman, J. 1992, ApJ, 388, 438

Salvesen, G., Simon, J. B., Armitage, P. J., & Begelman, M. C. 2016, MNRAS, 457, 857

Sandage, A. 1964, ApJ, 139, 416

Sano, T., Inutsuka, S.-i., Turner, N. J., & Stone, J. M. 2004, ApJ, 605, 321

Sądowski, A., Narayan, R., Tchekhovskoy, A., et al. 2015, MNRAS, 447, 49

Scaringi, S., Körding, E., Uttley, P., et al. 2012a, MNRAS, 427, 3396

—. 2012b, MNRAS, 421, 2854

Scaringi, S., Maccarone, T. J., & Middleton, M. 2014, MNRAS, 445, 1031

Scaringi, S., Maccarone, T. J., Kording, E., et al. 2015, Science Advances, 1, e1500686

Schnittman, J. D., & Krolik, J. H. 2010, ApJ, 712, 908

Schrinner, M., Rädler, K.-H., Schmitt, D., Rheinhardt, M., & Christensen, U. 2005, Astronomische Nachrichten, 326, 245

Schrinner, M., Rädler, K.-H., Schmitt, D., Rheinhardt, M., & Christensen, U. R. 2007, Geophysical and Astrophysical Fluid Dynamics, 101, 81

Shakura, N. I., & Sunyaev, R. A. 1973, A&A, 24, 337

—. 1976, MNRAS, 175, 613

Shapiro, S. L., Lightman, A. P., & Eardley, D. M. 1976, ApJ, 204, 187

Sharov, A. S., & Efremov, Y. N. 1963, Information Bulletin on Variable Stars, 23

Shidatsu, M., Ueda, Y., Yamada, S., et al. 2014, ApJ, 789, 100

Shields, J. C., Rix, H.-W., McIntosh, D. H., et al. 2000, ApJL, 534, L27

Simon, J. B., Beckwith, K., & Armitage, P. J. 2012, MNRAS, 422, 2685

Smith, H. J., & Hoffleit, D. 1963, Nature, 198, 650

Sorathia, K. A., Reynolds, C. S., & Armitage, P. J. 2010, ApJ, 712, 1241

Sorathia, K. A., Reynolds, C. S., Stone, J. M., & Beckwith, K. 2012, ApJ, 749, 189

Sriram, K., Agrawal, V. K., & Raghurama Rao, A. 2009, Research in Astronomy and Astrophysics, 9, 901

Stone, J. M., & Balbus, S. A. 1996, ApJ, 464, 364

Stone, J. M., Hawley, J. F., Gammie, C. F., & Balbus, S. A. 1996, ApJ, 463, 656

Stone, J. M., & Norman, M. L. 1992a, ApJS, 80, 753

—. 1992b, ApJS, 80, 791

Stone, J. M., & Pringle, J. E. 2001, MNRAS, 322, 461

Stone, J. M., Pringle, J. E., & Begelman, M. C. 1999, MNRAS, 310, 1002

Suzuki, T. K., & Inutsuka, S.-i. 2009, ApJL, 691, L49

Takahashi, H. R., Ohsuga, K., Kawashima, T., & Sekiguchi, Y. 2016, ApJ, 826, 23

Tomsick, J. A., Yamaoka, K., Corbel, S., et al. 2009, ApJL, 707, L87

Tout, C. A., & Pringle, J. E. 1992, MNRAS, 259, 604

Trump, J. R., Impey, C. D., Kelly, B. C., et al. 2011, ApJ, 733, 60

Turner, N. J. 2004, ApJL, 605, L45

Turner, N. J., Stone, J. M., & Sano, T. 2002, ApJ, 566, 148

Ulvestad, J. S., & Ho, L. C. 2001, ApJL, 562, L133

Urpin, V. A. 1984, Soviet Ast., 28, 50

Uttley, P., & McHardy, I. M. 2001, MNRAS, 323, L26

Uttley, P., McHardy, I. M., & Vaughan, S. 2005, MNRAS, 359, 345

Vaughan, S., Uttley, P., Markowitz, A. G., et al. 2016, MNRAS, 461, 3145

Velikhov. 1959, Soviet Ast.., 36, 1398

Vishniac, E. T., & Cho, J. 2001, ApJ, 550, 752

Walker, J., & Boldyrev, S. 2017, ArXiv e-prints, arXiv:1704.08636

Wilson, O. C. 1978, ApJ, 226, 379

Wu, M.-C., Xie, F.-G., Yuan, Y.-F., & Gan, Z. 2016a, MNRAS, 459, 1543

—. 2016b, MNRAS, arXiv:1604.02283

Yu, Z., Yuan, F., & Ho, L. C. 2011, ApJ, 726, 87

Yuan, F., Bu, D., & Wu, M. 2012, ApJ, 761, 130

Yuan, F., & Bu, D.-F. 2010, MNRAS, 408, 1051

Yuan, F., Cui, W., & Narayan, R. 2005, ApJ, 620, 905

Yuan, F., Gan, Z., Narayan, R., et al. 2015, ApJ, 804, 101

Yuan, F., & Narayan, R. 2014, ARA&A, 52, 529

Zdziarski, A. A., & Gierliński, M. 2004, Progress of Theoretical Physics Supplement, 155, 99

Zhou, X.-L., Zhang, S.-N., Wang, D.-X., & Zhu, L. 2010, ApJ, 710, 16

Ziegler, U., & Rüdiger, G. 2001, A&A, 378, 668